Multiscale approach for the pore space characterization of gas shales

Natalia Matskova

THESE

Pour l'obtention du Grade de

DOCTEUR DE L'UNIVERSITE DE POITIERS

(Faculté des Sciences Fondamentales et Appliquées)
(Diplôme National - Arrêté du 25 mai 2016)

Ecole Doctorale : **Gay Lussac**

Secteur de Recherche : **Terre solide et enveloppes superficielle**

Présentée par :

Natalia Matskova

****

APPROCHE MULTI-ÉCHELLE POUR LA CARACTÉRISATION DE L'ESPACE POREUX DES RESERVOIRS PETROLIERS ARGILEUX NON CONVENTIONELS

****

Soutenue le 06/07/2018

devant la Commission d'Examen

****

JURY

Rapporteur : *Laurent Michot (Directeur de recherche CNRS)*
Rapporteur : *Professeur Yves Geraud*
Examinatrice : *Docteur Claire Fialips*
Examinatrice : *Professeur Patricia Patrier*

Directeur de Thèse : *Professeur Philippe Cosenza*

Co-directeur de Thèse : *Docteur Dimitri Prêt*
Co-directeur de Thèse : *Docteur Stéphane Gaboreau*

****

MULTISCALE APPROACH FOR THE PORE SPACE CHARACTERIZATION OF GAS SHALES

Acknowledgements

Abstract

Gas shale reservoirs are characterized by pore systems, associated with a heterogeneous spatial distribution of mineral and organic phases at multiple scales. This high heterogeneity requires a multi-scale & multi-tool approach to characterize the pore network. Such an approach has been developed on 7 cores from the Vaca Muerta formation (Argentina), which belong to areas with various hydrocarbon maturities, but with comparable mineral compositions. 3D µtomography and quantitative 2D mapping of the connected porosity by autoradiography have been applied at the core scale, localize and analyze the spatial heterogeneities, and to identify similar homogenous areas for localizing comparable sub-samples.

The correlative coupling of various techniques was applied to achieve quantitative balance of porosity and pore size distribution, from mm to nm scales on representative sub-samples and for the first time, on preserved blocks rather than crushed powders, even for nitrogen gas adsorption experiments. Results of autoradiography are in very good agreement with other total bulk porosities, indicating that all pores are connected and accessed by the ^{14}C-MMA used for impregnation. Decreased total porosity and pore throat/body sizes were also observed as organic matter maturity increased.

An innovative approach for electron microscopy images acquisition and treatment provided large mosaics, with the distribution of mineral and organic phases at the cm scale. The correlative coupling with the autoradiography porosity map of the same zone, revealed the spatial correlations between mineralogical variations and porosity.

Key words: Earth science, clay, scanning electron microscopy, x-ray tomography, unconventional reservoirs, shale oil and gas, porosity, correlative imaging.

Résumé

Les réservoirs pétroliers argileux sont caractérisés par des systèmes de pores associés à une distribution spatiale hétérogène à plusieurs échelles des phases minérales et organiques. Cette hétérogénéité nécessite une approche multi-échelle et multi-outils pour caractériser le réseau de pores. Une telle approche a été développée grâce à la sélection rigoureuse de 7 carottes issues de la formation de Vaca Muerta (Argentine), avec différentes maturations d'hydrocarbures mais des compositions minérales comparables. La tomographie RX 3D et la cartographie de la porosité par autoradiographie ont révélé les hétérogénéités à l'échelle des carottes, et permis d'identifier des zones homogènes pour le prélèvement de sous-échantillons comparables et représentatifs.

Le couplage corrélatif de différentes techniques a permis d'atteindre un bilan quantitatif de la porosité / tailles de pores et pour la première fois, sur des blocs non broyés, notamment pour les expériences d'adsorption d'azote. Les résultats d'autoradiographie sont en accord avec les autres méthodes, indiquant que tous les pores sont connectés et accessibles par la résine d'imprégnation. Une diminution de la porosité totale ainsi que des tailles de pores a également été observée avec la maturation de la matière organique.

Une approche innovante pour l'acquisition et le traitement de mosaïques d'images MEB a fourni des cartographies de la distribution des phases minérales et organiques à l'échelle du cm. Le couplage corrélatif avec la carte de porosité par autoradiographie des mêmes zones, a révélé les corrélations spatiales entre variations minéralogiques et de porosité.

Les mots clés : science de la Terre, argile, microscopie électronique à balayage, tomographie aux rayons-x, réservoirs non-conventionnels, huile et gaz de schiste, porosité, imagerie corrélative.

Contents

List of figures

List of tables

Introduction

During the last decades, since 90's, the interest to the unconventional hydrocarbons sources has been significantly increased due to fast development of the industry, which requires more and more energy every year, and, at the same time, the depletion of the conventional sources. The development of alternative sources of energy (such as Sun, wind, alternative fuels, etc.) is still not covering the needs of the modern economic, while high productive atomic energy branch is remaining at a constant level with high risks during the nuclear plants exploitation.

Meanwhile, the exploitation of unconventional forms of gas and oil and the rapid shift from the dominance of traditional producers to plentiful domestic resources in many countries represents the dawn of a new era in global energy. There is the potential for job creation, business revitalization, the creation of markets for new by-products, greater energy independence, and newfound wealth for land owners, municipalities, and governments that hold subsurface mineral rights (Arthur and Cole, 2014).

In 2013, the U.S. Energy Information Administration estimated, that 4644 trillion cubic feet of gas-in-place could exist in potential shale gas formations in the United States (EIA, 2013). Shales, which are the organic rich sedimentary rocks, thus play an increasingly significant role in countries like U.S. for the energy supply. However, shale formation is still hard to evaluate using routine core analysis or petrophysical techniques, because of the compositional heterogeneity, pore structure complexity, and fine-grained nature of the rock. In the case of organic shales, large variations in formation properties and characteristics can exist both, laterally and vertically.

Understanding the geological and geochemical nature of gas shale formations and improving their productivity, thus, have been "at the heart of millions of dollars' worth" of research since the 1970's (Bernard et al., 2010). Indeed, the specific geological characteristics and structural features of unconventional formations create some potential risk due to fracturing processes, which, at the same time, may cause the uncontrolled migration of liquid hydrocarbons.

One of the main problem is water viability, as exploration requires big volumes of water, and the water contamination, which may impact to ground and surface water quality, public and private water supplies. Like that, the reduction of the local water resources quality has been detected in the areas of the long-term developing shale deposits in the Northern America (Vidic et al., 2013).

Another negative effect of uncontrolled gas or/and oil migration, which leads to the hazard impact on human infrastructure and environment by itself, is a release of naturally occurring radioactive materials and trace elements from the formation. Finally, the

atmospheric impacts of hydrocarbons extraction and utilization must be kept in mind to provide effective regulation and execution of such processes.

In general, the following targets of the investigations dealing with shale pore space can be underlined:

- disclosing the areas of hydrocarbons storage;
- describing the pathways of gas/oil migration from matrix;
- evaluation of parameters, controlling its microstructure of formation;
- improving the extraction techniques and productivity;
- preventing the negative effects from extracting processes;
- prediction and modelling of the reservoir properties (gas/oil storage capacity, permeability, mechanical behavior etc.).

To prevent the negative effects on the exploitation of these unconventional deposits, it is important to evaluate the potential behavior and the possibility for their safe extraction. The detailed investigation of shale rocks microstructure allows to disclose the areas of hydrocarbons storage and to evaluate the storage capacity of the formation, the mechanical behavior of the geological formation under hydraulic fracturing stress, and possible hydrocarbons migration pathways within the whole reservoir. Some works on different shales have been already presented in the literature being dedicated to the estimation of the parameters, which control their microstructure formation. The characterization of the pore sizes distribution, pores connectivity and pores morphology can improve the knowledge about the shale microstructure. These characteristics are crucial for the correct description of unconventional reservoirs and required for the preventing negative effects from extracting processes and for enhancement of the extraction techniques by themselves, that can lead to the significant increase of the productivity.

Since the 80's, all the studies, which are dedicated to the characterization of gas shale deposits, have improved the description of the microstructure of these organic rich formations. The published activities mainly described the pore morphology, volume and geometry using various petrophysical techniques to cover the multiscale pore network of such heterogeneous organo-rich sedimentary formations. Nonetheless, quantitative pore balance is still complicated when the data sets found in the literature are intercompared, as the evolution of the pore network with the varying maturity of the organic matter. The available literature data have not provided sufficient information to describe the pore size distribution in shales and the connectivity and interconnectivity between organic/inorganic compounds. More recently, with the evolution of imaging techniques, a more complete description of the pore space has been proposed as the pore hosted phases attribution. Meanwhile, the description has been done through high-resolution images limiting the representativity of the analyzed area in view of the heterogeneity and

the size of the probed sample (µm-mm). The quantitative spatial distribution of the pore network, using imaging techniques, is thus challenging because it requires the coupling of large probed areas (several mm) with high-resolution images. Nonetheless, these "big data" images are essential to provide accurate quantitative and representative characterization of these heterogeneous formations.

Thus, in view of these rich data set linked to the microstructure of non-conventional shales, and according to the spatial heterogeneities at the core/formation scales and the multi-scale pore system, only an integrated multi-techniques approach, applied on carefully localized core/sub-samples, is relevant to intercompare the different data obtained. To characterize the pore network of porous geological samples a lot of methods exist in the literature for both quantitative and qualitative descriptions. Classical bulk methods and innovative imaging techniques are used to improve the knowledge about shale microstructure. The characterization of the microstructure is suitable for petrophysical models to understand the hydrodynamic and mechanical properties of the geological formation. To characterize the porous space of the shale samples at a multiscale, the careful choice of the methods is required.

Based on the results of the bibliographical review, the present study is an attempt to develop:

(1) An integrated methodology to accurately characterize the pore network at a multiscale range in the connection with the varying microstructure at the core and at the formation scales. A combination of bulk methods (gas adsorption, NMR, He-pycnometry, MIP, etc.) was applied on a careful selection of a full cores set from zones with various hydrocarbons production, previously imaged by 3D µtomography to spatialize and localize the homogeneous regions of sub-sampling, which were later confirmed by autoradiography, to be analyzed without crushing. Such a set of sub-samples is expected to provide inter comparable data to supply quantitative balances of pore size distribution.

(2) An imaging technique to achieve a representative analyzed area with a resolution giving access to most of the microstructure details. This imaging technique is based on recent development in correlative imaging techniques offering the possibility to map large fields of view. The acquisition of large field SEM image mosaics and their treatment to calculate mineralogical map has been applied to correlate mineralogy and porosity map with a resolution of hundred nanometers within a pluri-centimetric field of view.

The manuscript presents four main chapters. A first one, chapter 1, which describes the different methods, employed to characterize the pore network of porous geological samples and could serve as a state of the art. A lot of methods are used and described in the literature for both, quantitative and qualitative, descriptions. Classical bulk methods and innovative imaging techniques are applied to improve the knowledge about shale

microstructure. The characterization of the microstructure is suitable for petrophysical models to understand the hydrodynamic and mechanical properties of the geological formation. The careful choice of techniques is required to characterize the porous space of the shale samples at a multiscale. A discussion about limitations, and advantages of the techniques is done to prove the interest of using integrated multi techniques approach.

The chapter 2 displays the materials and methods used in the presented study. Classical bulk techniques, as mercury intrusion porosimetry (MIP), gas adsorption, nuclear magnetic resonance (NMR) spectroscopy and innovative imaging techniques as autoradiography and correlative imaging methods are used and/or developed to characterize the pore size distribution of gas shale at different scales. The gas shale samples are presented through a brief geological setting, the sub sampling and preparation of the samples are described to well explain the importance and the impact on results of this step. Based on the available literature about the application of porosity techniques for shale samples investigations, an integrated multiscale and multitool approach has been developed. Using both, bulk and imaging, techniques the samples of various maturity from the Vaca Muerta formation (Neuquén basin, Western Argentina) were investigated.

The chapter 3 is a manuscript, submitted to AAPG bulletin, and displays a rigorous combined methodology to accurately characterize the spatial distribution of the pore network at different scales. The combination of methods was applied on a careful selection of full cores set from zones with various hydrocarbons production zones previously scanned by 3D µtomography to spatialize and localize the region of interest and to be able to provide integrated and inter comparable data. Combining the classical porosimetry methods, such as MIP, nitrogen adsorption, He-pycnometry and NMR spectroscopy, with the autoradiography porosity maps, the reliable pore balances were calculated for the shale samples for the first time.

The last one, chapter 4, is devoted to imaging techniques. Acquisition of backscattered electron images and mosaics through recent software development are presented. Mosaics allow to display large surface areas (further cm^2) with pixel size of hundred nanometers; such acquisitions generate mineral maps. The last step is the correlative imaging process, developed to superimposed porosity map, achieved by autoradiography, and mineral map. The correlative coupling of imaging data with porosity map and mineral map evinces the spatial distribution of porosity through large field of view and display the pore volume distribution with the variation of mineral and organic phases over the full core.

Chapter 1. Bibilographical review

Introduction

Shales are often considered as multiphase and multiscale sedimentary rocks. They are constituted of clay minerals and clay particles surrounding inclusions of other stiffer minerals (like carbonates, quartz, feldspars and pyrite) or more compliant organic phases. Clay containing rocks are characterized by a multiscale pore system, associated with variable spatial distribution of mineral and organic components. The accurate characterization of the pore network at multiple scales could be supplied by at least two groups of methodologies, which can be efficiently combined together: (i) the petrophysical laboratory techniques, often called bulk methods; and (ii) the imaging techniques, whose recent advances have provided many novel characterization opportunities for shale microstructures (e.g., Ma et al., 2017a). Both groups of methods may provide the information, from nanometric pores to centimetric scale, about spatial distribution of the microstructure, and are complementary to the log data, obtained at the scale of formation (cm – m), being the key methods used in this research. However, the transition between the description of a formation and centimetric sample is scale dependent and in the same way the structure of a sample can be disrupted during its extraction from the reservoir strata.

Despite the limitation on the probe size, which can be analyzed, bulk methods remain useful tools for deep investigations of shale microstructure. Most of the works, dedicated to the porosity investigations, are using a classification system that categorizes pore sizes according to physical adsorption properties and capillary condensation theory (Gregg and Sing, 1982). Pores are subdivided into three categories: macropores (>50 nm), mesopores (2–50 nm), and micropores (<2 nm) according to the IUPAC classification (Rouquerol et al., 1994; Thommes et al., 2015). This classification has been adopted in the present research.

Petrophysical laboratory techniques are based on introducing various fluids (gas/non-wetting liquids) with known characteristics within the pore space of the sample. Among others, the two most widely-used techniques, applied on shale samples are (i) gas or vapor (N_2, CO_2, CH_4, etc.) sorption methods and (ii) mercury intrusion porosimetry (MIP). Several factors dictate, how fluids migrate into and through porous media and ultimately react with the solid surfaces. These factors include the size, shape, distribution and interconnectivity of pores, as well as the chemistry and physical properties of the solid surfaces and fluid molecules (Melnichenko et al., 2012). Experimental data on pore size distribution, accessibility and adsorption selectivity may help to understand the fundamental limitations on the ability of shale for the storage and production of hydrocarbons. The production by itself is basically the process of gas

desorption from the pore space, which can be described under laboratory conditions. The minimum pore size, which can be probed by adsorption techniques is always limited by the diameter and the charge of the fluids molecules and their ability to penetrate the voids of the sample. Meanwhile, the detection range of these techniques, applying non-wetting fluids, is limited by the maximum pressure applied. Figure 1 illustrates approximate ranges of pore sizes probed by various bulk techniques, applied to shale structure investigations.

The development of imaging techniques allows also to use them as a tool for the investigation of nano-porous materials and localization of the pore space within the sample. Several methods exist nowadays to obtain digital images from the sample at different resolutions. Electron microscopy (in both, transmission and emission modes) and X-ray μtomography have found the widest application on shale samples. Their physical principles are widely described in the literature (see, among others, Goldstein et al., 2003; Reed, 1996). The main advantages of imaging techniques for microstructure investigations are: (i) their ability to directly connect the structural features with different phases; (ii) to visualize individual elements; and (iii) to quantify them directly from the image through image analysis techniques. The main limitation here is the large variety of resolutions, which control the minimum dimensions of the objects, which can be detected (Figure 1).

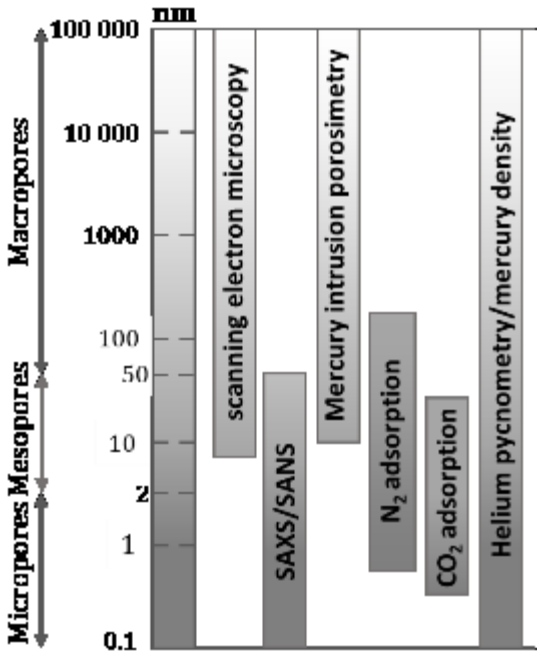

Figure 1. Resolution of various penetration methods, combined with imaging techniques, in common use for porous materials investigation.

Regarding the methods, which will be used in this work, the objectives of the first chapter are two-fold: (i) to critically review bulk and imaging techniques, used for the

characterization of shale microstructure; and (ii) to outline, how these techniques have been applied on shales, to address fundamental issues about porosity and texture. In the context of this review, it seemed also useful to recall the main geological features of the nature of shales and shale reservoirs.

Note that all the values given in the following chapter are directly extracted from the corresponding literature sources. To simplify the comparison for the readers, the Table 23 in Annex I represents the conversions of used parameters to system SI-units (Taylor and Thompson, 2008).

1.1. General characteristics of shales

Liquid hydrocarbons (mainly natural gas, but some oil as well) are trapped in subsurface formations called "reservoir rocks." Despite this terminology, these resources are not contained in very large, continuous "pools", but rather minuscule pore volumes between the grains, that make up the rock porous matrix. The term "unconventional gas" covers three main types of natural gas resources: shale gas, tight gas and coalbed methane (also known, as coal seam gas). Conventional and unconventional hydrocarbons differ not by their chemical compositions (they all are natural products), but rather by the geological characteristics of their reservoir rock (Figure 2).

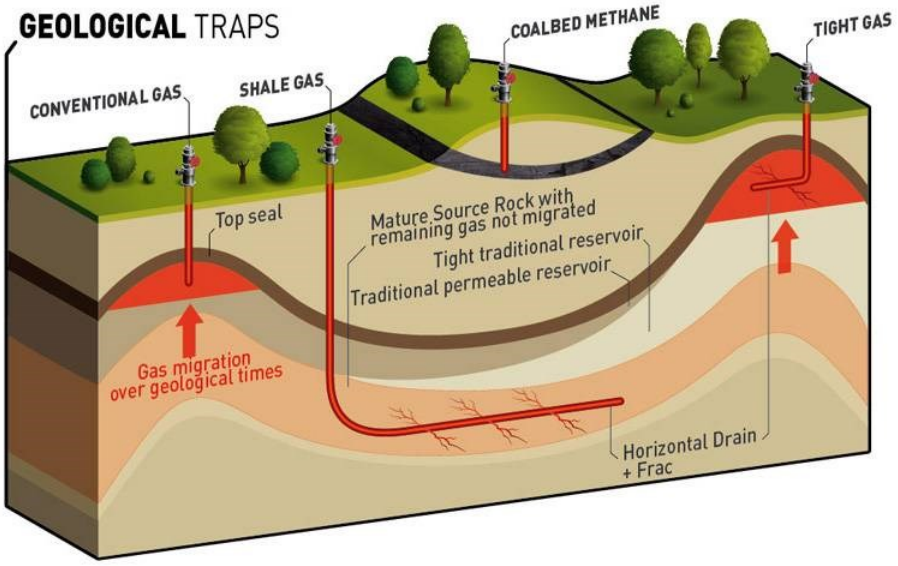

Figure 2. Geological characteristics of different types of gas reservoir rock (Total.com, 2014).

Unconventional reservoir formations are fine-grained, organic-rich, sedimentary rocks, classified as shales. These geological formations are both the source and the reservoir for oil and natural gas, unlike conventional petroleum reservoirs. The Society of Petroleum Engineers (SPE) describes “unconventional resources” as petroleum accumulations, that are pervasive throughout a large area, and that are not significantly

affected by pressure exerted by water (hydrodynamic influences). They are also called "continuous-type deposits" or "tight formations". In contrast, conventional oil and natural gas deposits occur in porous and permeable sandstones and carbonates reservoirs. Under pressure exerted by water, the liquid hydrocarbons migrate upward from organic sources until an impermeable cap-rock (such as shale) and get trapped it in the reservoir rock. Although unconventional reservoir formations may be as porous as other sedimentary reservoir rocks, their extremely small pore sizes make them low permeable and relatively resistant to hydrocarbon flow. The lack of permeability means that the oil and gas typically remain in the source rock, unless natural or artificial fractures occur (Ratner and Tiemann, 2014).

"Shale" is a term, that has been applied to describe a wide variety of rocks, which are composed of extremely fine-grained particles, typically less than 4 microns in diameter, but may contain variable amounts of silt-size particles (up to 62.5 microns) (e.g., Lazar et al., 2015; Ougier-Simonin et al., 2016).

From the nanoscale up to macroscale, shales are heterogeneous rocks with variations in the structure, the spatial distribution of mineral and organic matter (OM) in sedimentary levels. Their structure can differ dramatically between shale deposits and within the same reservoir, as well as mineral composition, type and maturity of kerogen presented, etc. A brief literature overview indicates the great variability of such geological objects across the world, which depends on the nature of the formation and the diagenetic processes impacting this formation during its "lifetime". On the example of Barnett shale (Fort Worth Basin, Texas, USA), the variability at the reservoir scale (Figure 3.A) is evidenced by strong vertical variation of log data, reflecting variations of mineralogical composition, porosity and fluids filling, within the well. Several layers with various properties can be subdivided within 10 meters. Lamination can be observed on the μCT (computer μtomography) image at the core scale (Figure 3.B), evidenced by various grey levels indicating the layers of different composition within several centimeters of the core. At the millimeter scale, the presence of very thin laminations can still be easily distinguished from the thin-section micrograph within a single millimeter (Figure 3.C), while the pore space heterogeneity can be investigated at the micrometric-nanometric scale (Figure 3.D and Figure 3.E). The high spatial heterogeneity (vertical and lateral, to a lesser extent) within a single reservoir formation over large scale requires complex investigations to characterize it.

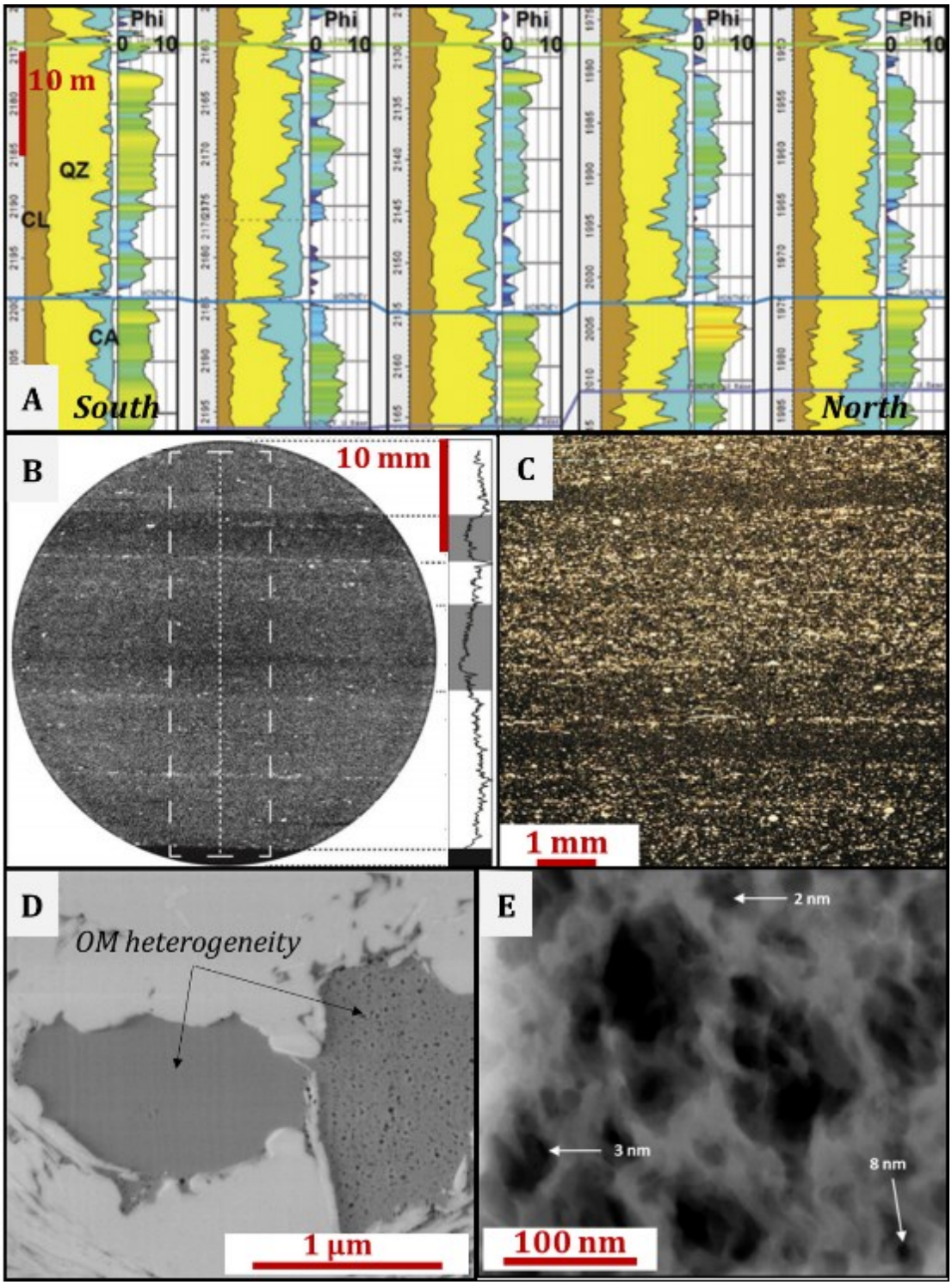

Figure 3. Illustration of spatial heterogeneities of shale formation at a multiscale on the example of Barnett shale (Fort Worth Basin, Texas, USA). A) North-to-south section through five wells (QZ=Quartz, CL=Clay, CA=Carbonate, Phi= neutron log porosity) (Close et al., 2010). B) µCT image of the core sample (200 keV, voxel size=41.56 µm) (Cronin, 2014). C) Thin-section micrograph (Loucks et al., 2009). D) FIB-SEM (focus ion milling coupled with scaning electron microscopy) image (accelerating voltage=1kV, working distance ~4 mm) (Curtis et al., 2012a). E) ADF STEM (angular dark field scanning transmission electron microscopy) image (Curtis and Ambrose, 2010).

The world largest and the most profitable shales have been already reviewed in details (Rezaee, 2015). Most current shale gas reservoirs have their origin as organic-rich mud deposits. These sediments have been settled in marine environments, in lakes, or in associated swamps and mires along the margins of lakes and seas. The particle size of such formations is small and does not exceed several micrometers (Passey et al., 2010). The distribution mineral phases within such objects is varying quite strongly as a function of sedimentation, burial and diagenesis processes. The main components can be distinguished from mineral composition, achieved on the well-known Northern American shales (Figure 4). The normalized mass fractions of carbonates (WCAR), sum quartz, feldspars and micas (WQFM) and clay minerals (WCLA) are presented on ternary plots, proposed for the classification of organic mudstones by Gamero-Diaz et al. (2012), and subdivided in sixteen different lithofacies. Figure 4.A displays the averaged bulk mineral composition for these various Northern American shales, while Figure 4.B represents the distribution of mineral composition, achieved for the Barnett shale samples by elementary capture spectroscopy (ECS) (Gamero-Diaz et al., 2012). These ternary diagrams highlight, that the mineralogical composition of shales varies as much within a same formation, as in between two different formations.

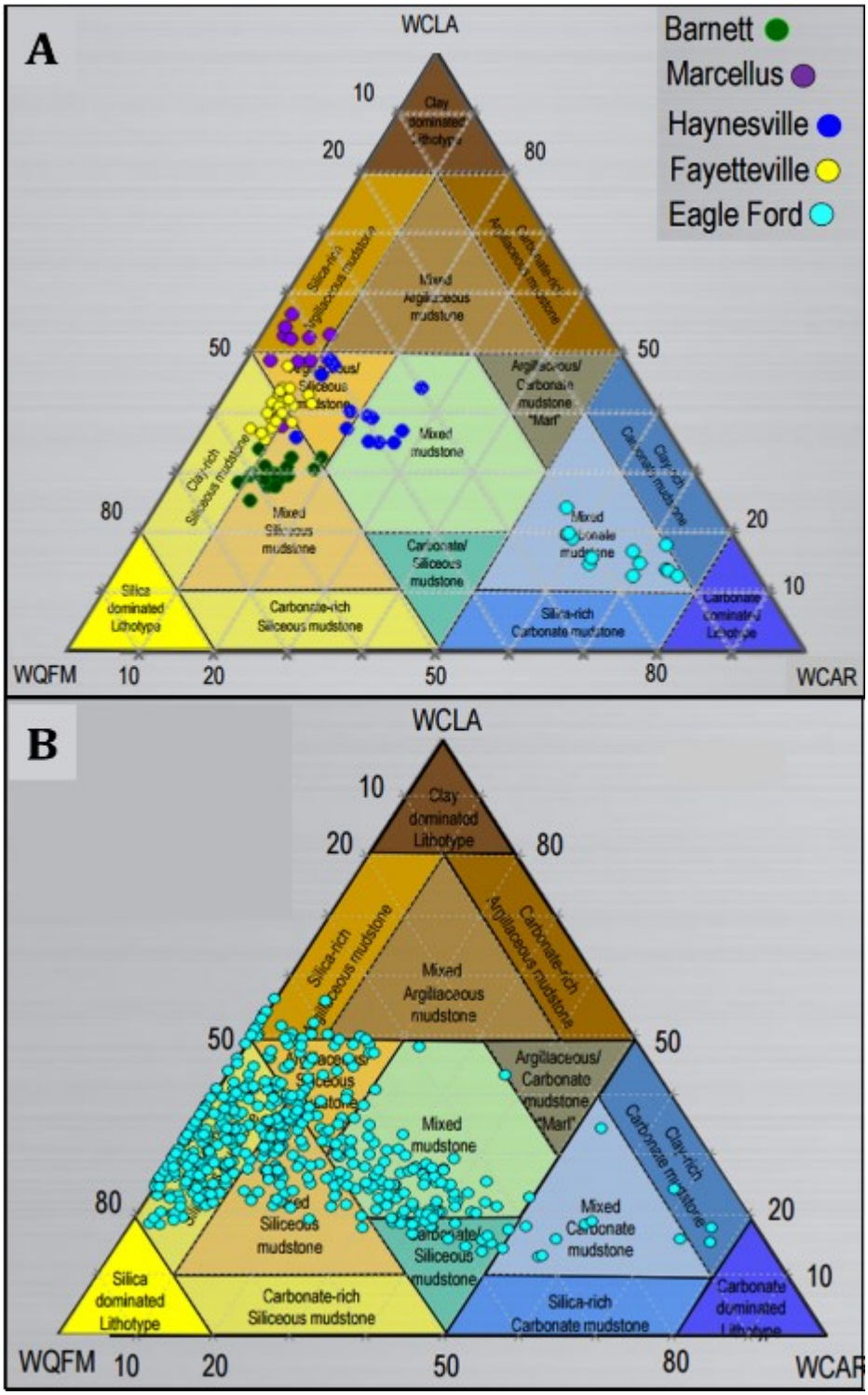

Figure 4. A) Variation of bulk mineral composition for Northern American shales; B) mineral composition distribution for Barnett shale samples (WCAR = mass fraction of carbonates, WCLA = of clay minerals, WQFM = of quartz/feldspar/micas) (Gamero-Diaz et al., 2012).

One of the common characteristics of pores within shale gas/oil reservoirs is general dimensions, which are an order of magnitude smaller (nano-/micrometer scale) than pores within conventional carbonate and sandstone reservoirs (generally micrometer scale or higher). Another characteristic of the shales formations is the highly

heterogenous pore network organization with high pore throat/pore body ratio (see, for instance, the review of Nelson (2009) or Loucks et al. (2012)), with pore throats dimensions generally at the detection limits of the most common porosimetry techniques. The pores size distribution and the pore network geometry affect directly the permeability and other mechanical properties of the reservoirs.

Unconventional gas/oil reservoirs are known as rich in solid OM, which is considered as a part of the rock fabric. The spatial distribution of solid OM has a significant effect on shales characteristics. The type of OM depends on the environment of deposition and the terminology varies from author to author. The term "kerogen" is often used for all total insoluble organic carbon (TOC), determined in the sample. For geochemists, "kerogen" is defined as a part of the organic material, which was not assimilated by microorganisms. It was turned into insoluble poly-condensate, due to chemical processes under "soft" conditions (low temperatures and pressures). Kerogen consists of macerals and amorphous matter (Tissot and Welte, 1984). In the literature, hydrogen-to-carbon (H/C) and oxygen-to-carbon (O/C) atomic ratios (Van Krevelen diagram) are often used to describe the several types of kerogen (Figure 5.A).

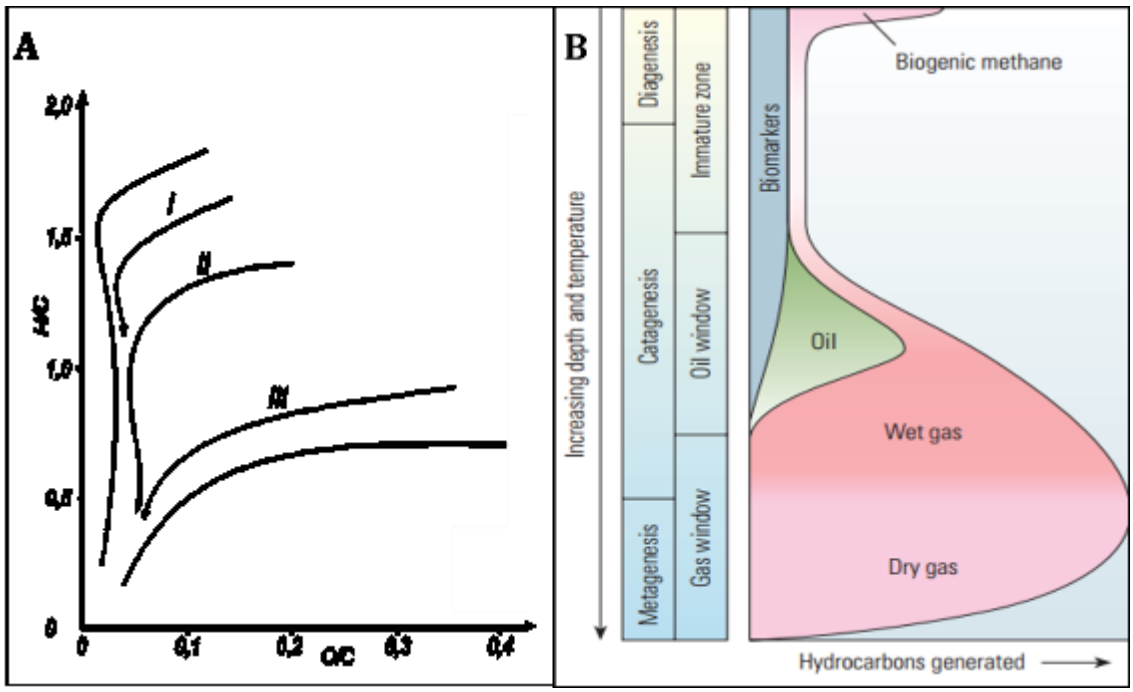

Figure 5. A) Van Krevelen diagram of three main types of kerogen (I, II and III), based on the elementary composition: hydrogen-to-carbon (H/C) ratio versus oxygen-to-carbon (O/C) ratio; and theirs evolution curves (after Tissot and Welte, 1984). B) Thermal maturation of kerogen (McCarthy et al., 2011).

There are three types of kerogen: (i) type I, which corresponds to high atomic H/C ratio (≥1.5) and low O/C ratio (<0.1), mainly consisting of lipid rich organic matter (aliphatic chains, particularly), originating from algal material or strong biologic

transformation of organic matter (mostly associated with lacustrine environment); (ii) type II can be found in most oil source and shale gas rocks, generated within marine sediments; (iii) type III (H/C<1.0, O/C up to 0.2-0.3), which is usually attributed to gas source rocks, does not contain esters groups (-COOR) and originated from terrestrial plants matter (Tissot and Welte, 1984).

According to Rezaee (2015), the total amount of carbon (TOC), measured in shale samples is usually in the 1.5 – 6 mass% range, rarely up to 10 - 13 mass% (measured for Devonian shale, Illinois, USA).

The kerogen maturation is a complex physical-chemical process, controlled by the conditions of kerogen environment at all the steps of organic matter evolution within the basin: accumulation/sedimentation, diagenesis, catagenesis and metamorphism. The illustration of thermal transformation of kerogen with generated products is presented in Figure 5.B. This process is not isolated in the geological formation and proceeds simultaneously with geological environment evolution. The model of oil/gas generation varies significantly for different reservoirs conditions and types of kerogen. The kerogen structure is affected by compaction, resulting from the increase in burial depth. At the same time, the thermal maturation with hydrocarbons generation results in the development of a complex pore network and induces over-pressure of fluids in the pore space (Tissot and Welte, 1984,). Due to the origin of these geological deposits, the hydrocarbons formation processes are in-situ source rocks phenomena within voids, where the products of kerogen maturation accumulate due to limited migration pathways. One of the direct result of these processes is the modification of the kerogen pore network. The gas production within the maturation processes leads to the increase of the porosity in the organic matter, due to expansion of the gaseous products of solid OM transformations. Meanwhile, the compaction over the diagenesis leads to the decrease of the formation total porosity, and hence of the kerogen.

Due to limitations of the techniques, classically applied for structural analysis at nanoscale, the investigations of kerogen's structure and its change with the maturation processes are difficult. Recent applications of molecular modelling tools helped to create the model of kerogen's nanostructure, which was found to be in a good agreement with experimental data (Bousige et al., 2016). Figure 6 illustrates the molecular models created for the kerogen of various origins. In summary, the overall picture, which thus emerges from these molecular calculations, is that the rupture mechanisms of gas shale at nanoscale are predetermined by the kerogen's maturation (Bousige et al., 2016).

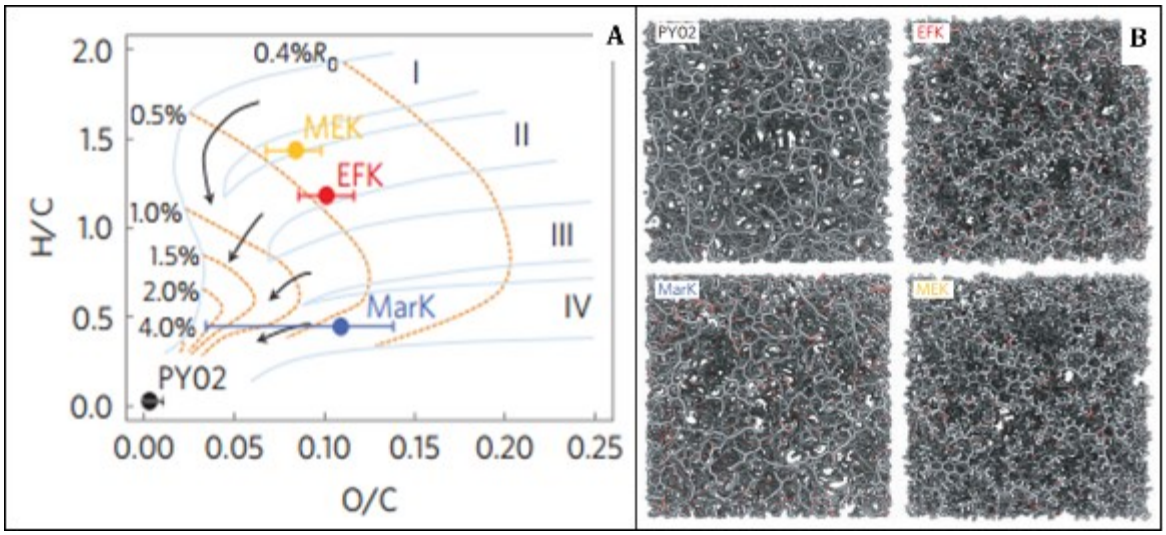

Figure 6. A) Van Krevelen diagram with the representation of the chemical evolution of immature kerogens of varying sources (Type I, II, III and IV) with increasing levels of maturity: MEK is a type IIS (sulfur reach) kerogen, whereas EFK and MarK are type II marine kerogens, VR_{eq} = 0.55, 0.65 and 2.2%, respectively, PYO2 is mineral free shungite; B) molecular models of the four samples under study with density of 1.2 g/cm^3, carbon, hydrogen and oxygen atoms are represented in grey, white and red, respectively; the box size is 50 Å in each direction (Bousige et al., 2016).

The data set on the shales microstructure, available in the literature, is mostly dedicated to dry gas samples (high maturity of solid OM). Indeed, the increase of the research activity in liquid producing shales investigation has been noticed only during last decade. Meanwhile, the organization of the pore space in the gaseous system is very different from oily shale, where more complicated pore surface/liquid hydrocarbons interactions occur.

The presence of the OM (both solid kerogen and liquid hydrocarbons) and hydrophilic minerals (especially clay minerals) also leads to complex solids-fluids interactions in these rocks. First of all, the "mixed" wettability of the porous network is impacted by the presence of matured solid OM, which can create pockets of the matrix to become oil wettable (Borysenko et al., 2009). Wettability is an important rock property, and it is defined as the preference of a solid to stay in contact with one fluid, rather than with another. "Mixed" wettability of the shale formation means that part of the rock grains is oil-wet, and another part is water-wet. Such rocks are often called "intermediate-wet" (Zhang et al., 2014). The work of Odusina et al. (2011), based on imbibition experiments with dodecane and water, has shown that shale samples from Northern America are of "mixed" wettability. The amount of imbibed oil is not only function of TOC content, but it also depends on the pore volume associated with organic matter. The results of measurements obtained on various shale samples are presented in Table 1.

Table 1. Summary of imbibed volumes, measured from weight changes after the second imbibition sequence. Reported volumes are normalized to the bulk volumes of the samples (cm^3/cm^3) (Odusina et al., 2011).

Formation	TOC range, %	Brine (NaCl), cm^3/cm^3	Dodecane, cm^3/cm^3	Ratio of Brine to Dodecane
Barnett	3.2 – 7.6	0.004	0.006	0.66
Eagle-Ford	2.3 – 6.3	0.014	0.015	0.95
Floyd	3.2 – 5.2	0.011	0.012	0.90
Woodford	0.2 – 8.6	0.003	0.015	0.19

The produced gas can be stored in shale resource rocks following two principal processes: as gas physically adsorbed and chemically absorbed, in a liquid state or within the organic matrix and as free gas in pore spaces, created either by OM decomposition or other diagenetic or tectonic processes (Jarvie et al., 2007).

To characterize the reservoir properties, for instance to evaluate the total hydrocarbons storage capacity or to estimate the permeability of the shale formation of interest, many parameters are needed. Based on key reservoir parameters that are available, the components balance calculations can be performed. For example, a simple model for gas shale was proposed by Ambrose et al. (2010) (Figure 7) aiming at prediction of gas in-place in terms of a total gas pore volume of the reservoir.

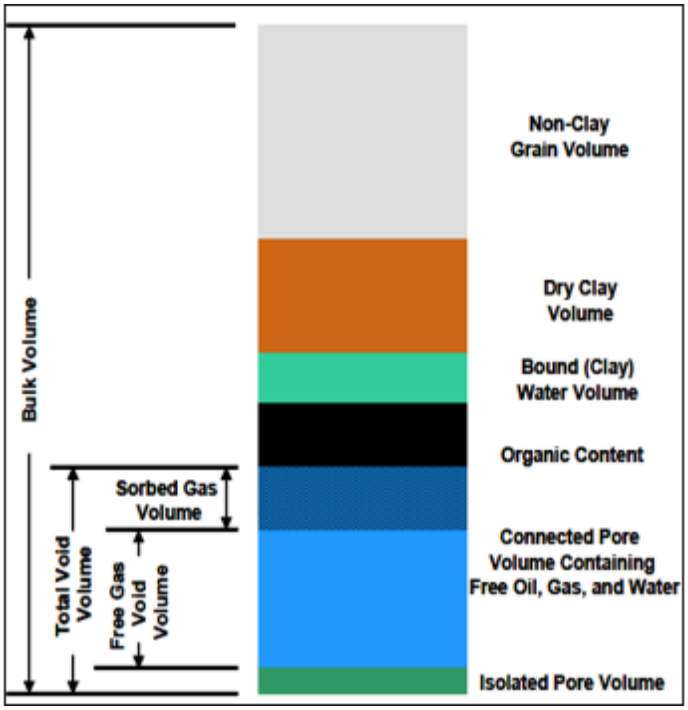

Figure 7. Schematic petrophysical model showing volumetric components of gas-shale matrix (Ambrose et al., 2010).

According to Ambrose et al. (2010), the total porosity can be determined on the basis of laboratory measurements of bulk sample density (by mercury intrusion) and solid density (by helium pycnometry). Total water and oil volumes can be calculated by weight difference and an assumed oil density of 0.8 g/cm^3. Hence, the total gas in-place, G_{st} [scf/ton], can be estimated with Equation 1.

Equation 1.

$$G_{st} = G_f + G_a + G_d,$$

where G_f, G_a and G_d are volumetric fractions of liquid hydrocarbons stored in the pore space as free gas, gas adsorbed on the surface of pores (quantified by adsorption isotherm measurements) and gas dissolved into liquid hydrocarbon and the formation water (often considered as negligible), respectively. Various approaches are discussed for the evaluation of these volumetric fractions (Hartman et al., 2008; Cui et al., 2009; Ambrose, 2011; Holmes et al., 2012), but all of them propose very simplified models, due to the limitations of the input parameters measurements.

Meanwhile, these types of models are suitable for the description of dry gas source rocks, but the presence of liquid hydrocarbons may change the calculation approach. Indeed the oil molecules can approach or exceed the size of pore throats, and the viscosity of oil is 20 times higher, than that of gas (McCain, 1990). The expandable interlayer space of smectite can also be a potential site for the oil polar molecules, producing a complex organo-clay association by incorporation of molecular-scale OM within the interlayer space (Berthonneau et al., 2016). At the same time, the presence of narrow pores throats induces the capillary bounding of water and liquid hydrocarbons, which properties would differ from the clay-bound and free liquids (Lewis et al., 2013).

Although petrophysical models, as proposed on Figure 7, allow to provide a simple reservoir description, accurate model for the real shale system is much more complicated and remains a challenging task. Due to such a complex multi-phase composition of shale, the pore network is expected to be multi-scale (Figure 8): from the interlayer space of clay minerals (nm scale) up to fractures network (mm scale).

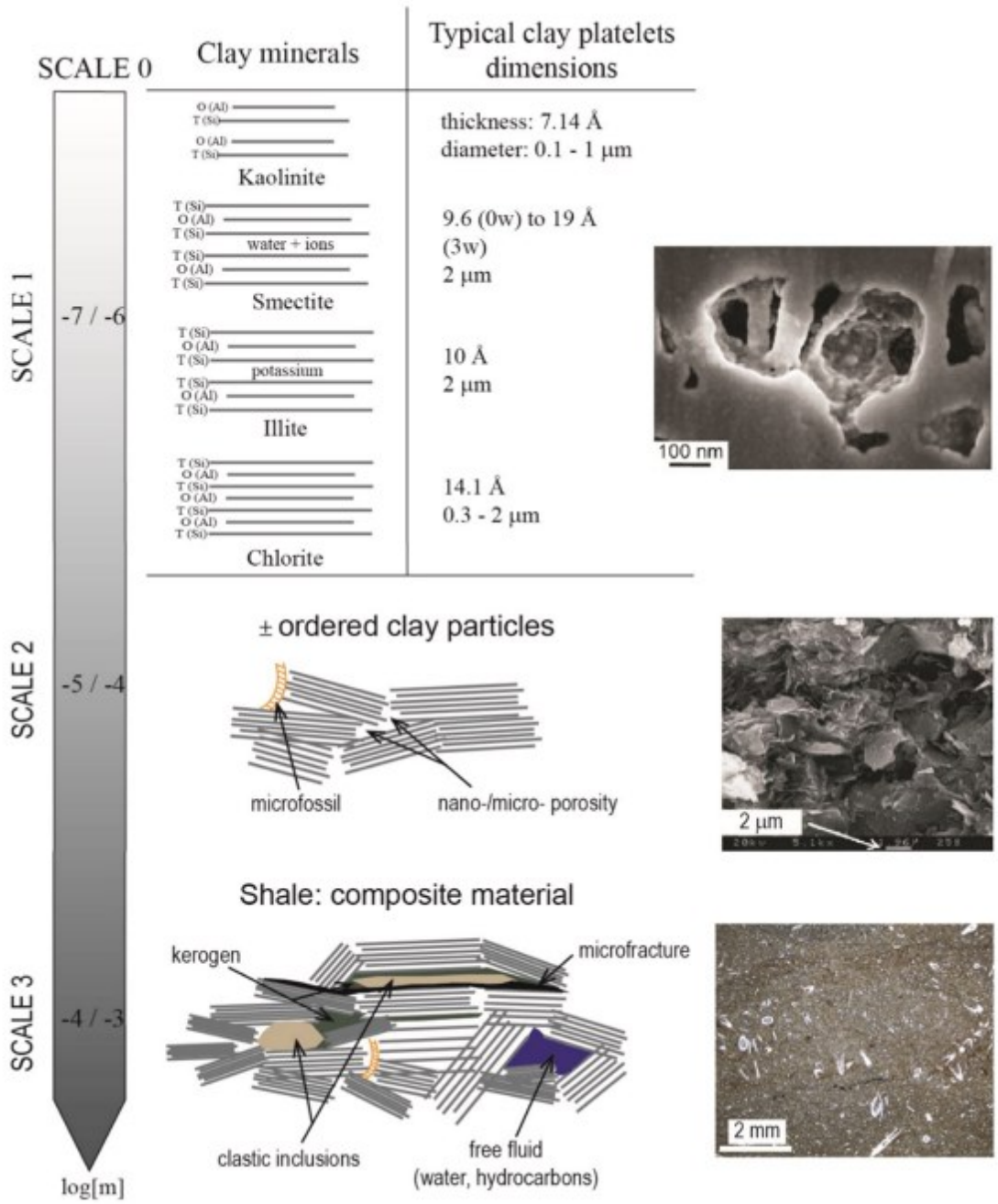

Figure 8. Multiscale structure of shale rocks with various heterogeneities, including pores at several scales, clays, kerogen patches and clastic grains (quartz, calcite, feldspar) embedded into the clay matrix. Relative dimensions of common clay minerals, and schematic view of the microstructure of shales at various scales (Ougier-Simonin et al., 2016).

1.2. Methods of shale pore space characterization

The precise characterization of the pore network of shales from macroscopic to nanoscopic scale requires a combination of several laboratory methods. The methods, which imply the penetration of fluids within the pore network, may be classified as indirect techniques, since they require the application of various models to describe the pore network organization. To convert the directly observed result to the pore size distribution (PSD), different assumptions should be considered.

From these methods, beyond the PSD description, the information about sample density may be obtained, to calculate the total porosity. While He-pycnometry is widely applied technique for grain density measurements with high precision (Thommes et al., 2015), different methods may be used to determine the bulk volume and corresponding density of the sample. The calculation of total porosity is based on the bulk and grain densities (Equation 2), where φ^T is the total porosity, V_p – volume of pores [m^3], V_s – volume of the solid phases [m^3], V_t – total volume of the sample [m^3], ρ^{bulk} – bulk density [kg/m^3] of the dried sample and ρ^{grain} – grain density [kg/m^3].

Equation 2.

$$\varphi^T = \frac{V_p}{V_t} = 1 - \frac{V_s}{V_t} = 1 - \frac{\rho^{bulk}}{\rho^{grain}}.$$

1.2.1. Sample preparation

Sample preparation is one of the most crucial step, which controls the reliability of the bulk measurements results. First, the selected drying method may directly impact the pore volume available for the measurements. Secondly, crushing the samples, which is a common preparation technique used for bulk measurements, may impact the microstructure organization. All the literature data, discussed in the present bibliographic section, have been achieved on crushed samples down to powder or broken into pieces (results obtained on well-preserved blocks were not found in the available publications). The application of outgassing, as well as time of outgassing, may lead to the split of the sample, the pore closure, some microstructural elements disruption, among many other artifacts.

Houben et al. (2016a) have reported gas adsorption measurements on small pieces of samples (~ 200 mg), which were either used as a “whole sample” or crushed into a coarse powder. The authors have not indicated in their paper if the displayed curves of adsorption and MIP were obtained from the coarse powder or from their “whole samples”.

According to the API core analysis practice (PR40-1, 1998) drying temperature should vary from 60°C for the shale samples up to 116°C for sandstones. In some case, this temperature range is applied to the shale samples (Chalmers et al., 2012b; Clarkson and Bustin, 1999b; Houben et al., 2016a, among many others). In some publications, the drying temperature is varying according to the method of analysis, like in the work of Kaufhold et al. (2016), for which outgassing at 150°C is proposed for CO_2 adsorption measurements (probing microporosity, Figure 1), while other methods are applied on samples dried at 105°C.

1.2.2. Mercury intrusion porosimetry

Mercury intrusion porosimetry (MIP) is widely accepted as a standard measurement of total pore volume and pore size distribution in the macro- and mesopores ranges (Thommes et al., 2015). This method is routinely applied and most of the researchers are using it to obtain the references values of total porosity. Most of the time, no details and supplementary data are given, including the shape of intrusion and extrusion curves or the apparent dry density.

Similarly, capillary pressure curves are a standard way to classify the porosity of reservoir rocks, that correlates to their capacity to produce hydrocarbons. For standard reservoir rocks, assuming comparable porosity, the higher the pressure, at which mercury intrusion occurs, the lower the permeability (Sigal, 2013).

Theoretically MIP relies on Washburn's equation (as well as other non-wetting intrusion techniques) (Equation 3), which indicates the minimum pressure, required for the fluid to penetrate the pore with given size (Washburn, 1921). The diameter of the intruded idealized cylindrical pore (d_p, [m]) is determined through surface tension of mercury-air interface (γ, [Pa·m]), which is temperature dependent, and contact angle between mercury and pore wall (θ), which is temperature and material type dependent, at each point of applied pressure (P_i, [Pa]).

Equation 3.

$$d_p = -4\gamma \cos\theta / P_i.$$

The kinetic diameter of Hg atom is around 0.3 nm, and the modern techniques allow applying high pressure up to 60'000 psi (or $4.14 \cdot 10^8$ Pa), which corresponds to the pore throat diameter of ~3 nm. This allows to apply the mercury intrusion for probing the pores in the range ~100000 – 3 nm.

While the surface tension of mercury is only temperature depended, solid/liquid contact angle varies as a function of the pores surface material (Figure 9). In the literature various values of θ are applied for the PSD calculation in the diapason of 130-140°.

Meanwhile, this range provides only a slight shift along d_p axe. For example, at maximum pressure of 60'000 psi, with θ =130° and γ (mercury-air) = 485.5 mN·m^{-1} (at 25°C), d_p is equal to 3.017 nm, while with θ =140°, d_p is 3.596 nm.

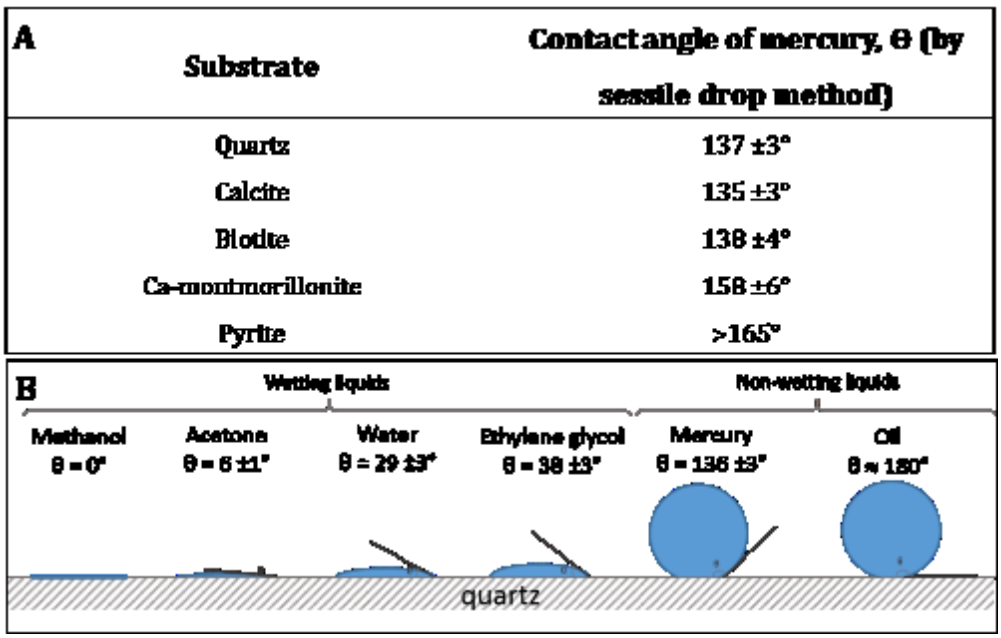

Figure 9. A) Interfacial contact angle of mercury, measured on various substrates; B) interfacial contact angle of various substrates on the surface of quartz (Ethington, 1990; information for pyrite is from Bagdigian and Myersont, 1986).

The main limitation, which is provided by Equation 3, is the geometry of pores. Equation 3 is often associated with cylindrical pores, for which the throat and the body are equal, considering porous materials, which contain the bundles of capillaries with different sizes (Lowell et al., 2004). In case of more complex pore network organization, like in shale samples, where throats are expected to be much smaller than the bodies (see section 1.1), this technique would provide information only about pores' throats. In addition, the equilibrium at each pressure step should be ensured, to allow the mercury to fill all the voids. Monitoring the amount of mercury intruded into pores as a function of increasing applied pressure, therefore, leads to pore throats sizes distribution. Meanwhile, often in the literature, the distribution, obtained by MIP is referred as pore body sizes.

Although, the mercury extrusion curves are not always provided for the shale samples (mostly only intrusion ones), they may give some useful information about the pore network of probed material. In most of the cases, a hysteresis appears between the intrusion and extrusion curves (Figure 10). Currently, three explanations of hysteresis loop, can be found in the literature: (i) the ink-bottle pore assumption (intrusion describes only the pore throats distribution, but not the pores body sizes); (ii) network

effects (an extension of the ink-bottle concept which is supported by complex computer simulations); and (iii) a pore potential theory (whereby mercury is not subjected to pore wall interactions during its initial intrusion but is partly held in pores upon extrusion as a function of wall interactions) (Leon y Leon, 1998).

For the total porosity calculation (φ_{MIP}^{T}, Equation 2), the bulk density can be estimated, when the sample is immersed in mercury, before the first pressure step (ρ_{MIP}^{bulk}, [kg/m^3]). The grain density may be measured with the last pressure step, assuming that mercury fills all the available pores, and no closed porosity is expected in the sample (ρ_{MIP}^{grain}, [kg/m^3]) (Micromeritics, 2012).

The disadvantage of the intrusion techniques is the destruction of the sample, excluding the opportunity to repeat the test on the same sample. This way of operating requires careful localization of studied rock volumes to be able to perform the intercomparison and correlation of the results, which have never been described in the available literature data sets. The dimensions of the sample, which can be probed by MIP, varies a lot and is limited only by available penetrometers (millimetric – centimetric sample), but always in the size range of observed laminae (Figure 3).

The raw intrusion curves may contain at least two experimental artifacts. The first one is associated with the compressibility of the mercury, the compressibility of some parts of the capillary set and that of the sample itself under high pressure (due to the existence of substantial amounts of ductile components, such as organic matter). This compressibility/compression effect, occurring in the region of maximum pressure, results in extra mercury injection into the system. This extra injected mercury volume is not part of the actual pore volume and must be corrected (Peng et al., 2017). To eliminate this effect, "blank" measurements are usually performed (measurement of mercury intrusion into the empty capillary, as these components contribute the most to the estimation error, while the compressibility of the sample is very difficult to account for, and often is assumed as negligible). Results of "blank" measurements are subtracted from the curves measured on samples.

The second source of error occurs at the low-pressure region. In the Micromeritics' manual book (Figure 10) the example of such an artifact is presented. At the low-pressure step, the high intrusion volume of mercury, which contributes up to 20% of the total intruded volume, was correlated with interparticle filling by mercury, so-called "confirmation error". Indeed, in MIP analysis, before mercury enters the pores of the sample, it first fills the voids between grains and irregularities on the crushed sample surfaces. The voids become smaller under increasing pressure; therefore, higher pressure is needed to fill all the voids before mercury intrusion to the actual pore system. This extra volume of injected mercury, that fills the grain voids and irregularities of the sample

surface, is not part of the pore volume in the sample and has to be corrected as well (Peng et al., 2017).

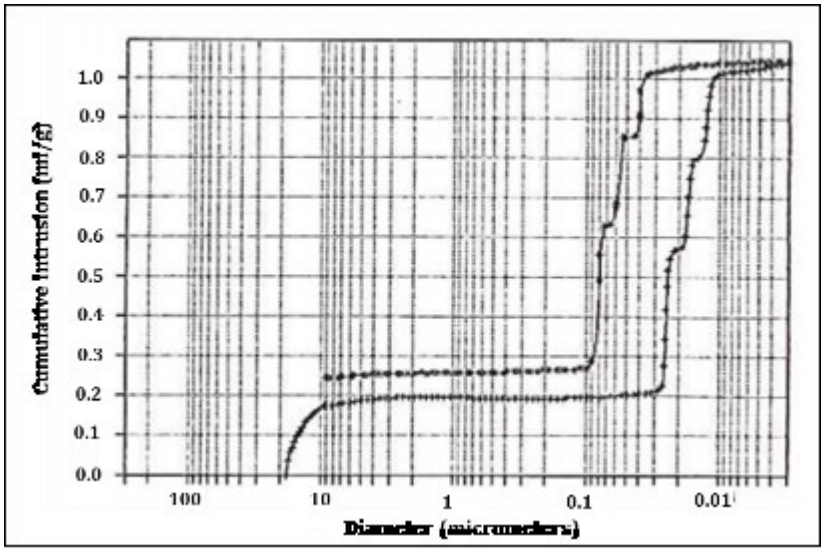

Figure 10. Uncorrected data from analysis of a glass sample with controlled porosity created of a mixture of three pore sizes. The apparent intrusion at size above 10 μm is explained to be due to interparticle filling (Micromeritics, 2012).

Considering unconventional hydrocarbons reservoirs, Sigal (2013) published an extensive set of mercury capillary pressure measurements from 92 plugs, taken from two Barnett-shale gas wells. The author has described several types of intrusion curves, which can be divided in four types: (i) Type 1 incremental intrusion curve with archived maximum; (ii) Type 2, incremental intrusion curve, which is "flat" at 60,000 psi; (iii) Type 3, curve with no apparent maximum; and (iv) Type 4, with no mercury intrusion. The incremental curves were normalized to the pore volume calculated from the He-porosimetry (Figure 11). Sigal (2009) reported a study, dedicated to the blank correction methodology on the samples, such as tight gas sands, in order to improve the post treatment and the interpretation of MIP intrusion/extrusion curves. Clarkson et al. (2013) published mercury intrusion curves for different shale deposits (Figure 12). Most of the estimated pore-throats have a diameter in the order of 30-100 Å, even if the authors erroneously assume to probe pore size distribution. Therefore pore sizes inferred from MIP are very often reported to be underestimated due to the ink-bottle effect (Münch and Holzer, 2008). Pores' "bottle" – shape is common for plate shaped clay particles and describes the pores with the throat radius smaller than the body radius.

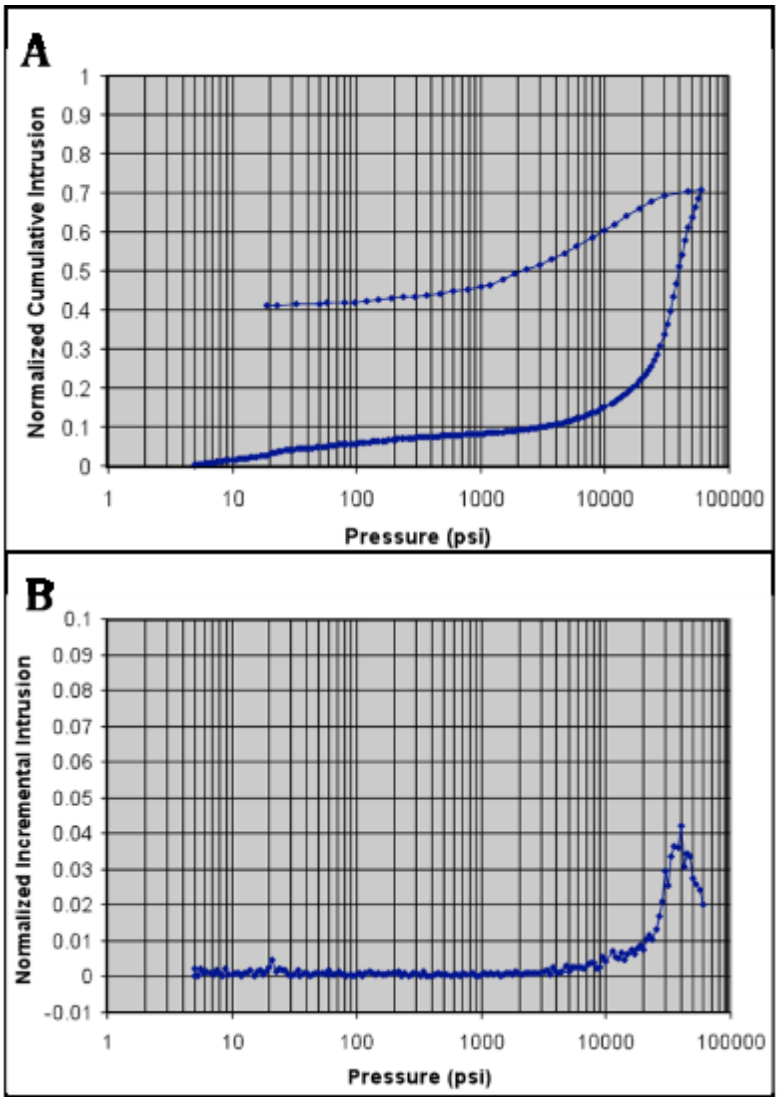

Figure 11. Capillary pressure curve for Barnet shale sample: A) normalized cumulative intrusion/extrusion curves; B) normalized incremental intrsuion curve (Sigal, 2013).

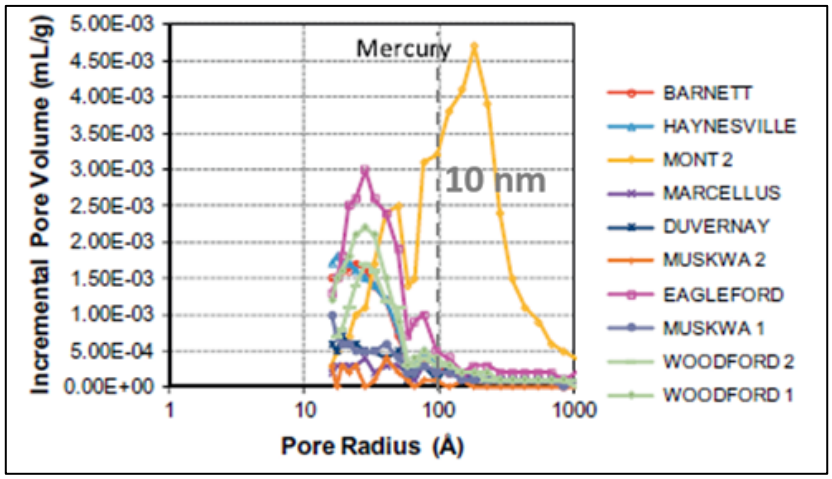

Figure 12. Incremental pore throats sizes distributions obtained for various shales (Clarkson et al., 2013).

In addition, most of the reported results obtained on shale samples show that the MIP measurements results often take place at the detection limits of the method, due to very small pore throats of the samples. This is, for example, illustrated in Figure 11, which demonstrates non-equilibrated (with continuous increase up to the maximum pressure, without any plateau) intrusion curve at the end of the test ("type 3" curve following the classification, proposed by Sigal (2013)). This indicates, that the method chosen in that case does not allow to reach the smallest pores within the sample, leading to an underestimation of grain density and total porosity.

1.2.3. Gas adsorption methods

Gas adsorption methods are extensively used for investigating porous materials. Since the first study of adsorption of nitrogen were performed by J. Dewar in 1904 (reviewed by Sing, 2001), these methods were developed for all kind of porous materials, and experiments were performed with different gases in a wide range of temperatures and pressures. For shale samples, these methods are often used to determine reference values for the pore size distribution and surface area calculations, when several methods are applied.

Low-pressure adsorption measurements are more convenient for pores system characterization (pore volume, pore size distribution, surface area, pores morphology and connectivity) than high-pressure methods, since the application of high pressure may lead to the pores collapse. The temperature, under which the isotherms are obtained, also depends on the gas applied for the measurements. Normally, it corresponds to the optimal physical state and kinetic diameter of the adsorptive (adsorbate, if liquid). Some of the gases, which have found an application for adsorption/desorption experiments on shales are presented in the Table 2.

Table 2. Average diameters of different gases (after Vermesse et al., 1996; data for CO_2 is from D'Alessandro et al., 2010).

Gas	Kinetic diameter, nm
Helium (He)	0.256
Water (H_2O)	0.265
Neon (Ne)	0.276
Carbon dioxide (CO_2)	0.330
Argon (Ar)	0.341
Krypton (Kr)	0.369
Nitrogen (N_2)	0.370
Methane (CH_4)	0.382

Two gases are mostly used for the characterization of porous materials: nitrogen (N_2) and carbon dioxide (CO_2). As for other penetration techniques, resolution of gas adsorption result is limited by the data treatment approach selected by the operator. The shape of adsorption/desorption isotherms can provide the information about adsorption energy, monolayer capacity, specific surface area and assessment of microporosity/mesoporosity of the sample. There are several methods, which can be used to analyze the adsorption/desorption data to extract the pore size distribution of the sample. The method of Brunauer, Emmet, and Teller (BET) is employed to determine surface area based on a model of adsorption, which incorporates multilayer coverage. The BET–method is the mathematical transformation, applied for calculating the monolayer capacity and energy constant (C), which depends on the adsorption energy of the first layer of gas molecules (Lowell et al., 2004).

Classically, the PSD for mesopores and macropores is achieved by N_2 adsorption/desorption experiments. The method of Barrett, Joyner, and Halenda (BJH) is a procedure for calculating pore size distributions from experimental isotherms using the Kelvin model of pore filling. This formalism integrates the pore diameter on the adsorption isotherm for each relative pressure. Application of the BJH treatment, which uses the Kelvin equation (Barrett et al., 1951), allows to distinguish both pores bodies and throats sizes, assuming cylindrical pores (Equation 4). This equation implies several assumptions on the pore network: (i) pores are perfect cylinders, open at both ends; (ii) gas perfectly wets the pores' walls ($cos\ \theta = 1$); (iii) nitrogen is considered to be in a liquid state.

Equation 4.

$$R_{gas}T \times \ln\left(\frac{P}{P_0}\right) = -f\gamma V_N \frac{\cos\theta}{r_k},$$

where r_k – Kelvin radius [m], γ – liquid nitrogen surface tension [Pa·m], θ – liquid nitrogen/sample contact angle, V_N – molar volume of adsorbed nitrogen [m^3/mol], f – form factor, R_{gas} – the gas constant (8.3144598(48) kg·m^2·s^{-2}·K^{-1}·mol^{-1}), T – absolute temperature [K], P/P_0 – relative adsorption/desorption pressure. The form factor $f = 1$ should be selected for cylindrical meniscus, expected for adsorption (Figure 13), and $f = 2$ – for the hemispherical meniscus, when applied for desorption. The term r_k indicates the radius, into which condensation occurs at the required relative pressure. The increasing thickness of the multilayer adsorbed on solid surface when the relative pressure increases is added to obtain the true pore radius r_p, [m] (Equation 5; Figure 13).

Equation 5.

$$r_p = r_k + t,$$

where r_k – Kelvin radius [m], t – monolayer thickness [m] (Figure 13).

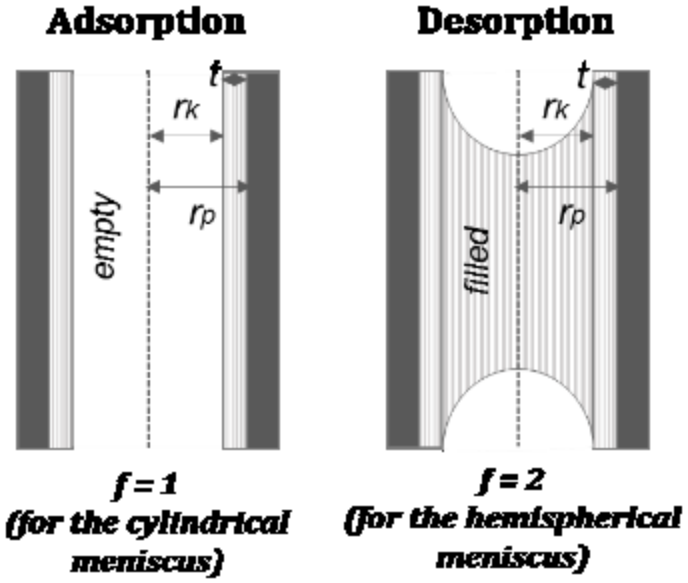

Figure 13. Schematic representation of the gas adsorption and desorption processes within cylindrical pore.

To estimate the monolayer thickness, adsorbed within the micropores, and defined by t-plot slope change, various equations can be found (Gregg and Sing, 1982). The t-plot approach based on the Harkins-Jura equation (Harkins and Jura, 1944) is widely used in practice (Equation 6).

Equation 6.

$$t = \sqrt{\frac{0.1399}{0.034 - \log(\frac{P}{P_0})}},$$

where t is the monolayer thickness [m], P/P_0 – relative adsorption pressure.

The BJH method is widely applied for the PSD calculation from N_2 adsorption/desorption experiments. Meanwhile, the theoretical description of the capillary condensation in nano-porous materials using nonlocal density functional theory (NLDFT) exists as well (Ravikovitch and Neimark, 2001).

Carbon dioxide, due to smaller kinetic diameter (Table 2), is widely used for the micropores characterization. For CO_2 isotherms, Dubinin and Radushkevich (DR) approach is often applied (Clarkson et al., 2013; Chalmers et al., 2012a), among many other models developed for the gas adsorption within micropores (Lowell et al., 2004). The basis of the DR theory puts forward an equation based on Polanyi's potential theory, which allows the micropore volume to be calculated from the adsorption isotherm (Equation 7).

Equation 7.

$$\log W_a = \log\left(V_\mu \rho_a^{liq}\right) - K^{DR}[\log(P_0/P)]^2,$$

where W_a [kg] and ρ_a^{liq} [kg/m^3] are the weight adsorbed and the liquid adsorbate density, respectively, V_μ is the micropore volume [m^3], K^{DR} is a constant, which can be defined with Equation 8.

Equation 8.

$$K^{DR} = 2.303k\left(\frac{R_{gas}T}{\beta}\right)^2,$$

where β_{af} is the so-called "affinity coefficient", and k is a constant, determined by the shape of the pore size distribution, R_{gas} is the gas constant and T is the absolute temperature in Kelvins (Lowell et al., 2004). The transformation of the volumetric measurements to the pore size distribution is possible through the assumption about the pores shape. For example, volume of the cylindrical pore V_p [m^3] with radius r_p [m] and length l_p [m]can be calculated with Equation 9.

Equation 9.

$$V_p = \pi r_p^2 l_p.$$

Further extension of this theory on microporosity estimation from adsorption isotherms performed on coals can be found in the work of Marsh (1987). Indeed, historically, at the dawn of unconventional hydrocarbons development, shales were very often compared with coals. Due to the similarity in pore size range, the methods developed for coals characterization, are often directly applied on shale samples. Coals are also heterogeneous material composed of both organic and inorganic substances. The organic contents, called "coal macerals", are the useful portion of the coal (up to 100%). The inorganic contents, called mineral matter, are pollution components that dilute coals and are undesirable. Meanwhile, porosity measurements on coals often show, that most of the pores are less than 10 nm in diameter (Gan et al., 1972), exhibiting mono- or bimodal distribution, which corresponds to the pore size expected in shale samples (Figure 14 and Figure 8). The N_2 adsorption/desorption isotherms obtained on coal also present an irreversible hysteresis indicating some trapping of N_2. The PSD provided on Figure 14.B was achieved using the BJH method (transformations of desorption curve, which corresponds to the pore throat size distribution). In that case the intense peak at ~4 nm on Figure 14.B is an artifact, induced by the cavitation occurring at P/P_0 ~0.45 on the desorption isotherm. The pores of coals, filled by gas are, however, located mainly within OM, with a relatively homogeneous spatial distribution, whereas the pores spatial distribution of shales is more complex.

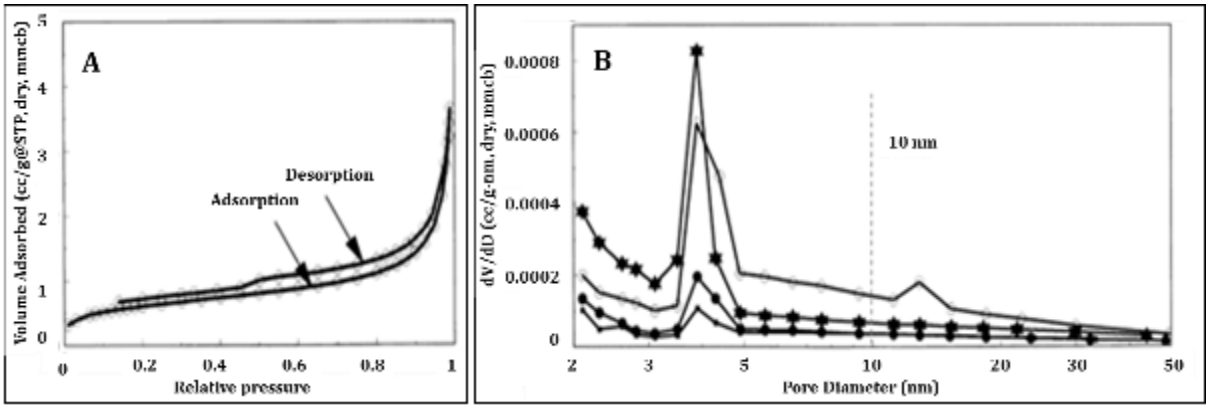

Figure 14. A) Nitrogen adsorption and desorption isotherms for coal sample: B) pore size distribution by BJH transformations on desorption curves (Clarkson and Bustin, 1999a).

To evaluate a wide range of pores sizes adsorption measurements using different gases are often combined. For example, Clarkson et al. (2013) and Chalmers et al. (2012a) used a combination of N_2 (at -196°C) and CO_2 adsorption (at 0°C) techniques for shale samples. Due to smaller kinetic diameter of CO_2 (0.33 nm, compared with 0.37 nm for N_2 (Table 2)), this combination allowed investigation of pores sizes in the range of 7-1000 Å, which includes some part of microporosity (Figure 15). The reliability of such a combination is questionable, since different mathematical calculations are applied for different measurements, the assumptions and limitations of each model should be correlated, i.e. consistent in between each other. The same way of combining nitrogen and carbon dioxide adsorption measurements can be found in Kaufhold et al. (2016) or Mastalerz et al. (2013).

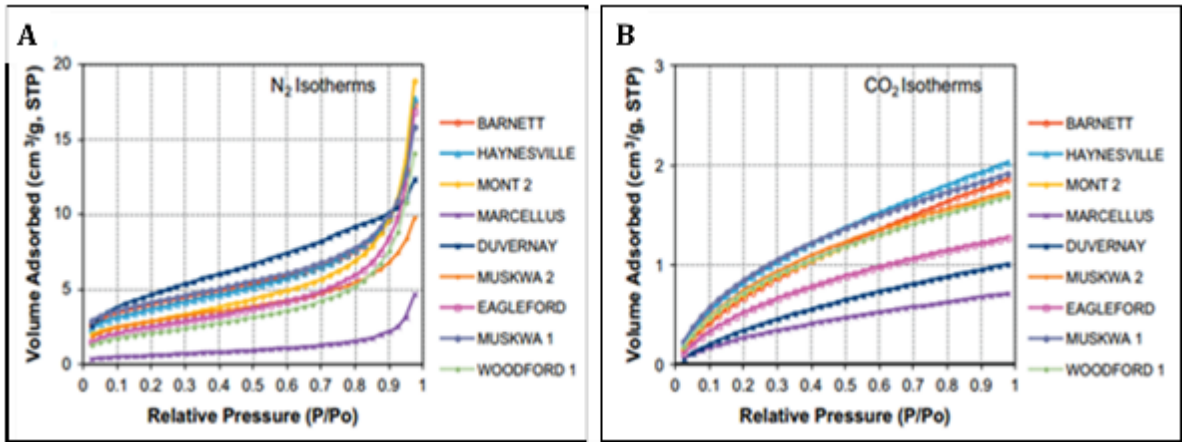

Figure 15. Nitrogen (A) and carbon dioxide (B) isotherms collected for the shale samples (Clarkson et al., 2013).

The pore size distributions achieved by BJH and DP approaches are presented in Figure 16, where most of the pores correspond to micropores smaller than 2 nm.

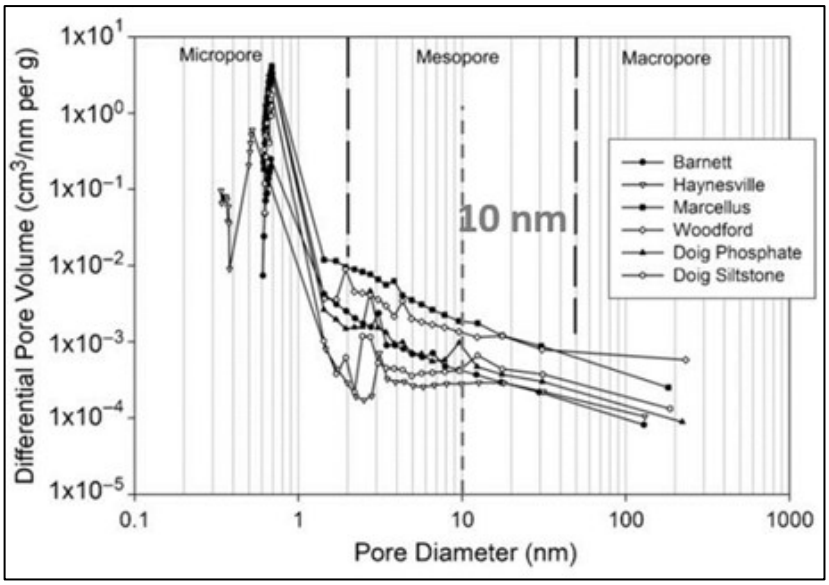

Figure 16. Pore size distribution curves for shale samples, defined by differential pore volume using low-pressure gas (N_2 and CO_2) adsorption analysis (Chalmers et al., 2012a).

From the reviewed list of publications, most of adsorption/desorption isotherms (when they were shown) do not present the desorption curves. Meanwhile, the hysteresis loop provides important information about the geometry of the pores, which can be defined through its shape (Lowell et al., 2004). Figure 17 illustrates the isotherms for powdered shale samples, exhibiting a very small hysteresis loop. Such a close shape of adsorption and desorption isotherms indicates the homogenized pore network of the powdered sample (throats size distribution is expected to be close to pore bodies' sizes distribution). This feature does not reflect the real microstructure organization of the rock. Meanwhile, the measurements by gas adsorption on centimetric blocks were not found in the literature.

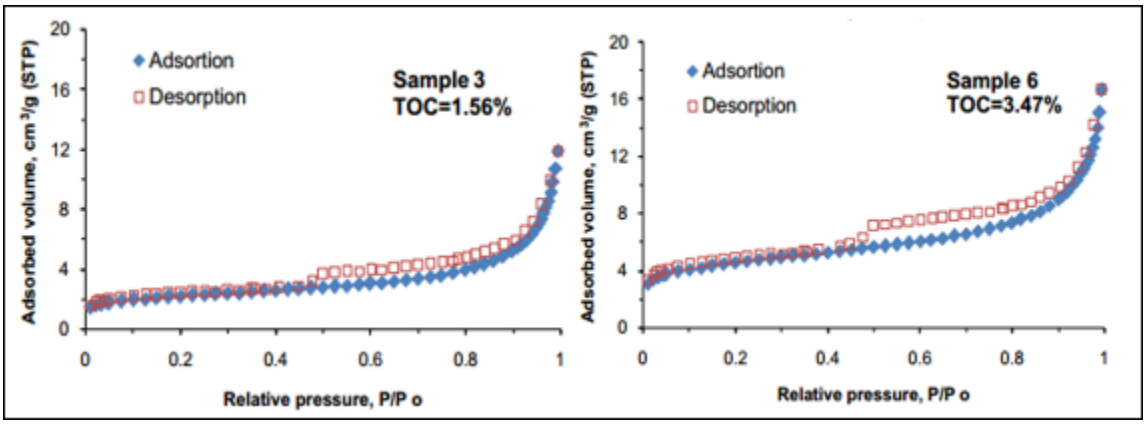

Figure 17. Nitrogen gas adsorption and desorption isotherms for the samples from lower Silurian black shales (Tian et al., 2013).

Moreover, with gas adsorption experiments it is possible to quantify the relative pore volume content hosted in organic matter. For example, Kuila et al. (2014) performed gas adsorption before and after solid organic matter removal for Baltic shale samples (Figure 18).

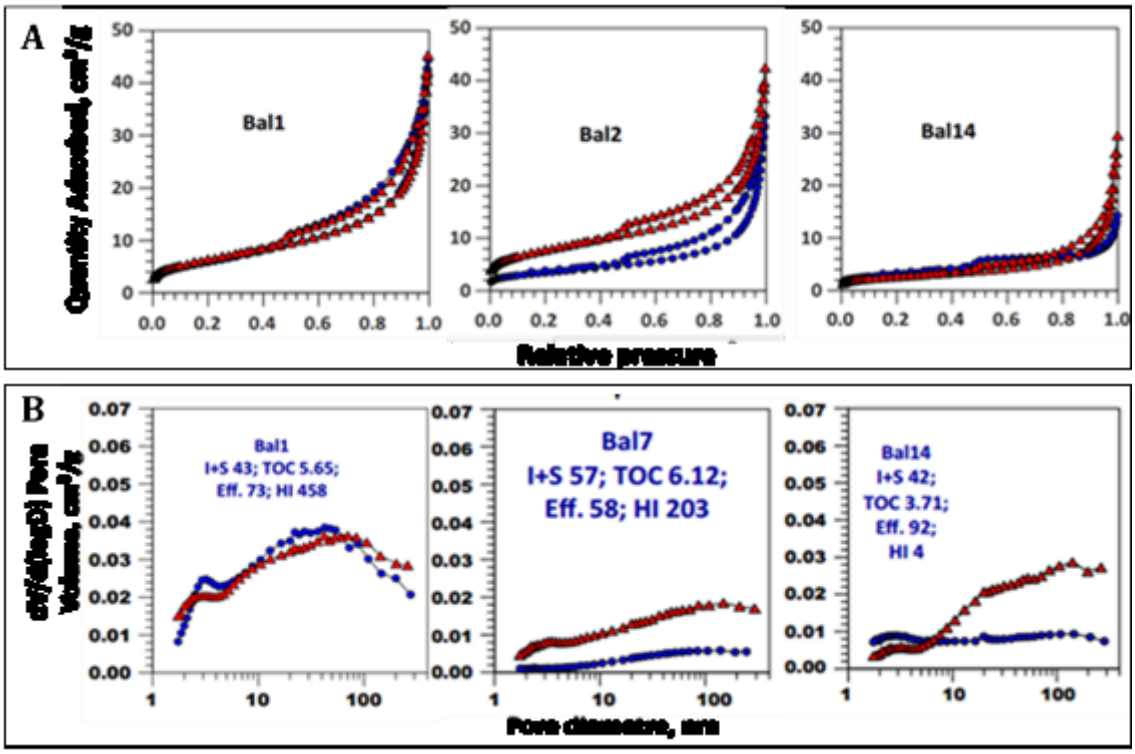

Figure 18. Representative isotherms (A) on natural (in blue) and NaOCl treated (in red) samples and (B) corresponding pore size distribution curves (I+S = illite + smectite clay group in mass%; TOC = Total Organic Carbon in mass%; Eff. = OM removal efficiency in %; HI = Hydrogen Index in mg HC/g TOC) (Kuila et al., 2014).

These data have shown that the distribution of OM, with respect to the clay microstructure, is heterogeneous (Figure 18, Table 3). Solid OM exists as separate particles or laminations, where clay porosity may be open to adsorption, or OM can partially or completely fill the space between clay aggregates within dimensions <5 nm. Removal of OM from thermally mature organic rich shales resulted in a significant reduction of the pore volume network below a diameter of 5 nm. This reduction of pore volume is interpreted as an indication of pores, hosted within organic matter (which would account for 24–77% of the total pore volume within the < 5 nm pore-size interval) (Table 3; Kuila et al., 2014).

Table 3. Proportion of pores <5 nm estimated as the sum of micropore (<2 nm) volume (derived from N_2 adsorption isotherm applying t-plot method) and total pore volume between 2 and 5 nm pores size (estimated from BJH inversion with Harkins-Jura thickness equation) (see details in Kuila et al., 2014).

Sample	Proportion of pores < 5nm	
	Clay hosted	OM-hosted
	% Vp<5nm	% Vp<5nm
Silurian shale	33	67
Haynesville 1	74	26
Haynesville 2	23	77
Haynesville 3	55	45
Paleozoic shale	37	63
Marcellus 1	21	79
Marcellus 2	14	86
Baltic basin 1	39	61
Baltic basin 2	70	30
Baltic basin 3	47	53
Baltic basin 4	76	24

Besides the porosity characterization, gas adsorption experiments can be done to understand natural gas adsorption selectivity. Such experiments were performed by Gasparik et al. (2014) (where the high-pressure adsorption of separated components of natural gas was carrying out) and by Cheng and Huang (2004) who used the hydrocarbon gas mixture as adsorbate, controlling the changes in gas composition after desorption.

For shale samples investigations, the most suitable fluids will be those with the smallest kinetic diameter (Table 2). However, due to complex organization of the shales and presence of kerogen, the reactivity of the pore space is likely heterogeneous even within a single sample and the characterization of this heterogeneity at the sample scale remains a challenging area of research.

Some important parameters, which may influence the adsorption isotherms are temperature, moisture, total organic carbon content and mineral composition, which affect the characteristics of isotherms. Hartman et al. (2008) indicated, that changing the relative humidity within the apparatus could alter the shape of the shale gas adsorption isotherm (methane was used here), due to large surface area exposed by dehydrated clays (Figure 19). Meanwhile, temperature plays much smaller role than moisture content if clays are only considered. The reliability of the data depends on equilibrium occurring at every pressure step in the adsorption isotherm experiments (in gas shale due to low diffusion rate, the penetration of gas to the system could take a long time) (Hartman et al., 2008). The high-pressure adsorption measurement can be used to determine the adsorbed gas capacity at simulated reservoir pressure and temperature conditions (Ross

and Marc Bustin, 2009). Such a kind of experiments is needed to study the rock behavior in modelled "in-situ" environments.

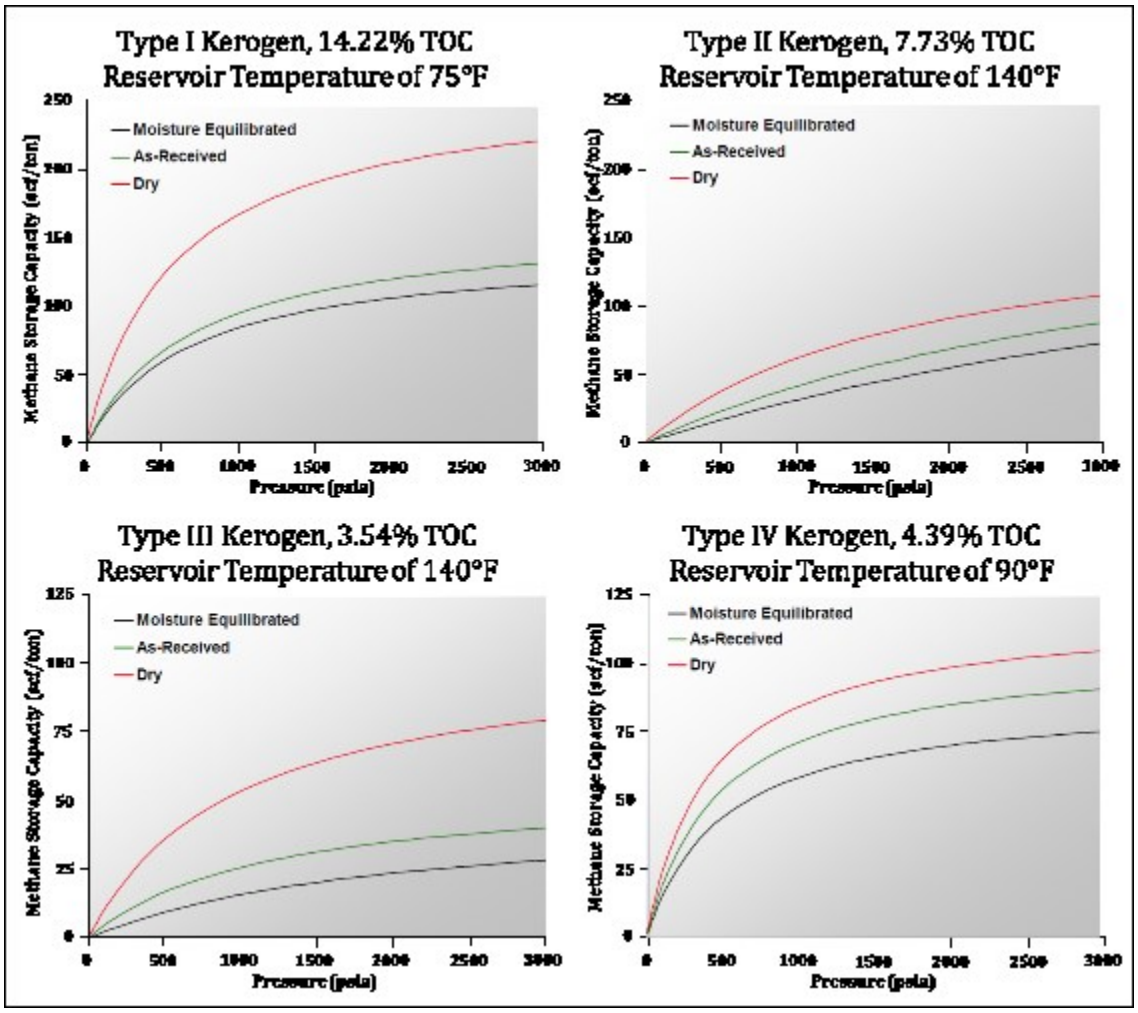

Figure 19. Methane adsorption isotherms on powder shale samples of various maturity under different temperature and humidity conditions (Hartman et al., 2008).

1.2.4. Nuclear magnetic resonance spectroscopy

Nuclear magnetic resonance (NMR) spectroscopy is a useful tool for conventional reservoirs investigations. Based on hydrogen contents measurements, NMR spectroscopy can be applied during boreholes evaluation to obtain information about the matrix porosity, fluids content and lithology of the well. A lot of modelling methods for interpretation of NMR measurements were investigated (Schlumberger, 1991a). NMR methodology is based on the existence of a strong magnetic moment of the proton in the hydrogen nucleus. At thermal equilibrium in a static magnetic field, the volume of interstitial fluids (hydrocarbons/water) in a shale sample exhibits a small net magnetic moment that results from the sum of all the magnetic moment associated with each of the protons in the volume.

As a matter of fact, in a classical NMR relaxometry experiment, the moments of protons, initially at thermal equilibrium, are perturbed by an energizing pulse tuned to the Larmor frequency, which is an intrinsic physical property of a given nucleus. If this pulse is applied and then removed, these moments process from their thermal equilibrium and then relax back to this same thermal equilibrium. As these moments relax, they emit a measurable magnetic signal which allows the calculation of two parameters: relaxation times T_1 and T_2, which are associated with relaxation longitudinal and transversal to the static field, respectively. Considering transverse relaxation, which is most commonly used to estimate pore size distribution, parameter T_2 is usually described by two relaxation processes occurring in parallel (Equation 10).

Equation 10.

$$\frac{1}{T_2} = \frac{1}{T_{2S}} + \frac{1}{T_{2B}},$$

where T_{2B} is the transverse bulk fluid relaxation time, T_{2S} is the transverse surface relaxation time (in this writing, it is also assumed a homogeneous magnetic field).

Most geological applications of NMR relaxometry are based on four fundamental assumptions. First, it is assumed that relaxation occurs in the fast diffusion regime. The fast diffusion regime is satisfied $k_{NMR} << 1$, where the control parameter k_{NMR} is defined by Brownstein and Tarr (1979) (Equation 11).

Equation 11.

$$k_{NMR} = \frac{\rho_r \alpha_d}{D_{H2O}},$$

where ρ_r, [μm/s], is the so-called "surface relaxivity" (it is often considered as a measure of the ability of a pore surface to enhance relaxation), which is typically in the range between 1 and 10 μm/s (Fleury et al., 2013); α_d is the average distance of a proton travel before encountering a paramagnetic site [m]; and D_{H2O} is the self-diffusion coefficient of water ($D_{H2O} = 2.46 \cdot 10^{-9}$ m^2/s at 30°C). The fast-diffusion regime can be seen as the regime, in which a proton can move to interact with the surface of a pore within the time scale of the NMR measurement (Behroozmand et al., 2014)

The second assumption is that there is no pore coupling. This assumption is satisfied when the average pore size is greater than the diffusion length scale, l_{dif} [m], which is defined by Einstein equation for self-diffusion (Equation 12), where T is the time scale of the NMR experiment [s].

Equation 12.

$$l_{dif} = \sqrt{6 D_{H2O} T}.$$

The third assumption states that the bulk fluid relaxation time T_{2B} is negligible. In practice, T_{2B} is expected to range from 1.1 to 3.4 s and can be considered to be long, when compared to surface relaxation time T_{2S} (Behroozmand et al., 2014).

The fourth assumption is quite classical in NMR methodology: the surface relaxivity, ρ is supposed to be a constant for a given porous material.

These four assumptions constitute the foundation of NMR-estimated pore-size distributions. Under these assumptions, each pore can be considered to contribute separately to the overall relaxation time distribution and consequently the relaxation time T_2 is approximated by Sørland et al. (2007) (Equation 13).

Equation 13.

$$\frac{1}{T_2} \approx \rho_r \frac{f}{r_p} = \rho \left(\frac{S}{V}\right)_{pore},$$

where f is a shape factor accounting for the geometry of the pore (f = 1 for planar pores, 2 for cylindrical pores and 3 for spherical pores); r_p is the characteristic radius of the pore [m]; $\left(\frac{S}{V}\right)_{pore}$ is the surface area-to volume ratio of the pore [m^{-1}]. Parameter $\left(\frac{S}{V}\right)_{pore}$ is equivalent to $\frac{f}{r_p}$ for ideal pore shape. Equation 13 clearly shows that the evolution of relaxation times T_2 is linearly proportional to the pore-size distribution.

Sørland et al. (2007) reported a resolution of pores down to 1 μm in diameter. The results of measurements, which have been performed on a sample slice filled with brine, are presented on Figure 20. This allows to directly correlate T_2 relaxation time with pores volume through simple relation, leading to the approximated pore size distribution, despite the use of approximate diffusion coefficient. Also, the presence of artifacts due to sample preparation cannot be eliminated. As it was discussed above, the mercury intrusion measurements provide the pore throat sizes distribution and cannot be compared directly with pore size distribution, achieved by different methods.

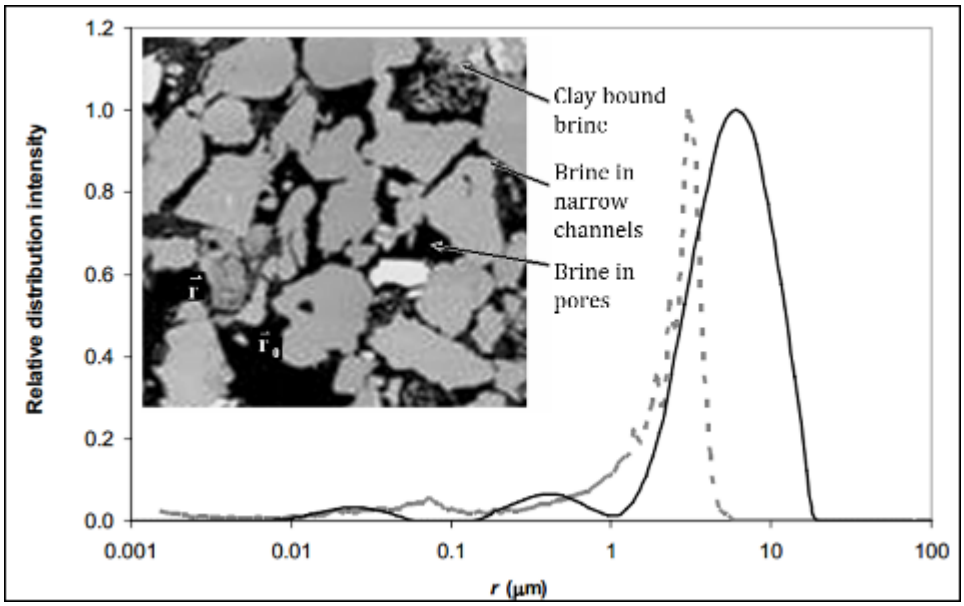

Figure 20. Pore size distribution of porous rock sample from NMR method (solid line) and from mercury intrusion (dashed line) (Sørland et al., 2007).

As it was mentioned before, shale samples can demonstrate different types of wettability within the matrix due to the presence of OM with variable maturity. This property can be evaluated using the sensibility of relaxation time for the fluid media, through experiments on oil and water interactions with hydrophobic and hydrophilic surfaces (Borysenko et al., 2006). For the example, the relaxation time distribution as a function of surface wettability is presented in Figure 21.

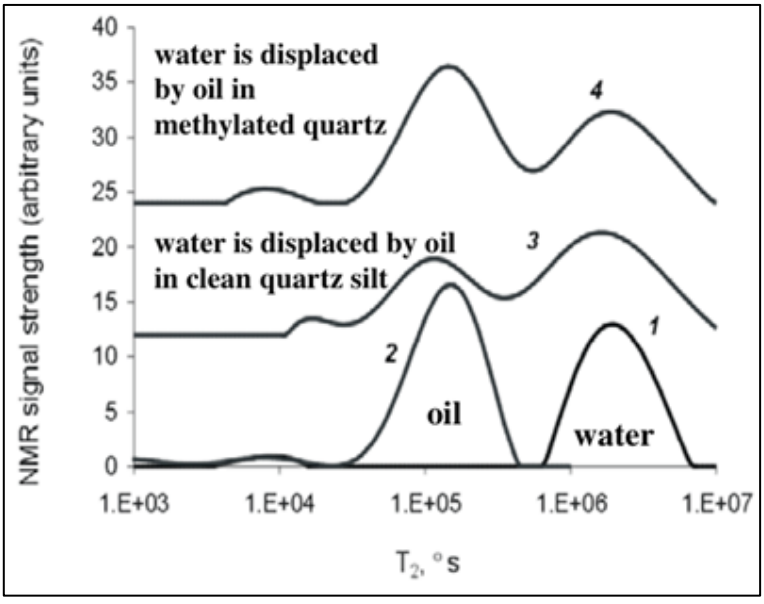

Figure 21. T_2 (relaxation time) – distribution: (1) pure water and (2) pure oil saturated methylated quartz powder; (3) for clean quartz silt; (4) for methylated quartz particle bed (150-180 μm grain size) (Borysenko et al., 2006).

More recently, NMR measurements on shale samples (Barnett Shale samples) have shown that T_1-T_2 maps is an interesting tool to discriminate the nature of the interstitial fluid saturating pore space (Lewis et al., 2013, Fleury, 2014; Fleury and Romero-Sarmiento, 2016). By combining T_1/T_2 ratio and T_2 values, these authors have shown that the following populations of protons (*Pi*) could be detected (Figure 22) (Fleury and Romero-Sarmiento, 2016):

- *P1*: hydroxyls group (i.e., OH^- part of the clay structure or at the edges of clay minerals); the associated signal is always at the limit of resolution, typically below 0.1 ms.
- *P2*: protons which are part of the kerogen: depending on the maturity, their area in the T_1-T_2 map can overlap with that of hydroxyl groups.
- *P3*: protons associated with water: this signal is typically located on or close to the line $T_1/T_2 \sim 2$ even for very small pore sizes such as interlayer space in clays,
- *P4*: protons associated with methane: when considering T_2 only, signal may overlap with the water signal. However, by combining both T_2 and T_1, corresponding protons population can be easily discriminated: $T_1/T_2 \sim 10$. Note that adsorbed methane has no specific signature because it is in fast exchange with free methane.

In this work, the signature of oil was not considered. Moreover, from diffusion coefficient measurements on the same shale samples and from Equation 13, these authors claimed that the diffusion pore coupling effect in shales would be also significant: T_2 distribution measured in shales would not represent a pore size distribution for pore sizes smaller than about 1 µm. Most of the pores smaller than about 1 µm and explored by the molecules during diffusion would correspond to a single relaxation time (Fleury and Romero-Sarmiento, 2016). This interesting result should be confirmed on other shale samples.

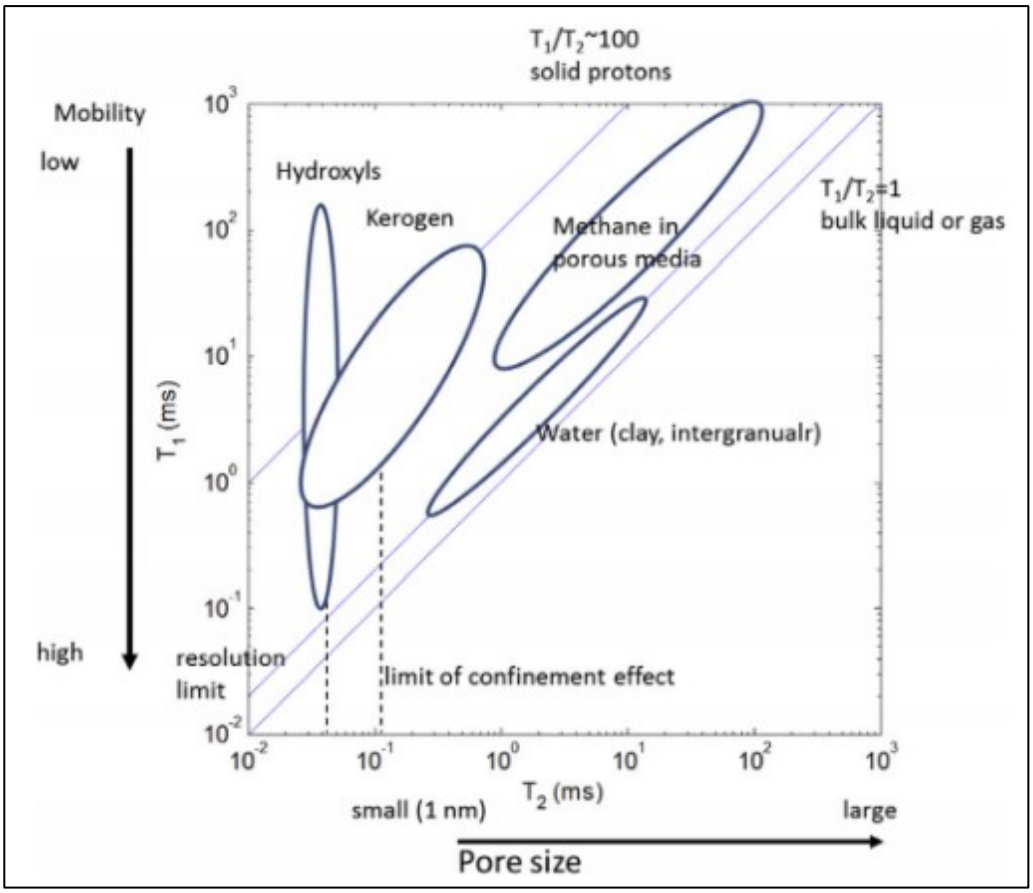

Figure 22. Fluid or proton typing using T_1-T_2 map (Fleury and Romero-Sarmiento, 2016).

Applying this kind of techniques, it must be considered that shales typically have only a few percent porosity and nano- or pico-Darcy permeability (Table 23). These results with low signal-to-noise ratio on large samples require long run times to obtain useful data. The pore sizes are also typically in the nanometer range, leading to very short relaxation times (Washburn and Birdwell, 2013). The NMR relaxometry must be used with caution to estimate the pore size distributions of shales, since NMR-estimated por size distributions for such a heterogeneous material remains a challenging area of research.

1.2.5. Small angle scattering techniques (SANS/USANS)

In small angle (SANS) and ultra-small angle (USANS) neutron-scattering experiments, a neutron beam is directed to a rock sample, and the neutrons are elastically scattered due to their interaction with nuclei of atoms in the sample (e.g., Curtis et al., 2014; Melnichenko et al., 2012; Clarkson et al., 2012; Clarkson et al., 2013). Position-sensitive detectors measure the scattering intensity *I(Q)*, [m^{-1}], as a function of the scattering angle, which is defined as the angular deviation from the incident beam. The

scattered intensity, *I(Q)*, is measured over several decades of the scattering vector Q, whose modulus can be calculated with Equation 14.

Equation 14.

$$Q = 4 \cdot \pi \lambda^{-1} \cdot \sin\theta,$$

where λ is the incident wavelength [m], and 2θ is the scattering angle. In porous media, *I(Q)* can be expressed as a Fourier transform of the pore/solid microstructure. As a result, a statistically representative pore size distribution can be calculated from *I(Q)* profiles (Figure 23).

For a wide range of porous media, the small-angle scattering (SAS) data are generally interpreted using a two-phase approximation. Following this approximation, the scattering volume is viewed as comprised of supra-molecular-size regions, each characterized by one of two possible values of the physical property that provides the scattering contrast. For instance, for porous rocks, these two regions are the solid matrix and the pore space, respectively (e.g., Radlinski, 2006). Following this two-phase approximation, *I(Q)* is proportional to the scattering contrast (*ΔSLD,* [m^{-2}]; Equation 15).

Equation 15.

$$\Delta SLD^2 = \left(SLD_m - SLD_p\right)^2,$$

where SLD_m and SLD_p are the scattering length densities (*SLD,* [m^{-2}]) of solid matrix and pore space, respectively. In practice, for shale samples, the value of the *SLD* for solid matrix (mineral grains) can be considered as approximately uniform and can be estimated if the mineral composition is known (Radlinski, 2006; Clarkson et al., 2012). This *SLD* value for solid matrix is much higher than the *SLD* of pores filled with air ($SLD_{pore} \sim 0$). But there exist fluids or mixture of fluids, whose *SLD* values can be like that of solid matrix: the *SLD* values of these fluids "match" the *SLD* value of the shale matrix. These "matching" fluids concern for instance mixtures of H_2O and D_2O (see Gu et al., 2016). The "matching property "can be used to quantify the closed porosity in a shale sample: if the sample is soaked in the appropriate fluid mixture, the accessible pores become indistinguishable from the solid phase (i.e., scattering contrast close to 0), leaving only the inaccessible pores as detectable ones. As a matter of fact, the approach of scattering techniques is often seen as the analysis of small-angle scattering patterns obtained from indigenous porous media and same media saturated with a contrast matching fluid. (Figure 23) (Melnichenko et al., 2012). These SAS techniques allow (i) to wider the range of pore sizes (typically 1.2 – 10000 nm) that can be investigated based on an idealized spherical shape of pores; and (ii) to distinguish closed versus open porosity when the saturation by the contrast matching fluid is successfully applied. Thereby, a recent study carried out on Marcellus shale samples has shown that OM hosted 24–47%

of the total porosity for both organic-rich and -poor samples (Barrett et al., 1951). Indeed, in contrast to the classical paradigm in the literature that OM porosity is organophilic and, therefore, not likely to contain water, this work demonstrated that OM pores with widths >20 nm exhibited the characteristics of water accessibility.

The SANS and USANS neutron-scattering analyses initially applied for homogenous coal samples (Melnichenko et al., 2012) are more complicated for shales samples due to wide range of heterogeneities, not only in porosity but also due to the variability of solid compounds with varying *SLD* values: the calculation for highly heterogeneous shale matrix SLD_m may not be straightforward and requires an accurate determination of rock sample mineralogy.

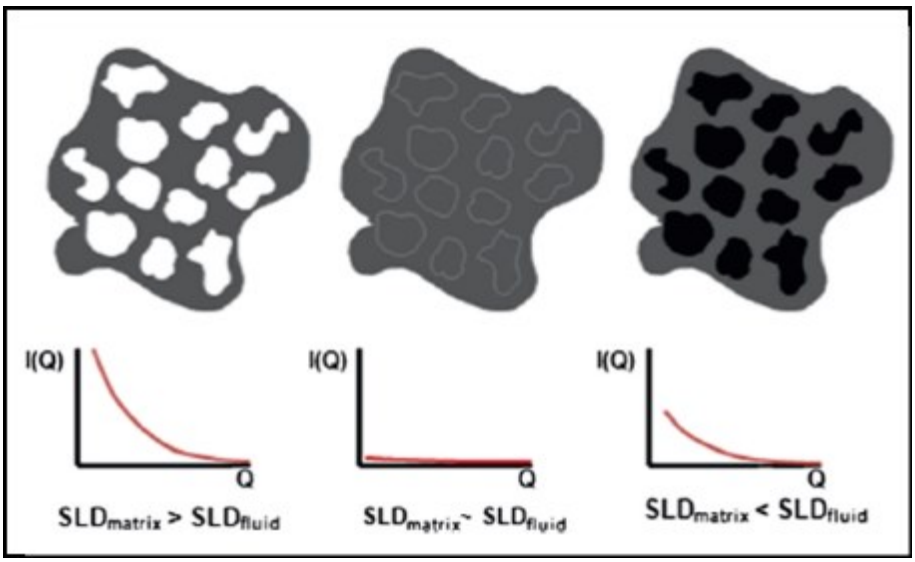

Figure 23. Qualitative presentation of contrast-matching experiments with fluid saturated porous systems (Melnichenko et al., 2012).

Table 4 displays an example of SLD calculations performed on samples from the Triassic Montney tight gas reservoir in Western Canada (Clarkson et al., 2012). The values of SLD for the mineral phases (Table 4.A; Clarkson et al., 2012) were calculated through mineral composition achieved by XRD analysis, and demonstrated the close result for different samples. Meanwhile, values for simple components, which were calculated by the NIST SLD calculator (Table 4.B; NIST, 2015), indicate that different components can have SLD values varying in a wide range.

Table 4. A) Comparison of SLD values for the shale samples (Clarkson et al., 2012). B) SLD values for some compounds expected in shale sample (calculated by "NICT neutron activation and scattering calculator" for neutron source λ=4.8 Å; NIST, 2015).

A

Sample	SLD
	10^{10} cm^{-2}
4	4.26
5	4.27
24	4.40

B

Component formula	Density	SLD
	g/cm^3	10^{10} cm^{-2}
Calcite	2.71	4.690
Quartz	2.66	4.202
Illite	2.61	3.315
Kaolinite	2.61	3.195
Carbon	1	3.333
$Benszene_{cond}$	1	1.345
Benzene	0.001	0.001
$Xylen_{cond}$	1	0.462
Xylen	0.001	0.000
Water	1	0.561

This variability of SLD values can be explained by the amount of hydrogen in each compound: hydrogen exhibits negative SLD value whereas the other main elements bared by the solids have positive SLD values. As a result, the SLD values of water, methane or any organic compounds like kerogen (with a lot of hydrogen regardless to minerals), strongly differ from those of the other minerals. In addition, hydroxylated minerals such as clay minerals exhibit very different SLD values than other minerals like tectosilicates and carbonates.

In addition, SANS and USANS neutron-scattering data have two main disadvantages. First, to prevent the multiple neutron scattering (Clarkson et al., 2012; Clarkson et al., 2013), these techniques are often applied on confined samples inside a thin-wall quartz cell (like described by Jin et al. (2011)) with sample thicknesses ~150 nm. Such a small sample thickness for clay materials may induce a critical damage of the network of pores during the sample preparation. That is why these scattering methods are often considered to provide only information on the sample surface (Ma et al., 2017b).

Second, to transform the SAS data to pore size distributions, a polydisperse spherical pore (PDSP) model is often introduced (Radlinski, 2006; Gu et al., 2016). The PDSP assumes that the pore space of a rock can be represented by a polydisperse distribution of independently scattering spheres. This assumption is clearly questionable with regard the recent morphological and topological information provided by recent imaging techniques (e.g., Ma et al., 2017b).

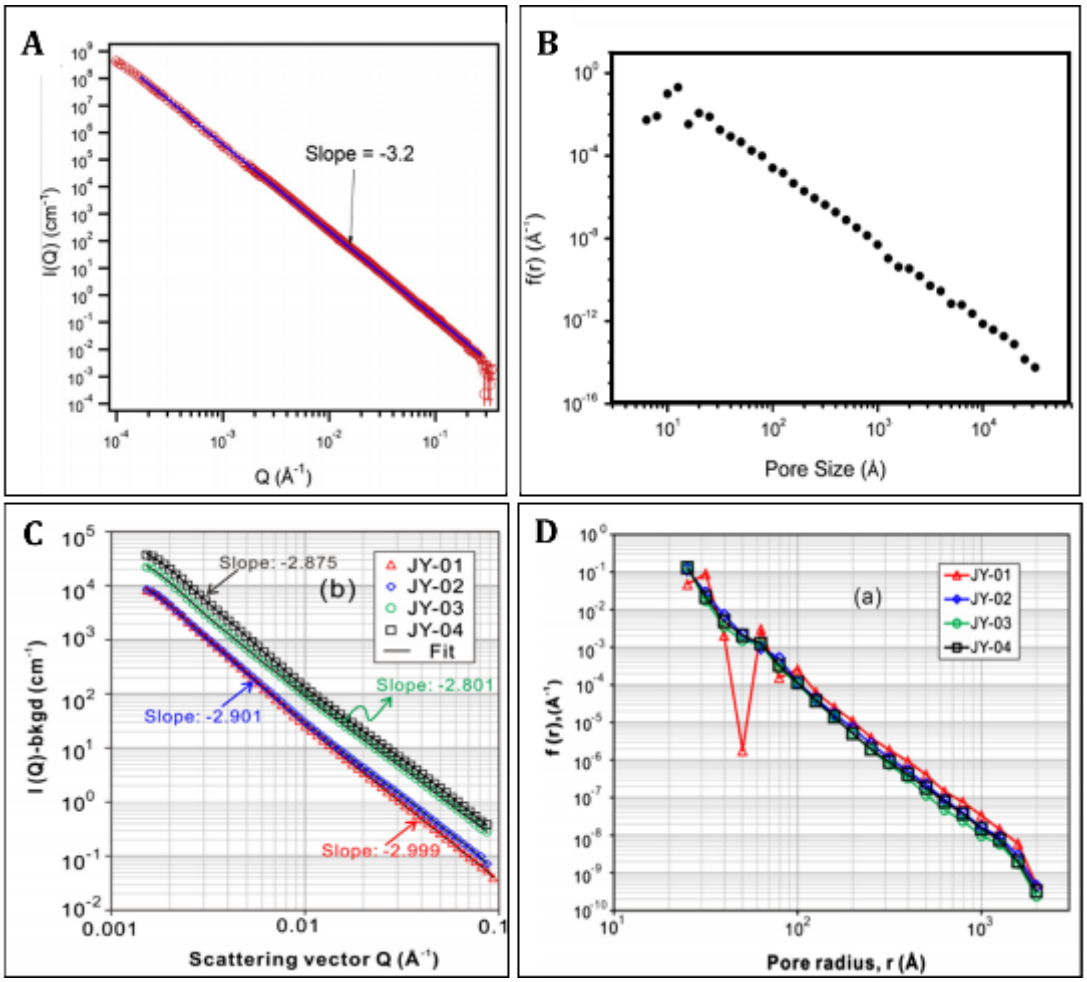

Figure 24. SANS measurements result on tight gas samples (Clarkson et al., 2012): A) scattering profile with background subtracted (solid line represents fit to the power low model applied); B) pore size distribution based on the fitting of polydisperse spherical particles model to the scattering data. Example of SANS measurements result on shale samples (Yang et al., 2017): C) scattering profile with background subtracted; D) pore size distribution based on the fitting of polydisperse spherical particles model to the scattering data.

In summary, the scattering techniques allow to distinguish the materials structure organization over a large-scale range (from nanometers to tens of micrometers), with the detection limits down to ~1 nm. But, the dimensions of the sample probed during the acquisition questions the representativity of the data. Meanwhile, application of such tools in case of heterogeneous shale samples is challenging, and the efficiency of these methods is much more significant for the simple mono/duo component systems.

1.2.6. Thermal analysis

Thermal analysis (TA) are widely used for the prediction of physical and chemical properties of rocks. In general, various measurements (calorimetrical, thermogravimetric, etc.) can be done on the sample under a thermal stress. For example, this technique allows to determine the characteristic temperatures of moisture loss by

the rock, to investigate decomposition processes of OM and mineral phases (since distinct phases are degrading within known temperature diapasons), to evaluate the reactions of the sample with chamber environment. Different capabilities of such a technique are described in the literature (ex. Smykatz-Kloss and Warne, 1991). Coupling the sample chamber with Mass Spectroscopy detector provides information about the products formed under the temperature stress. For organic-rich shales, this technique is widely applied to perform the compositional analysis of produced hydrocarbons (ex. Lee, 1991) Such an approach was applied on Green River shale samples by Tiwari (2012).

Thermogravimetric analyses can help to find out the temperature, at which all the moisture will be removed from the pore space. At the low temperatures region (up to 250 °C) the mass loss is expected to be mostly due to dehydration processes. It is assumed that full removal of the free water in pore space is occurring at 100-110°C (Earnest, 1991). In shale reservoir rocks the change of the pore space characteristics can be expected, due to presence of gaseous and liquid hydrocarbons, leading to the change of the surface/water interactions. The removal of free water may not, therefore, be complete at the expected temperature for these organic-rich rocks. Another reason to assume that the dehydration temperature may be different from standard one is the presence of extremely small pore size within these rocks, which can lead to the shift of the efficient drying temperature to higher values. Also, clay minerals, which demonstrate various dehydration temperatures (Table 5), may require higher temperatures, to remove the water molecules from the interlayer space, than tectosilicates or carbonates.

Table 5. Dehydration temperatures for different clay minerals (Grim and Bradley, 1948).

Sample	**Surface dehydration temperature, °C**	**Lattice dihydroxylation temperature, °C**
Na-Montmorillonite (*Wyoming bentonite*)	160°C (~100-195°C)	700°C (~560-760°C)
Ca-Montmorillonite (*Arizona bentonite*)	180 & 230°C (~100-265°C)	670°C (~500-740°C)
Illite (*Fithian, Illinois*)	130°C (~100-270°C)	560°C (~475-650°C)
Illite (*Grandy County, Illinois*)	160°C (~100-270°C)	550°C (~400-650°C)
Illite (*Minford silt, Ohio*)	125°C (~100-220°C)	520°C (~375-650°C)
Kaolinite (*Anna, Illinois*)	160°C (~100-200°C)	580°C (~450-650°C)

In the literature, for shale samples, even if the weight loss curve is shown with water release at low temperature, no data with exact position of onset was found. In the work of Rajeshwar (1981), the end of the dehydration process can be approximately found at ~180°C for Green River formation sample, with the heating rate of 20° C/min. Based on

the observations of the samples from the same formation under various heating rates, the shift to a smaller temperature is expected with a lower heating rate (Tiwari, 2012). Thus, beyond the temperature of outgassing, which depends on the nature of the material and the compounds to outgas, the heating rate, and consequently the time of the dehydration, is an important parameter to consider.

Such a control of the drying parameters by TA before the application of porosimetry techniques was found only on clay samples. For example, Kuila and Prasad (2013) have proposed the shale sample preparation at 200°C under vacuum, while the selected temperature is based on the TA measurements on pure montmorillonite. The same preparation procedure is described as well in several publications (Kuila and Prasad, 2013; Kuila et al., 2014; Topór et al., 2016). The discrepancies in the sample preparation method may lead to mismatches in the pore balances, when various methods are combined within the single work or in between the authors.

1.3. Imaging techniques

While the bulk techniques allow to study large representative volumes of samples at a broad range of pore scales, they remain indirect methods, which imply significant limitations and assumptions, impacting directly the reliability of the result obtained on such heterogeneous materials as shales. Providing data about porosity and pore size distribution of the sample, bulk methods are not accessing the information about spatial distribution of pores, neither about the porosity of distinct compounds (i.e. solid OM, clay matrix, mineral grains). Conversely, imaging techniques allow to visualize the pore space, revealing the direct information about pores geometry and morphology. Traditional 2D imaging techniques, such as optical microscopy and scanning electron microscopy (SEM), have shown their ability of imaging microstructure in single plane. But their 2D quantitative porosity estimations are expected to have poor reliability, when measured from small 2D surface (like single SEM image), which is not representative regarding the heterogeneities scale of shale samples (Figure 3). In 2D images the porosity would be estimated following Equation 16, where S_p is the measured surface of the pores [m^2], and S_T – total observed area [m^2].

Equation 16.

$$\varphi_{2D}^{T} = \frac{S_p}{S_T} \cdot 100\%.$$

Other techniques (3D focused ion beam scanning electron microscopy (FIB-SEM), µtomography, autoradiography, etc.) provide information to evaluate 3D microstructures. Imaging techniques are reproducible (same sample can be observed in different modes and at different conditions), and very have found wide applications for shale samples investigations can be found (Curtis et al., 2012a; 2012b; Loucks et al., 2009; 2012; Milliken et al., 2013; 2014; Ma et al., 2017a; among many others). Although complex microstructural organization associated with highly heterogeneous distribution of various phases questions the representativity of the sample probed due to limited resolution and field of view of these methods, as illustrated further.

1.3.1. Representativity

Since shales represent complex pore networks at multiple scales, including nanopores (Figure 8), high spatial resolution of imaging techniques is required. But this requirement may be contradictory with a large area of investigation needed to describe comprehensively all the parameters of interest: the question of the representativity of probed area/volume should be pointed out. In the literature, there are diverse ways to define representative elementary volume (REV, in 3D) or area (REA, in 2D). Some

definitions, used by various authors for different objectives are listed by Gitman et al. (2005). These definitions all correspond to the fact that the chosen elementary volume (or area) should be small enough to distinguish microstructural properties but also large enough to represent effective (macro scale) properties of the sample.

Different strategies to access REV were developed especially for imaging techniques (see, for instance, the review by Rozenbaum and du Roscoat (2014)). One possibility is to evaluate a "deterministic" REV following a multi-steps procedure, often called "counting box" method (e.g., Kameda et al., 2006). In a first step, a small volume within an image is considered and the property of interest (grey level, porosity, phase content, etc.) is calculated. Then in the following steps, this volume is expanded in all directions and the property is recalculated for each sub-volume. The "deterministic" REV is then estimated as the volume, over which the property of interest remains close to the constant. Another approach aims at calculating a "statistical" REV, which is defined as the size of a volume beyond which the mean of the estimated property becomes approximately constant, and the coefficient of variation, defined as the ratio between the standard deviation and the mean, is less than a given value (typically 20 % e.g., Zhang et al., 2000).

In case of shale materials, the most popular technique to estimate REV or REA is likely the "counting box" method (e.g., Klaver et al., 2012; Klaver et al., 2015; Houben et al., 2013; Houben et al., 2014; Fauchille, 2015) (Figure 29). Following this approach, the properties of interest are mainly the surface content of phases or minerals. The calculations are performed on SEM images which are assumed to be representative of the spatial scale of interest (typically between some fractions of micrometers up to few hundreds of micrometers).

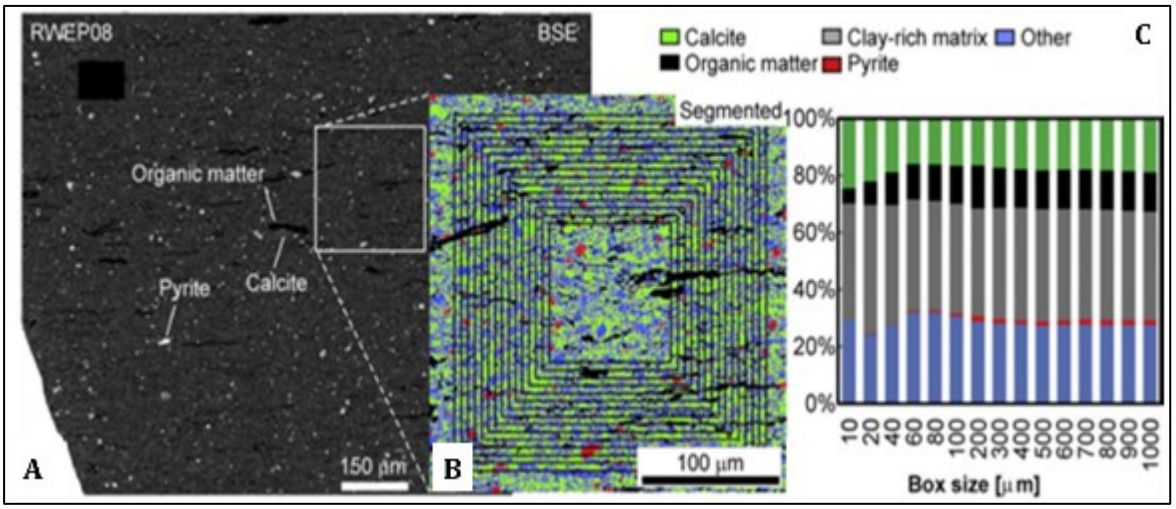

Figure 25. Princip of representative elementary area calculation (REA): (A) BSE mosaic is segmented according to the different gray level and EDX analysis; (B) a stepwise growing grid is placed on the segmented BSE mosaic to perform the box counting method; (C) counting box analysis indicating REA, which is between 100 µm×100 µm and 200 µm×200 µm (Klaver et al., 2012).

1.3.2. Sample preparation

One of the most challenging part of SEM experiments is the preparation of the sample to eliminate its roughness: the surface for the investigation should be extremely flat and well-polished. This condition prevents artifacts from obscuring the sample, reduces image blurring caused by high surface relief and allows high-quality atomic number contrast on SEM images (e.g., Krinsley et al., 2005; Ma et al., 2017a). Several methods exist, which allow to obtain such a proper surface: (i) mechanical polishing, providing representative large surface area of few cm^2-dm^2; (ii) focus ion beam (FIB) milling on area of few μm^2, which allows to prepare small regions of interest; and (iii) Broad Ion Beam (BIB) milling, which resulting area of intermediate size in-between last two methods – few mm^2. The ion milling techniques are highly efficient providing the surface roughness in nm scale. The preliminary overview of the available literature, concerning the application of imaging techniques on shale samples, has revealed that ion milling is the most popular technique for surface preparation, despite all the disadvantages. Meanwhile, some authors confirm, that ion milled surface area cannot be representative for such a heterogeneous object, as shale sample (Kelly et al., 2015). However, application of these methods raises the question of representativity, since the dimensions of produced surface areas never exceed few mm^2 for BIB and few hundreds μm^2 for FIB. In addition, some specific artifacts can be produced, mainly the milling stripes, caused by low scattering of ion beam at the interface of compounds with different behaviors (especially pores when not fully filled by a resin), can be observed (Figure 26). Due to small investigation area which can be obtained by ion milling (for FIB it is around 10-80 μm per side, for BIB – up to 2 mm), some microstructural components, which exceed these dimensions, cannot be observed.

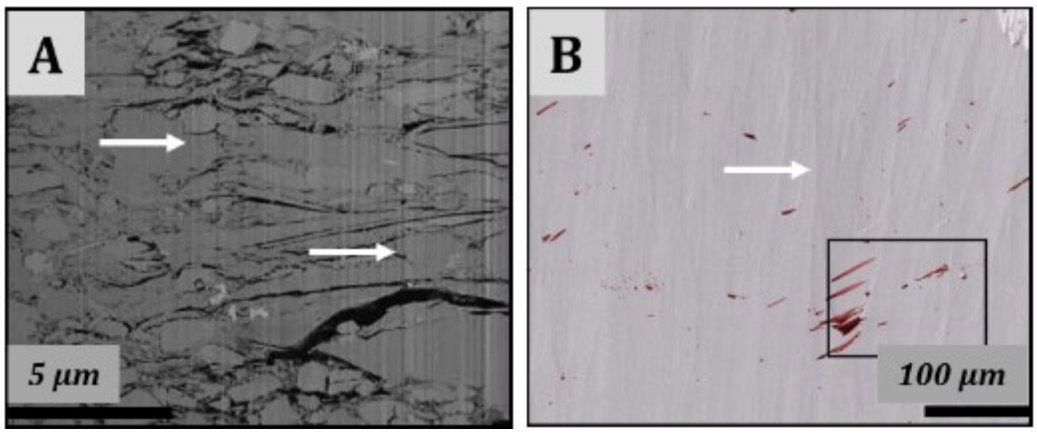

Figure 26. Ion milled surfaces with ion current striations (white arrows) from literature: A) focus ion beam milling on Haynesville sample, Ga-beam, 2 kV, FE-SEM, area n*100 μm^2 (Chalmers et al., 2012a); B) broad ion beam milling on Fusinite maceral, Ar-beam, 6 kV, SE, n*100 mm^2 (Giffin et al., 2013).

In the context of shale samples, the application of mechanical polishing is very scarce (for non-impregnated samples), most of the times the authors have reported that this method of the surface preparation is not suitable due to considerable number of artifacts, which may be created on the surface. Loucks et al. (2009) has noted that topographic features induced by standard polishing procedure greatly exceed the average size of pores in the sample (Figure 27). These irregularities on the surface have been assumed to be a result of heterogeneity in grain hardness within the sample. Shale mechanical microstructure can be presented as simplified system with "hard" grains immersed in "soft" clay matrix.

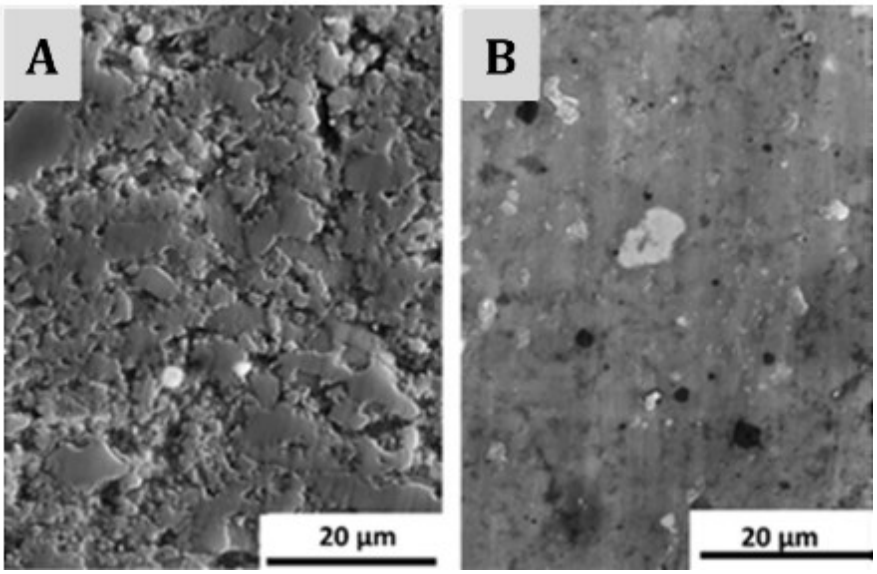

Figure 27. Secondary electron (SE) images for sample after surface impregnation at same scale showing the difference in topography between A) a mechanically polished surface; and B) an Ar-ion beam cut surface (Loucks et al., 2009).

Indeed, the sample surface presented in the Figure 27.A, is not suitable for mineral mapping, also due to strong dependence of back scattered electrons on tilt of the probed surface (the complement of the angle between the beam and the surface plane). At very high tilt angles the backscattered electrons coefficient values for different elements tend towards unity (Figure 28), providing a poor contrast between elements. Another consequence is that highly energetic backscattered electrons are mostly emitted away from the detector, when sample surface is tilted, leading to the confusion of crystal boarders with pores.

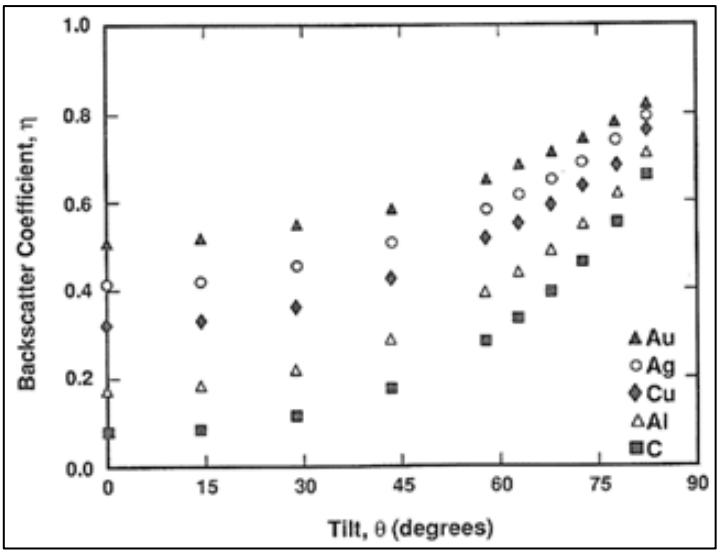

Figure 28. Backscattered electron coefficient as a function of tilt as calculated for several elements by Monte Carlo electron simulation (Goldstein et al., 2003).

The fact that mechanical polishing can be efficient for surface preparation even for non-impregnated samples, was proved, however, in the work of Fauchille (2015), where the manual mechanical polishing was applied on the large area (e. g., centimeter scale) of non-impregnated samples. Here the manual polishing allowed to obtain a proper surface for SEM mineral mapping (Figure 29) with little artifact, in comparison with surface on Figure 27.A, but requires time consuming optimization of the procedure. However, the two main disadvantages of this procedure are: (i) time to achieve such a polished surface and (ii) a low reproducibility of the result. Optimization of such a manual polishing procedure to produce the surface without topography artifact is of pivotal interest for reaching SEM observation on representative area of several centimeters (i.e., at the scale of the core sample).

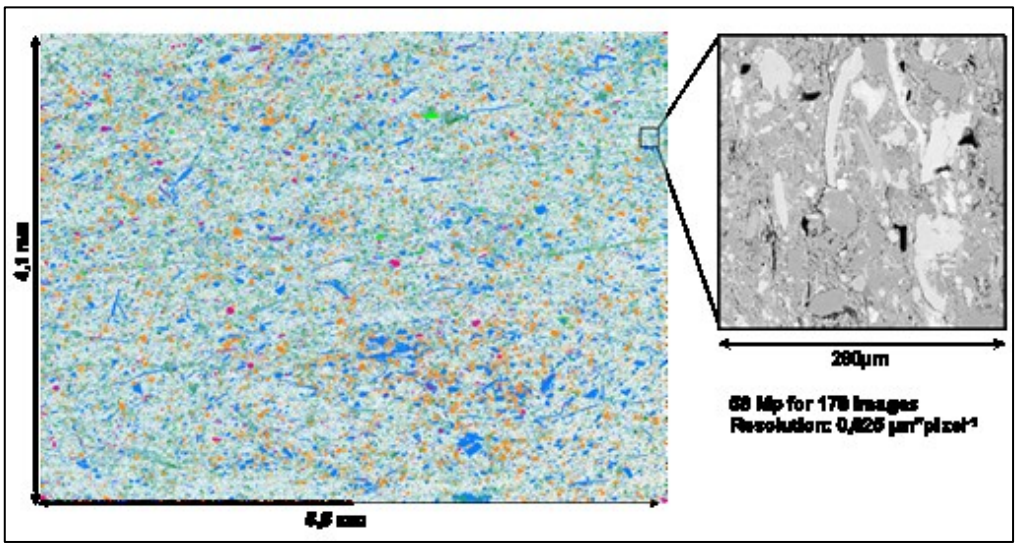

Figure 29. Large field and beam drift corrected SEM-BSE mosaics (mineral mapping – left), performed on manually polished sample and region of interest of the initial BSE images (right) (Fauchille, 2015).

Table 7 represents the summary of the acquisition parameters selected for shale samples investigation by some authors, which are grouped by sample preparation method selected for the imaging techniques. Sample preparation controls the flatness and the dimensions of the surface to acquire, impacting the representativity of the resulting information. As well, the topography of the surface controls the resolution of the final image (Figure 28). FIB milling technique is providing the most efficient result with the minimum topographical variations of the surface, however allowing to prepare only areas of few μm^2. Although the BIB milling increases the area of investigation up to few mm^2, the quality of the resulting image is decreasing as well, as broad beam would provide larger artifacts. To overcome this disadvantage, some procedures of BIB preparation with the decreasing beam current and sample rotation have been developed for the surface preparation (i.e. Smith et al., 2001; Fishman et al., 2012). Although BIB images result is often referencing as representative one, when the deterministic REA estimated (i.e. Houben et al., 2014; Klaver et al., 2015), the high heterogeneity of shale formations (Figure 3) and multiscale pore network (Figure 8) should be considered, when interpreting and upscaling such data. However only mechanical polishing allows to achieve the areas large enough to represent the full variability within the shale cores (e.g. sedimentary laminae), the quality of such surfaces often does not allow to apply the automatic image processing procedures due to significant presence of non-regular artifacts created. Ion milling techniques provoke artifacts as well, but due to automatic procedures applied for surface preparation they have regular character (Figure 26) and may be eliminated with some filtering procedures (Carpentier, 2004).

1.3.3. Autoradiography

Autoradiography is an imaging technique based on radiolabeled resin impregnation of the porous sample, from which the beta activity allows to calculate local porosity within the sample. Autoradiography has been first applied on the crystalline rock characterization (Hellmuth et al., 1993). The purpose of the new ^{14}C-polymethylmethacrylate (^{14}C-PMMA) method was to obtain information that can be provided by an ideal, non-sorbing tracer in a rock matrix. The detailed procedures were developed for the samples impregnation, exposition and autoradiographs calibration to obtain the porosity values by Hellmuth and Siitari-Kauppi (1990). The ^{14}C-PMMA impregnation method can give valuable qualitative and quantitative information on the spatial distribution and local variability of porosity in solid rocks. The results can be visualized directly as porosity maps. The method allows the investigation of dynamic processes, such as movement of infiltration or diffusion fronts (Hellmuth et al., 1991).

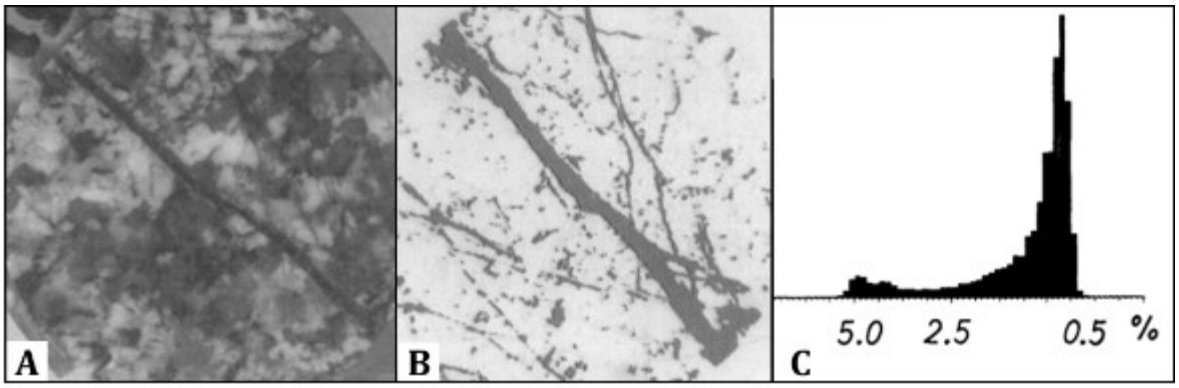

Figure 30. Rock section (A) and false-colour binary image (B) superposed on the autoradiograph of the labelled granite sample (porosity level ~1.5%); sample diameter is 32 mm; C) histogram of the spatial porosity distribution ordinate – number of pixels (area units) (Hellmuth et al., 1993).

The properties of the MMA are close to those of water molecule (listed in comparison with other known polymers in Table 6). The small molecule size allows to penetrate the smaller voids, providing the well-reproducible result on the crystalline rocks (Figure 30). Meanwhile, the close dipole moment gives the ability to penetrate the interlayer space of clay minerals and may lead to the swelling and destruction of the microstructure of studied material (Prêt, 2003; Prêt et al., 2010a; Prêt et al., 2013).

Table 6. Comparison of the parameters of various monomers with water.

Monomer	Dipole moment, D	Viscosity, mPa·s	Molecule size, nm	Monomer density, g/cm³	Polymer density, g/cm³
Acrolein	3.1	0.33		0.84	1.35
Acrylic acid	1.6-2.6	1.3		1.05	
Acrylonitrile	3.9	0.42	0.468	0.8	1.17
Styrene	0.12	0.69	0.593	0.9	1.05
LR White		0.8			
MMA	1.6-1.97	0.6	0.534	0.94	1.18
Water	**1.83**	**1**	**0.343**	**1**	

The ^{14}C-PMMA impregnation has been, first, adapted to sedimentary clay rocks by Sammartino et al. (2002), who demonstrated how the autoradiography could be applied for shale characterization but in a poorly reproducible way as a lot of sample damages were observed. Further development of the MMA impregnation technique, applied on clay materials (Prêt, 2003; Prêt et al., 2010a; Prêt et al., 2013), permitted the efficient impregnation of the entire sample down to the interlayer space of clay minerals without losing the clay confinement or modifying the pore space geometry during sample

manipulation (sectioning, polishing, and image acquisition). The resin impregnation method (with both, ^{14}C - labeled or pure monomer based, resins) developed for the bentonite (Prêt, 2003) and clay-rich rocks (Prêt et al., 2004), was than successfully proved to be efficient and reproducible for fully impregnate shales and cement materials (Robinet et al., 2012; Gaboreau et al., 2011; Gaboreau et al., 2016).

Thus, the ^{14}C-PMMA impregnation technique affords the possibility to map the connected porosity of clayey materials in a hydrated-like state. The same exposed polished surface, used to calculate porosity map, can be investigated by other imaging techniques to obtain intercomparable data. Such an approach has been applied on cement/argillite interactions investigations, where BSE images were recorded on the surface of impregnated samples allowing the comparison with autoradiography porosity maps (Figure 31; Prêt, 2003; Prêt et al., 2004; Gaboreau et al., 2011; Robinet et al., 2012; Gaboreau et al., 2016).

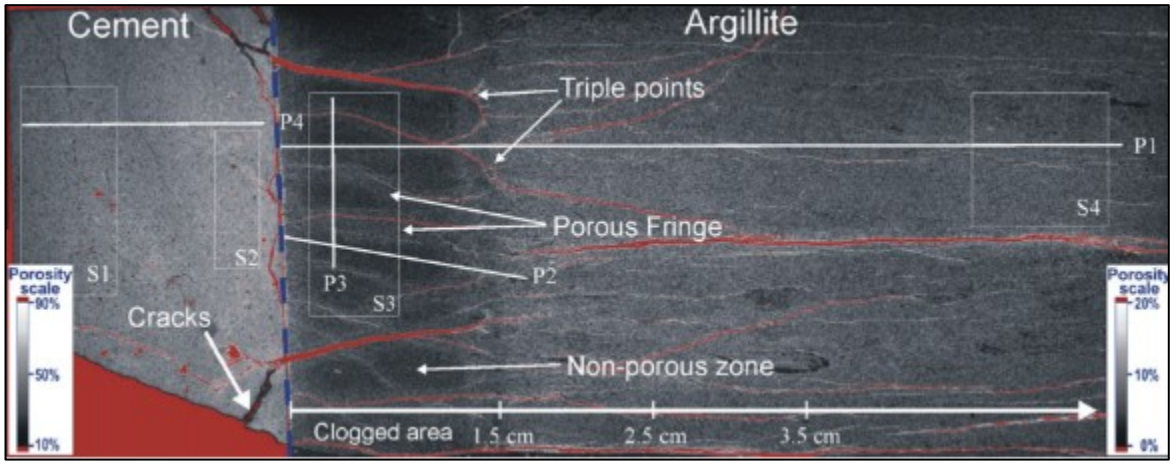

Figure 31. Porosity map of the linear cement/clay interface; positions of the porosity sub-areas and profile measurements are shown; white arrow indicates distance from the interface (Gaboreau et al., 2011).

Since there is no limitation of the field of view (as large as the surface of films used for autoradiography, of the order of several cm^2) for this method, a large representative sample can be investigated: large porosity maps of the connected porosity distribution with a µm pixel size can be obtained. The contrast of the separate phases within the sample can be controlled by the exposition time, while the resolution of the final images is limited only by the resolution of the film by itself (i.e. *Kodak BioMaxMR©* film has the resolution of 20 µm per pixel) and by the resolution of the selected digitalization. To improve the resolution of the resulting images, ^{3}H labeled PMMA can be applied, due to lower beta energy for ^{3}H in comparison with ^{14}C and the application of specific ^{3}H-film with higher resolution (i.e., ^{3}H-Hyperfilms). ^{3}H-PMMA autoradiographs improve the detection of fine porosity variations (Prêt, 2003; Robinet et al., 2015).

Indeed, autoradiography is the only technique that provides a porosity map drawn from physical information at the micrometer to decimeter scale, allowing to access to the visualization of spatial distribution of the local connected porosity with the µm resolution and including all the pores down to the interlayer.

1.3.4. X-Ray tomography

The development of imaging techniques based on measurements of the adsorption of X-rays allows the acquisition of three-dimensional reconstructions of local linear attenuation coefficient (LAC) from a series of two-dimensional projections taken at different angles. The X-rays transmission rate by sample is defined by Beer-Lambert law (Equation 17).

Equation 17.

$$\frac{I}{I_0} = e^{-LAC \cdot x} \cdot 100\% ,$$

where I_0 is the intensity of X-rays emitted by the source, I – the intensity of the X-Rays captured by the detector, LAC - linear attenuation coefficient [m^{-1}], which is a function of X-ray energy, x – sample thickness [m]. The resulting resolution is the function of sample size and the detector size in pixels; the smaller the sample (µm scale) the better resolution and larger transmission rate (i.e. a better signal-to-noise ratio) may be achieved.

In a laboratory-based setup, low- or high-flux X-ray tubes with a polychromatic cone beam are used. In synchrotron-based setup, a parallel beam of highly spatially coherent monochromatic X-rays is generated using insertion devices such as bending magnets. A synchrotron source is expected to provide more accurate and precise data than a polychromatic cone beam, due to the absence of cone beam artefact and a unique X-ray energy. The comparison of these two setups was done, for example, by Brunke et al. (2014), who demonstrates, that the synchrotron-based acquisitions provide the result with less artifacts, than the laboratory measurements. The example of such data acquisition and treatment, in the case of the organic-rich shale samples, can be found in Panahi et al. (2017). The authors have demonstrated, how the deformation and fracturing of shales during heating can be investigated. Their approach has provided images at resolutions of few microns with short scanning time, among other benefits (monochromatic beam to avoid beam hardening artifact, etc.).

Most of X-ray µtomography devices achieve 3D volume of image with a resolution down to 1 µm, with just some systems exhibiting resolution of 50 nm (Noiriel, 2015). At this scale only macropores or part of them could be probed for gas shale (Figure 32) (Kaufhold et al., 2016). The macroporosity detected here is very low (0.2-1%).

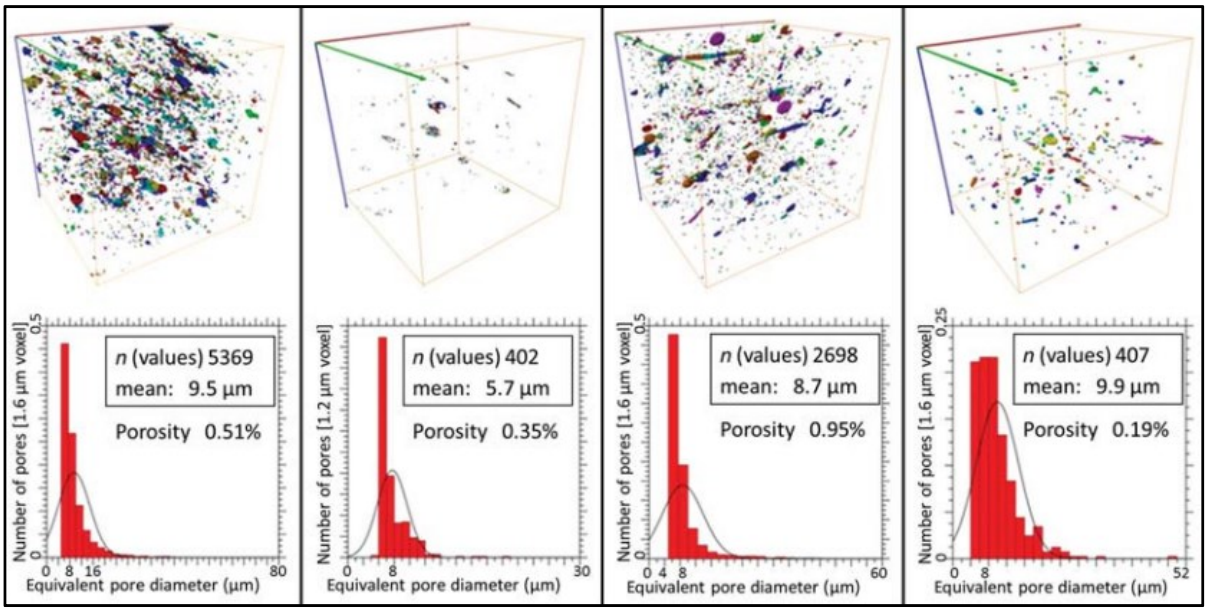

Figure 32. Equivalent pore-diameter distributions for Posidonia shale achieved by µCT volumes segmentation (Kaufhold et al., 2016).

The main limitation of this technique is the lack of contrast (ΔLAC) of the linear attenuation coefficient (LAC) of various compounds expected in shale sample: quartz and illite have almost the same linear attenuation coefficient whatever the x-ray energy could not be contrasted (Figure 33). Enough contrast is reached at very low energy (< 40 keV), which strongly limits the size of the sample analyzed in term of transmission rate (I/I_0 ratio, Equation 17). The contrast between solids and pore full filled by resin or any other liquids is also very small.

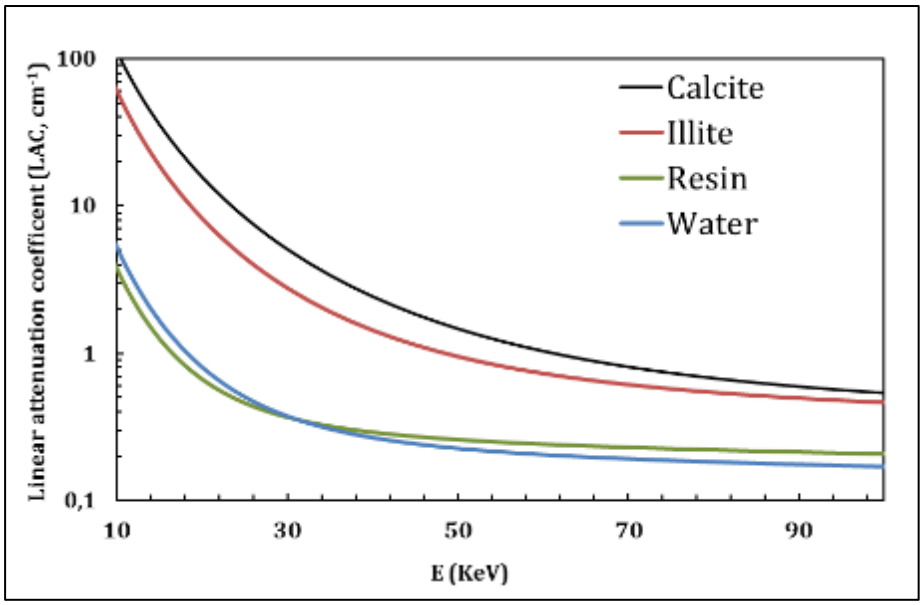

Figure 33. Linear attenuation coefficient, calculated for various minerals and carbon with increasing source energy (calculations done with XOP2.4 software; Sanchez del Rio and Dejus, 2011)

Therefore, robust segmentation and quantification of macropores is not straightforward. The dual energy acquisition can be applied to improve the contrast between different phases (Noiriel, 2015).

The various application of μtomography may be found in literature, from large fractures network investigation (cm-μm scale) down to pores within mineral and organic phases (nm-μm scale) (Ma et al., 2017a). Such a large scale information is used for the estimation of the anisotropic mechanical properties and permeability (Ougier-Simonin et al., 2016); deformation and fracturing of shales during heating (Panahi et al., 2017), or damage evolution of rocks undergoing brittle failure through the dynamic microtomography images (Renard et al., 2017); among many other applications (Noiriel, 2015).

Despite the limitations of this technique, leading to the complicated interpretation of the phases and its segmentation, the μtomography acquisitions allow to observe the large volumes in 3D, to describe the pore volume morphology and connectivity (Noiriel, 2015; Figure 34.A) Some modern segmentation tools developed to visualize each class of elements separately and quantify and classify them within the sample volume (Robinet et al., 2012; Figure 34.B).

μTomography techniques allow to visualize and evaluate various elements of the sample structure in 3D, but the limitations on the sample size, to achieve the best resolution of the separate elements, question the representativity of such a sample regardless to the heterogeneities in shales formations (Figure 3). At the opposite, the scanning of the layered sample limits the achieved result of the 3D volume to μm, leading to the visualization of part of macropores domain. Due to the possible difficulties of the image segmentation (low LAC contrast, acquisition artifacts, etc.) the reliability of the porosity result extracted from μtomography images is directly depended on the procedure selected for the images treatment, which can vary significantly between authors, thus, making difficult the comparison of the result. Most of the time, x-ray μtomography found application in 3D visualization of macroscopic properties under variable conditions, more than in microstructure characterization, remaining useful tool for the shale sample heterogeneities visualization.

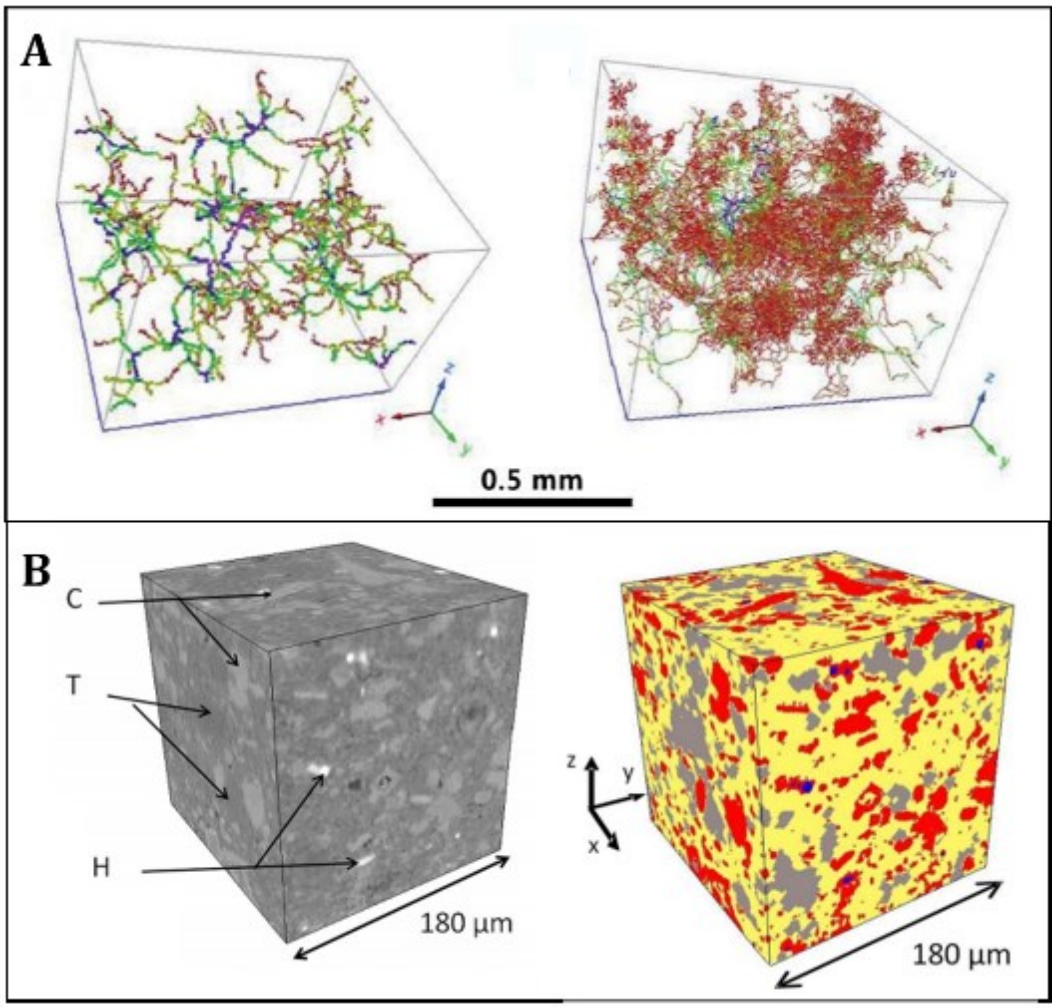

Figure 34. A) Medial ax is for two data sets of Berea sandstone showing different pore network connectivity estimates depending on the image resolution, i.e., 5.92 µm (left) and 1.85 µm (right) (Noiriel, 2015). B) Mesostructure of Callovo-Oxfordian mudstone visualized (on the left) by synchrotron µCT (voxel 0.34mm; C: carbonates, T: tectosilicates, H: heavy minerals); and corresponding mineral group spatial distribution (on right: red is for carbonates, grey – tectosilicates, yellow - clay matrix, blue – carbonates) (Robinet et al., 2012).

1.3.5. Scanning electron microscopy

Among imaging techniques involved into the shale pore space characterization, Scanning Electron Microscopy (SEM) is probably the most widely applied technique. It is used as imaging tool in geology and mineralogy and it has already established its applicability for such heterogeneous materials as shales. The main detection modes are secondary electrons (SE) and back-scattered electrons (BSE) imaging. The sample preparation and parameters of acquisition, which are setting by the operator, contribute

greatly to the signal-to-noise ratio, the final resolution of image and, finally, to the quality of the image (Reed et al., 2014).

Dual beam FIB-SEM

With the development of FIB, and so the quality of the surface obtained by ion milling, the investigations of pore space down to nanometer range is accessible through SEM imaging. Since pore size of shale sample is extremely small, this technique has found a wide application on unconventional reservoirs characterization (Curtis et al., 2012a; 2012b; Kelly et al., 2015; Kaufhold et al., 2016; among many others). Application of 2D imaging techniques usually allows to estimate porosity values and provide a description of the pore space organization, associated with one or another phase (Figure 35). For example, on the basis of such images the heterogeneity among different particles of OM - hosted nanopores may be investigated (Han et al., 2017).

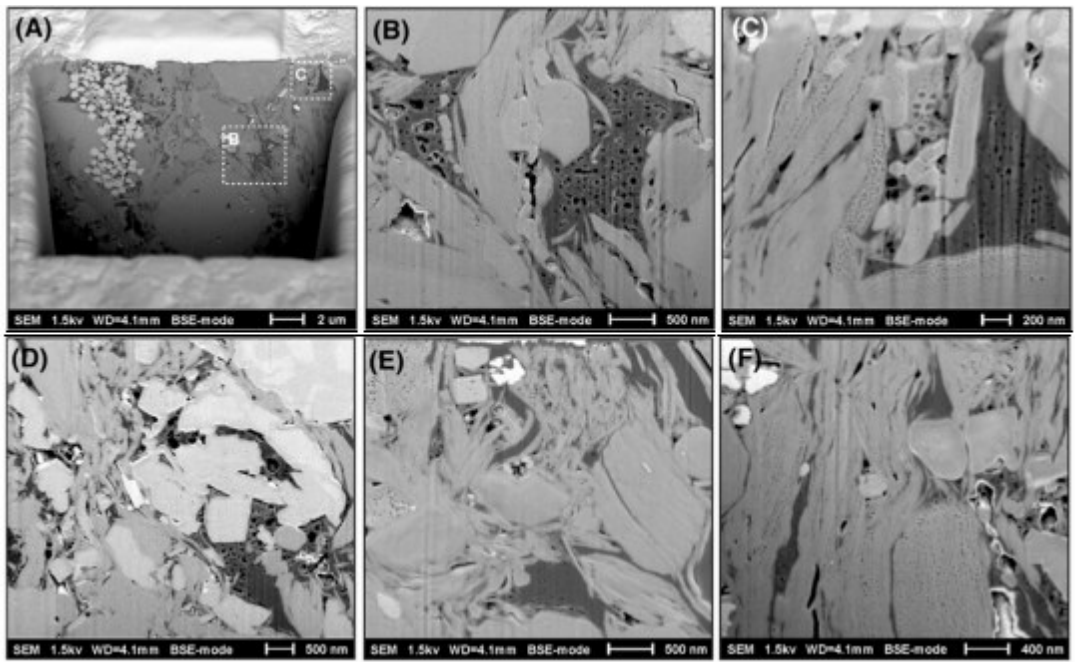

Figure 35. Back scattered electron (BSE) scanning electron microscopy (SEM) images acquired with focused ion beam milling from the gas-mature Haddessen well (Toarcian Posidonia Shale, Germany): areas marked with dashed rectangles in A are magnified in B and C (Han et al., 2017).

FIB - SEM equipment (dual beam FIB-SEM) allows to characterize the pore space in 3D through sequential imaging, milling layer by layer (Anovitz and Cole, 2015). The reconstructed 3D volumes permit to perform “true” pore size distribution”. Figure 36 displays some examples of pore-size distribution obtained on various shales with 3D FIB-SEM imaging. The calculated PSDs are continuous with a probable mode at the minimum detection value (the distribution is continuous with the broad distribution mode at around the minimum pore size). If this mode exists, the presented cases would illustrate

that the resolution of the method, applied in this case, is not enough to distinguish the smallest pores (lower than 40x40x25 nm for example on the Figure 36.A and lower than 2.5x2.5x10 nm for example on the Figure 36.B). The calculated volumetric contribution of such narrow pores to the total porosity is very small regarding to the PSD (see Figure 36.B): this result is not in agreement with the results of bulk measurements, obtained on the same shale samples in the same study (see, Figure 42; Curtis et al., 2012b). This inconsistency could be related to a poor detection efficiency of the smallest pores (i.e., subjective manual thresholding on BSE images without electron energy filtration, inducing a true resolution largely worse than the voxel size of 2.5nm).

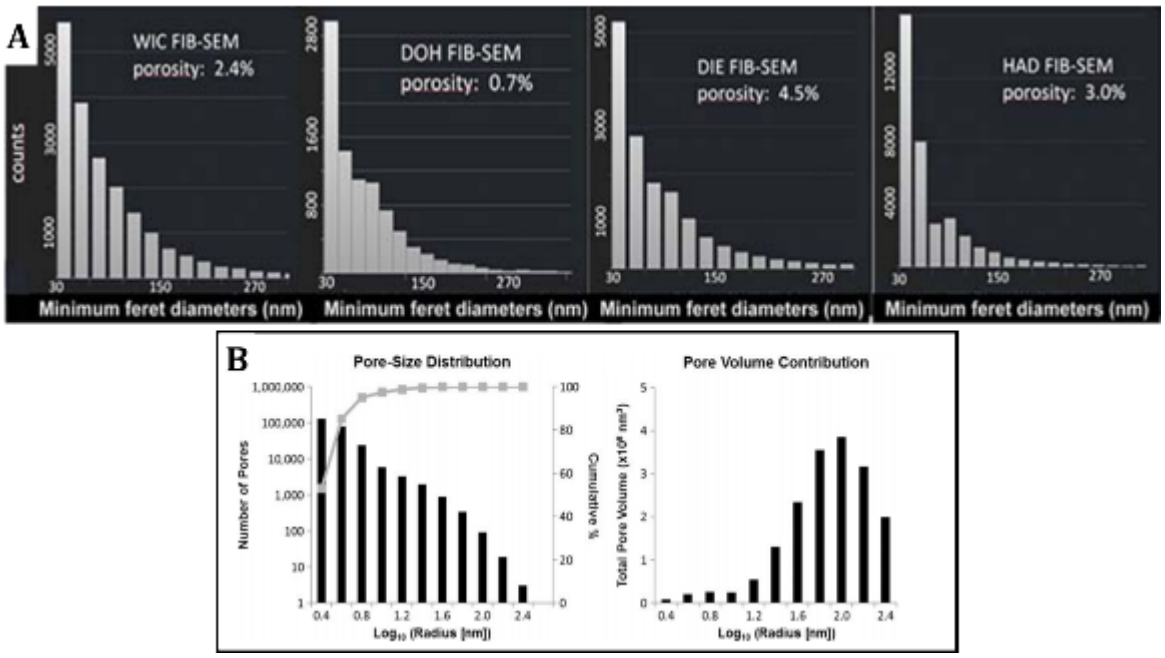

Figure 36. Pore size distribution obtained with 3D FIB-SEM: A) pore size distribution for different samples from German shales, 1kV, voxel size 40x40x25 nm (Kaufhold et al., 2016); B) pore size distribution and volumetric contribution of the pores estimated for the 3D reconstruction of samples taken from Horn River formation (British Columbia, Canada), 1kV, voxel size 2.5x2.5x10 nm (Curtis et al., 2012b).

Three-dimensional characterization of pore space allows to reveal the connected clusters of pores, which provide the additional information about the effective porosity and pore network organization. The choice of criteria for interconnected pore space is crucial (Figure 37). Here the threshold for pore connectivity was arbitrary defined as 10^5 connected voxels (Curtis et al., 2012b), while a valid estimation of the connectivity is only allowed, when the narrow throats connecting the pore bodies are efficiently detected (Figure 42) (Gaboreau et al., 2016). Here such a condition is not satisfied with the true resolution of 10-20 nm, while the throats of gas shales probed by MIP are always smaller than 10 nm (Figure 10). Dewers et al. (2012) used more advanced pores segmentation approach for gas shale on FIB volumes with interpolated voxels of 7.14 nm. The resulting detection of the connected part of the pore network by propagation from the image

border (Figure 37) is more efficient, as also pointed by Gaboreau et al. (2016) with proportion of connected pores around 90 %.

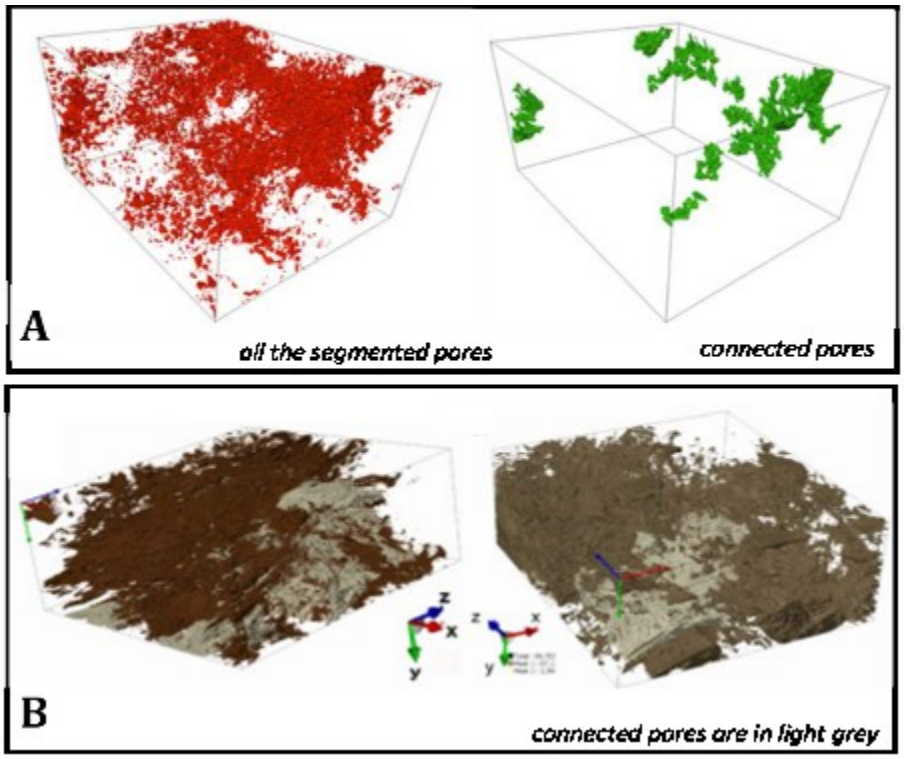

Figure 37. 3D FIB volumes of pore thresholding and connected pores segmentation: A) for Horn River formation (British Columbia, Canada) (1 kV, 2.5x2.5x10 µm) (Curtis et al., 2012b); B) for Haynesville formation (1 kV, voxel size interpolated 7.14 nm) (Dewers et al., 2012).

Image analyses provide a visual appreciation of pore system, but very often they are not a statistically valid method to evaluate the heterogeneity of hydrocarbon reservoirs in shales. Most of the authors do not provide the quantitate information about pores, confining their work to similar qualitative evaluation of pore morphology, geometry and distribution within the sample (Erdman and Drenzek, 2013; Fishman et al., 2012; Chalmers et al., 2012a; among many others). Due to small area of studied sample, the calculations of total porosity from images are not representative, being mostly local descriptive tools for the pore network characterization of shale samples. Most of the time, with the voxel size and the resolution of the image used in many publications, a volume of few hundreds μm^3 is obtained, regard to the microstructure heterogeneity, of shale material, information about pore origin, location and geometry can be visualized and analyzed, but the representativity of such a 3D volume is limited to the local information.

1.3.6. Transmission electron microscopy/scanning transmission electron microscopy (TEM/STEM)

Transmission electron microscopy (TEM) have been used for long time to characterize clay minerals microstructure (Tessier, 1984; Kim et al., 1995) and recently has been used in the characterization of compacted clay materials (Gaboreau et al., 2016, Han et al., 2017) at the nanometric scale. The recent developments of tools, like TEM (transmission electron microscopy) and STEM (scanning transmission electron microscopy), are reviewed by Brydson et al. (2014). To perform the image analysis in transmission mode (bright field, dark field or HAADF images) with the spatial resolution down to 1 nm (5 nm in case of Bernard et al. (2012a)), the sample should be electron transparent, thinner than ~250 nm (lamella is never thinner than 50 nm). To prepare such a thin section, FIB milling technology is applied (Smith et al., 2001). An example of TEM analyses can be found in Bernard et al. (2010) (here the techniques were applied to localize STXM (Scanning Transmission X-Ray Spectroscopy) measurements. These methods have been successfully used to perform localized observations of the sample, but the representativity of such a small area is always questionable for geologists (Bernard et al., 2012a; Reed et al., 2014; Bernard and Horsfield, 2014; Han et al., 2017). Authors have used TEM/STEM to characterize shale microstructure, as Bernard et al. (2012a), who has also applied STXM. With this apparatus the authors display carbon distribution and the pores associated with OM (Figure 39).

Since TEM imaging does not provide information about a 2D plane of the sample, being a projection with averaged information from a 50 nm thick lamella, the detection of the smallest pores remains a challenging task. The resulting data are not a spatial distribution of pores (i.e., a map of pores), but rather a distribution of local porosity (i.e., mixture of solid and pores through the lamella thickness) (Figure 38.B). Moreover, calculations of PSD including the micropores are not satisfying with these techniques: the characteristic lengths of the fine microstructure of the studied sample may be of the same order of magnitude of the thickness of TEM lamella (Figure 38.C) (Gaboreau et al., 2016).

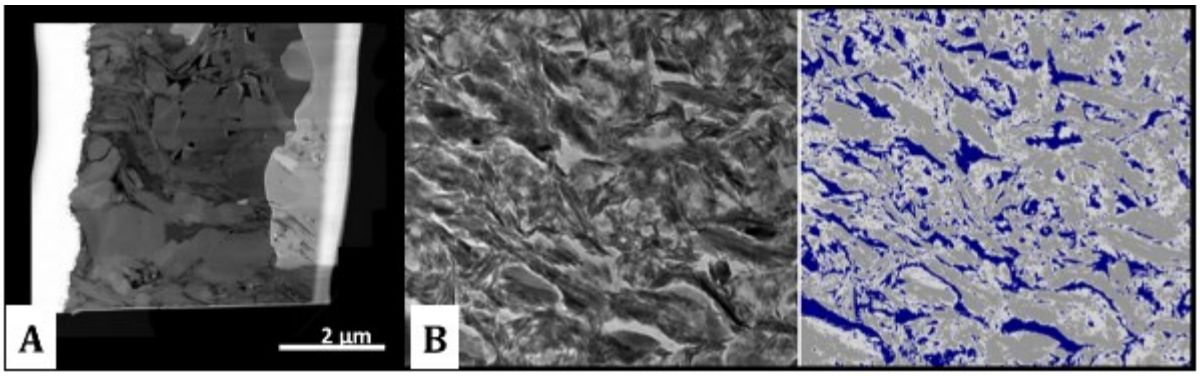

Figure 38. A) STEM (HAADF mode) image (~100 nm thick lamella; 200 kV) (Bernard et al., 2010). B) Segmented 2D TEM image (<100 nm thick lamella; 200 kV, point resolution 0.14 nm, field of view 2µm) (Gaboreau et al., 2016).

Although the field of view of these imaging techniques is extremely small (never exceed few µm), it allows to achieve the maximum resolution, investigating the smallest elements of sample microstructure, including the nanopores with OM, which are not easily achievable to visualize by other imaging techniques. For example, Han et al. (2017) reported the existence of organic nanopores of irregular shapes within Haddessen shale samples (Figure 39). The observed OM is extremely porous (>50%) with a possible bitumen origin.

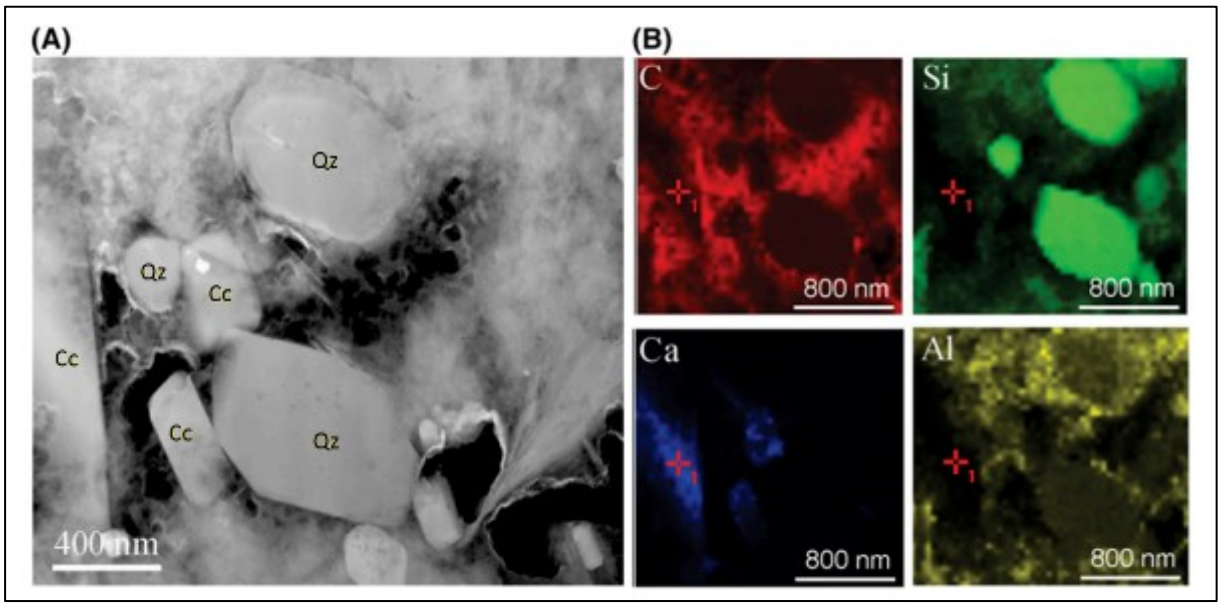

Figure 39. A) Transmission electron microscopy image (high-angle annular dark-field, Z-contrast mode) of a focused ion beam foil from the Haddessen well. Pores appear black, organic matter appears dark, and silicates and carbonates appear gray; (B) Energy-dispersive x-ray spectroscopy elemental maps: carbon (C), silicon (Si), calcium (Ca), and aluminum (Al). Authigenic calcium carbonates (Cc) and quartz (Qz) cements are identified (Han et al., 2017).

1.3.7. Imaging acquisition and data treatment

The resolution and the quality of the images obtained from various imaging techniques (see sections 1.3.4 - 1.3.6) are directly dependent, first, on the parameters of acquisition. The choice of these parameters is based on the preliminary information about the composition of the studied material. As it was described above, the main phases of shale samples are inorganic minerals, solid organic matter and hydrocarbons (see section 1.1). The acquisition of the images with enough contrast between these elements is, thus, the pivotal.

For SEM, the choice between very low (1-5 kV, Table 6) and low accelerating voltage (5-20 kV) is conditioned by the detector selected for the investigation. Secondary electrons are emitting from the near surface sample volume with very low energies (few eV) and require higher accelerating voltage of the initial beam to obtain the better image resolution associated to a smaller probe diameter. For back scattered electrons emitted with the energies of several keV, a better resolution is achieved at low accelerating voltage as it is controlled by the BSE emission volume diameter and poorly influenced by the probe size (Reed, 1996). The application of very low acceleration voltage is preferable for shale samples for several reasons. The firs reason is, to decrease the probability of the sample heating under the electrons beam. It is known, that the surface temperature increase in case of mica may be expected up to 160 K (with 20 kV accelerating voltage of initial beam, Reed, 1996). This heating may lead to the instability of OM and resin under the electrons irradiation. Second, to improve the resolution: (i) operating at low overvoltage; (ii) operating at low incident beam energy; or (iii) operating on thin foil specimen at high beam energy, – are the known strategies to improve the resolution of the resulting SEM images (Newburry, 1997). The size of the interaction volume is a function of the energy with which the beam of electrons interacts with the target. The interaction volume in iron is shown as a function of beam energy for the range 10-30 keV (Figure 40, Goldstein et al., 2003), illustrating that the smaller accelerating voltage of the beam may provide the better resolution of the BSSEM image. Energy selective detector (EsB), capturing the electrons only of specific energy, may allow to improve the resolution, due to limitation of the number of electrons interactions before being backscattered quasi-elastically to the surface. Recent investigation demonstrated how the selection of the parameters at each step of the image acquisition controls the final result, being the key factor for the proper image segmentation (Gaboreau et al., 2016).

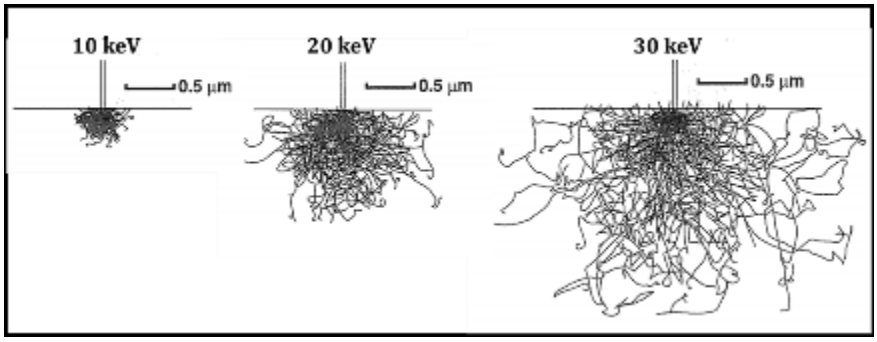

Figure 40. Monte Carlo electron trajectory simulations of the interaction volume in iron as a function of beam energy (Goldstein et al., 2003).

Another crucial step in the characterization process, which can dramatically affect the quality of resulted information, is the way of analyzing image and data treatment. First, the images provided by imaging techniques often contain several types of artifacts, which can appear at any step of sample preparation or acquisition. The different ways of removing these artifacts can cause the reduction of image quality (especially its resolution). Second, to analyze porous network, pores must be segmented from other phases (as well as segmentation of all the phases from each other is needed). There are two main principles for outlining pores and features within the electronic images: automatic or manual thresholding. It must be taken into the account, that the subjective point of view of the operator may be inconvenient with manual thresholding. It was shown by an experiment with a group of students, which were asked to threshold a SEM image of kaolinite (Tovey and Hounslow, 1995). The results vary significantly from 20 up to 55% of total porosity (Figure 41) from the simple bi-phase image However, it should be mentioned that in some cases the automatic segmentation result is in the good agreement with manual pores outlining (Houben et al., 2013). Some programs can be used to outline manually and measure the individual pores (Loucks et al., 2009, Table 7).

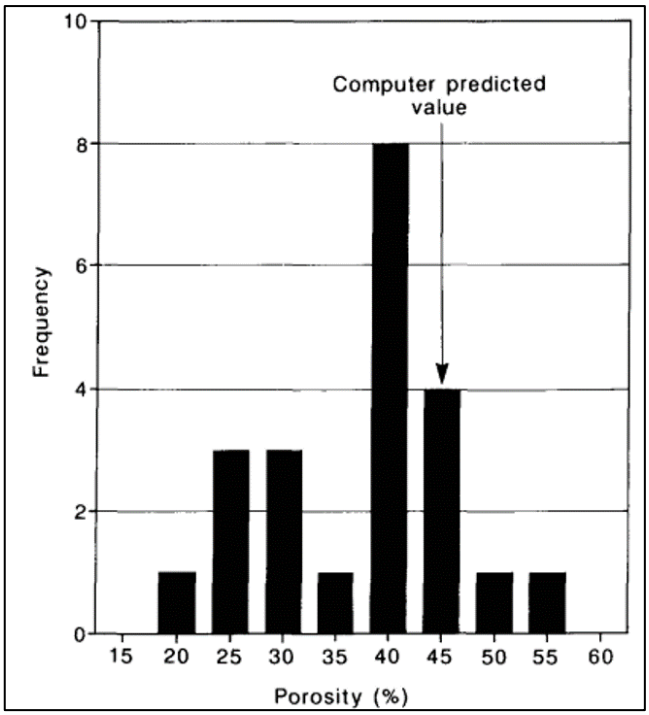

Figure 41. Histogram showing porosity measured by group of researches using subjective methods alone to manually threshold (Tovey and Hounslow, 1995).

One of the most widlly used approachs for the automatic thresholding is the Otsu thresholding (Otsu, 1979) of SEM images. This approach applied on 3D FIB volumes of SEM images (1 kV, voxel size of 40x40x25 nm) for gas shales, Kaufhold et al. (2016) have shown that only ~20% of pore space was probed regardless to the total porosity provided by bulk techniques (N_2 adsorption and MIP). Such a result is not unexpected, when considering that most of the pores are smaller than 10 nm (Figure 18, Figure 12). Gaboreau et al. (2016) demonstrated also that the Otsu method applied on energy filtered BSE images of synthetic compacted illite sample (1.5 kV, voxel size 5x5x5 nm) allows to detect only 30% of the pore space. By improving the data treatment (image restoration and more advanced image segmentation) the same authors have shown that more than 70% of porosity has been probed, clearly demonstrating that using the classical approach is not efficient enough whatever the resolution (Figure 42).

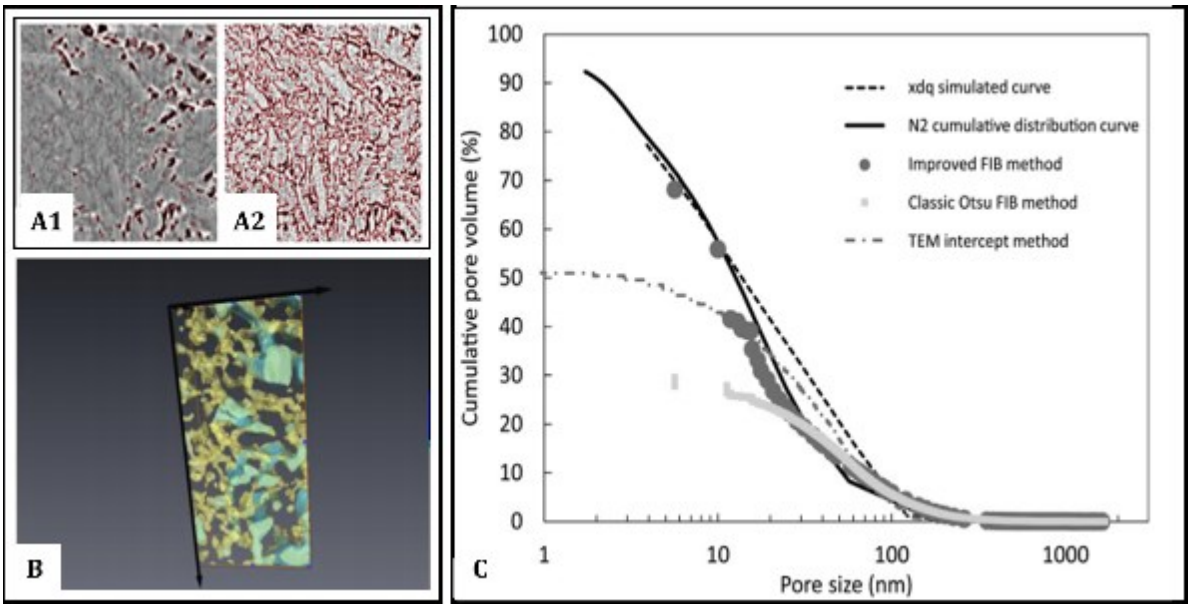

Figure 42. Pore pace characterization of synthetic compacted illite sample: A1) SE image thresholded by the Otsu method; A2) EsB image representing the advanced approach of the segmentation of the smallest pores (the red outlines represent the borders of the pores recognized and thresholding); B) region of interest illustrating the pores segmented from Otsu thresholding (light blue) and from the developed method (yellow); C) intercomparison of pore size distribution achieved by various techniques (Gaboreau et al., 2016).

Table 7. Acquisition and data treatment parameters selected for different imaging techniques and applied for the shale samples characterization.

Reference	Shale	Sample preparation	Acquisition parameters					Data treatment	Results and observations
			Microscope/ Tomograph	Detectors/ modes	Voltage, kV	WD, mm	Pixel size		
BIB-SEM (sample of several mm²)									
Fishman et al., 2012	Kimmeridge, UK	BIB (Ar beam), impregnated (blue epoxy); C-coat		SE; BSE; EDS	15			Qualitative observations	Pores geometry and morphology
Giffin et al., 2013	Ruhr and Munsterland basins, Germany	BIB; Au-coat	Zeiss Supra 55	SE; BSE; EDX			Min. pores detection- 15 µm	ArcGIS© manual segmentation	Pores geometry and morphology, PSD
Hemes et al., 2014	Boom Clay, Belgium	BIB (Ar beam), Au-coat	Zeiss supra 55	SE2 ; SE in-lens ; BSE ; EDX			10 nm/ Min. pores detection - 1000 nm²	Autopano©; MATLAB© (thresholding, sable-edge detection) & manual cleaning with ArcGIS©	REA, PSD, pores classification, connectivity of pore network
Houben et al., 2014	Opalinus Clay, Switzerland	BIB (Ar beam), Au-coat	Zeiss supra 55	SE; BSE; EDX	5-20	6-8		Autopano©; manual segmentation with ARCMAP9.3© & automatic segmentation with MATLAB© (thresholding, sobel-edge detection, watershed)	REA, PSD, pores classification
Houben et al., 2013	Opalinus Clay, Switzerland	BIB (Ar beam), Au-coat	Zeiss supra 56	SE; BSE; EDX	5-10	7-8	15 nm/ Min. pores detection - 45 nm	Kolor Autopano giga2.0©; MATLAB© segmentation & Arcmap10© for manual correction	REA, PSD, pores classification

Houben et al., 2016b	Toarcian Posidonia, Germany and The Netherlands	Mechanical polishing; BIB (PIPS-Ar beam); Au-coat	FEI XL30S FEG-SEM, FEI Nova 600 Nano lab	SE; BSE; EDX			300 nm-mechanical polishing; 25 nm-ion milled	Microsoft Image Composite Editor©, MATLAB© (for pyrite and OM only) & manual segmentation with ARCMAP©	REA, PSD, pores classification
Klaver et al., 2012	Posidonia, Germany	BIB (Ar beam); Au-coat	Zeiss Supra 55	SE; BSE; EDS			Min. pores detection - 10 µm	AutoPano2 © & ArcGIS© manual segmentation	REA, PSD, pores classification
Klaver et al., 2015	Haynesville and Bossier, USA	BIB (Ar beam)	Zeiss supra 55	SE2 ; SE-in-lens ; BSE ; EDX (Appolo10 SDD, EDAX)	5-20	4-8		Kolor Autopano giga2.0©; MATLAB© for pores segmentation & ArcGIS© for manual cleaning	REA, PSD, pores classification
Ko et al., 2017	Eagle Ford, USA	BIB (Ar beam); Ir-coat	FEI Nova NanoSEM 430 FE-SEM	SE; SE-TLD	10-15	4-5	58-2.6 nm	Point counting JMicroVision©	REA, PSD, pores classification
Löhr et al., 2015	Woodford, Monterey, USA	BIB (Ar beam)	FEI Quanta 450 FE-ESEM	BSE; EDX				Fiji© (contrast and size measurements)	Pores geometry and morphology
Loucks et al., 2009	Barnett, USA	BIB (Ar beam); Au/Pt -coat	Zeiss Supra 40 VP Philips XL30	SE; BSE; EDS	20	3-6	Down to 5 nm	Points counting JMicrovison©	Pores geometry and morphology, porosity
Loucks et al., 2012	North America shales	BIB (Ar-beam)	Zeiss Supra 40 VP; FEI Nova NanoSEM 430	in-lens SE BSE	1-10	3-7	Down to 5 nm	Qualitative observations	Pores geometry and morphology, pores classification
Milliken et al., 2013	Marcellus, USA	Mechanical polishing (impregnated)/ BIB (Ar beam); C-coat	FEI Nova NanoSEM 430 FE-SEM	SE; BSE; F	10 (spot 3)		7-4 nm	Manual & digital tracing JMicroVision©	Pores geometry and morphology, porosity

Milliken et al., 2014	Eagle Ford, USA	Mechanical polishing (impregnated)/ BIB (Ar beam); C-coat	FEI Nova NanoSEM 430 FE-SEM	BSE; SE	10 (spot 5)		~7 nm	Qualitative observations	Pores classification
Pommer and Milliken, 2015	Eagle Ford, USA	BIB (Ar), Ir-coat	FE-SEM	BSE; SE-TLD	10-16 (spot 3)	4.2-10	14.6 nm/ Min. pores detection-40 nm	Point counting and manual segmentation JMicroVision©	Pores geometry and morphology, porosity
Tian et al., 2013	Longmaxi, China	BIB (Ar beam), Pt-coat	FEI Helios Nano Lab 600	SE; BSE	1-5	1.5-8		Qualitative observations	Pores geometry and morphology
FIB-SEM (sample of several µm²)									
Curtis et al., 2012a	Woodford, USA	FIB; Au/Pd-coat	FEI Helios 600 dual beam FIB-SEM	BSE (2D); SE	1 -20			Image J© relative area	Pores geometry and morphology
Curtis et al., 2012b	9 shales, USA, Canada, UK	FIB 3D ; Au/Pd-Coat	FEI Helios 600 dual beam FIB/SEM	BSE	1	~4	2.5 nm	Avizo Fire 6.2©	PSD, 3D volumes, connectivity
Curtis et al., 2014	Wolfcamp, USA	FIB 3D	FEI Helios 650 NanolabDual Beam FIB-SEM	BSE	1 (beam current 0.40nA)		2.5 nm	FEI maps© & Avizo Fire ©	PSD, 3D volumes, connectivity
Dewers et al., 2012	Haynesville, USA	FIB 3D ; Au/Pd-Coat	FEI Helios 600 NanolabDual Beam FIB-SEM	BSE	1 (beam current 1.4 nA)		7.14 nm	automatic thresholding procedure ImageJ©	PSD, 3D volumes, connectivity
Gu et al., 2015	Marcellus, USA	FIB (Ga beam)	FEI Quanta 200eD Dual Beam FIB; Fei NanoSEM 630 FE-SEM	BSE (low-voltage high contrast detector); EDS	3-4			Qualitative observations	Pores geometry and morphology, pores classification

Heath et al., 2011	Gothic shale, Kirtland and Tuscaloosa mudstones, USA	FIB (Ga beam) ; Au/Pd-Coat & silver dag	FEI Helios 60 Nano lab Dual Beam	BSE (TLD)	1 (beam current 1.4 nA)			ImageJ© (interpolation); ScanIP© (Sipleware, volume rendering, pore calculation), 3DMA-rock code © (quantification and pores statistic)	3D volumes, connectivity
Jiao et al., 2014	Longmaxi, China	FIB; Au-coat	FEI Helios 600 dual beam FIB-SEM	BSE; SE	1-5			PCAS © (for pores counting)	Pores geometry and morphology, porosity
Kaufhold et al., 2016	Lower Saxony Basin, Germany	FIB	Zeiss Auriga	BSE; SE; EDX	1.5 (current 500pA)		40x40x25 nm	Avizo© (image denoising and treatment)	Pores geometry and morphology, porosity, PSD
Kelly et al., 2015		FIB	FEI Helios Nano lab dual beam	CBS	1 (current 400pA)	3	5 nm	FIJI © (image transformations and filtering) & MATLAB© (image treatment and segmentation)	PSD, pores geometry and morphology,
			FEI FIB-SEM	ETD	2 (current 40-80 pA)	4	15-20 nm		
TEM/STEM (sample of several µm²)									
Bernard et al., 2010	German shales, kerogen of various origin	FIB	Tecnai F20 XTWIN TEM; FEI FIB 200 TEM	Fishione HAADF, (Gatana Tridiem energy filter), EDAX Genesis	200		4 nm	Avizo® Fire 6.2	pores geometry and morphology, pores classifications
Bernard et al., 2012b	Barnett shale	FIB	Tecnai F20 XTWIN TEM; FEI FIB 200 TEM	TEM (+STXM)/ HAADF	200		5 nm	Avizo® Fire 6.3	
Han et al., 2017	Posidonia, Germany; Barnett, USA	FIB	Tecnai F20 X-Twin FE TEM-EDXS	HAADF/ Z-contrast mode	200		2 nm	Qualitative observations	pores geometry and morphology

Janssen et al., 2011	SAFOD, USA	FIB	FEI Tecnai G2F20 X-Twin TEM/AEM	HAADF/EDX (gatan Tridiem energy filter)			Qualitative observations	Pores geometry and morphology, relative porosity
µTomography								
Kaufhold et al., 2016	German gas shale	3-4 mm sample	Nanotom Phoenix	Hamamatsu CMOS flat panel	180 kV, 15W	1.6 µm	manual and Otsu segmentation	REV, 3D volumes reconstructions, PSD
Ma et al., 2016	Bowland, UK	1 cm sample	XT H 225, Nikon			7.7µm;	Avizo© (image denoising segmentation and treatment)	REV, 3D volumes reconstructions, multisalle PSD
		1 mm sample	The Diamond- Manchester Beamline, Diamond Light Source			0.5 µm		
		65 µm sample	Xradia Ultra, Zeiss			0.13 µm		
Ma et al., 2017b	Lublin and Baltic Basins, Poland and Lithuania	5 cm sample	XT H 225, Nikon			44µm	Avizo© (image denoising segmentation and treatment)	REV, 3D volumes reconstructions, multisalle PSD
		1 mm sample	The Diamond- Manchester Beamline, Diamond Light Source			0.5 µm		
		65 µm sample	Xradia Ultra, Zeiss			0.12 µm		

1.4. Combination of methods for pore space characterization – role of the organic matter maturity

Such a heterogeneous multiscale object as a shale sample requires a multitool and multiscale approach for the pore network investigations. Classical bulk measurements involve a lot of limitations on the result interpretation, due to assumptions implied for the pore network characterization by these techniques. The data treatment of the results obtained by MIP and N_2 adsorption is based on simple mathematical models (Washburn's or Kelvin's equations) describing the pore network with a single geometry over the sample (cylinder or spheres) seen as a mono-material. Thus, a comprehensive pore network characterization of shales based only on bulk measurements is very difficult.

As it was demonstrated, none of the mercury intrusion curves for the shale samples is at the equilibrium; adsorption measurements are available only on powder and do not represent the real sample pore network organization, questioning the reliability of the single measurement. High complicity and heterogeneity of the shale samples implies, that a single non-localized probe does not allow a complete description of the pore network. Often throats are confused with pores bodies, leading to an erroneous pore size distribution. Some theoretical tools (e.g., fractal analysis, molecular modeling) are available to characterize the organization of the pore space, its connectivity, and permeability. Meanwhile, all these calculations assume simplistic and uniformly distributed pore networks.

Sample localization and representativity are also poorly discussed in the studies, where bulk measurements have been performed. None of the published data gives precise information on the sub-samples localization, while shales are well-known to be highly heterogeneous with the layering of clay deposits, OM and carbonates. Without an accurate localization of the subsampling, it is impossible to conclude about pore size distribution with the vertical and lateral variability of the microstructure. In many publications, it is assumed that the sample of mm-cm scale is representative by default. Meanwhile, the lamination of the shale samples may exceed this range of space scale (see section 1.1). Only authors dealing with imaging techniques propose some ways to localize the probes to correlate the images acquired at different fields of view.

The main disadvantages of imaging techniques are the limited resolution and field of view, which strongly discredit the representativity of the achieved result. Meanwhile, the careful intercomparison and the combination of different imaging techniques with various resolution may allow to achieve reliable data (Figure 43).

Ma et al. (2017a) have succeed to achieve the pore network characterization at the multiscale by implication of multitool imaging techniques and µtomography acquisitions of various resolutions on well -localized probes(Table 7, Ma et al., 2017a).

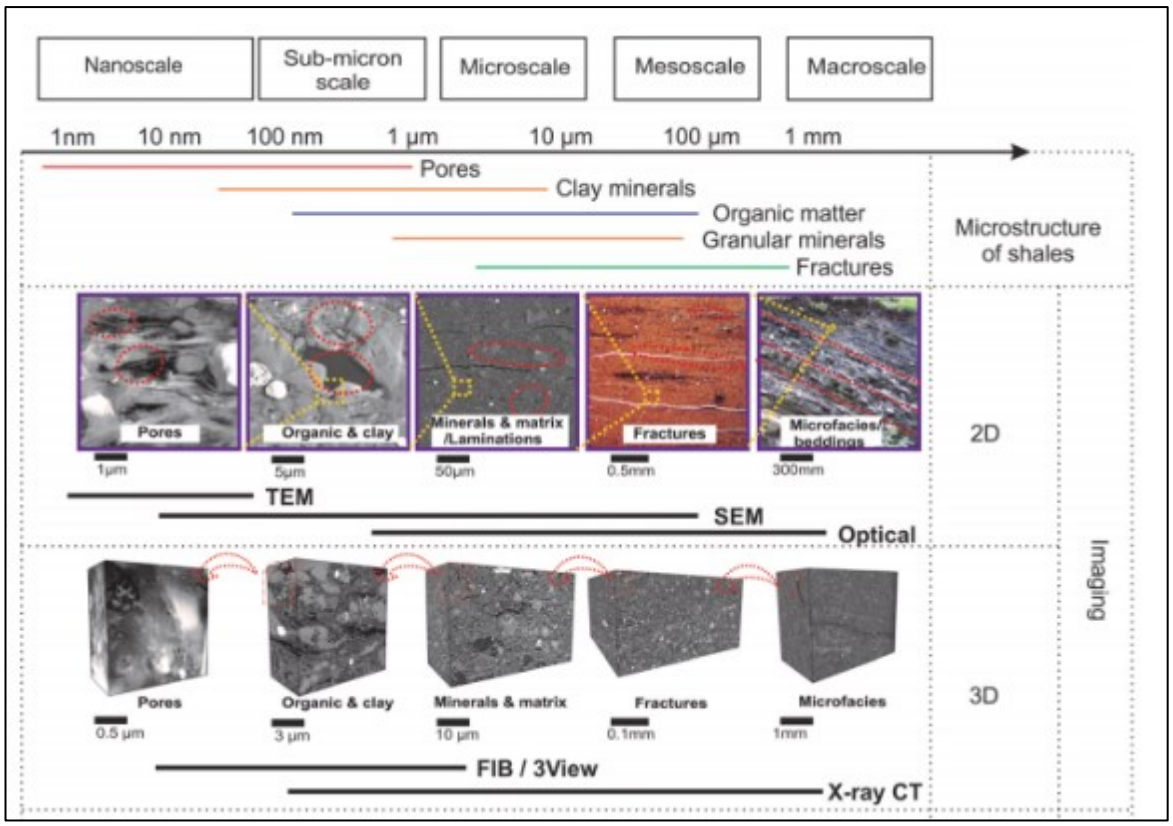

Figure 43. Scales and techniques used in correlative multi-scale imaging data of shales (Ma et al., 2017a).

The qualitative description of the pore network of the shale samples vary from an author to author, mainly depending on the shale formation and the methods of characterization applied at the different scales. However, several publications use the same classification to distinguish pores and to assign them to the inorganic or organic phases. Such an approach has been proposed by Loucks et al. (2012), who suggested to classify pores following their location within the microstructure elements: within the clay matrix, non-clay grains or OM; the fractures (natural or artificial) are considered separated from the rest of pores. .

The quantitative analysis involved in imaging techniques is complicated, as it requires a careful image segmentation (see section 1.3.7). The imaging techniques are mainly used only for the qualitative description of the pores morphology and geometry. Examples of FIB-SEM imaging on shale samples (Curtis and Ambrose, 2010; Figure 44) illustrate the variability of shales microstructure from different deposits. The pores of various dimensions (up to ~500 nm) and shapes can be associated with both, inorganic and inorganic phases. The organization of the microstructure (clay matrix/hard grains/OM ratios, distribution of grains and OM within the sample, the orientation of

grains etc.) varies with the geological history of reservoir. Meanwhile, the organic part also changes with composition and maturation.

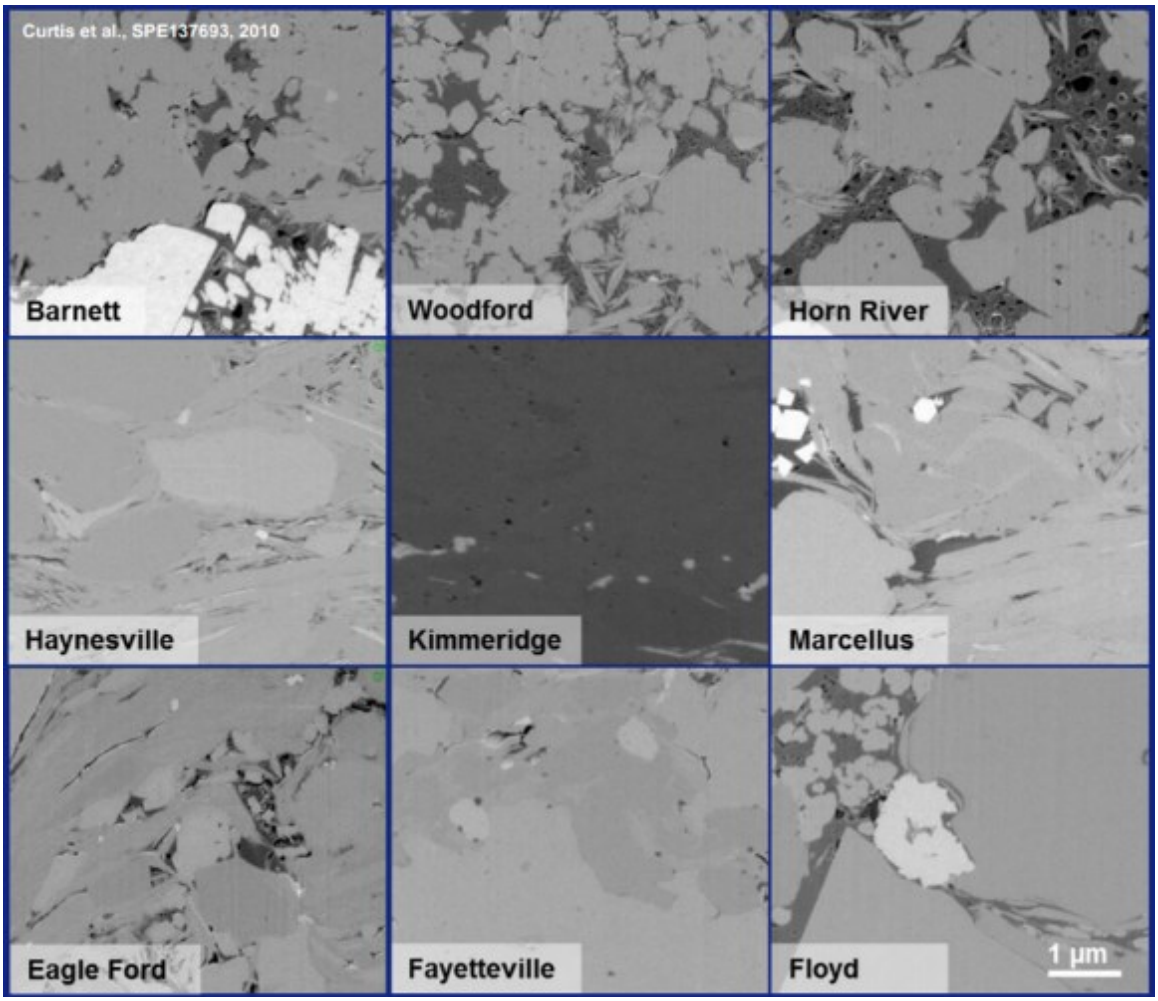

Figure 44. FIB-SEM images of some American shales samples (Curtis and Ambrose, 2010).

As it was mentioned (see section 1.1), the processes of kerogen maturation influence the pore network formation, and the OM investigation is crucial to understand the reservoir behavior. While mass fraction of OM within a shale sample is considered at the range of 2-6 %, the volumetric fraction can have a greater contribution due to significantly lower density of solid OM (1.1-1.3g/cm^3 in organic-rich shales).

Based on the idea that nano- and micropores control the major storage space in the shale reservoirs, these types of pores are regarded as playing a significant role in unconventional gas systems (see review by Jiao et al. (2014)). This has motivated a lot of works to be dedicated to the investigation of (i) pore network within OM and its correlation with OM evolution; (ii) connectivity of porosity with maturity of kerogen, total organic carbon content (Chalmers and Bustin, 2007; Curtis et al., 2012b; Schieber, 2013; etc.). These works confirmed (Curtis et al., 2012a) that porosity within the kerogen is a

result of not only OM transformation, but also of many other geological processes, occurring simultaneously within the geological formation (e.g., complex interactions between OM maturation and compaction processes associated with diagenesis) (Figure 45.D). Indeed, Curtis et al. (2012a) has reported the presence of heterogeneous porosity within the OM of the same maturity, demonstrating the coexistence of the solid kerogen patches with visible pore network (pores >10 nm) and non-porous one at a given pixel size.

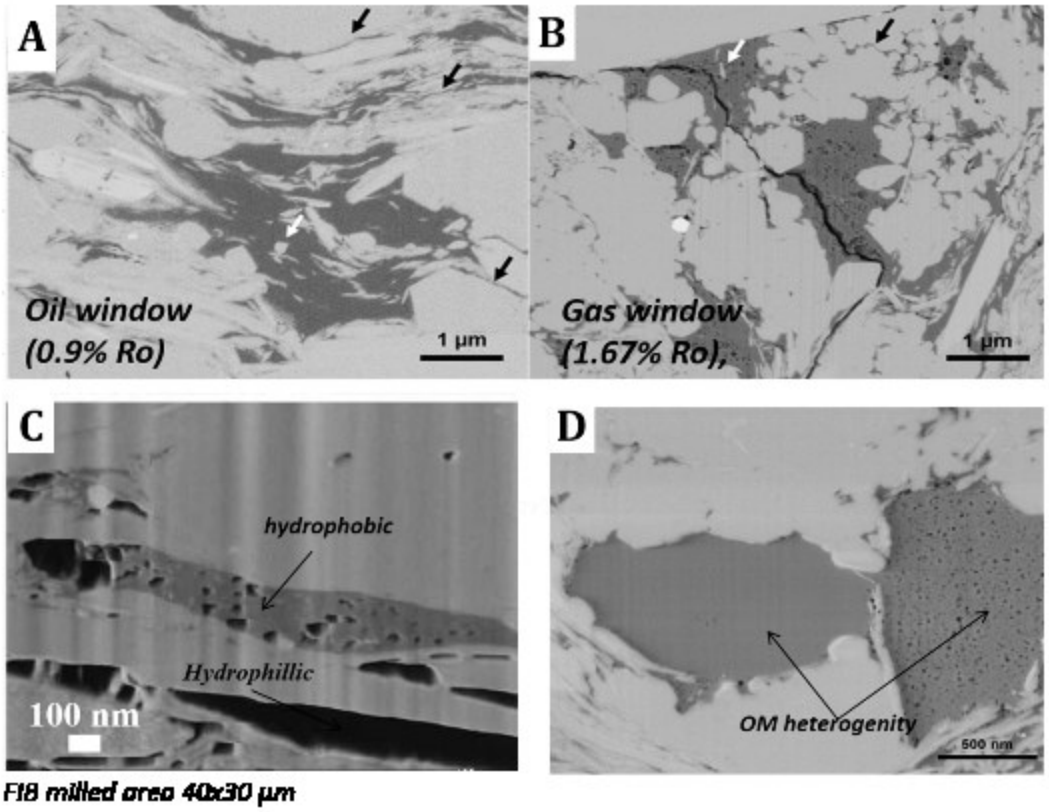

Figure 45. Localized 2D FIB-SEM imaging (at 1kV) of OM within the shale sample: A), B) organic matter of different maturity (Curtis et al., 2012a); C) porous kerogen (Chalmers et al., 2012a); D) heterogeneous organic matter of the same maturity (Curtis et al., 2012a).

By the correlation of the pore size distribution, obtained by bulk measurements, with the nature of OM in the samples, total OM content and its maturity, authors have addressed the controversial issue of the porosity origins.

The pore network organization of shale samples is a result of the diagenetic processes occurring simultaneously during the formation. The increase of burial depth leads to the increase of compaction with the decrease of the average pore size and total porosity. Meanwhile, the OM maturation occurs with the kerogen transformation to the gaseous forms that increases the pores abundance within the organic matter (Durand, 1980; Vandenbroucke and Largeau, 2007). The tectonic processes may impact the rocks fractures network development as well.

That is why most of the conclusions done on this subject have a local character and do not display general behavior of shale samples. Ross and Marc Bustin (2009) have presented the dependence of the pore size distribution on the mineral composition and total organic carbon content by investigation of Devonian-Mississippian shale samples (Figure 46). The result demonstrated that, the same tendency has not been observed in general for Jurassic shales (Ross and Marc Bustin, 2009). If the presence of some pores within solid OM is assumed, thus the increase of total porosity with the increase of the volumetric organic matter content is predictable.

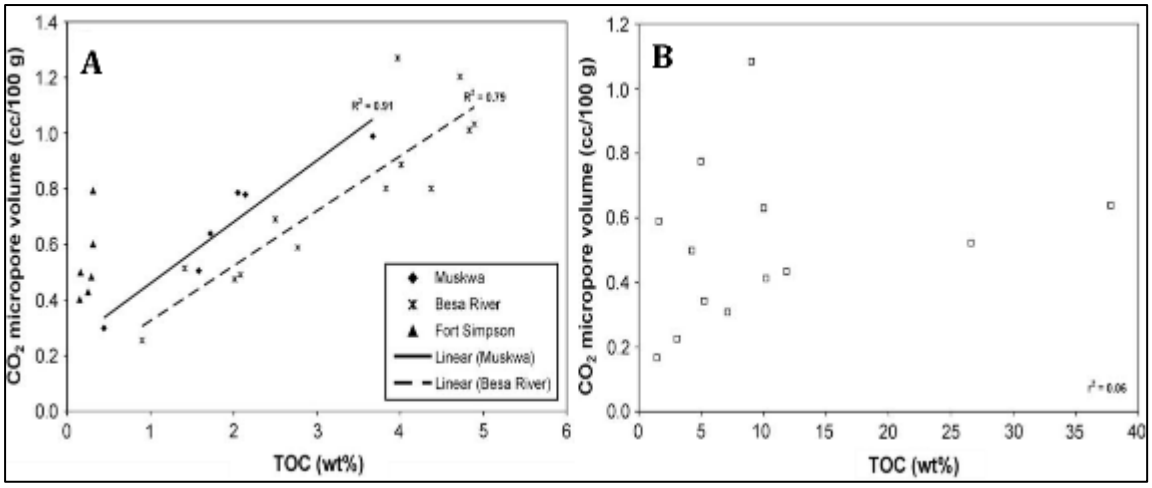

Figure 46. A) Relationship between micropores volume and TOC for Devonian-Mississippian shale (r^2= 0.4, not shown); B) variation in micropores volume with TOC for Jurassic shales (Ross and Marc Bustin, 2009).

Attempts to correlate the porosity values with the OM maturity have led to as well contradictory results and controversial issues between the authors. The nitrogen adsorption results, published by Ojha et al. (2017), have shown an increase in the pore network complexity with OM maturation (here quantified in terms of the change in fractal dimension calculated from gas adsorption/desorption isotherms). The authors have also observed the increase of the nitrogen adsorbed volumes with the maturity (measurements were carried out on powders, after and before liquid hydrocarbons removal, Figure 47). Although a decrease of the average pore diameter with maturity has been also evidenced.

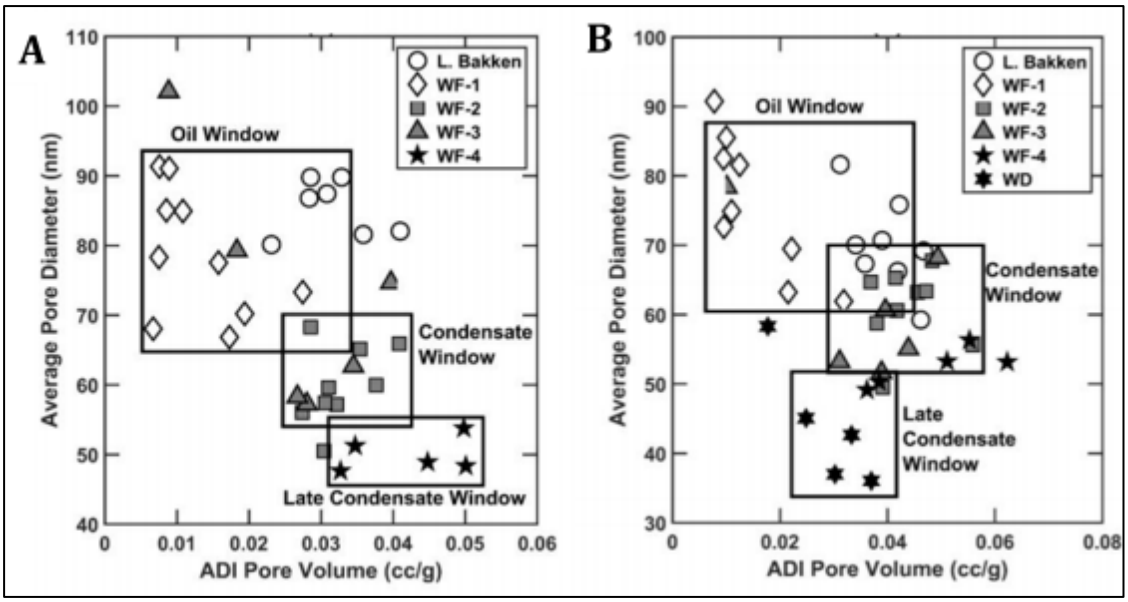

Figure 47. Crossplots of average pore diameter versus average pore volume, obtained by N_2 adsorption (ADI - Adsorption-Desorption Isotherm) for (A) native samples, and (B) cleaned samples (treated with 4:1 mixture of toluene and methanol at 110°C for 24h) from various maturity windows (Ojha et al., 2017).

Following the same topic, Mastalerz et al. (2013) have shown that the total porosity of 9.1 % in the immature New Albany Shale samples decreases to 1.5 % in the late mature sample, whereas total pore volumes decrease from 0.0365 to 0.0059 cm^3/g in the same sequence. However, reversing the trend at even higher maturity, the post-mature New Albany Shale has shown higher porosity and larger total pore volumes compared to the late mature sample. With increasing maturity, changes in total porosity clearly evolve in a non-linear way. Similar non-linear evolutions of total porosity with maturity have been observed by Han et al. (2017), and by Pommer and Milliken (2015). These results suggest that the formation of the pore network in shale samples cannot be easily correlated with maturity and its development is much more complex regarding that of OM. In other words, the intercomparison of various data reveals that there is no direct correlation (i.e., a simple relationship of proportionality) between the total porosity and OM maturity (Figure 48).

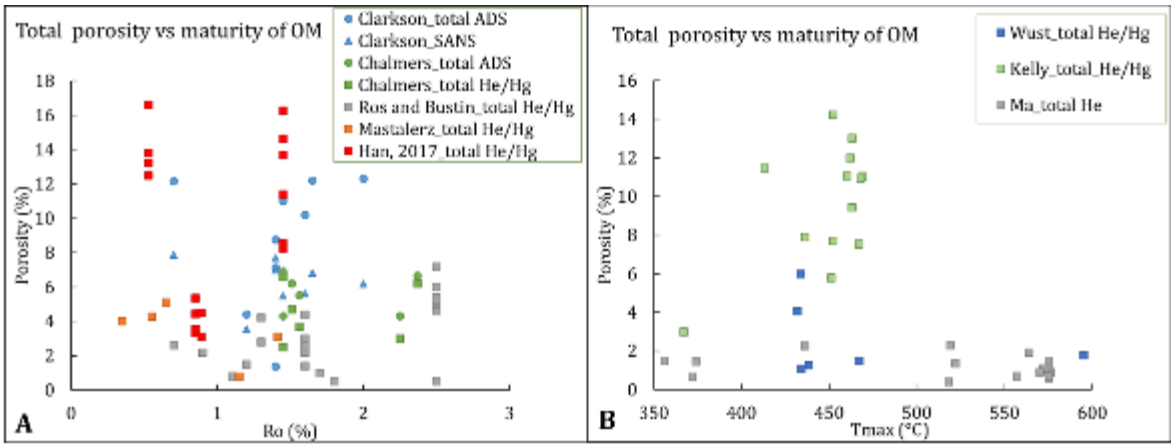

Figure 48. Relationship between total porosity volume (achieved by gas adsorption isotherms) and TOC (data combined from Clarkson et al., 2013; Chalmers et al., 2012a; Ross and Marc Bustin, 2009; Mastalerz et al., 2013; Ma et al., 2015; Kelly et al., 2015; Wust et al., 2014; Han et al., 2017): A) data with thermal maturity based on vitrinite reflectance measurements (R_0%); B) data with thermal maturity based on T_{max} measurements.

Based on the observations of samples taken from Eagle fort formation of various maturities, Pommer and Milliken (2015) proposed a simplified diagram displaying common diagenetic pathways, emphasizing the processes with the greatest effects on porosity (Figure 49.A). Five stages of diagenesis affecting the distribution and abundance of porosity have been identified: (i) early, uncompacted sediment with some early cementation (Figure 49.A-A); (ii) low maturity sediments under early burial conditions where most of porosity has been lost by compaction (Figure 49.A-B); (iii) sediments that have developed late calcite and quartz overgrowths as well as microcrystalline quartz and further compaction, but have not had pore space in-filled by secondary OM (Figure 49.A-C); (iv) sediments in the oil window where secondary OM has pervaded into primary pore space, leaving behind a small portion of residual mineral-associated porosity (Figure 49.A-D); and (v) sediments in the wet-gas window that have developed abundant, small secondary pores within OM (Figure 49.A-D). Primary porosity has been lost by compaction, cementation, and infill by secondary OM. Meanwhile, the effects of diagenesis are highly variable, and can differentially affect different grain assemblages. Two samples with similar maturities may or may not have undergone the processes in the order described above (e.g., early secondary OM infill can inhibit later cementation) (Pommer and Milliken, 2015). A similar scheme describing the pathway of the OM and mineral porosity evolution with the maturation has been proposed by Ko et al. (2017), based also on the investigation of Eagle Ford samples.

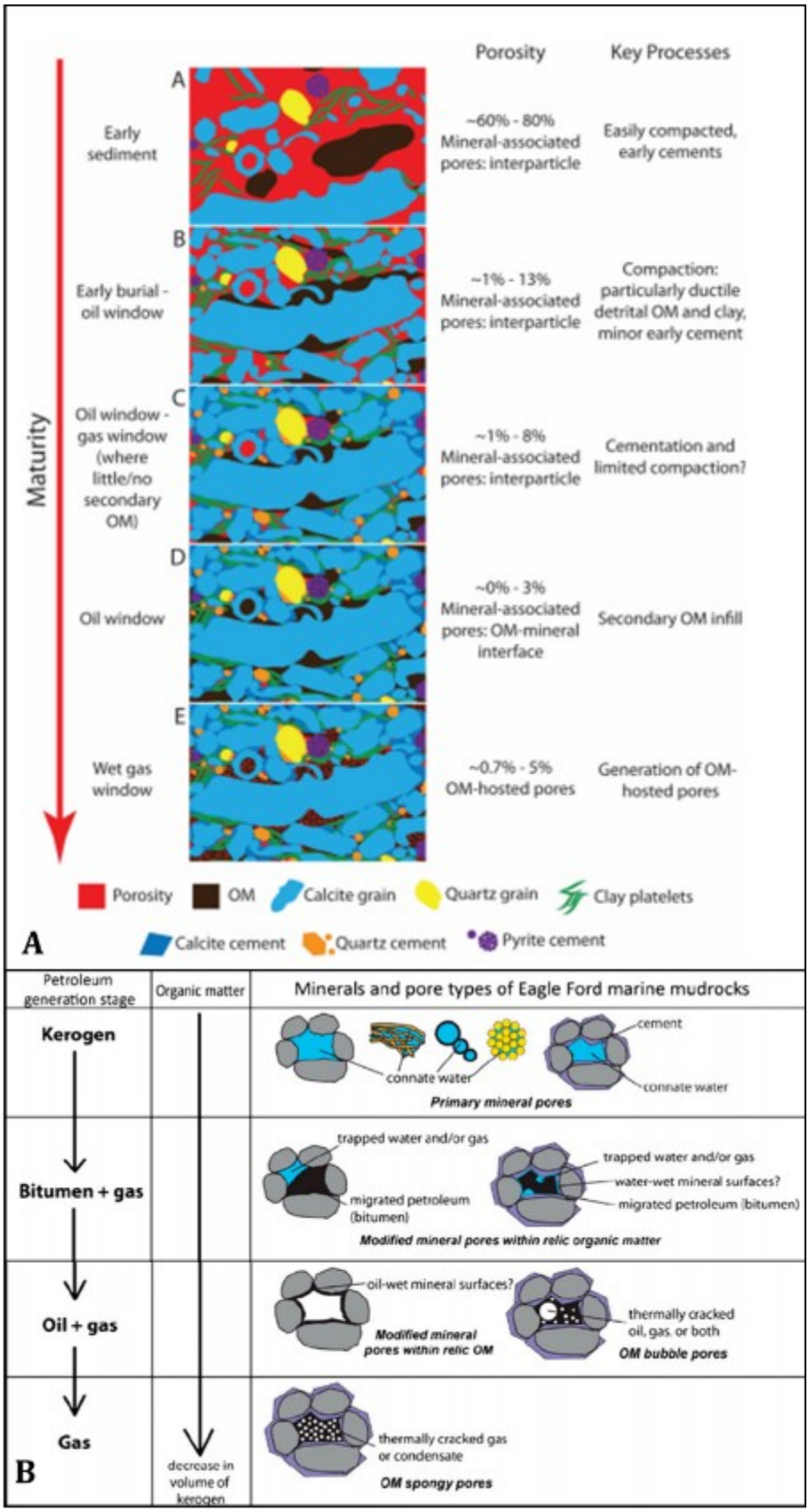

Figure 49. A) Simplified diagram displaying common diagenetic pathways of coccolithic Eagle Ford sediments, emphasizing processes with the greatest effects on porosity (see the description in the text) (Pommer and Milliken, 2015). B) Evolution of Minerals and Pore Types in the Eagle Ford Marine Mudrocks (Ko et al., 2017).

Results consistency, achieved by bulk measurements and by quantitative (or semi-quantitative) image analyses, is almost impossible due to several factors. First, the non-localized sampling: samples are always taken from various parts of the core (well), which can induce non-correlating values due to strong spatial heterogeneities. Second, observations and conclusions done on the small non-representative field of view of imaging technique are often generalized on the entire sample. Ko et al. (2017) has illustrated this aspect by comparing the porosity estimated by SEM observations and the total porosity obtained by a bulk measurement, i.e., helium porosimetry measurement. These authors have demonstrated that the comparison of SEM observation with total bulk porosity were better correlated with the images of large fields of view (Figure 50).

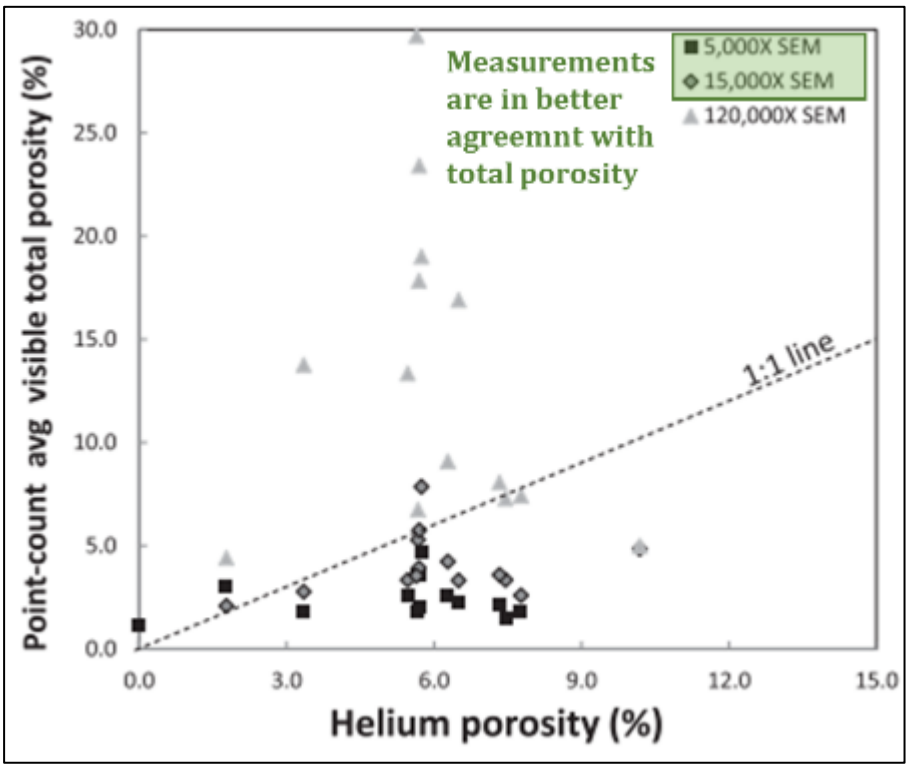

Figure 50. Plot comparing visible total porosity from point-count methods with helium porosity from crushed-rock Gas Research Institute analysis (avg = average) (Ko et al., 2017).

Another illustration of the same difficulty is provided from the works of Hemes et al. (2014). Comparison of porosities measured using the BIB-SEM method and MIP on Boom clay samples has shown that BIB-SEM porosities were below the porosities measured by MIP (Hemes et al., 2014) (Figure 51.A). The authors have proposed two origins to explain this discrepancy. First, the size of REA was not reached for the samples investigated by BIB-SEM. Second, big pores or cracks, because of sample preparation were not accounted during BIB-SEM analysis. These two statements question once again the representativity of areas investigated by the conventional imaging techniques here the BIB-SEM approach. The direct comparison of the pores throats distribution achieved by MIP with PSD provided by FIB-SEM for gas shale is not consistently matching as well:

Dewers et al. (2012) has reported mismatching of PSD obtained by MIP and FIB-SEM (Figure 51.B). But Heath et al. (2011) has demonstrated close PSDs with nearly the same slope (Figure 51.C).

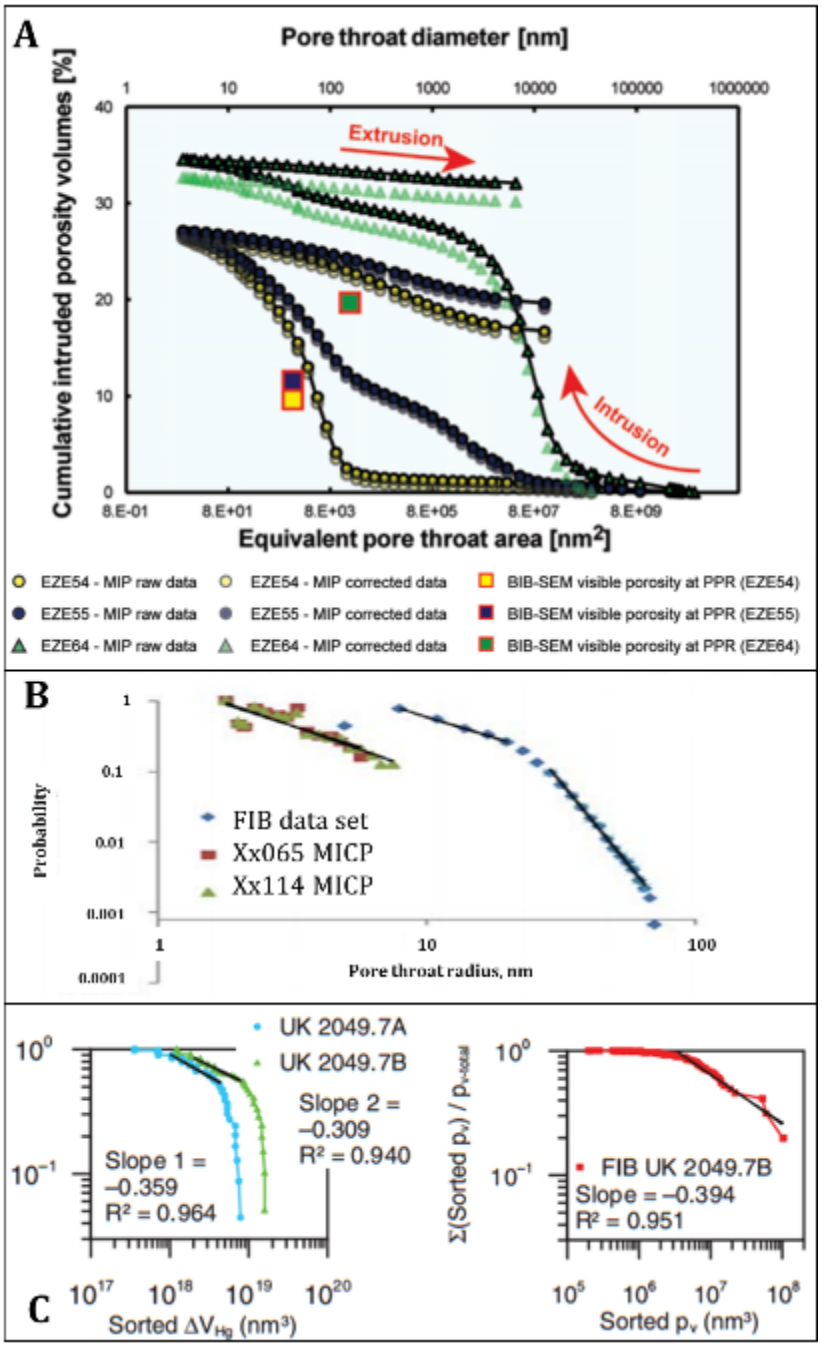

Figure 51. A) Cumulative Mercury intrusion and extrusion curves, as a function of pore-throat size; full symbols indicating uncorrected data and transparent symbols, data corrected for surface roughness effects. Total BIB-SEM visible porosities at practical pore detection resolutions (PPRs) are indicated by squared symbols (Hemes et al., 2014); B) the intercomparison of PSD obtained by MIP and FIB-SEM (1 kV, interpolated voxel size is 7.14 nm) (Dewers et al., 2012); C) Sorted cumulative volumetric distributions (SVPD) based on mercury intrusion porosimetry (MIP) and focused ion beam (FIB) pore network models (green and blue lines are for MIP, red – for FIB, example for upper Kirtland data) (Heath et al., 2011).

An intercomparison of imaging techniques with bulk measurements on shale samples can be found in Kaufhold et al. (2016). The authors have compared the results achieved by μCT and FIB-SEM with MIP, He pycnometry (dry flow) and N_2 adsorption results on Posidonia shale samples. Porosity results were presented in mm^3/g, or converted, for some of them, in volumetric fraction, using an unexpected constant density of 2.5 cm^3/g regardless to the varying dry bulk density of the samples with contrasted total porosity (Table 8). The proportion of unprobed pores by imaging techniques used was high (between 84-54 %). And clear balances of the contribution of micro-, meso- and macropores to the total porosity were not straightforward.

Figure 52 illustrates the intercomparison of different techniques used by Kaufhold et al. (2016) to characterize the pore network of gas shale. One of the conclusion provided by authors is that the samples contain high fraction of macroporosity according to the N_2 BJH pore size distribution, which provides the broad polymodal peak in range of the macroporosity (Figure 52.C); but such macropores were not detected by MIP (Figure 52.C). Since mercury intrusion provides the size distribution of pore-throats, not of pore bodies, we can conclude that all the throats correspond to micro- and mesopores controlling the access to the macropores. Such narrow throats, thinner than the voxel size provided by FIB-SEM (<25 nm) were not detected by imaging techniques (Figure 52.A, B).

Table 8. The results of the characterization of the pore space by a combination of methods (Kaufhold et al., 2016).

Sample	1	2	3	4
He (dry flow) density, g/cm^3	2.40	2.55	2.47	2.53
He total porosity, %	15.25	6.50	12.50	9.75
Visible porosity by FIB-SEM (>25 nm), %	2.4	0.7	4.5	3.0
Visible porosity by CT (>8µm), %	0.5	0.4	1.0	0.2
MIP porosity (meso+macroporosity), %	16.00	5.75	11.25	9.50
N_2 ads porosity (BJH mesoporosity), %	14.75	8.50	11.25	11.50
CO_2 ads porosity (microporosity), %	1.00	0.50	1.00	1.25
SUM pores imaging, %	2.9	1.1	5.5	3.2
Unprobed pores by imaging, %	81	84	54	68
SUM Micro &Meso porosity (CO_2 &N_2 ads), %	15.75	9.00	12.25	12.75

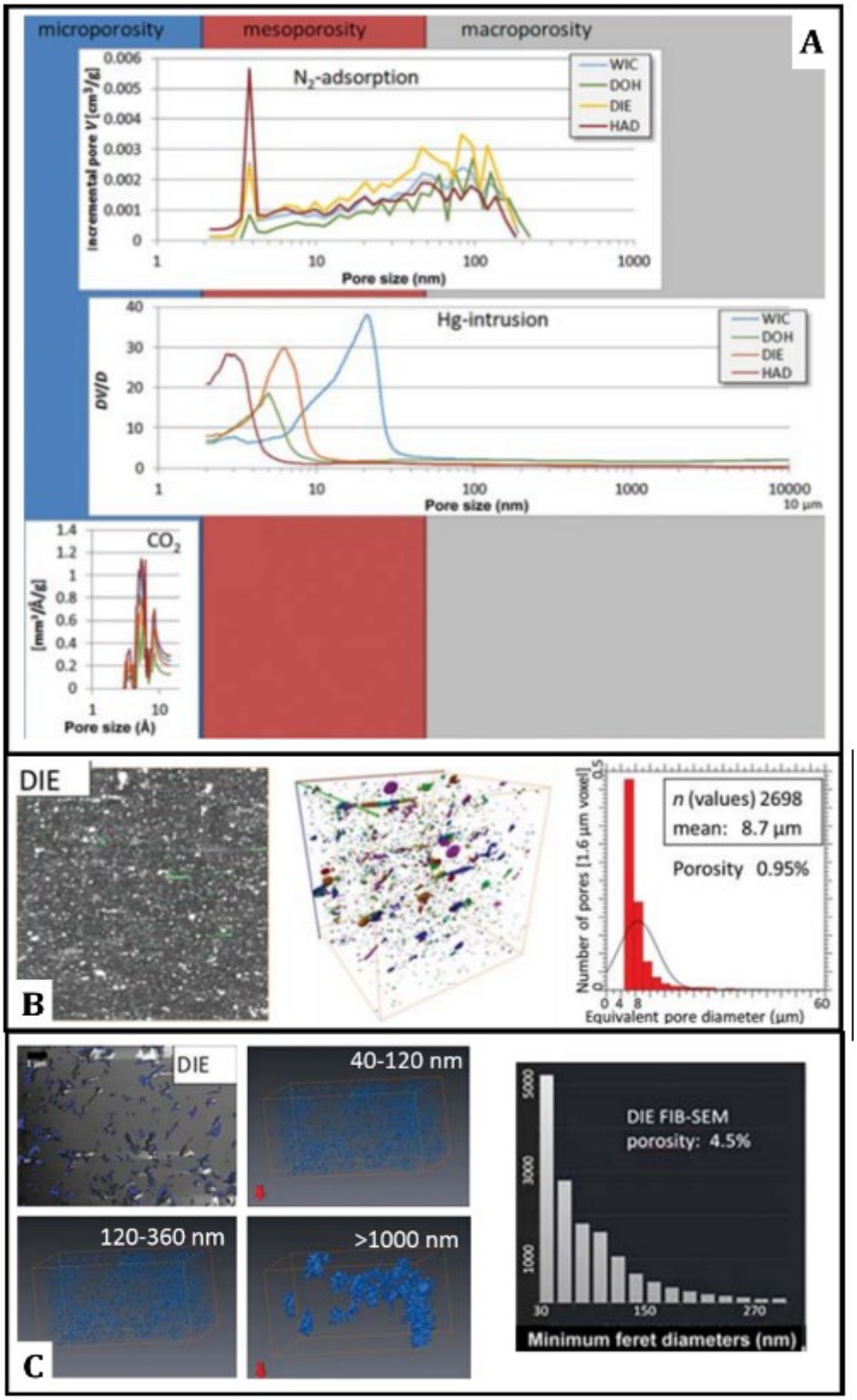

Figure 52. The comparison of the results of pore network characterization of Posidonia shale samples. A) µCT images segmentation and pore size destribution (180 kV, 15W). B) FIB-SEM segmantation and fpores feret diameteres destribution. C) results of gas adsorption (N_2 and CO_2) and mercury intrusion measurements (Kaufhold et al., 2016).

The resolution and the FOV archived by imaging techniques, are not sufficient for the comparison of the data from different methods (30-300 nm pore range detected by FIB-SEM and 8000-60000 nm by μCT). The comparison of PSD from FIB-SEM measurements with the PSD achieved by N_2 adsorption is theoretically possible, but the FIB-SEM pore size distribution results are covering only limited non-representative sample area, although the visualization of various pores ranges is performed (Figure 52.B).

Figure 53 displays a synthesis of some porosity data available in the literature and suitable for the comparison of FIB SEM result with varying bulk techniques. The strong variation of porosity values achieved by similar methods for samples from the same shale deposit is highlighted, probably due to non-similar localization of samples used for the comparison. Even if the direct inter comparison of results achieved by different methods is not balancing due to potential factors described above, two main tendencies can be distinguished, reflecting some limitations of the employed methods.

First, values provided by imaging techniques, in comparison with bulk measurements results are always underestimated due to the lack of resolution; and second, MIP results for total porosity is lower than adsorption measurements. Even if the detection limit of MIP is larger than of N_2 adsorption techniques, the underestimation of the porosity by MIP can be explained by large amount of unrobed porosity lower than ~3nm (lowest detection limit of MIP). The comparison of the percentage of micropores to the total porosity for the 5 northern American shales in Figure 53 illustrate that the measured micropores contribute only up to 20% of pore volume probed. Only for Marcellus shale the microporosity/total porosity ration is reaching 0.6 according to the data provided by Chalmers et al. (2012a). In addition, SANS data do not mostly match with data obtained from other techniques, as expected, to the results from other bulk techniques. This discrepancy could also be attributed to the strong underlying assumptions associated with SANS data treatment.

The quantitative up-scaling of pore network from FIB-SEM fine-scaled result up to representative volume (REV or REA in 2D) is now possible for relatively homogeneous materials, since the modelling of pore network of such homogeneous materials to characterize their flow properties is developing fast (e.g., Blunt et al., 2013). However, in case of shale samples this up-scaling would require outstanding volume of data to obtain the statistically reliable measurements due to extremely high spatial heterogeneity. Until now only simple models can be found in literature, accounting just for a few levels of heterogeneities within shale samples (based mainly on μCT and FIB-SEM images) (Zhang et al., 2012). In case of shale reservoirs, only the improvement of imaging technologies would allow to apply such a modelling.

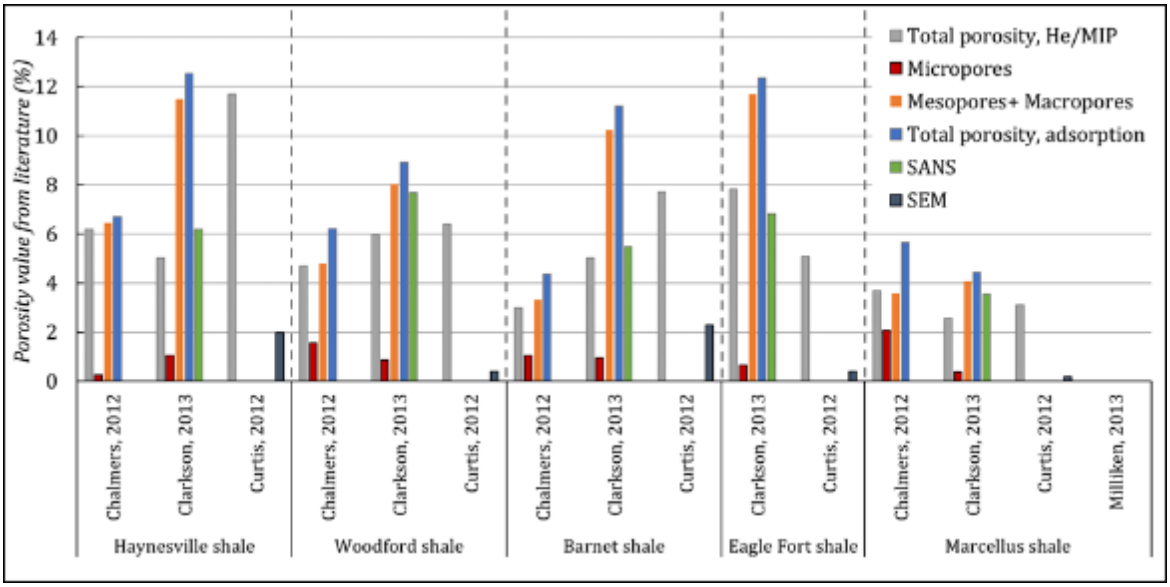

Figure 53. The intercomparison of porosity measurements for some shales (Chalmers et al., 2012a; Clarkson et al., 2013; Curtis et al., 2012b; Milliken et al., 2013).

Conclusions

Shales are heterogeneous materials including layers with different mineral composition, organic matter content and porosity. These heterogeneities exist in both vertical and lateral directions, leading to a multiscale network of pores. Such a complex organization of this material requires a multitool approach for its characterization. In this context, both, bulk and imaging techniques, have found an application for the investigation of shale samples. The application of combination of different methods is definitively essential point in the study of porosity of shale samples. Most often, these methods inherit from methodologies, whose efficiency has been proven on coal samples.

Last years some imaging techniques have become “standard”, but their accuracy is still limited mostly by their resolution and the field of view. Meanwhile, the accuracy of bulk techniques is limited by the complexity of physical and chemical phenomena, occurring within the sample and thus impacting the result of quantitative processing of the data. Values of porosity for different shales, even when they have been obtained by the same technique, are often not comparable due to difference in sample preparation and parameters of acquisition.

Even though, nowadays the exploration of the shale gas and oil deposits is growing, and the techniques of investigation are developing very fast, reaching unprecedented accuracy and resolutions, it is still challenging to provide the evaluation for such a complex material as shales. In this context, present bibliographical review has highlighted the following points:

- The parameters for different methods should be chosen carefully to allow some posteriori the comparison between results.
- The multiscale approach is needed to evaluate the porosity and pore size distribution.
- Only application of combination of methods can reveal the information of real pore size distribution over 4 to 5 orders of magnitude.
- The parameters describing the morphology and geometry of the pores can be estimated only based on images analyses.

The intercomparison of various data, obtained from bulk and imaging techniques, reveals that there is no direct correlation (i.e., a simple relationship of proportionality) between the total porosity and OM maturity.

Among the numerous modern tools and techniques, used to characterize shale pore space, it is difficult to choose the one, that would provide the most adequate and representative data. The multiscale and multitool analysis are strongly required to investigate the pore space of such a heterogeneous object as a shale sample. Unfortunately for unconventional reservoirs there is no direct and general guidance for porosity measurements. Thus, the objective of this research is to estimate the appropriate approach for the comprehensive pore network characterization of organic-rich shale samples.

Chapter 2. Materials and methods

Introduction

The available literature on the characterization of shale pore volumes demonstrates that the direct comparison of results obtained from different methodologies is not possible. Measurements on non-localized and non-identified samples from such highly heterogeneous formations, make impossible to correlate the data for the same formation from various research groups. The results of the porosity quantification are often interpreted without careful estimation of acquisition parameters and data treatment, leading to the poor reliability of the data published. Pore balance quantification of such shale formation is challenging regarding the range of scale to characterize and may integrate various levels of information. Thus, a multitool approach applied on comparable and localized samples should be considered. To achieve such a quantitative pore balance description a multitool and multiscale approach has been proposed in this research, including the core selection up to the data treatment to make the porosity values comparable. The proposed multitool and multiscale approach considered the following steps:

1. Selection of samples from petrophysical well log data;
2. 3D µtomography visualization of the core, identification of the areas of interest, localization of the sub-samples for measurements;
3. porosity characterization through classical bulk methods (NMR, MIP, He - pycnometry, N_2 adsorption) on localized well-preserved blocks;
4. acquisition of BSE-SEM mosaics on the large representative areas to obtain the mineral and organic phases distribution;
5. correlation of mineral composition spatial distributions with quantitative connected porosity – 2D porosity map (autoradiography) vs 2D mineral map (BSE-SEM mosaic).

Such an approach allows to obtain information following a downscaling process: from the well scale (m), through the core scale (mm), down to the mineral/micropore scale (µm). It was applied on samples the from Vaca Muerta formation (Argentina), provided by the company *Total (Total E&P, France and Total Austral, Argentina)*.

2.1. Materials

2.1.1. Geological settings of the basin

The samples were taken from the Late Jurassic (Tithonian) to Early Cretaceous (Berriasian) shales of the Vaca Muerta (VM) formation, located within the Neuquén basin (western Argentina), which are composed of black offshore organic-rich mudstones to wackestone (Howell et al., 2005). The VM formation originates from the accumulation of a thick column of clastic sediments from the Jurassic to Cretaceous (Figure 54) followed by successive geological evolution, from rift to sag and foredeep, leading to an anisotropic sedimentary formation up to 600 m thick (Magoon and Dow, 1994; Badessich et al., 2016; Zeller et al., 2015).

The geological evolution and development of the basin has been described by Howell et al. (2005) and can be considered in three steps:

1. Late Triassic – Early Jurassic: prior to the onset of subduction on its western margin, this part of Gondwana was characterized by large transcurrent fault system. This led to extensional tectonics within the Neuquén Basin and the evolution of a series of narrow, isolated depocenters.
2. Early Jurassic-Early Cretaceous: development of a sleepy dipping, active subduction zone and the associated evolution of a magmatic arc along the western margin of Gondwana led to back-ark subsidence within the Neuquén Basin. This post-rift stage of basin development locally accounts for more than 4000 m of the basin fill.
3. Late Cretaceous – Cenozoic: transition to a shallowly dipping subduction zone resulting in compression and flexural subsidence, associated with 45-57 km of crustal shortening and uplift of the foreland thrust belt.

The VM formation belongs to the Late Jurassic-Early Cretaceous post-rift phase (which is starting in Early Jurassic): During the Early-Middle Jurassic the subduction regime along the western Gondwana margin was initiated and by late Jurassic the Andean magmatic arc was almost fully developed. Back arc subsidence led to an expansion of the marine realm and flooding of the basin, which was connected to the proto-Pacific through gaps in the arc.

As in the case for all mixed carbonate-siliclastic systems, the VM formation is heterogeneous, with vertical and lateral variations of porosity, mineralogy and organic matter content throughout the basin and at different scales.

The high microstructure variability is well established at the core scale with the presence of various micro-facies (Kietzmann et al., 2016; Kietzmann and Vennari, 2013; Kietzmann et al., 2008) involving the alternation of parallel bedded laminae of carbonates mm-µm thick (so called “beef” veins, Lejay et al., 2017), nodules, and siliclastic rich

intervals in between more porous clayey facies related to cyclic depositional sequences. This succession has been developed on a slightly inclined shelf during Greenhouse climate with lower amplitude changes in the relative sea-level, with a predominant non-skeletal – heterozoan carbonate factory (Zeller et al., 2015). The succession can be subdivided into 14 lithofacies types based on their lithologies, textures, main components and sedimentary structures. This subdivision covers the entire suite from pure siliciclastic to pure carbonate facies. Zeller (2013) has illustrated and described these facies at the outcrop and the micrographs scales, combining them into 6 lithofacies groups: a) SH - Shales and Marls; b) S – Siltstones and Sandstones; c) SXB – Cross-bedded Sandstones; d) WP – Skeletal Wackestones and Packstones; e) F – Float – Framestones; f) G – Grainstones.

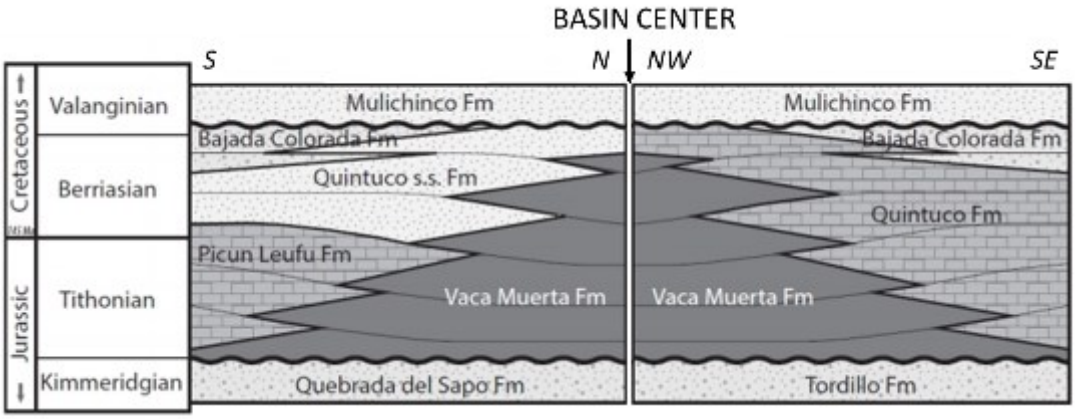

Figure 54. Stratigraphic subdivision of the Late Jurassic to Early Cretaceous successions in the Neuquén Basin in the subsurface areas within along the Andean foothill (left) and the Neuquén Embayment (right) (Zeller, 2013).

The formation contains hydrocarbons of various maturity, from black oil to dry gas window. The schematic distribution of the different production zones within the formation is displayed in Figure 55.

The hydrogen indexes, based on Rock-Eval pyrolysis data, within the VM formation range from 200 to 675 (mgHC/gTOC), which corresponds to kerogen of types I and II on a van Krevelen diagram (Figure 56). Total organic content is varying in the 2-6 mass% range with the highest concentration at the basin center (Magoon and Dow, 1994).

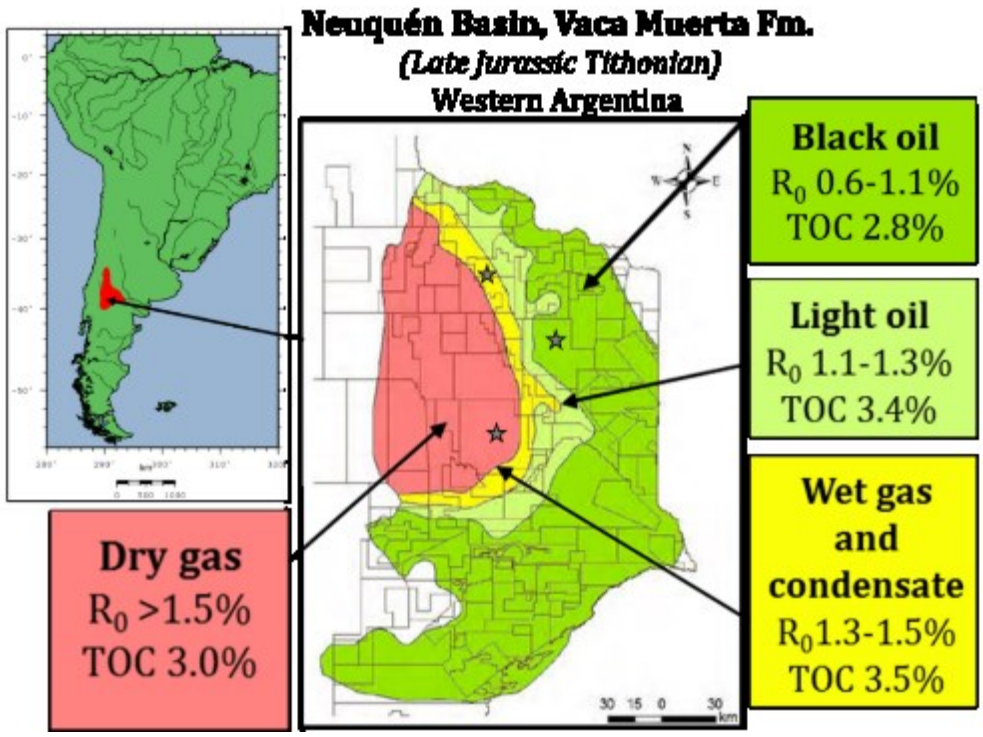

Figure 55. A schematic distribution of various hydrocarbons areas within the Vaca Muerta formation (modified from Schmidt et al., 2014). The stars indicate the approximate locations of the samples, selected for the present study.

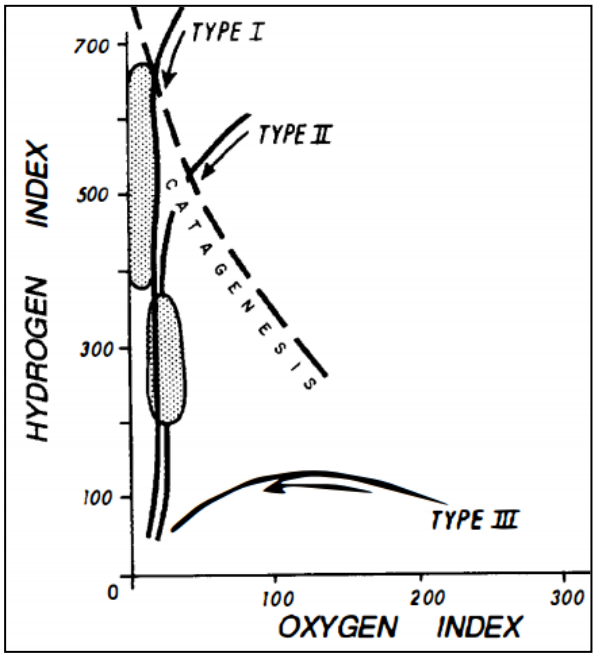

Figure 56. Vaca Muerta kerogen types plotted on a modified van Krevelen diagram (stippled) (Magoon and Dow, 1994).

The well log data, which were used for the cores selection (Figure 57), demonstrate the high heterogeneity of mineral phases distribution over the well, with multiscale lamination, and strong variation of neutron porosity.

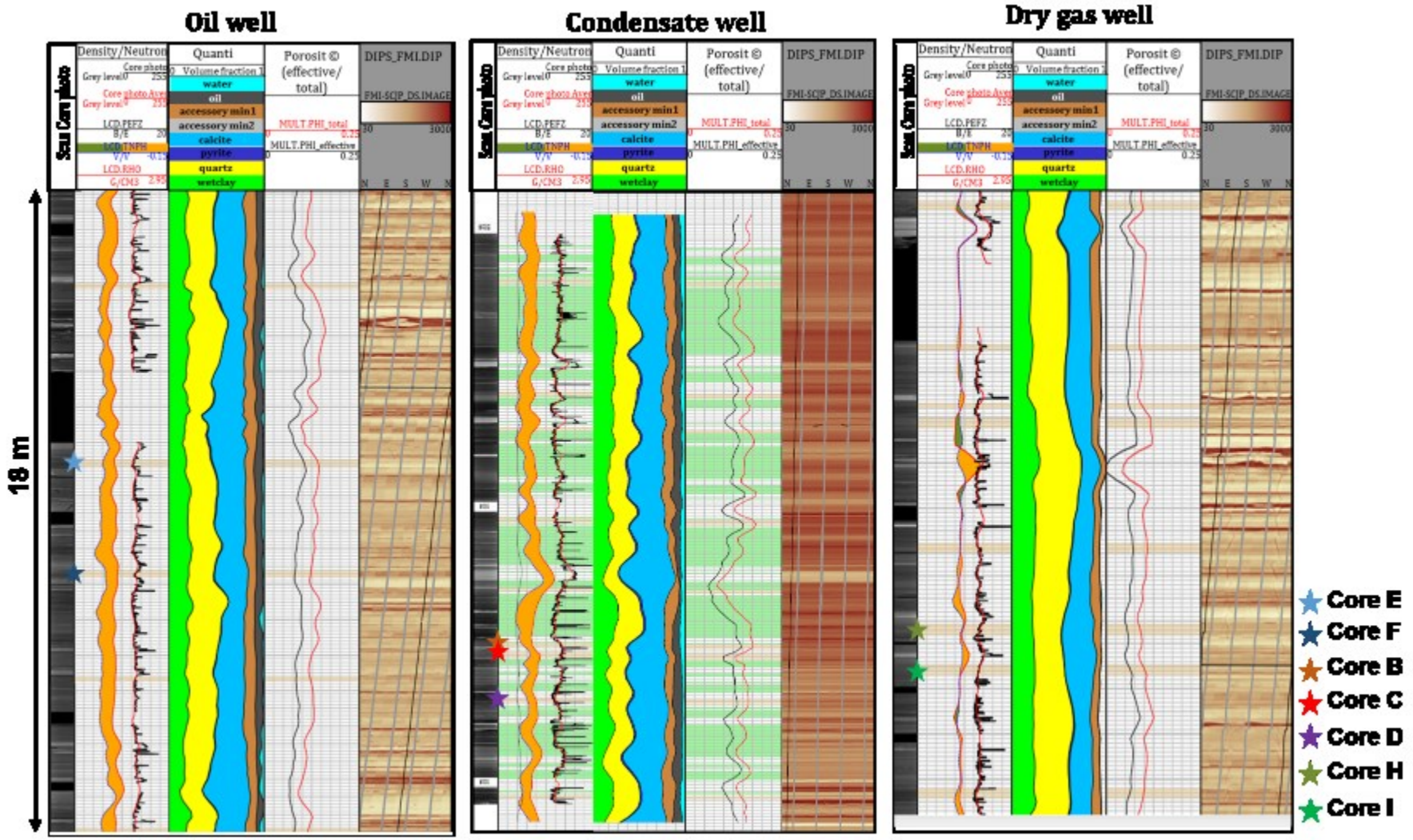

Figure 57. Well log data, given for the wells of interest (the locations of the seven core samples of this study are indicated with stars).

2.1.2. Core sampling

The first step of the multiscale/multitool approach proposed in this study is the selection of seven full-size core samples. This selection was done using the CT-scans of cores collected from three vertical wells and well log data. The careful choice of the studied samples was based on the availability of "preserved" full-size core samples and on average neutron density, total porosity, resistivity, oil/water ratio and mineralogy data (Figure 57).

One of the properties that indicates the presence of shale material within the well is the gamma radiation. Gamma ray logging can be used, through linear GR index, to calculate the shale volume, as shales usually emit more gamma-ray than other sedimentary rocks due to large amount of clay matrix with ^{+}K presence (Serra, 1984). The corrected Gamma Ray (HCGR, API) is used to evaluate the intervals with high clay content.

The CT-Scan core photos provide information about grey level distribution (reflects the linear attenuation coefficient of the sample, *LAC*), which corresponds to the x-ray attenuation coefficients. These data allow to evaluate the homogeneity of the formation intervals and to detect specific features, such as large grains, inclusions, cracks and any perturbation of the core during drilling and/or extraction.

Although none of logs directly measures porosity, a combination of the neutron (nuclear measurements) and sonic (acoustic measurements) logs gives good indications for lithology and an estimation of porosity. Neutron porosity corresponds to the hydrogen contents measurements. Combining the hydrogen index data with bulk density (RHOB, g/cm^3 allows evaluating porosity values, with some specific environmental and logging corrections (generally done by the contractor).

Density log, which measures the electron density of a formation also provides another source of porosity data. The density porosity (DPHI) obtained from density log is defined by Equation 18.

Equation 18.

$$DPHI = \frac{\rho_{ma} - \rho_b}{\rho_{ma} - \rho_f}.$$

Consequently, the density porosity (DPHI) is calculated from the formation bulk density (ρ_b, log data), the matrix density (ρ_{ma}), and the formation fluid density (ρ_f) (the matrix density and fluid density are to be known *a priori*).

Resistivity is a basic measurement of a reservoir's fluid saturation and is a function of porosity, type of fluid, amount of fluid and type of rock. It can be used (in combination with other porosity logs, e.g., neutron and density log) to calculate kerogen weight fraction (Rezaee, 2015).

For the three given wells considered in the presented study, the variation in porosity and mineral composition within the formation have been estimated by a calibrated *MULTIMIN* quantitative petrophysical well log interpretation approach (GEOLOG® software module by *Paradigm*®, calibrated with laboratory petrophysical and mineralogical measurements on a limited set of core plugs) based on the combination the following parameters: rocks density, neutron porosity, acoustic properties and resistivity. Such an approach provides an evaluation of mineral composition and estimated values of total porosity (*PhiT*) and effective porosity (*PhiE*).

The selection of these seven samples has respected the following procedure and was based on the CT-scan core photos (acquired using x-ray µtomography at Total), the log data and the GEOLOG® *MULTIMIN* modelling results. First, the samples which show the minimum heterogeneity, according to the spatial resolution of the CT-scan, except laminae were chosen. Second, the d mineral composition data were used to avoid (i) strong variations in the zone around samples (to be able to establish further potential correlation between samples), (ii) extreme cases in terms of mineral composition (i.e., to handle homogeneous samples in mineralogical point of view) and (iii) especially variation in detrital quartz content. The variation of x-ray attenuation coefficients, which corresponds to contrasted carbonates/porosity and clay matrix/kerogen ratios through the grey level variation, was used to identify two sets of samples for the condensate zone: a first set and a second set associated with the local maximum and the local minimum of that parameter, respectively.

According to these criteria, 7 full-size cylindrical core samples, with dimensions of ~7cm in diameter x 7 cm in length, were collected from three wells with different hydrocarbon types (Figure 57, values of estimated mineral and physical parameters for the selected samples are listed in the Table 9). Three samples from a condensate zone with a maximum thermal maturity measured on bitumen of 1.3% VReq (cores B, C and D), two samples from an oil zone with a maturity of 1.1% VReq (cores E and F) and two samples from a dry gas zone with a maturity of 1.6% VReq (cores H and I), within the VM thick intervals (~150 m) of the wells. The samples were chosen with similar mineral compositions but contrasted wave velocities, resistivities and porosities (Table 9, Figure 58). Moreover, for the samples from both, oil and dry gas window, the selected samples were also located in the same stratigraphic sequence. The aim of this sample selection was to study the effect of burial and OM maturity without being impacted by variations in mineralogy and deposit processes. The samples which show the minimum vertical heterogeneities except laminae were selected to perform direct correlations between cores at the log scale.

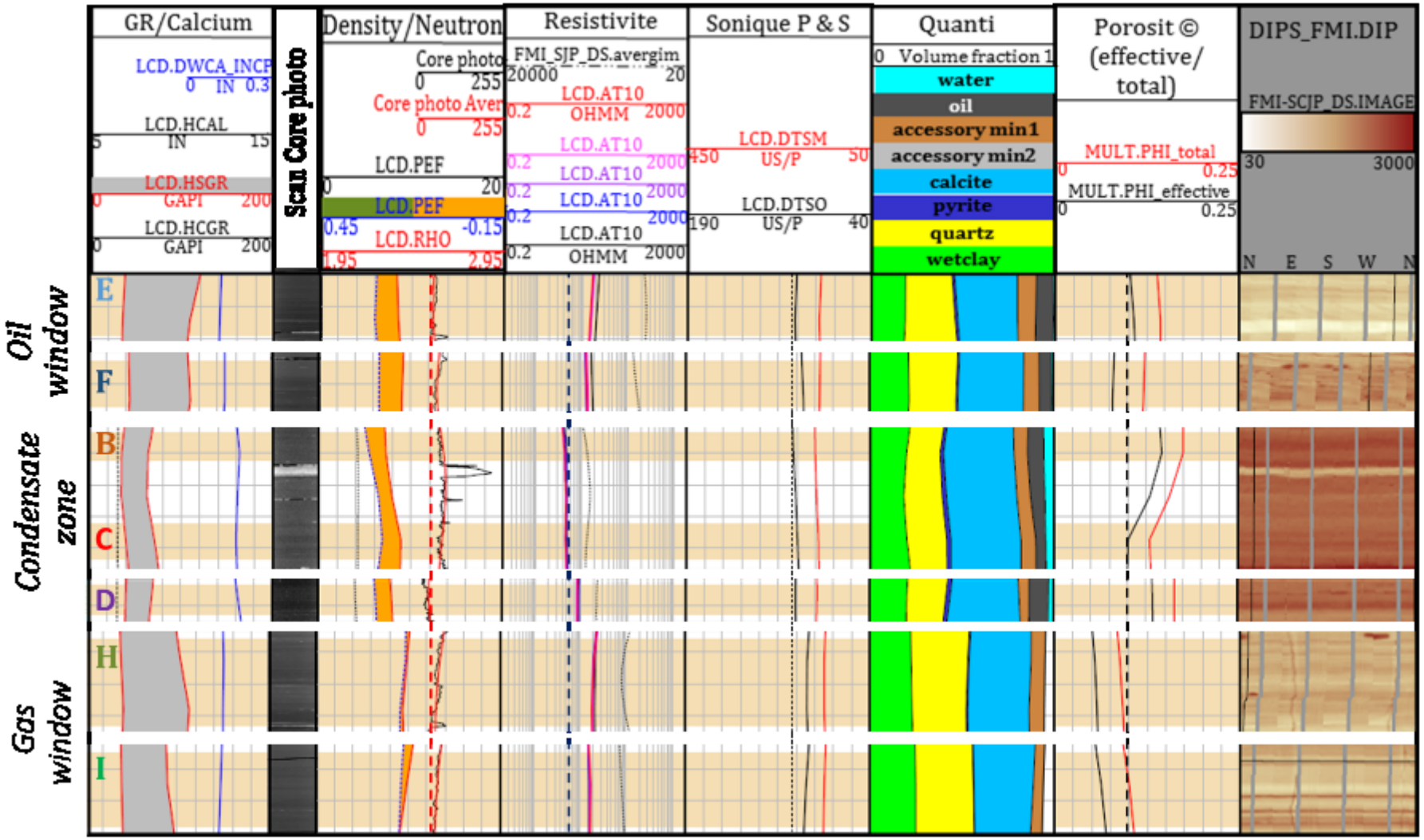

Figure 58. The well log data corresponding to the selected cores.

From all the available well log data, seven samples from Vaca Muerta formation, sample was selected from zones with different hydrocarbons production: three samples from condensate zone (wet gas and condensate), two samples from oil zone and two samples from dry gas zone (Figure 57, parameters' values for the selected samples are listed in the Table 9).

All the cores, fresh and old ones, should have been immersed into resin and hermetically sealed into plastic bags on the rig site to limit water desaturation. Nonetheless, the oil and gas samples were only sealed into plastic bags and some of them were unfortunately damaged (Figure 59).

After their reception, the seven cores (protected as possible in hermetic bags) were rapidly scanned by X-ray µtomography using an EasyTom XL duo system (RX Solutions) (see next section). Then, they were embedded into resin to preserve them from the atmosphere and to limit water desaturation and to minimize the perturbation of the structure during the subsampling.

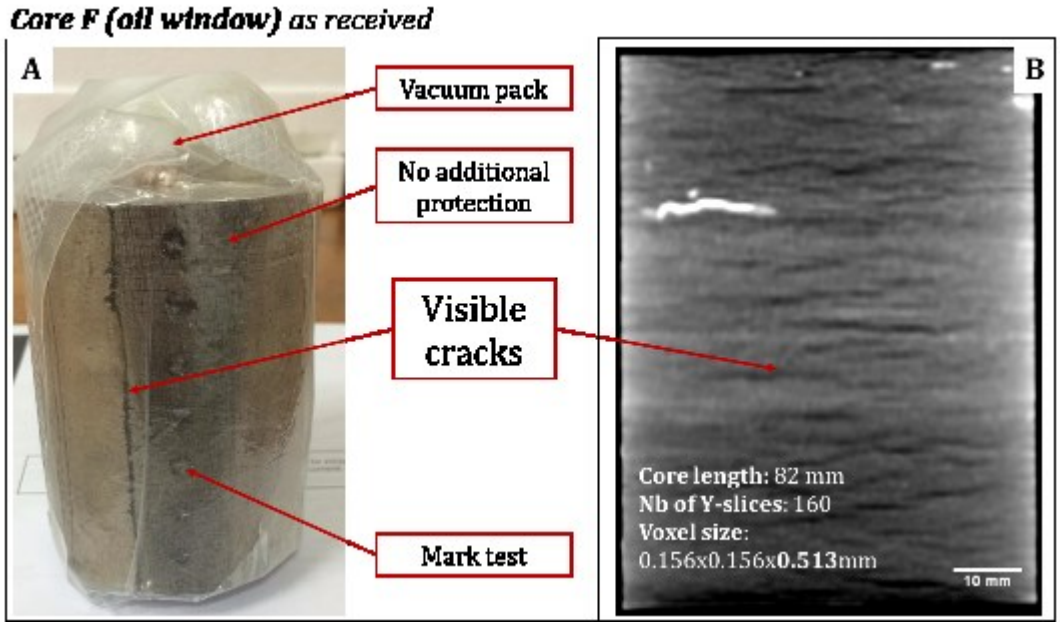

Figure 59. Damaged core (core F, oil window): A) photo of the core "as received"; B) central slice of the µtomography volume, acquired on the core (note the cracks at the mm scale all over the core).

Table 9. Mineral compositions and physical parameters estimated from log data by a calibrated MULTIMIN© approach for the selected samples from three different exploration wells in zones of various hydrocarbon maturities (Vreq - maximum thermal maturity measured on bitumen, LAC – linear attenuation coefficient, DTSM – shear slowness, DTCO – compressional slowness, PhiT – total porosity, PhiE – effective porosity).

		Estimated MULTIMIN composition, mass%								**Estimated petrophysical parameters**						
Zone	**Core sample**	**Wet clay**	**Quartz**	**Pyrite**	**Calcite**	**Accessory minerals**	**Hydro-carbons**	**Water**	**Vreq, %**	**Standard Gamma Ray, API**	**Bulk density (RHOB), g/cm³**	**Average LAC**	**Resistivity, Ω·m**	**Sonic (DTSM/ DTCO), µs/m**	**MULTIMIN PhiT, %**	**MULTIMIN PhiE, %**
Oil	Core E	19	25.5	2.5	33	9.5	9.5	1	1.1	37	2.35	50	20	518/331	14	10
	Core F	21.5	26.5	1.5	35	8.5	5	2		39	2.4	75	20	509/308	12.5	8
Condensate	Core B	18.5	18.5	3.5	38	7.5	9	5		38	2.3	85	4	558/338	17.5	15
	Core C	20	22.5	3	37.5	8	5	4	1.3	40	2.4	85	4	522/325	12.5	10
	Core D	20.5	21.5	2.5	37	4.5	11	3		40	2.35	50	10	535/328	16	13
Dry gas	Core H	22	31	1	33	8	5	0	1.6	38	2.4	75	20	476/289	9	5
	Core I	24	32	0.5	32	5.5	6	0		42	2.4	75	20	492/302	10	6

2.2. Methods

As it was described, such heterogeneous shale samples (Figure 57) represent an analytical challenge for the characterization of pore network, with pores ranging from millimetric to nanometric size, which are below or close to the detection limits of commonly used techniques. The resolution of each method is directly dependent on the dimensions of the sample and on the probe size (Figure 60). The approach, proposed in the presented study to achieve a representative data set on the shale samples at multiscale, includes several steps.

- Subsamples localization within the core, to obtain results on comparable layers of interest;
- Careful planning for the subsampling, to obtain the precise localization of each measurement within the core;
- Selection of the experiment parameters for each required measurement, regarding the limitations and assumptions;
- Data treatment to convert the raw values to intercomparable results.

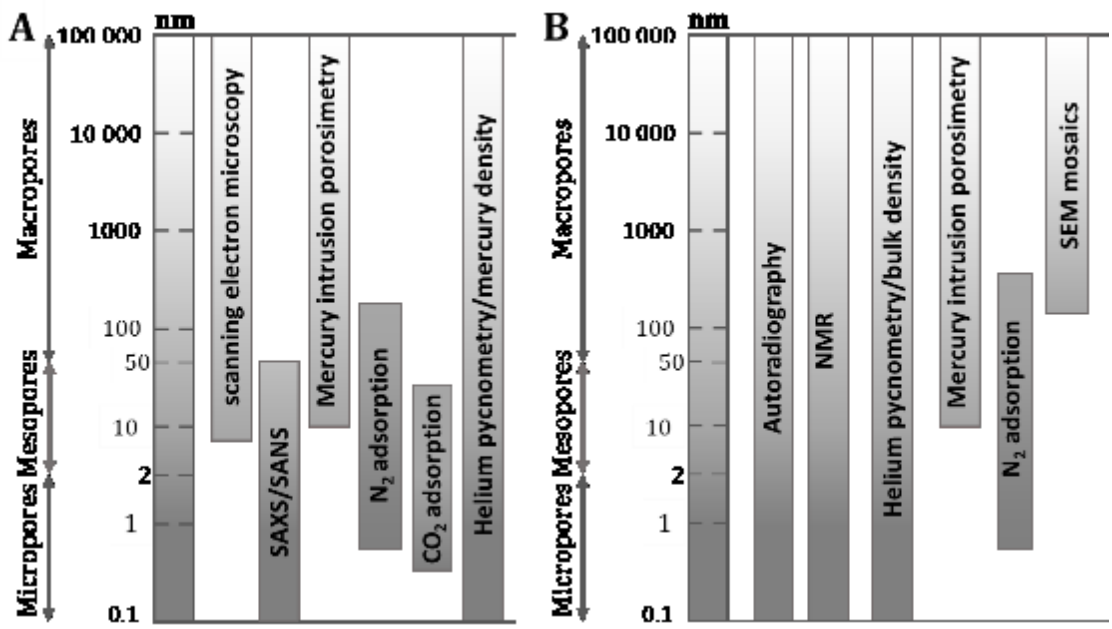

Figure 60. Methods of pore network characterization and their resolutions: A) applied on shale samples in literature; B) applied in the present research.

2.2.1. X-Ray µtomography 3D localized subsampling

To visualize the entire sample microstructure and to define the local regions of interest (ROI) for subsequent laboratory bulk measurements, the seven core samples were scanned by X-ray µtomography using an EasyTom XL duo system (RX Solutions)

with Hamamatsu reflection 150 kV microfocus X-ray tube, coupled to a Varian Paxscan 2520DX flat panel detector with a 1920x1536 pixel matrix. The entire cores were scanned in continuous helicoidal mode, by recording 1700 projections with a spot size of 60 µm, a target power of 39 W and an accelerating voltage of 140 kV. For each sample, a virtual 3D linear attenuation coefficient (LAC) volume with a voxel size of 78.8 µm was obtained using a back-projection algorithm coupled with a beam drift and beam hardening corrections (Figure 61.A). Indeed, even at such a high accelerating voltage, the transmitting rate, which is the ratio of the X-Rays intensity captured by the detector (I) to the X-Rays intensity emitted by the source (I_0) (Equation 17), is not exceeding 1% for the large, dense cores. For all the µtomography images a non-local mean denoising has been applied (see 2.2.12 for details) before the image analysis and 3D volumes visualization.

From the 7 imaged volumes, Avizo® software was used to accurately localize the cutting planes and the sub-samples for the various laboratory measurements, applied for pore network characterization (Figure 61), and for the segmentation and the visualization of various components within the cores. From the 3D views, sub-regions of interest with horizontal layers presenting similar non-clay grain amounts, LAC, and no macro heterogeneities, were virtually selected (blue selection, Figure 61.B).

Avoiding large heterogeneities and perturbed zones, a 1.5-centimeter-thick block (with the full length of the core) was localized from the center of the core for resin impregnation and a latter use for autoradiography porosity mapping (Figure 61.A, IS block). Just in front of the IS block, a similar one (Figure 61.A, BS-block) was selected, from which the different sub-samples dedicated to the bulk measurements were localized (i.e., gas adsorption and MIP; Figure 61.B). Maximum and minimum 2D z-projection maps (i.e., detecting the maximum, minimum or average LAC through the thickness, Figure 61.B) were also calculated for the BS block. Such 2D maps allow to observe the location of "heavy" grains (i.e., with high density and high atomic numbers, like pyrite and carbonates) and cracks/large voids (low density objects), to avoid them, when selecting the position of sub-blocks (Figure 62). An exploded view of the sub sampling performed on the BS block is presented in Figure 64 to illustrate the localization of each analyzed sub-sample.

The NMR1, NMR2 and PS1, PS2 core chips were sub-sampled for nuclear magnetic resonance measurements and analyses on powder (quantitative mineralogy, thermal analysis and grain density measurements), respectively (Figure 61.A).

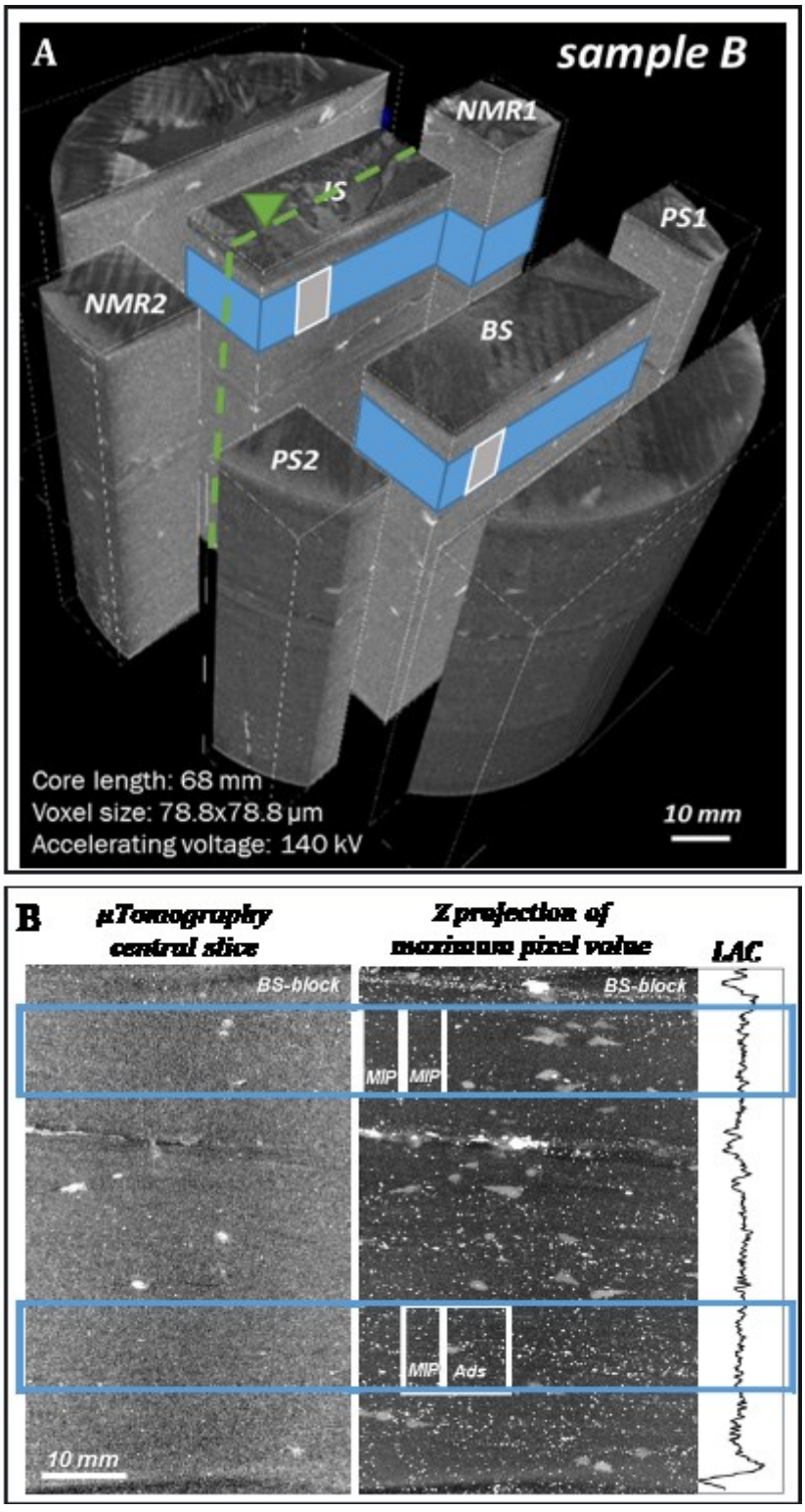

Figure 61. µTomography 3D visualization and subsamples localization (core sample B, condensate zone): A) virtually cut core (IS – block for impregnation and imaging techniques application, the green line corersponds to the position of the surace polished; BS – block for bulk porosity measurements; PS – blocks for measurements on powder; NMR – blocks for nuclear magnetic resonance spectroscopy); B) virtual cut and image analyses, evaluating the core vertical heterogeneities (central slice, Z-projection of maximum values thorough the block and vertical LAC profile with 300 pix width).

Careful subsampling of the core, according to virtual cuts, allowed the proper spatial inter-comparison of various bulk methods with imaging techniques - i.e. the exact positions of sub-blocks for gas adsorption and MIP can be projected on the surface studied by imaging techniques (Figure 61, white rectangles). The virtual slices corresponding to the planes analyzed by autoradiography and vertical profile of LAC were estimated for further analyzing of spatial heterogeneities.

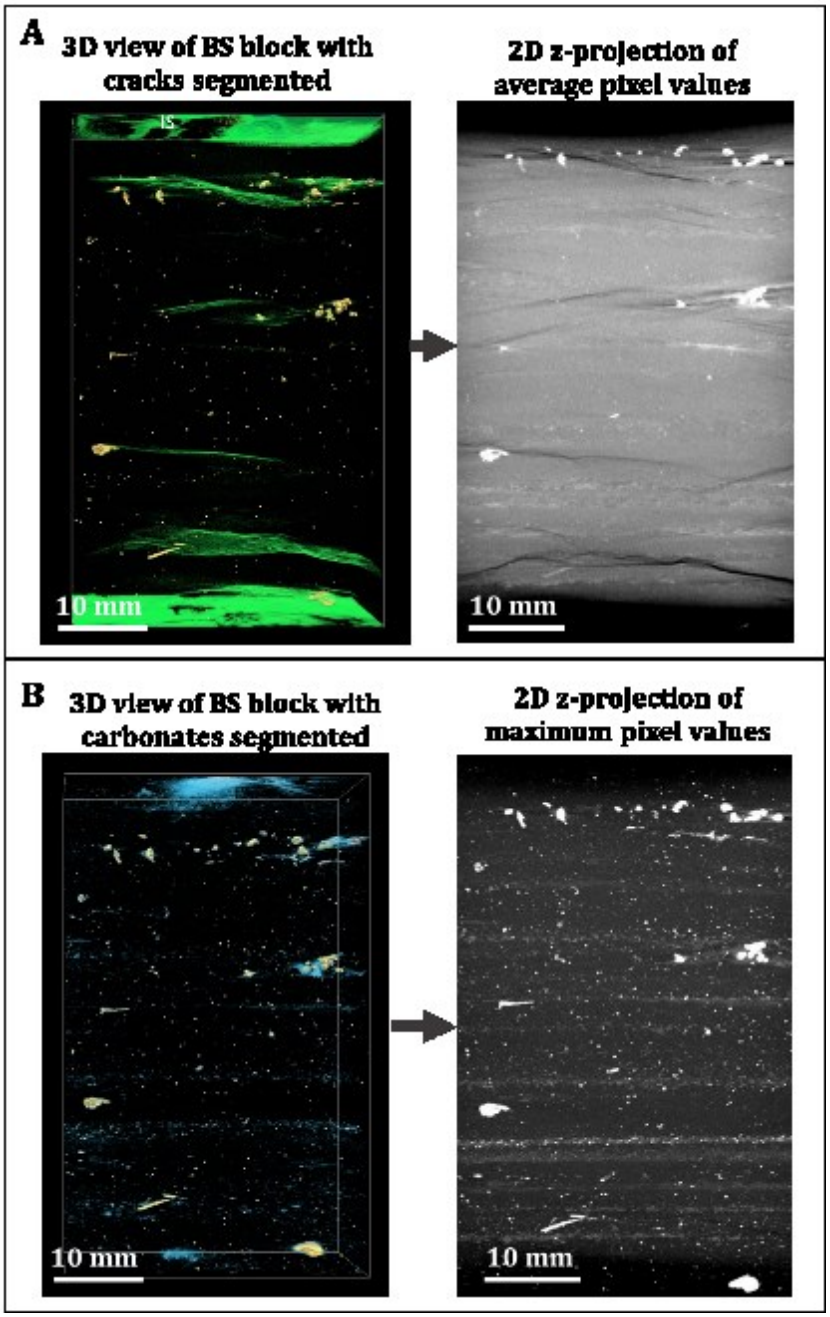

Figure 62. Visualization of BS block from the sample core H (dry gas window): A) 3D view with cracks (in green) and "heavy" grains (in yellow) segmented and corresponding z-projection of average values; B) 3D view with carbonates (in blue) and "heavy" grains (in yellow) segmented and corresponding z-projection of maximum values (note that some of the pixels, located around heavy grains, are in the same range of intensity as carbonates, due to X-Ray scattering artifacts).

The selection of the sub-samples for the laboratory measurements, based on µtomography measurements, allows to overcome the difficulties with results interpretation and intercomparison due to the high heterogeneity of the objects of interest. The cores were then carefully cut with diamond wire saw, according to the 3D visualization virtual plan of the different sub-blocks, to minimize the damaged zone at the cut planes. This procedure was applied to each of the 7 cores to select the sub-blocks for the pore network characterization by "bulk" and imaging techniques.

2.2.2. Mineral composition

The quantitative mineralogical composition of the selected samples was measured on crushed PS1/PS2 core blocks within the selected layers of interest (Figure 61.A) with the reference quantitative mineralogy method of *Total,* called *MinEval QM* (Fialips et al., 2018).

This approach allows quantifying the mineralogical composition of rock samples through the integration of results from various measurements performed on crushed powders. First the samples were washed free of soluble OM by Soxhlet extraction with chloroform at standard conditions (boiling of the chloroform at 50°C) and dried under a fume hood at room temperature (to remove any residual chloroform). The dry samples were then crushed down to <500µm and further dried at 110°C. Subsets of the crushed samples were milled down to <10µm with a *McCrone*® mill with water and dried again prior to a preliminary evaluation of bulk mineralogical composition by powder X-Ray Diffraction (XRD) and Rietveld refinement (with Siroquant software). This preliminary evaluation was then optimized through integration of various physical/chemical measurements performed on the < 500µm samples: (i) Loss On Ignition (LOI) at 1000°C, (ii) X-Ray Fluorescence (XRF) analysis (complete suite of major, minor and trace elements) after LOI treatment and fusion into a glass bead with lithium tetraborate, (iii) Insoluble Residue (IR) upon HCl 15% treatment at room temperature, (iv) Bulk solid density by helium pycnometry on crushed powder, (v) Bulk Cation Exchange Capacity (CEC) using the Cobalt-hexamine reference technique (Orsini and Remy, 1976), and (vi) Insoluble Organic Carbon (IOC) content of residual bulk samples after RI measurement, converted into Insoluble Organic Matter (IOM) content by arbitrarily multiplying by 1.2 (approximation to C_2H_5 composition). Later, this complex set of analyses will be called XRD-XRF measurements. To clearly identify the clay minerals and their swelling behavior, the < 5µm fraction of the samples were also extracted and analyzed by XRD (oriented clay films obtained with the filter transfer method and analyzed by XRD after air drying and after treatment with ethylene glycol).

2.2.3. Thermal analysis

To identify an efficient drying temperature to be used prior to the different porosity characterization methods, thermal gravimetric analysis (TGA) coupled with mass spectroscopy (MS) was applied on powder from the localized blocks (PS1/PS2, Figure 61.A). The experiments were performed on a TA instrument (*SDT Q6010*) in argon atmosphere (with a gas flow of 50 mL/min). Before the measurements, the samples were stored at 50°C. The analysis was done on ~30-50 mg of powdery sample by heating from 50 °C up to 900°C, with a heating rate of 5°C/min. The products of thermal decomposition were investigated by *Hiden Analytical QGA* gas analysis system. Spectra of masses in the range of mass 10-200 were evaluated. Additional tests were performed on one sample with a lower heating rate of 1°C/min in both air and argon atmospheres to investigate the behavior of the components in oxygen and inert conditions.

2.2.4. Total porosity calculation

The calculation of total porosity of the sample (φ^T) is based on the measurements of dry bulk and grain densities (Equation 19).

Equation 19.

$$\varphi^T = \frac{V_p}{V_t} = 1 - \frac{V_s}{V_t} = 1 - \frac{\rho^{bulk}}{\rho^{grain}},$$

where V_p – volume of pores [m^3], V_s – volume of the solid phases [m^3], V_t – total volume of the sample [m^3], ρ^{bulk} – dry bulk density [kg/m^3] of the sample and ρ^{grain} – grain density [kg/m^3].

Grain density measurement: He-pycnometry

The grain density can be measured in the end of the mercury intrusion during MIP experiment, assuming that (i) mercury could penetrate all the voids, and (ii) no closed porosity is present (Micromeritics, 2012). However, due to the expected complexity of the pore network, the grain density measurements were done preferentially by He-pycnometry, using *Accupyc 2020* equipment (Micromeritics, 2012). These measurements have been performed on samples taken from three sub-blocks of the cores corresponding to three preparation procedures (Figure 63).

First, one of the measurements was done on the "averaged powder" collected from the full length of the core, plug PS (ρ_{aver}^{grain}). These samples were only dried at 150°C during 36h.

Following the second preparation procedure, the parts of the PS plug, which were selected for XRD-XRF analysis, were also used for He-pycnometry measurements (ρ_{PS}^{grain}).

In this case, the samples were first washed free of soluble OM by Soxhlet extraction with chloroform at standard conditions (boiling of the chloroform at 50°C), then dried under a fume hood at room temperature (to remove any residual chloroform). The dry samples were then crushed and further dried at 110°C.

Following the third preparation procedure, the small cylindrical plugs (100 mm in diameter and 16 mm in length), taken from the blocks selected for NMR analysis, were washed by Soxhlet extraction with isopropanol after their analysis by NMR and dried at 150°C for 3 days before grain density measurement by He- pycnometry (ρ_{NMR}^{grain}).

Symbol/ sample state	Soluble OM removal	Drying
ρ_{aver}^{grain} powder	No	150°C
ρ_{PS}^{grain} powder	Yes	110°C
ρ_{NMR}^{grain} block	Yes	150°C

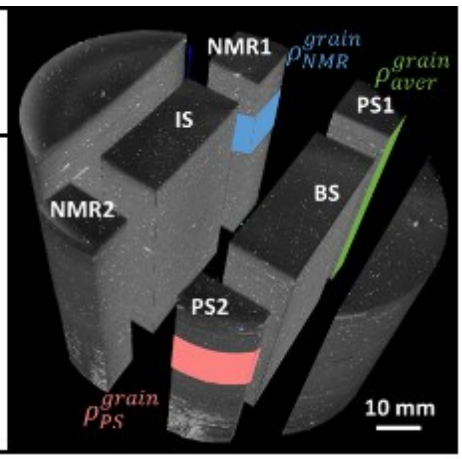

Figure 63. Left: procedures used for preparing grain density measurements by He-pycnometry. Right: localization of sub-blocks used for grain density measurements by He-pycnometry (illustrated on 3D view of virtually subsampled core D, condensate zone).

Bulk density measurements

While He-pycnometry – is widely used technique for the grain density measurements with high precision (Thommes et al., 2015), various methods may be employed to determine the bulk volume and density of the rocks. In the present research these measurements were done by different techniques to control the reliability of the result.

Laser measurements

The small plugs taken from the localized NMR blocks (Figure 61.A) were washed free of liquid hydrocarbons by Soxhlet extraction with chloroform then isopropanol, followed by drying at 60°C for 3 days. Before saturation with a brine solution (70 g/l NaCl), the total plug volume (V_t, [m^3]) was measured by slide gauge and laser to obtain the bulk density (ρ_{NMR}^{bulk}, [kg/m^3]). The total porosity calculated with ρ_{NMR}^{bulk} and ρ_{NMR}^{grain}, (see Equation 19), is called φ_{NMR}^{T} (total porosity on NMR blocks).

Immersion in mercury

Bulk density measurement of each sample was also performed by mercury immersion on the MIP blocks (ρ_{MIP}^{bulk}, [kg/m^3]) (Figure 61Figure 61.B). The blocks were dried under vacuum at 150°C during 36h.

The bulk density was determined during MIP experiment (before the first pressure step of $3 \cdot 10^3$ Pa) by weighing the sample prior to immersion in mercury and then dividing the mass of the sample by the bulk volume of the sample (as determined by mercury immersion-technique).

Following this procedure, due to high surface tension of the mercury/air interface, mercury does not penetrate the pore space, till the pressure applied is high enough. The minimum pressure, at which the bulk volume of the sample (V_{sample}^{bulk}) is measured, is equal to 0.5 psi (or ~0.003MPa), which corresponds to the penetration of mercury into pores with ~400 µm diameter. The bulk volume of the sample (V_{sample}^{bulk}) is given by Equation 20.

Equation 20.

$$V_{sample}^{bulk} = V_P - \left[\frac{m_{PSHg} - m_P - m_S}{\rho_{Hg}}\right],$$

where V_P is the penetrometer volume [m^3], m_{PSHg} – mass of penetrometer with the sample and mercury [kg], m_P – mass of the penetrometer [kg], m_S – mass of the sample [kg], ρ_{Hg} – mercury density [kg/m^3]. Notice that V_{sample}^{bulk} is most commonly a small number derived by subtracting two larger numbers, which are nearly equal. All the values for computing V_{sample}^{bulk} are supplied by the operator and are derived primarily from weighting procedures. The major risk for instrument error to affect V_{sample}^{bulk} is in the filling process. The penetrometer should not be filled completely, the excess volume is assigned to the sample. The exact pressure applied to the mercury at the starting point for the pore volume measurement also affects the bulk volume, as higher pressures fill progressively smaller pores. If the material has a significant pore volume distribution in the 100-500-µm range, it will be difficult to obtain reproducible bulk volume measurements due to the requirement for a highly precise and reproducible starting pressure (*Micromeritics, 2012*).

The total porosity of MIP blocks, named hereafter φ_{MIP}^{T}, was calculated from Equation 19, in which the grain density (ρ^{grain}) was taken equal to the grain density of NMR plugs (ρ_{NMR}^{grain}) for the corresponding layer of interest.

µTomography on localized blocks

Some of the sub-samples prepared for MIP measurements were also scanned by µtomography at lower voltage, than the entire cores (70 kV, see section 2.2.1), to improve

the resolution (voxel size: 17.65 µm) and to measure the apparent volume and bulk density ($\rho_{\mu Tomo}^{bulk}$) (Figure 64). Preliminary drying at 150°C under vacuum was performed, and images were acquired in a dry atmosphere. For all the µtomography images a non-local mean denoising has been applied (see 0 for the details. The volume was measured with *Avizo*© segmentations tools.

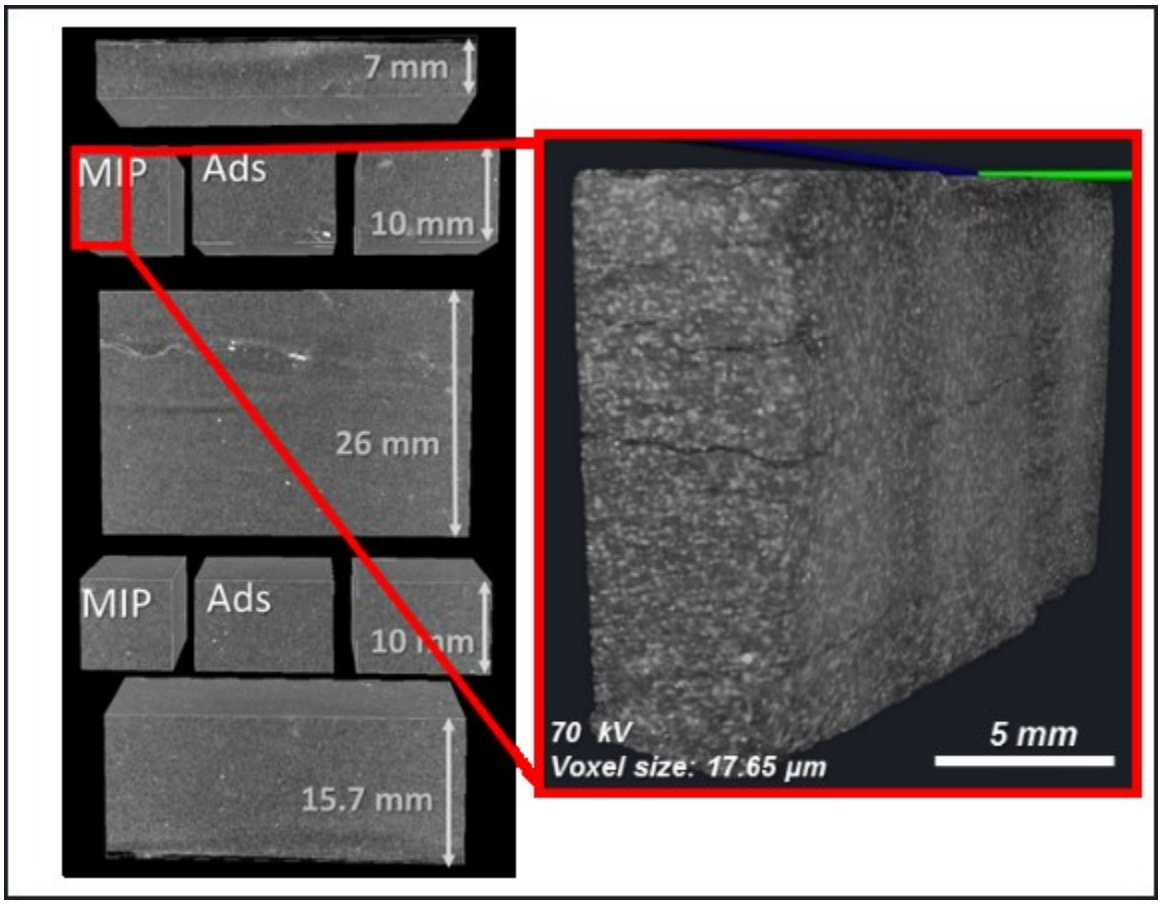

Figure 64. Left: virtually sub-sampled BS-block (MIP – mercury intrusion porosimetry, Ads – nitrogen adsorption). Rigth: a scanned individual sub-sample block.

2.2.5. Sample impregnation

The impregnation of the samples was done following the procedure developed by Prêt (2003) for the sedimentary rocks. To prepare the samples for the impregnation, large IS blocks (Figure 61.A) were immediately surrounded with an epoxy resin, keeping two large parallel planes open, and packed into special "sandwiches" in between porous stone and metallic plates (Figure 65.B). Such a construction is needed to ensure mechanical confinement and constrain the sample volume upon drying and swelling during impregnation processes. The samples were placed into impregnation cells (Figure 65.A),

manufactured especially for such large samples, and conserved at 90°C till the impregnation procedure. Before the impregnation the cells were outgassed at 90°C under vacuum for 4 days. The impregnation with methylmethacrylate (MMA) resin, marked with ^{14}C isotope (^{14}C-MMA), was done by diffusion and lasted approximately 3 months, to ensure the full sample saturation.

The impregnation method with (^{14}C-MMA) resin, has proved to be efficient to preserve the texture in a water-like saturation state without losing the clay confinement or modifying the pore space geometry during sample manipulation (sectioning, polishing, and image acquisition). The monomer properties permit complete sample impregnation, including the micropores and interlayer of swelling clay minerals (Prêt, 2003; Prêt et al., 2013).

The initial activity of the resin was controlled by liquid scintillator method (8.26 µci/ml). After this period, ^{14}C-MMA was polymerized through gamma irradiation. The static batch radiation of the ^{60}Co source was applied for all the samples at the same time with the dose rate >100 kGy (the adsorbed dose in samples 116 kGy ± 5%). Such a high dose rate was selected to ensure the full polymerization of all the resin. After this step, the impregnated IS blocks could be handled without damaging their microstructure. Once impregnated, the large IS blocks were sawn across the bedding plane. These samples were used to prepare polished thick sections for multi-technique image acquisition.

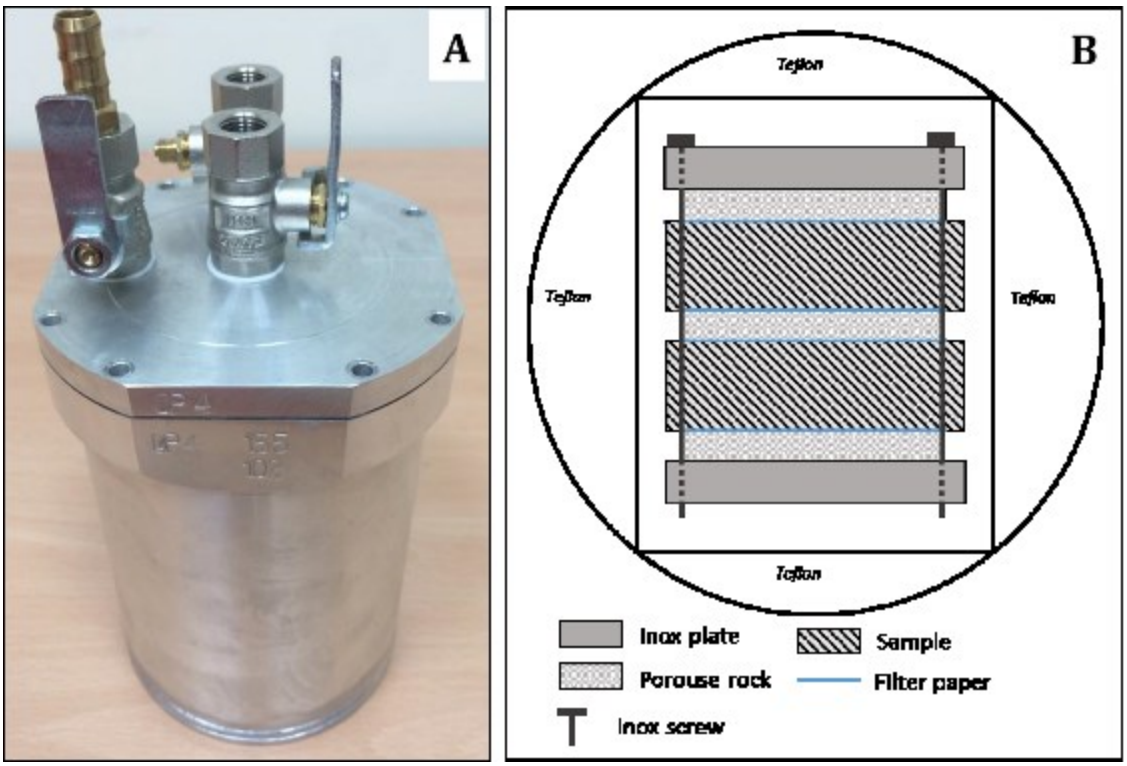

Figure 65. A) Impregnation cell. B) Scheme of the sample "sandwich" preparation for the impregnation (after Prêt, 2003).

2.2.6. Sample surface preparation

For the sample surface preparation, a polishing procedure was especially developed for large radioactive samples. To limit the pollution due to dust, the procedure was fully automatic and was performed with the polishing set *Tegramin-30* (*Struers).* A specific sample holder has been developed (Figure 66), to ensure the sample position during the procedure and to obtain a flat surface without any inclinations. To evaluate the quality of polishing procedures several techniques were used.

First, when polishing precision was in the range of 125-5 μm, thickness loss was manually evaluated with calipers. When lower polishing precision was considered, the thickness loss was too small to be manually detected and confocal microscopy was applied.

Figure 66. A) Polishing set Tegramine-30 (*Struers*); B) sample holder, adapted for large samples surfaces preparation.

The samples, which were achieved during polishing tests at different steps, were investigated using confocal microscopy (CFM). The control of the surface roughness of the surface was done during the polishing, observing the samples without removing from the sample holder, to estimate an optimum time of polishing at each step. Microscope Leica DCM8 was used for the observations. One of the mean features of this device is its dual core system, which has both confocal scanning and interferometry mode (Figure 67.A). All samples were scanned at the confocal mode. As the light source the LED sources are installed (red - 630 nm, green - 530 nm, blue - 460 nm and white, which was used for performed investigations).

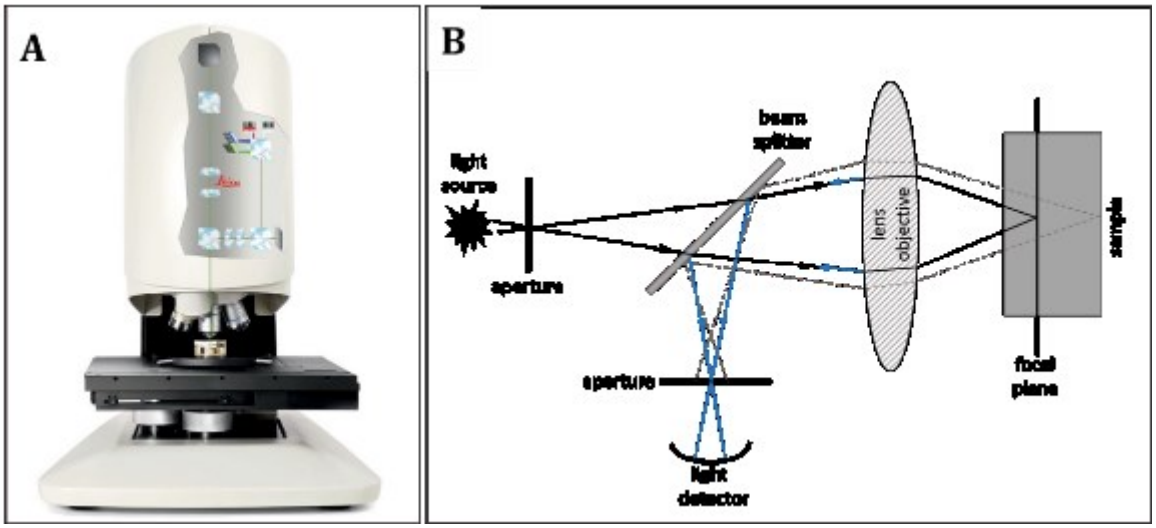

Figure 67. A) Microscope Leica DCM8 at confocal scanning mode (photo from *http://www.leica-microsystems.com*); B) general principle of confocal microscopy (after Minsky, 1988).

The general principle of confocal microscope is based on point-by-point image reconstruction by focusing a point of light sequentially across a surface and then collecting some of returning rays: after passing through the pinhole aperture only rays that arrived directly from the focal point are collecting (Figure 67.B). Thus, the confocal microscope creates sharp images of the surface that would otherwise appear blurred when viewed with a conventional light microscope. Software, operating the microscope, combines the 2D images to create a 3D reconstruction, representing the topography of the sample surface. The construction of the CFM microscope allows to investigate large samples, thus the control of the surface roughness was performed continuously during the polishing, after each polishing step, without removing the samples from the holder.

Two magnifications were used to evaluate the quality of polishing: at large scale (to control the tilt of the entire surface and the amplitude of z values across the surface) – x20; and at local scale (to evaluate the quality of the grains surfaces, grain/matrix border, homogeneity of clay matrix) – x100. The acquired images contain the information of the spatial coordinates of each pixel and pixel value, which corresponds to the absolute z in µm. LeicaMap software was used to treat the confocal images.

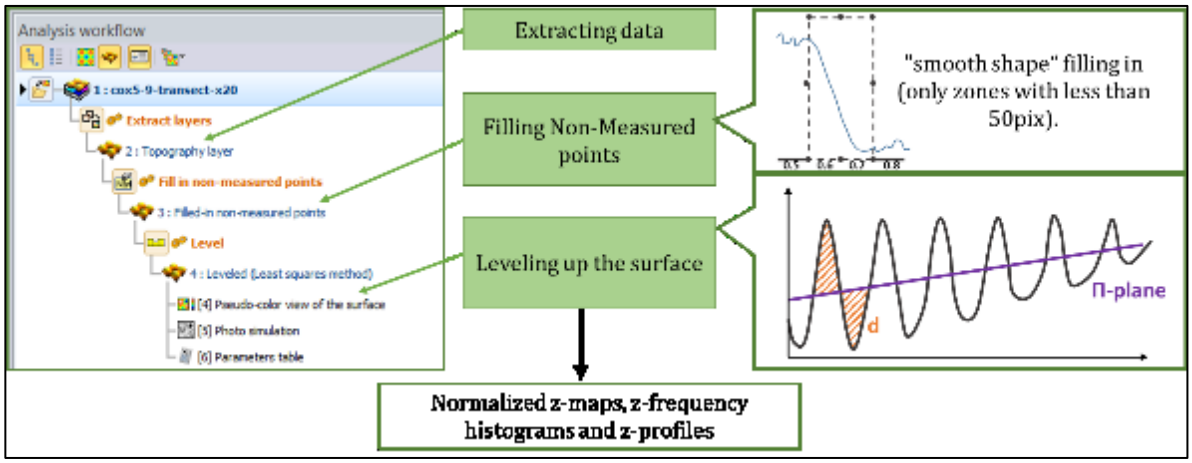

Figure 68. Workflow of Image treatment by *Leica-Map* ©.

Workflow of image treatment using *LeicaMap* © is displayed in Figure 68 and consists of 3 main steps: (i) extracting data (through extracting the tomography layer); (ii) filling non-measured points, using a "smooth shape" (matching the neighborhood as much as possible, to make the correction as invisible as possible); (iii) levelling up the surface. Last step is needed to remove the general slope of a surface. It is done using least squares method: removing the least squares plane consists in calculating the equation of the Π plane (Equation 21) which minimizes the sum of the squares of the basic distances d(x, y) at the point (x, y, z), d(x, y) being the distance between the point (x, y, z) of the surface and the point (x, y, z') of the plane (Figure 68). This method is recommended for surfaces with non-regular texture, like shale samples.

Equation 21.

$$\Pi = d_1^2 + d_2^2 + \cdots + d_{n-1}^2 + d_n^2 = \sum_{i-1}^{n} d_i^2 = \sum_{i-1}^{n} [y_i - (a + bx_i)]^2.$$

After the treatment, the normalized z maps, z-variance maps, z frequency histograms and z profiles using "in-house" batch *ImageJ* (Rasband, 2010) routines were created to quantify the surface roughness and the quality of the polishing procedure (Figure 69). All the calculations have been performed on the representative areas (larger than REA; see **Erreur ! Source du renvoi introuvable.** for the details). To calculate the variance of z-values (*Var*, [µm²]) Equation 22 was used, where v is the pixel values, collected over the surface with the dimensions *m* and *n*.

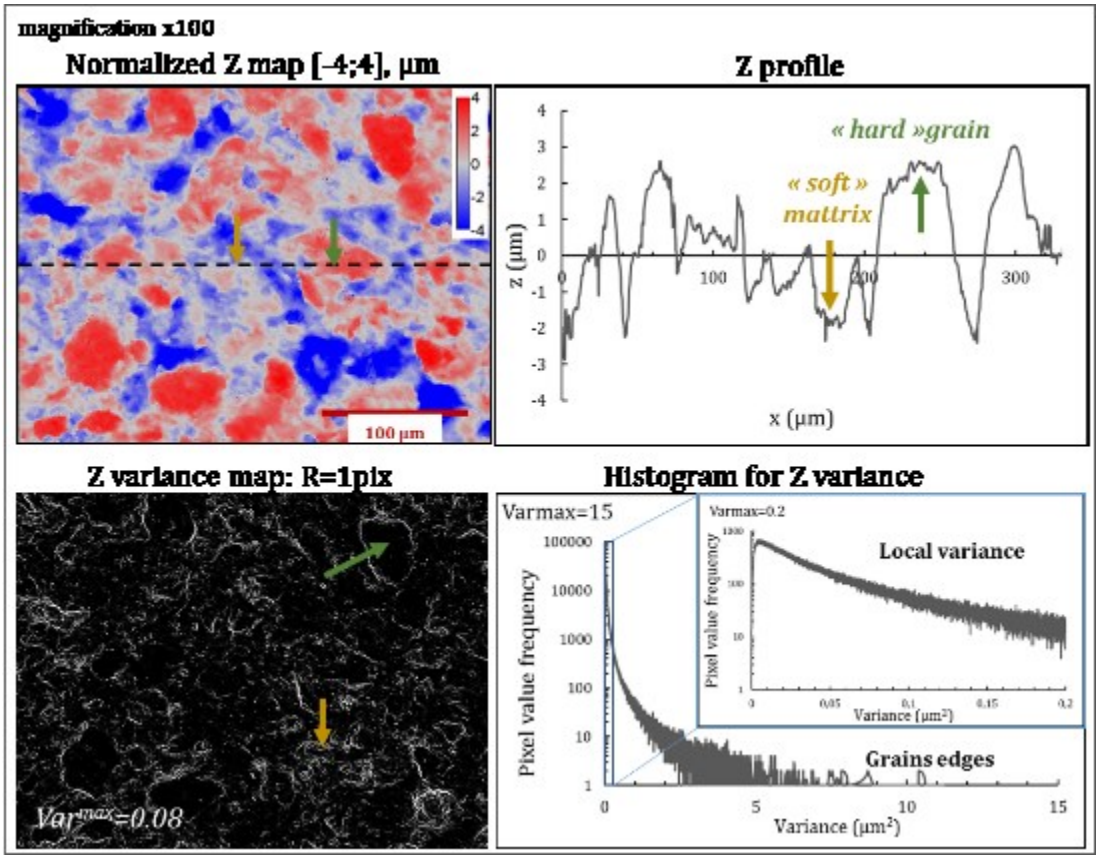

Figure 69. Example of analyses of images recorded at x100 magnification with confocal microscope.

Equation 22.

$$Var = \frac{\sum_{i,j=1}^{mn}(v_{ij}-\overline{v_{ij}})^2}{m*n}.$$

Polishing protocol, developed in consequence, contains several steps. The first part contains 4 steps and represents polishing with silicon-carbon discs of decreasing at each step grain sizes and water as lubricant upon a total time of 110 min. Then, polishing with tissue discs and diamond suspension were used with decreasing grain size (3 steps, down to 1/4µm) upon a total time up to 125 min. The last step has provided the result with only ± 0.5µm of surface topography variation over ~25 cm^2 of the surface. Surface roughness is defined as mean surface roughness (S_A, [µm]) and calculated with Equation 23 (ISO 25178-2, 2012). For the final surface this value is in the range 0.15 - 0.18 µm (Figure 70). This quality is efficient for autoradiography but may still cause a few artifacts with scanning electron microscopy applications (on the border between grains and clay matrix).

Equation 23.

$$S_A = \frac{1}{n}\sum_{i=0}^{n}|z_i - z_{ar.mean}|,$$

where z_i is a measurement of the surface topography [µm] at i pixel, $z_{ar.mean}$ – arithmetic mean [µm] over the surface with n pixels.

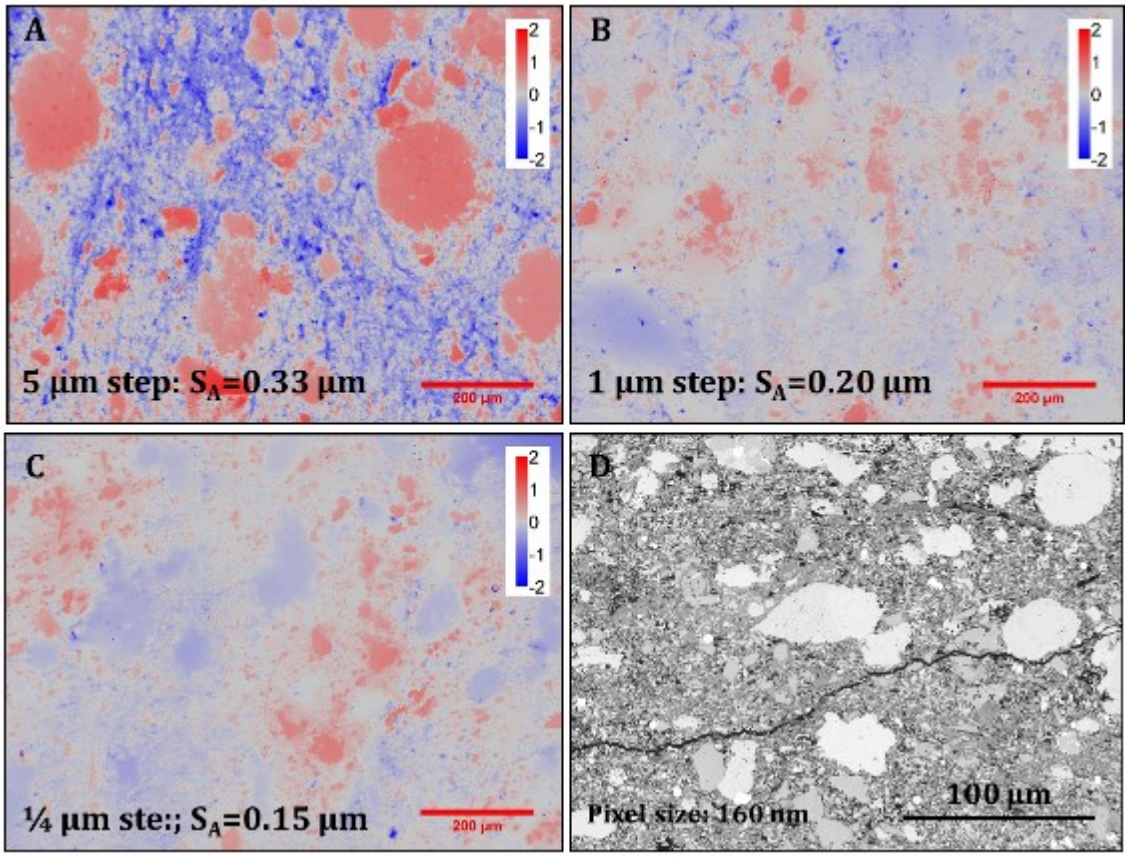

Figure 70. CFM images (calibration bar: ±2µm, scale bar: 200µm) of the central part of impregnated sample C (condensate zone) at different polishing steps with the indication of surface roughness: A) in the end of polishing with 5 µm SiC foil disc; B) in the end of polishing with 1µm suspension; C) final surface in the end of 1/4 µm step; D) BSE-SEM image on the center of the same sample prepared for the autoradiography (FEG-SEM Zeiss Ultra 55, accelerating voltage - 5 kV, working distance - 10.3 mm).

2.2.7. Autoradiography

The whole autoradiography method includes sample preparation, impregnation, polymerization and porosity mapping acquisition (Prêt, 2003). The steps for the exposition to obtain autoradiograph are illustrated with Figure 71.A. The autoradiography technique affords thus the possibility to map the connected porosity in a hydrated-like state.

After the impregnation and the surface preparation through the mechanical polishing, the samples are exposed in dark room simultaneously with the standards of known activity on a film (Figure 71.B, *Kodak BioMaxMR©*), which is capturing beta particles emission (contrasting the areas with varying amount of resin, i.e. porosity). The depth of the emission is ~120 µm, and strongly dependent on the chemical composition and density of the sample (126 µm – for pure montmorillonite, 228 µm – pure MMA, Prêt, 2003).

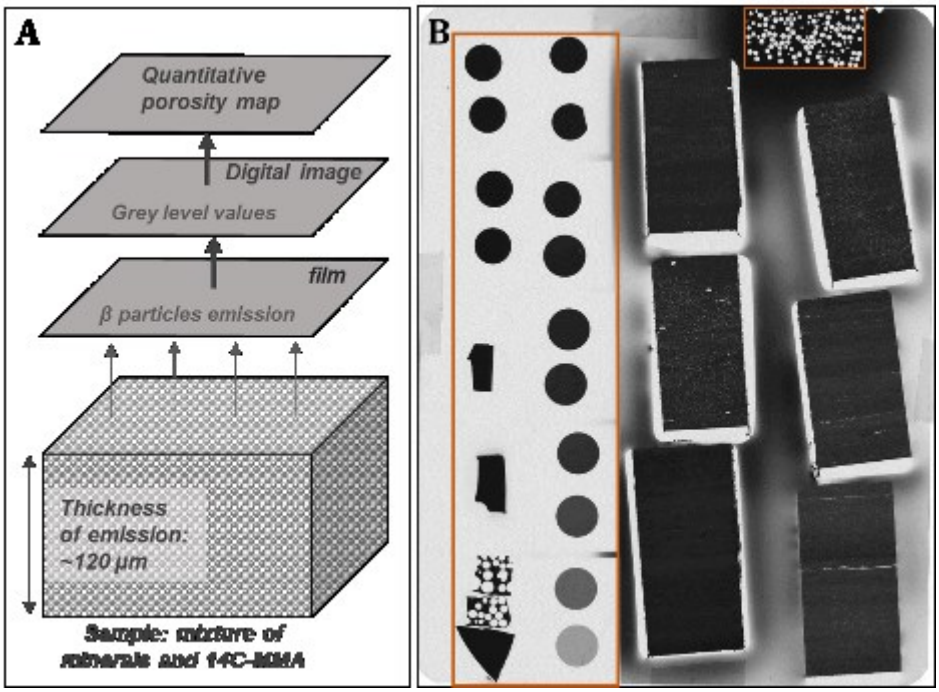

Figure 71. A) Scheme of the procedure of autoradiography exposition (modified from Prêt, 2003); B) an example of the scanned film, after development, with samples (dark grey rectangles, white rings correspond to the non-porous resin, surrounding the sample) and standards of pure ^{14}C-PMMA with known activity (in orange rectangles).

For all the porosity maps obtained, the autoradiography images have been denoised through a non-local mean filter application (see section 2.2.12 for details).

The image resolution is limited by the resolution obtained on the digitization of the autoradiographic film (pixel size: 10.65 µm). Optical density of each pixel, named hereafter *D*, corresponding to the sample surface, may be recalculated, using the value of grey level for the film by itself (Equation 24).

Equation 24.

$$D = \log(\frac{N_{go}}{N_g}),$$

where N_{g0} – grey level of the background (film by itself), Ng – mean grey level of selected area.

Using the values of the optical density of the standards, with known activity and exposed simultaneously with the samples, the calibration curve can be found, correlating the optical density and the resin activity (Figure 72).

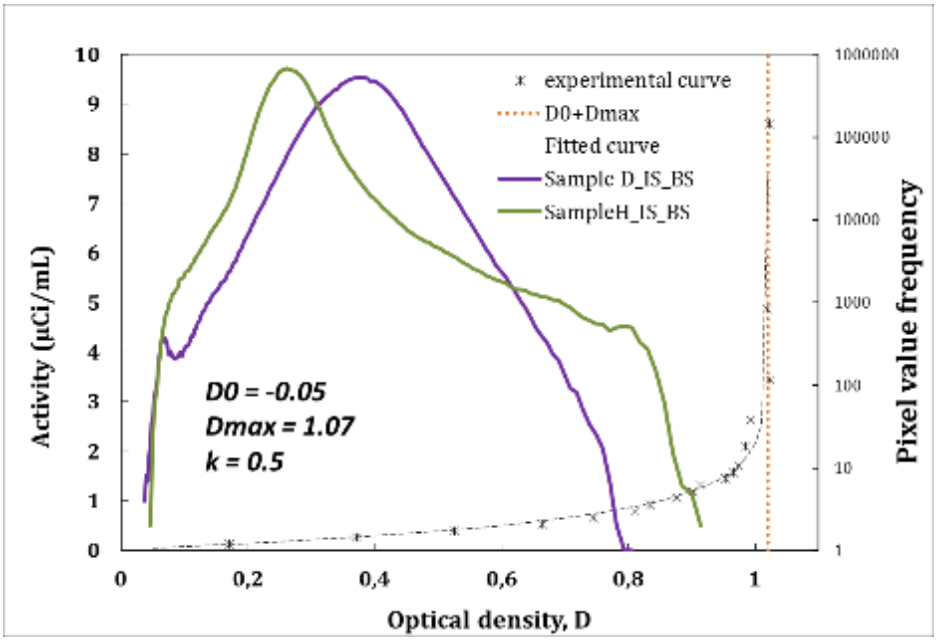

Figure 72. Calibration curve, obtained by the optical density of the standard with known activity, collected for the VM samples exposition, plotted together with pixl value frequence histograms collected over the ful autoradiograph surface.

The longer the exposal time, the higher amount of beta particle can be captured by the film, providing higher optical density (Hellmuth et al., 1993, Prêt, 2003). In the present research, the exposition of 149H have been performed.

Using a fitting curve, the equation for the activity estimation from optical density maybe obtained, through the definition of coefficient k, D_0 and D_{max} (Equation 25).

Equation 25.

$$A_0 = -k^{-1}\ln(1 - \frac{D-D_0}{D_{max}}),$$

where k, D_0, and D_{max} are parameters to define from calibration curve by fitting the experimental points for the standard samples with calculated/measured activity.

Using the developed equation for the particular exposition time, the activity, measured at each pixel of the surface sample, is calculated. Thus, it can be transformed to the porosity (Equation 26).

Equation 26.

$$\varphi_{Auto}^{Con} = \beta A_0^{-1} f(D) \cdot 100\%,$$

where the correction factor β is connected to the ability of the sample to absorb the radiation with its density and chemical composition. This correction factor is directly dependent on the grain density of the sample and can be calculated with Equation 27 (Sammartino et al., 2002; Prêt, 2003).

Equation 27.

$$\beta = \frac{\rho_{mix}}{\rho_{res}},$$

Where ρ_{res}, [kg/m3], is the density of the polymerized resin (was assumed constant over the sample volume and equal to 1.19 g/cm^3; Prêt, 2003); ρ_{mix}, [kg/m3], is the density of the resin-sample mixture. The major assumption of the calculation is that resin is considered to be "diluted" by minerals that absorb radiation in proportion to their density.

Since value of β is not known for each pixel, but strongly varies as a function of chemical composition (shale samples contain both mineral and organic phases), this may cause some errors on the porosity quantification).

From the digitalized autoradiographs, using *AUTORADIO* software (Prêt, 2003), the maps with spatial distributions of the connected porosity were calculated for each sample.

Several types of information can be extracted from such a map (Figure 73), as the total connected porosity of the core (φ_{Auto}^{Con}) over the full autoradiograph surface, more localized porosity of the layers of interest ($\varphi_{Auto}^{Con\_L}$), for which all other bulk techniques were applied, as well, as the porosity of the projections of sub-blocks on the autoradiography surface ($\varphi_{Auto}^{Con\_B}$). Following this methodology, several types of information can be directly compared, since they have been obtained on the same layer of interest. Vertical profiles along the core axis and frequency histograms of porosity have been also computed to highlight spatial heterogeneities (i.e. layers with various porosity values).

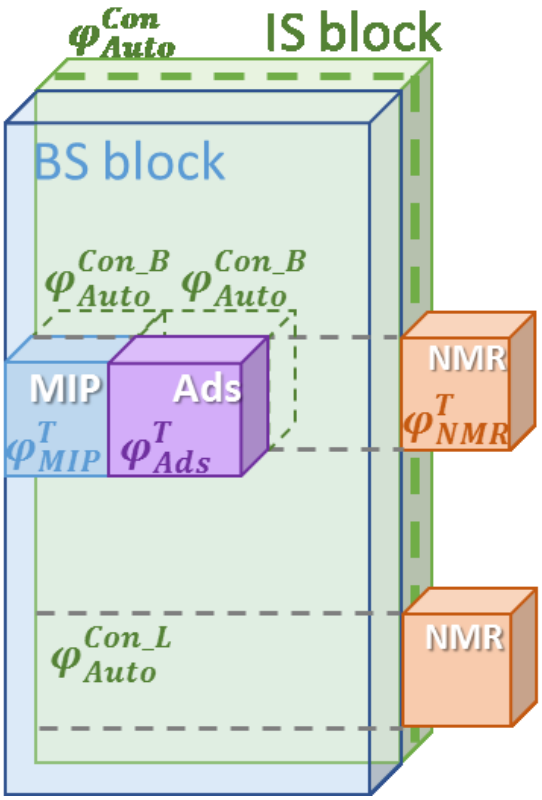

Figure 73. A scheme for the correlation of autoradiography porosity maps with other techniques: layers of interest and projections of blocks, where bulk measurements were performed, can be found on the autoradiography surface (green line) to extract the connected porosity value of corresponding area ($\varphi_{Auto}^{Con\_L}$ and $\varphi_{Auto}^{Con\_B}$, respectively).

2.2.8. Mercury intrusion porosimetry

Mercury intrusion and extrusion curves were obtained using Micromeritics *Autopore IV 9500* volumetric set up on localized sub-blocks (Figure 64) ~5 x 10 x 15 mm from atmospheric pressure up to $200 \cdot 10^6$ Pa. All the samples were heated under vacuum at 150°C for at least 36 hours and cooled under vacuum. Cumulative pore throat size distribution, up to the critical pore diameter, is calculated from the intrusion curve based on Washburn's law with a contact angle of 141.3° (Equation 3), assuming a cylindrical pore shape.

The MIP intrusion porosity φ_{MIP} is also estimated (Equation 28) from the maximum intruded specific volume of mercury $V_{intr.max}$ [m^3/kg] and bulk density ρ_{NMR}^{bulk}, [kg/m^3] for the corresponding layer of interest.

Equation 28.

$$\varphi_{MIP} = V_{intr.max} \cdot \rho_{NMR}^{bulk} .$$

All the curves are blank corrected (Sigal, 2009), by removing the impact of mercury compressibility under the high pressure applied. For this purpose, the MIP test has been done at the same conditions on the empty penetrometer, used for the measurements, with the same program of acquisition.

2.2.9. Nitrogen adsorption

Nitrogen adsorption is a classical method widely used for shale sample characterization, but only applied on crushed powder in the available literature. Adsorption/desorption isotherms were therefore acquired on powder and on blocks, for the localized sub-samples of the BS block (Figure 64), with a *BelSorpMax* volume meter device. For these measurements, the samples were dried at 150°C under secondary vacuum. Drying efficiency was evaluated by monitoring the pressure decrease on the process, which took up to 5 days for blocks (~5 x 10 x 15 mm). The isotherms were acquired at 77 K with continuous nitrogen Dewar refilling and dead volume correction. The equilibrium kinetics for each relative pressure point were tracked by recording the pressure variation in the sample cell versus time to stabilization, with the aim of finding the true equilibration point (Figure 74).

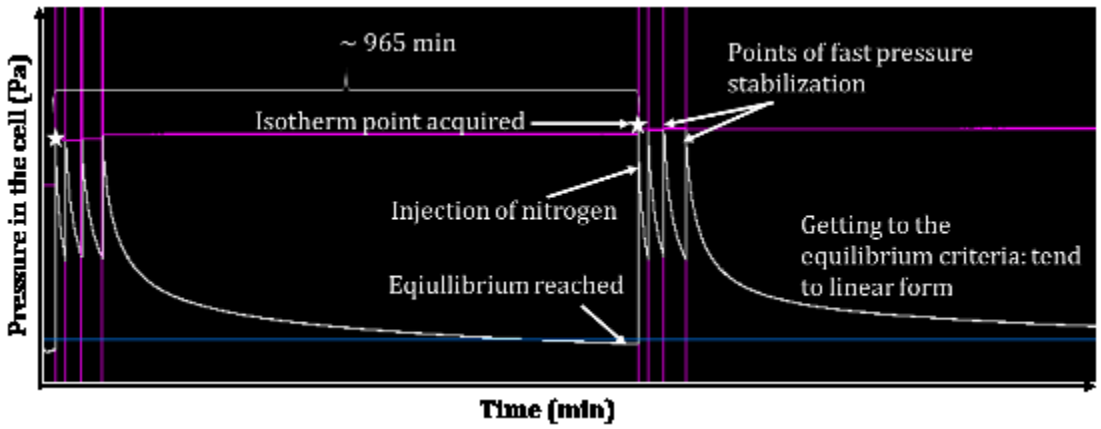

Figure 74. The trend graph, tracking the pressure equilibrium in the system over nitrogen adsorption measurements.

Equilibration time per point of up to 1 day at low partial pressures and a total acquisition time of isotherms raising up to 20 days were observed for blocks (Table 10). Due to such a long time, required for the blocks acquisition, only few samples were investigated. Adsorption porosity (φ_{Ads}) was calculated from the maximum adsorbed specific volumes of nitrogen in a liquid state (Va, [m^3/kg]) at the maximum relative pressure (P/P_0) and ρ_{NMR}^{bulk}, [kg/m^3] (Equation 29).

Equation 29.

$$\varphi_{Ads} = Va \cdot \rho_{NMR}^{bulk}.$$

Table 10. Time required for the N_2 adsorption/desorption acquisition on blocks.

Zone	Sub-sample block	Duration of the acquisition, hours
Oil	F_BS_2Nleft	131.7
Condensate	B_BS_4Nleft	227.0
	C_BS_2Nleft	227.0
Dry gas	H_BS_3Nleft	528.8
	I_BS_4Nleft	453.4

The t-plot approach (Harkins and Jura, 1944) was used to determine the micropores' specific volumes, using the Equation 6 to calculate the monolayer thickness. The associated microporosity can be calculated with Equation 29 (φ_{Ads}^{μ}), where Va would correspond to the volume of nitrogen used to feel only micropores (defined by t-plot slope change, Lowell et al., 2004).

The PSD for mesopores and macropores (up to 640 nm) was also achieved by applying the Barrett-Joyner-Halenda (BJH) treatment, for which the Kelvin equation was used (Barrett et al., 1951), assuming cylindrical pores (Equation 4). The pore body and pore throat diameter distributions were calculated from adsorption curves (form factor *f* of meniscus of 1), and desorption curves (form factor *f* of meniscus of 2), respectively.

2.2.10. Nuclear magnetic resonance spectroscopy

Localized NMR plugs (cylindrical plugs 10 mm in diameter x 16 mm in length) were taken on both sides of the IS blocks corresponding to the layers of interest (Figure 61). After a Soxhlet extraction of liquid hydrocarbons by chloroform then isopropanol, followed by drying at 60°C for 3 days, the blocks were then saturated with a synthetic 70 g/L NaCl brine at a pressure of 200 bars for 2 days. NMR acquisitions were performed at 23 MHz, allowing to determine the total volume of brine (V_{NMR}, [m^3]). From this parameter, coupled with the information about grain density (Vs, ρ_{NMR}^{grain}) and bulk density (Vt, ρ_{NMR}^{bulk}), obtained on the same blocks (2.2.4), the connected NMR porosity ($\varphi_{NMR}^{Con\_Vs}$, $\varphi_{NMR}^{Con\_Vt}$) can be calculated using Equation 30 and Equation 31, where m_{sat} – mass of the saturated sample [kg] and ρ^{brine} – density of the brine solution [kg/m^3].

Equation 30.

$$\varphi_{NMR}^{Con\_Vs} = \frac{V_{NMR}}{V_{NMR} + \frac{m_{sat} - V_{NMR} \times \rho^{brine}}{\rho_{NMR}^{grain}}}.$$

Equation 31.

$$\varphi_{NMR}^{Con\_Vt} = \frac{V_{NMR}}{V_t}.$$

NMR is expected to be the most representative way to obtain both effective and total porosity on the same sample block assuming that water in the pores is used as the probe due to its high penetration ability.

2.2.11. Scanning electron microscopy

Due to limitations on the representativity of single SEM image, as discussed in Chapter 1 (1.3.1), three large mosaics have been recorded for three samples taken from each production zone (Table 11). These mosaics allowed to image the surface area with length up to 4.5 cm, covered by 1764 correlated single images (tiles) with a nanometric resolution. The acquisition has been performed with FEG-SEM (field emission gun SEM) microscope Zeiss Ultra 55, on the surfaces exposed for autoradiography (Figure 61.A, green line), for the large impregnated IS blocks (section 2.2.1.), to allow the direct comparison of SEM mosaics with obtained 2D porosity maps. In addition, an "in-house" sample holder was constructed to minimize the variations of the distances of focalization, which induce varying solid angle of detection and blurring. Indeed, no autofocus was applied to prevent the potential rotation and deformation of individual images. The aim of the acquisition parameters selection is to achieve a spatial resolution good enough for observing the largest pores unprobed by gas adsorption (typically pore diameters > 640nm). The mosaics were acquired with an in-chamber annular backscattered electrons (BSE) detector maximizing the signal to noise ratio of images. Before the FEG-SEM observations, the samples have been coated with a thin layer of carbon (< 5 nm).

Since the energy of the incident beam impacts significantly the emission volume of the BSE (Figure 40, Goldstein et al., 2003), the accelerating voltage would be the main parameter, which controls the resolution of the acquired image as the probe diameter of a few tens of nanometer is smaller of one order of magnitude.

Being the function of several parameters, incident beam energy, chemical composition of the sample surface and the surface tilt (Goldstein et al., 2003), the BSE emission has distribution with a "sombrero like" shape at the sample surface (Figure 75.A), with the maximum intensity at the beam position. The entire penetration volume of the primary electrons within the sample can be described by the electron range (R_{K0},

[µm]), which is controlled by the chemical composition and the density of the sample (i.e. the sample electron density). One of the ways to evaluate this parameter is Kanaya – Okayama equation (Equation 32; Kanaya and Okayama, 1972).

Equation 32.

$$R_{KO} = \frac{0.0276*10^{-6}AE_0^{1.67}}{Z^{0.89}\rho^{bulk}},$$

where A is the average atomic weight [g/mole], Z – the average atomic number, ρ^{bulk} – the average bulk density [g/cm^3], E_0 – the incident beam energy [keV]. Within the electron range, the density of scattering events changes sharply with distance from the beam impact area (Goldstein et al., 2003).

The size of the BSE emission volumes (Figure 75.A), depth (P_{BSE}, [µm]) and diameter (D_{BSE}, [µm]), normalized to the electron range, both can be described as a non-linear function of the atomic number (Z), and can be calculated, following the quadratic fit equations (Equation 33 and Equation 34) at a given energy of the incident beam.

Equation 33.

$$\frac{D_{BSE}}{2R_{KO}} = M_0 + M_1 Z + M_2 Z^2.$$

Equation 34.

$$\frac{P_{BSE}}{R_{KO}} = M_0 + M_1 Z + M_2 Z^2,$$

where M_0, M_1 and M_2 are the constants to a power series in atomic number that describes the cumulative radial distribution at given beam energy. For example, with the E_0 = 20 keV, the volume, where 95% of BSE trajectories accounted, would be described with constants: $M_0 = 0.6745$, $M_1 = -9.754 \cdot 10^{-3}$, $M_2 = 6.304 \cdot 10^{-5}$, - for the lateral distribution (D_{BSE}); and $M_0 = 0.333$, $M_1 = -0.00374$, $M_2 = 2.469.10\text{-}5$, - for the emission volume depth (P_{BSE}) (Goldstein et al., 2003).

The application of these calculations, considering the theoretical chemical compositions for the phases, allows to estimate the BSE emission volume for the sample (Figure 75.B). Based on Equation 32 - Equation 34, for the incident beam with a 5 keV energy, the approximate depth (P_{BSE}) for the mixture is in 100 – 230 nm range (for the volume, accounting 90% of the BSE in depth), and the approximate diameter (D_{BSE}) is in 350 – 700 nm range (for the volume, accounting 80% of the BSE closely emitted from the beam position), for minerals and pore fulfilled of resin respectively. With such an electron landing energy of 5 keV, pure resin should be analyzed in the center of pores > 700nm without any mixture with the neighboring minerals. To obtain the information with the

proper resolution, the pixel size should be almost two times smaller than BSE emission volume and chosen at 160 nm.

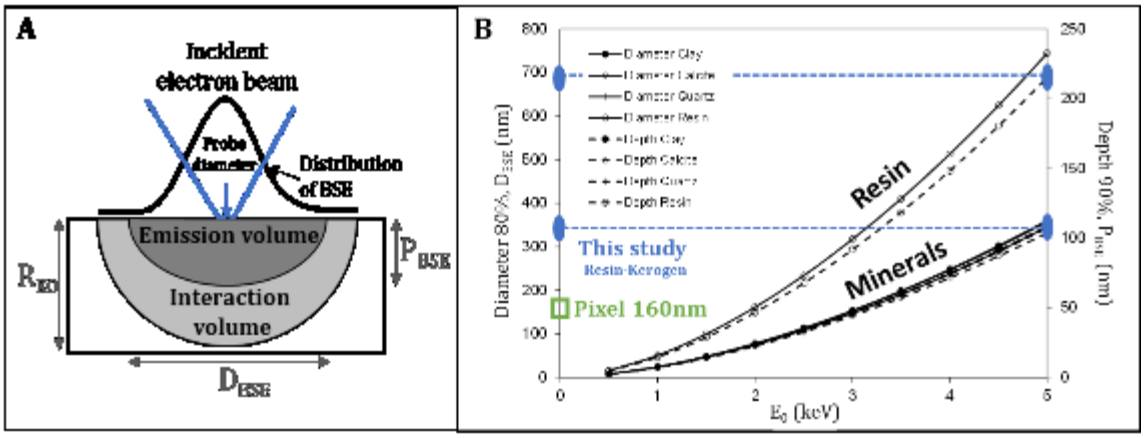

Figure 75. A) Spatial distribution of the backscattered electrons emission within the homogeneous material (after Prêt, 2003). B) Depth (P_{BSE}) and the diameter (D_{BSE}) of the zone of backscattered electrons emmision as a function of incident beam energy (E_0) for mineral and organic phases (assuming the beam normal to the sample surface, *tilt* = *0*°), calculated by Kanaya – Okayama equation (Kanaya and Okayama, 1972): blue lines are for the range of the dimensions for the phases in this stydy; green sqeare is for the pixel size, selected for the BSE-SEM mosaics.

Parameters of acquisition were selected to achieve the best contrast between phases and high signal-to-noise ratio, being the same for all the images and listed in the Table 11.A. The resolution, indicated in Table 11, was selected to catch the smallest grains within the clay matrix and to ensure a reasonable time of acquisition, regarding the accelerating voltage.

The mosaics were localized on the samples surfaces in a correlative way using ATLAS5© (*Zeiss*) software. The localization of the mosaics was done through the comparison of autoradiography image and SEM field of view (following a three-points correlation method, Figure 76). On the surface of the autoradiography three characteristic points were selected for the correlation (sample/resin borders and large grains), then the SEM images (grabs) associated with these points were acquired. In other words, this correlation consisted in superimposing manually the autoradiograph and the SEM field of view (FOV) by rotating and resizing the grabs from the positions of the three characteristic points identified precisely on the two images. As a result, three mosaics have been obtained (Table 11.B).

Table 11. A) Parameters selected for the mosaics acquisition. B) Dimensions and acquisition time for the acquired mosaics (8-bit images).

A

Single image dimensions, pixels	2048x2048
Beam, kV	5
Probe current, nA	5.76
WD, mm	10.26
Overlap, %	6
Dwell time, µs	4.6
Cycle time, s	132
Pixel size, nm	160

B

Sample	**F_IS**	**C_IS**	**I_IS**
Zone	oil	condensate	gas
Area to map, mm x mm	4.6 x 41.3	2.6 x 22.0	5.2 x 38.3
Tiles, x	14	8	16
Tiles, y	126	67	117
Total nb of pixels	$65.4 \cdot 10^8$	$19.9 \cdot 10^8$	$69.4 \cdot 10^8$
Mosaic size, Gb	6.09	1.85	6.46
Acquisition time, h	63.1	19.7	52.9

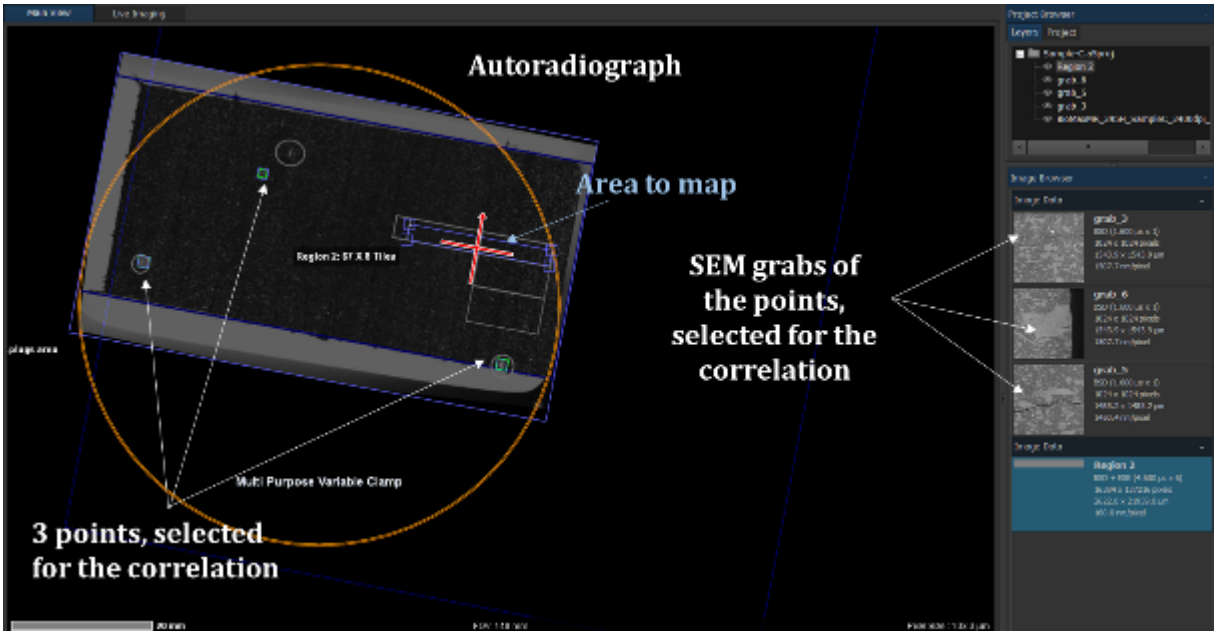

Figure 76. The ATLAS5© window screenshot, during the three points correlation process of autoradiograph and SEM FOV.

2.2.12. Image denoizing

For all the imaging technics results, before any numerical treatment, the images were denoised to improve the signal-to-noise ratio. The choice of the suitable filter was done by the direct comparison of filtered images and their histograms with the initially obtained data. The aims of such a comparison are two: (i) to improve signal-to-noise ratio for the main phases; and (ii) to avoid the loss of information about the smallest objects.

Since pixel size and detection method are different for various techniques the proper filter window size would be different, regarding the dimensions of the objects visualized (Table 12). To calculate the filtered images and the corresponding histograms the *ImageJ* (Rasband, 2010) software was used.

Filtered image, is one, where each pixel value is replaced with a recalculated one regarding the neighborhood. Several filters have been tested: (i) mean filter (Equation 35); (ii) median filter; (iii) gaussian blur (*Gaussian Blur3D plugin*, Rasband (2012); Equation 36); (iv) non-local mean (*NLM plugin*, Buades et al. (2011); Equation 37).

The tests, described in this section, were applied on all the imaging techniques results, but illustrated only with the autoradiography images (Figure 77 - Figure 80). To analyze the impact of each filter, two contrasted samples were selected (samples D, condensate zone, and H, gas window). The autoradiograph is a digital image, where each pixel corresponds to the amount of resin intruded into the pore space, i.e., porosity (see section 2.2.7). The pixels with higher grey level would correspond to non-porous grains (bright pixels), and pixels with the low grey level – to the pore network, filled with the resin (dark pixels). The large broad mode on the histograms is due to the high content of porous clay matrix.

For both, mean (Figure 77) and median (Figure 78) filters, the calculations were done with the kernel of varied sizes. The pixels of filtered images were calculated from the neighborhood, through the arithmetical mean (Equation 35) and median (**Erreur ! Source du renvoi introuvable.**) estimations, respectively.

Equation 35.

$$v_{ij}^{filtered} = \frac{1}{\mathrm{mn}} \sum_{m,n} v(i+m,\ j+n),$$

where $v_{ij}^{filtered}$ is the arithmetical mean value, for the data set of pixel values ($v_{ij}^{initial}$) within the given kernel radius *R*.

Median and mean linear filters, both, do not give extra weight to the pixels at the image borders, and provide the similar effect on the images (Figure 77; Figure 78), as both samples demonstrate similar distributions with large broad mode (mean and median values are close).

Kernel radius of 5 pixels for the autoradiography image corresponds to the window size of ~100 μm, which is larger than average dimensions of the individual objects and almost equal to the blurring due to the lateral range of beta particles emitted from the ^{14}C-MMA. When *R* is < 5 pixels, the resulting images demonstrate the improvement of the signal-to-noise ratio, but only narrow change can be observed on the histograms (Figure 77; Figure 78). When 5< *R* <20 pixels, the final images illustrate the objects smoothing and the averaging of the lateral heterogeneities. With *R* > 20 pixels, the final images

provide only the information about the lamination of grey level (underlining the lamination within the core by removing the cracks and small grains).

The application of such filters leads to the blurring of the images objects, removal of the cracks and smoothing of small grains (Figure 77; Figure 78). The resulting images demonstrate the significant loss of information even with the small filtering window size.

The calculation of the gaussian filter was done, according to the Equation 36. Such a nonlinear filter prevents and restore the blurring at the border of big objects.

Equation 36.

$$v_{ij}^{filtered} = \frac{1}{2\pi R^2}\sum_{m,n} e^{\frac{-(m^2+n^2)}{2v^2}} v(i+m,\ j+n),$$

where *R* is the selected kernel radius of blurring for the data set of pixel values (v_{ij}). The gaussian blur method has the effect of reducing the image's high-frequency components (Figure 79). Already at the *R*>5 pixels, the strong blurring of the objects can be observed, leading to the significant loss of the information.

For the NLM filter application, each pixel is substituted with weighted average of all the similar pixels within the image (Buades et al., 2011; Equation 37).

Equation 37.

$$NLM[v]_{(i)} = \sum_j w(i,\ j)v(i,j),$$

where *w (i, j)* is the family of weights, depending on the similarity between the pixels *v (i, j).* The similarity between the pixels is defined through the standard deviation of the noise within the search window (*sigma*). With *sigma* less than 10, the final images provide the improvement of the signal-to-noise ratio without loss of information about small objects and borders (Figure 80). When sigma is higher than 10, the boarders of grains are slightly blurred, and the smallest objects disappear. NLM filtering provides the preservation of the grains (in comparison with median, mean and gaussian filters), leading to the improvement of resolution. Since *sigma* noise level (operator imputing parameter) is automatically linked to the search window dimensions (for larger noise standard deviation, higher sigma value is needed).

The NLM filter has demonstrated the most propriate result for all the imaging methods, performed in present study, and was selected for the filtering the images obtained by various imaging techniques. Note that 3D data, which are always noisier, than 2D imaging, require larger sigma (and window radius) to be successfully denoised.

Table 12. Result of the filters, selected for image denoizing

Data set	**Pixel/Voxel size, µm**	**Filter selected**	**Sigma**
µTomography	78.8	NLM	25
	17.65		29
Autoradiography	10.65		5
SEM mosaics	0.16		10

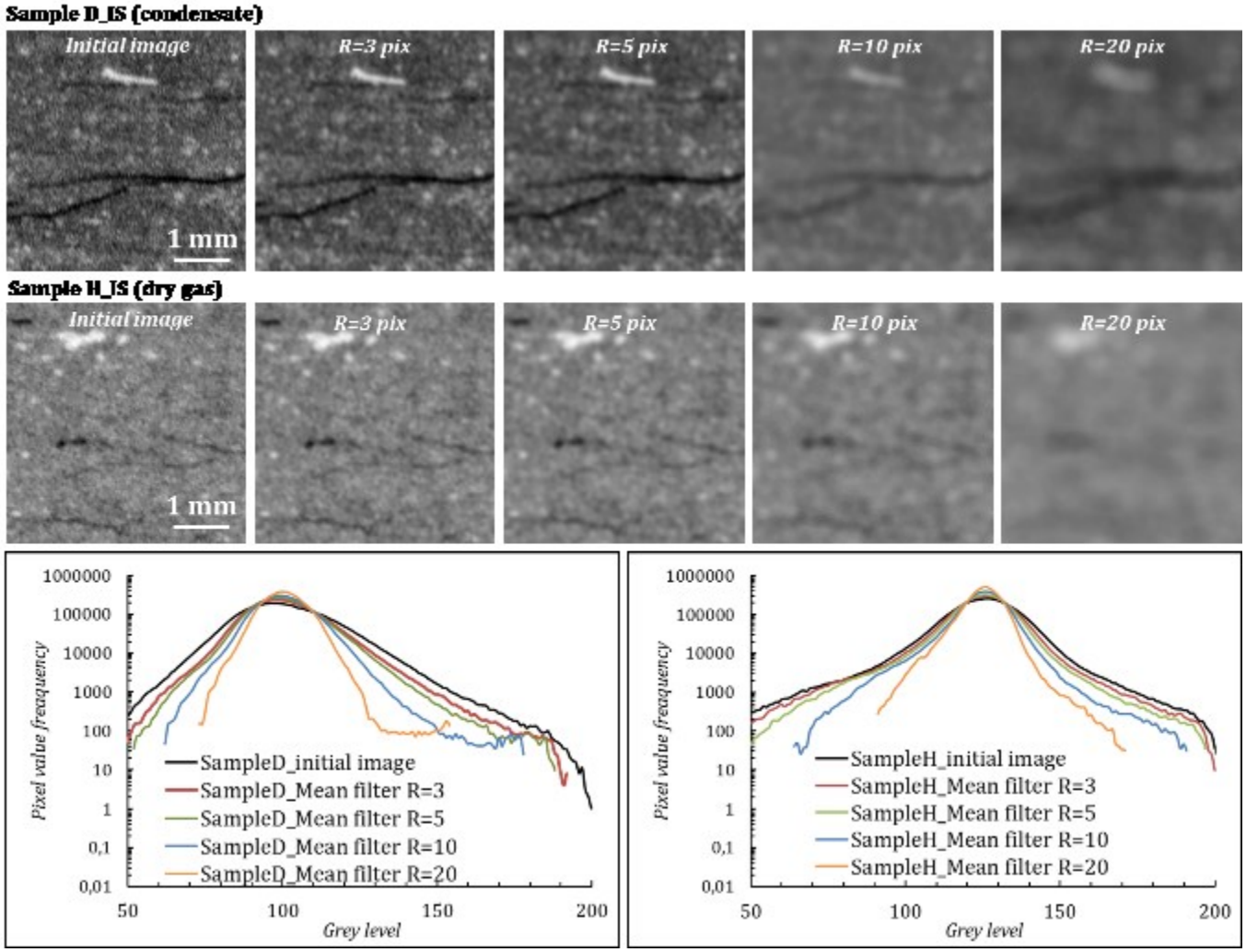

Figure 77. Mean filter application on the autoradiography images (display grey level range is 50-200, ROI to display is 400x400 pixels, histograms were collected on ROI of 2412x2412 pixels, 1 pixel = 10.65 µm).

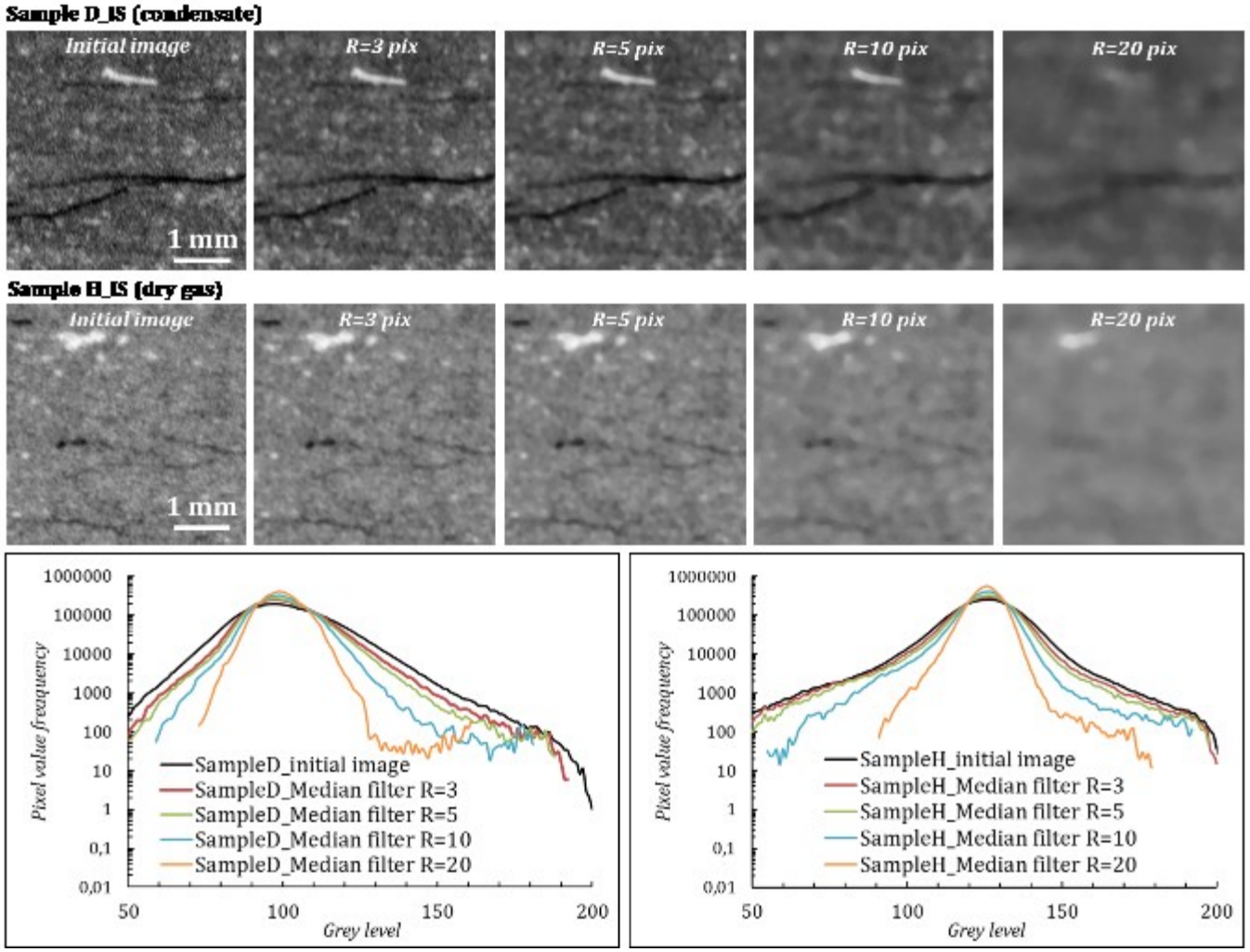

Figure 78. Median filter application on the autoradiography images (display grey level range is 50-200, ROI to display is 400x400 pixels, histograms were collected on ROI of 2412x2412 pixels, 1 pixel =10.65 µm).

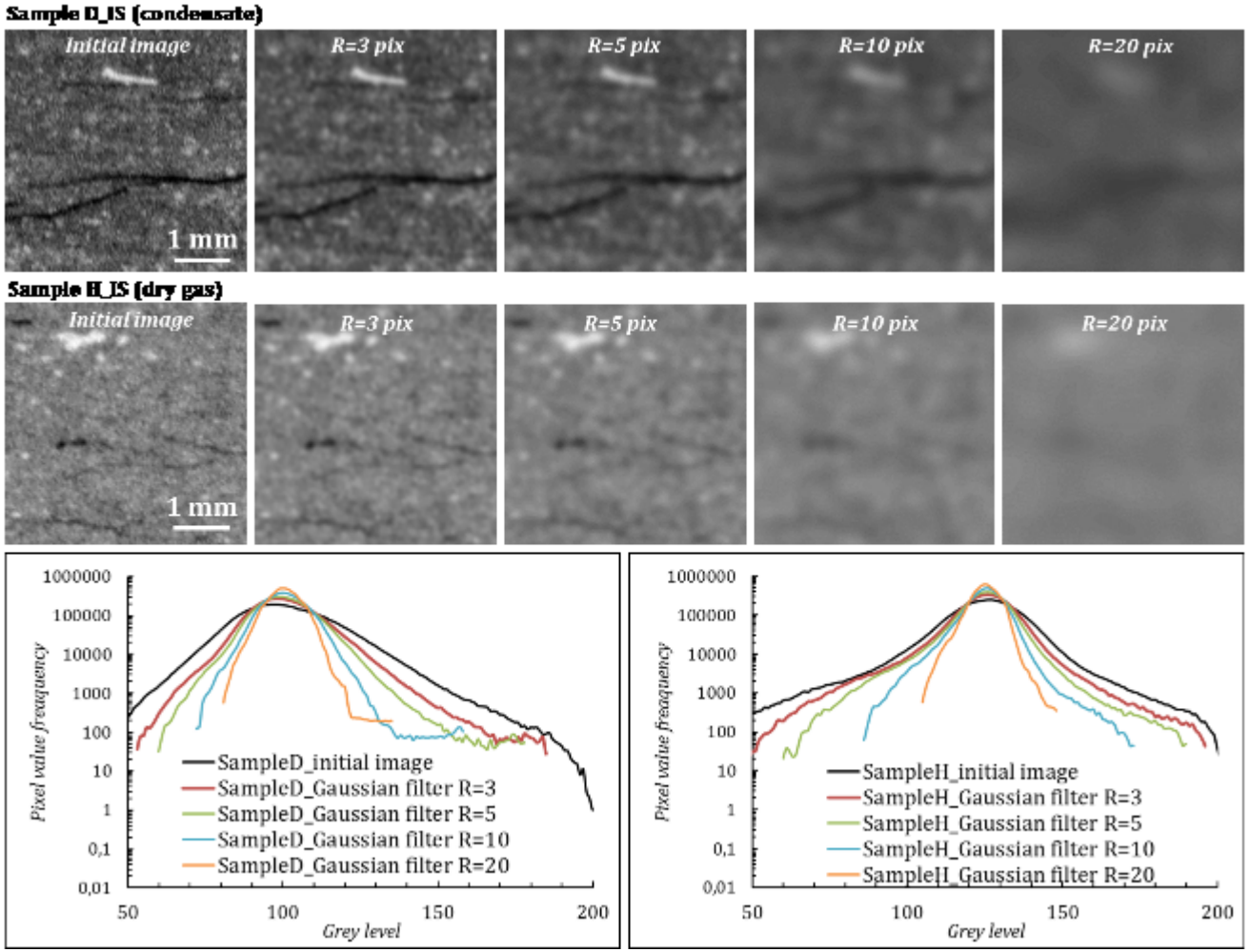

Figure 79. Gaussian filter application on the autoradiography images (display grey level range is 50-200, ROI to display is 400x400 pixels, histograms were collected on ROI of 2412x2412 pixels, 1 pixel =10.65 µm).

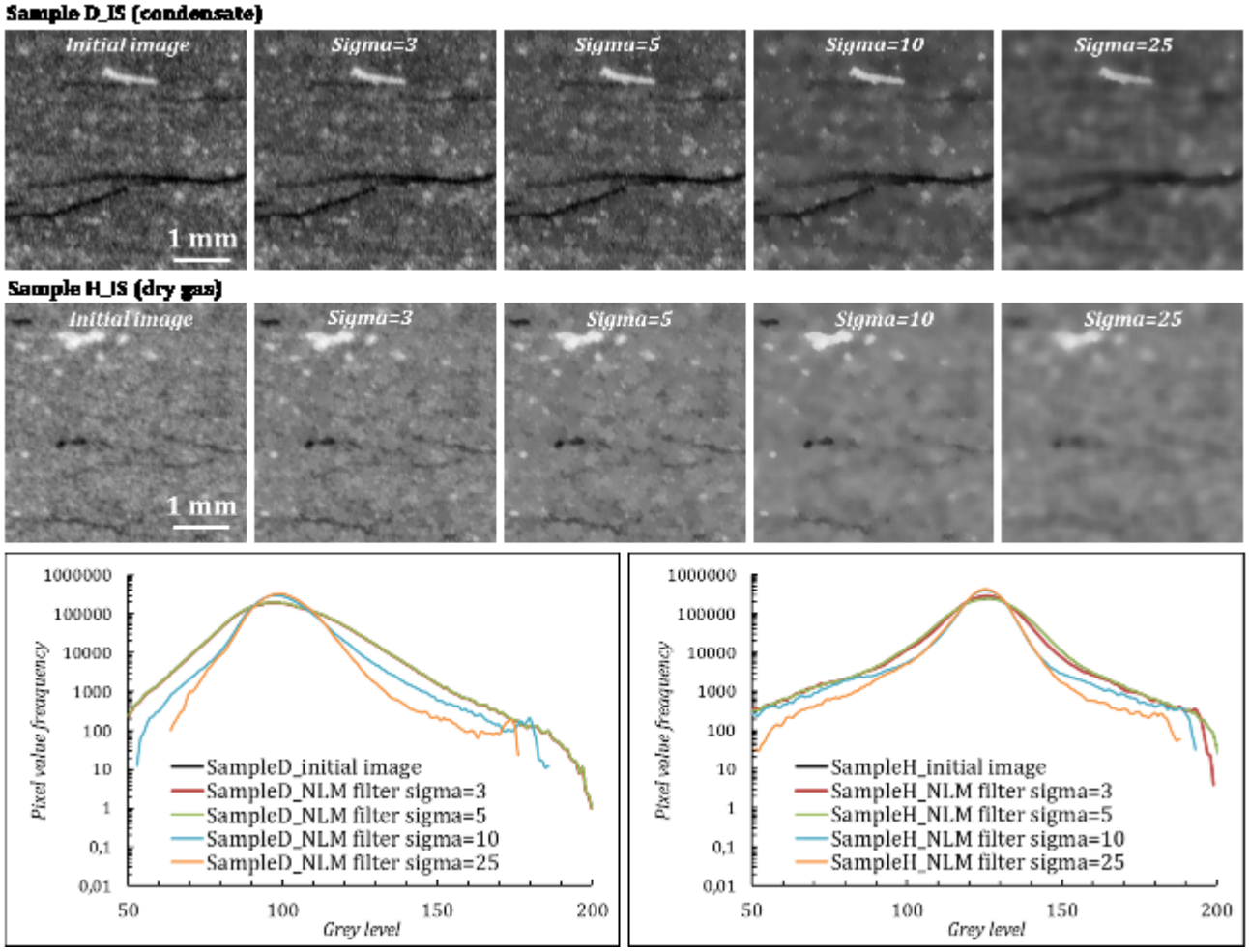

Figure 80. NLM filter application on the autoradiography images (display grey level range is 50-200, ROI to display is 400x400 pixels, histograms were collected on ROI of 2412x2412 pixels, 1 pixel =10.65 µm).

Chapter 3. Combination of bulk and imaging techniques

Introduction

As it was described, only an integrated multiscale & multitool approach, applied on well-localized samples, can achieve a quantitative balance of pore size distribution of shales. Seven samples were selected to represent three different zones with various hydrocarbons production, which may allow to study the impact of the organic matter maturation on the pore network of shale samples. Both, bulk and imaging techniques, were combined to obtain the full pore network characterization. This chapter presents the results of such a characterization, obtained for each core. Some of these data are provided in a manuscript submitted for publication (see section 3.1), but this manuscript does not include all the information used to make the conclusions. It is why, all the acquired data on each VM sample core are presented hereafter, including mineral composition, thermal analysis results coupled with mass spectroscopy, mercury intrusion porosimetry, nitrogen adsorption and autoradiography.

3.1. Correlative coupling of imaging and bulk techniques for quantitative pore network analysis of unconventional shale reservoirs: Vaca Muerta formation, Neuquén basin, Argentina

This part presents a manuscript submitted for publication in the AAPG bulletin.

Correlative Coupling of Imaging and Bulk Techniques for Quantitative Pore Network Analysis of Unconventional Shale Reservoirs: Vaca Muerta Formation, Neuquén Basin, Argentina

N. Matskova[1,2,3], D. Prêt[1], S. Gaboreau[2], P. Cosenza[1], I. Batonneau-Gener[1], F. Claret[2], J-C. Parneix[3], F. Gelin[4], G. Dubès[4], C.I. Fialips[4].

[1] IC2MP/HydrASA(E2), University of Poitiers, CNRS UMR 7285, Bât B27-TSA 51106, 4, rue Michel Brunet, 86073 Poitiers Cedex 9, France ; [2] BRGM - Team D3E/SVP, 3, avenue Claude-Guillemin, BP 36009, 45060 Orléans Cedex 2, France ; [3] ERM, 4, rue Carol Heitz, 86000 Poitiers Cedex 9, France ; [4] TOTAL E&P, CSTJF – Avenue Larribau, 64018 Pau Cedex, France.

ACKNOWLEDGMENTS

The authors would like to acknowledge *Total* and *Total Austral* for allowing this publication, the laboratory team that provided mineralogical and petrophysical analysis (*Total*, Pau), Arnaud Mazurier (*IC2MP*, Poitiers) for helping with the µtomography acquisitions, Claude Laforest (*IC2MP*, Poitiers) for the priceless help with the sample preparation, and Pascal Auger (*BRGM*, Orleans) for the MIP measurements.

ABSTRACT

Unconventional shale reservoirs are characterized by a multi-scaled pore system closely associated with a heterogeneous spatial distribution of mineral and organic components. Therefore, an integrated multi-technique approach is needed to provide a quantitative balance of pore size distribution; which is not achievable, when the methods to be coupled are applied to samples that are randomly selected within the formation.

An integrated method is proposed to characterize the pore network of unconventional shale formations. Samples from the Vaca Muerta formation (Argentina) were selected from different exploration wells located in areas presenting different hydrocarbon maturities (dry gas, condensate and oil), but with comparable mineral compositions. The spatial heterogeneity of the core samples was first analyzed at the core scale by 3D µ-tomography and quantitative 2D mapping of the total connected porosity by autoradiography to identify similar homogenous areas for localizing comparable sub-samples.

The multiscale/multitool approach has allowed reaching a quantitative balance of porosity and pore size distribution, from macrometer to nanometer scale, and the inter-correlation with petrophysical data, acquired on representative sub-samples. Results of 2D autoradiography are in very good agreement with NMR porosity, indicating that all pores are connected and accessed by the ^{14}C-MMA. For the first time, most of the acquisitions were performed on preserved core blocks, rather than crushed powders, including nitrogen gas adsorption experiments, as it is now established that classical crushing for powder analysis damages the pore space. Decreased total porosity and pore throat/body sizes were also observed as burial and organic matter maturity increased.

INTRODUCTION

In organic-rich shale reservoirs, large variations can exist within the same formation both, laterally and vertically, in terms of mineralogical, textural, geomechanical and petrophysical properties (Bryndzia and Braunsdorf, 2014). The extent of these variations is often much greater than what is encountered in conventional reservoirs. In many cases, heterogeneity in unconventional reservoir formations originates from the accumulation of thick columns of clastic sediments, composed of silt-sized quartz and feldspar grains

with clay and organic-rich mud, followed by successive geological evolution, i.e. diagenesis and organic matter maturity with burial depth, leading to anisotropic sedimentary formation (Passey et al., 2010). Consequently, unconventional resource deposits often display varied vertical and lateral porosity, texture, mineralogy and organic matter (OM) content and maturity throughout a same basin. Accurate petrophysical and geomechanical characterization of unconventional shale formations is nonetheless of primary importance to allow predicting unconventional hydrocarbons resources and to help defining well spacing and identifying sweet-spots for optimal fracturing and production. To accurately model fluid flow and fracture generation, detailed analyses of rock organization and pore space are required. Microstructure characterization within organic-rich shale has been so the subject of numerous studies since the end of the 90's. A large amount of data have been collected with different techniques, including bulk measurements such as gas adsorption, mercury intrusion porosimetry (MIP) and He-pycnometry (Clarkson and Bustin, 1996, 1999b; Ross and Marc Bustin, 2009; Clarkson et al., 2012; 2013; Chalmers et al., 2012a; Mastalerz et al., 2013; Sigal, 2013; Kuila et al., 2014; Kuila and Prasad, 2013; Kaufhold et al., 2016 ; Ojha et al., 2017; etc.), nuclear resonance spectroscopy (Sørland et al., 2007; Fleury, 2014; Fleury and Romero-Sarmiento, 2016, etc.), small and ultra-small scattering techniques (Clarkson et al., 2012; 2013; Gu et al., 2016, etc.), and imaging techniques, like scanning electron microscopy (SEM) in 2D and later, with the development of ion milling approaches, in 3D (Curtis et al., 2012a; 2012b; Loucks et al., 2009; 2012; Chalmers et al., 2012b; Milliken et al., 2013; 2014; Kelly et al., 2015; Pommer and Milliken, 2015; Ma et al., 2015; Kaufhold et al., 2016; Houben et al., 2016a; 2016b; etc.), transmission electron microscopy (Bernard et al., 2010; 2012a; 2012b ; Janssen et al., 2011), and µtomography (Noiriel, 2015; Kaufhold et al., 2016, among many others, e.g., review by Anovitz and Cole, 2015). With this very large set of data, pore types and pore distribution have been described as a function of thermal maturity for various unconventional shale reservoirs. The classification of Loucks et al. (2012) is widely accepted to describe pore distribution in shales, through differentiating pores that are hosted by solid OM from pores, that are not related to organic matter (inorganic inter- and intra-particle pores), allowing a uniform qualitative description of various shale samples using imaging techniques. The contribution of distinct phases, i.e. OM and inorganic minerals, to the total pore system of various shale formations has been widely discussed (Jansen et al., 2011; Klaver et al., 2015; Pommer and Milliken, 2015; Houben et al., 2016b; Han et al., 2017; etc.). The origin, volume, pore size distribution (PSD) and mass balance are however still debated, as contradictory conclusions were reached. Each formation is a unique geological object, for which the pore network is the result of complex successive processes, that controlled its creation and evolution. The size and volume of OM-hosted pores are described depending on the thermal maturity and/or

the abundance and origin of OM (Ross and Marc Bustin, 2009; Mastalerz et al., 2013; Pommer and Milliken, 2015; Ko et al., 2017; etc.), yet no uniform explanation can be found. Burial diagenesis of the rocks leads to their compaction, decreasing the total porosity of the initial sediments. At the same time, the maturation of OM is leading to pore network development in the solid OM due to gas production (Ko et al., 2017). However, solid OM without pores (or with pores less than resolution of the microscopy technique in diameter) is sometimes present within samples with high maturity (Curtis et al., 2012a). Although there is a large volume of work, reported in literature (Figure 81), it is difficult to find a clear and quantitative overview of the pore network in such heterogeneous unconventional deposits. Most of the discussions are only qualitative, based mostly on imaging techniques results with limited field of view and resolution, while the other measurements often provide non-representative values. Indeed, organic-rich shales display pore sizes ranging over 4 to 5 orders of magnitude and the relevance of their porosity characterization is directly linked to the quality of sample preparation and the nature and limitations of the analytical methods. The comparison of porosity data, reported in the literature by different authors, obtained through a combination of various techniques for shale samples from all continents, is possible by recalculating mean porosity values using the published specific volumes of intruded or adsorbed fluids, provided by classical bulk methods (Figure 81). Large discrepancies are observed (Figure 81), resulting from the lack of representativeness of the compared samples, as they were collected randomly from different formations, different wells and/or at different burial depths. In addition, the differences in size of the samples, probed by bulk techniques (several centimeters or millimeters) and imaging techniques (several micrometers), and the fact, that the location of the analyzed core chips within the heterogeneous microstructure of the full cores are rarely indicated, strongly impacts the relevance of any comparison. Different authors even report different porosity values for samples collected from the same shale deposits, although, similar methods were used. For example, the total porosity, measured on Haynesville shale samples, by He-pycnometry and MIP combination, ranges from 5 to 12%, although, all the samples were collected in the dry gas production zone with high OM maturity (Figure 81). Meanwhile, the organization of the pore space in shale gas samples is very different from that of shale oil samples, where more complicated pore surface/hydrocarbons interactions occur. Average values of density over the depth of probed samples in a same well were also considered to calculate porosity (Han et al., 2017) while the different density values reflect the sample heterogeneity (porosity and/ or mineralogy) and strongly vary at a millimeter scale. Consequently, the total porosity values provided by different methods within a single study rarely match. Porosity values, obtained by SEM image analysis, are always underestimated in comparison with porosity values, obtained using bulk methods (Figure

81). This is due to poor image resolution (pixel size is larger than most of the pore dimensions) and non-representative fields of view (generally thousands of times larger than the pixel size but much smaller than the volumes probed by bulk methods). Another factor, that impedes correlation of the available literature data, is that porosimetry techniques imply varying sample preparation/experimental procedures, assumptions, and limitations. The PSD ranges, probed by MIP and gas adsorption, are different, providing several types of information about pore network organization, and cannot be directly compared. In addition, gas adsorption is traditionally applied to powdered samples, even though crushing could damage the pore network. Total porosity provided by gas adsorption is therefore generally overestimated (Figure 81).

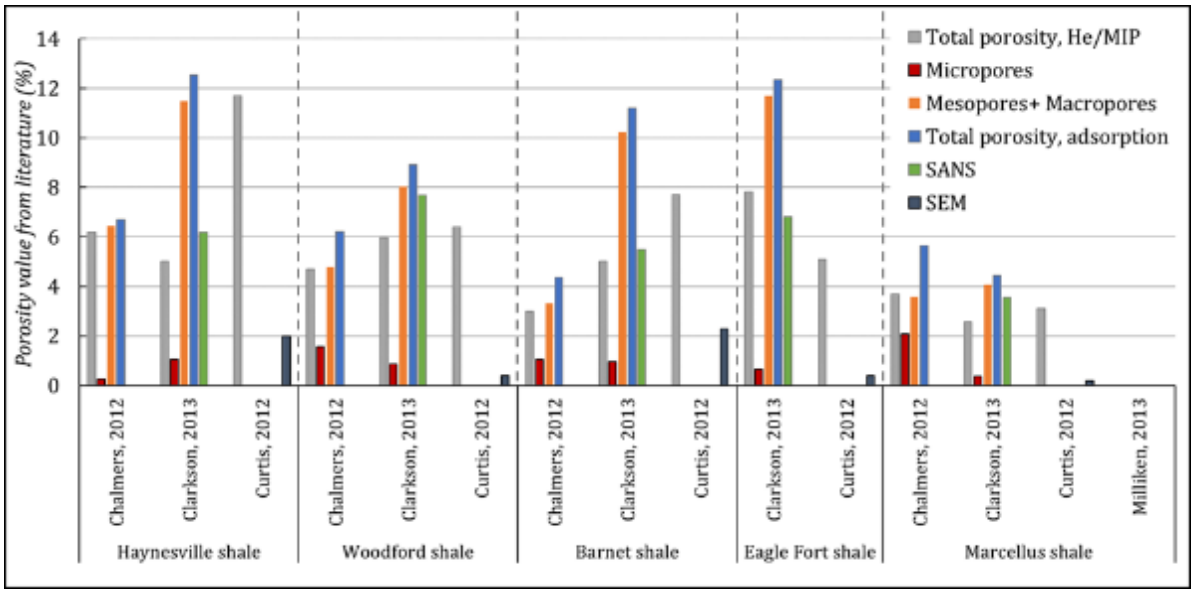

Figure 81. Porosity values recalculated from published literature data sets (e.g., gas adsorbed and intruded mercury volumes), obtained using various methods on several unconventional shale formations: He – helium pycnometry, MIP – mercury intrusion porosimetry, SANS – small angle neutron scattering, SEM – scanning electron microscopy, micropores – porosity measured by CO2 adsorption, mesopores & macropores – porosity measured by nitrogen adsorption and mercury intrusion (the displayed data are not exhaustive but representative of most litterature data).

Moreover, even if authors attempt to discuss the role of the inorganic phase, such as clays and the organic/inorganic interfaces in the distribution of the pore network (Rexer et al., 2014), little data are available on the connectivity of the different porous domains and their interconnectivity. Due to the resolution of the imaging techniques, most of the published data relate low connectivity (Curtis et al., 2012b; Ma et al., 2015).

Considering the spatial heterogeneities of organic-rich shale formations at the core/formation scales and their multi-scale pore system, only a multi-technique approach, applied to carefully localized cores/sub-samples, makes the quantitative comparison of the different data sets relevant. In this study, an integrated methodology workflow was developed to accurately and fully characterize the pore network of several

shale samples of various OM maturities at multi-centimetric down to nanometric scale, and accounting for the varying microstructure at the core and deposit scales. A set of full size cores from the unconventional Vaca Muerta Formation were carefully selected from zones with varying hydrocarbon production, but similar deposit conditions and mineral compositions to tackle porosity heterogeneity at the formation scale. These cores were previously visualized by 3D µtomography to spatialize and localize the homogeneous sub-sampling regions of interest. A combination of bulk methods (gas adsorption, NMR, densitometry, MIP) was then applied to carefully localized and comparable set of sub-samples to provide quantitative balances and PSD, allowing a correlation to spatial porosity distribution at core scale obtained by autoradiography.

MATERIALS AND METHODS

The Vaca Muerta formation, which is located within the Neuquén basin in western Argentina, originates from the accumulation of a thick column of clastic sediments from the Jurassic to Cretaceous followed by successive geological evolution, leading to an anisotropic sedimentary formation up to 600 m thick (Magoon and Dow, 1994; Badessich et al., 2016). Seven full-size cylindrical core samples (Table 13), with dimensions of ~7cm in diameter x 7cm in length, were collected from three vertical wells within Vaca Muerta intervals presenting different hydrocarbon maturities: three samples from a condensate zone with a maximum thermal maturity, measured on bitumen, of 1.3% VReq (cores B, C and D), two samples from an oil zone with a maturity of 1.1% VReq (cores E and F) and two samples from a dry gas zone with a maturity of 1.6% VReq (cores H and I). Sample selection was based on well logs data, X-ray tomography of the cores (CT-scan), and diagraph logs of the cores (Gamma Rays and Gamma Density) within the investigated Vaca Muerta intervals (~150 m). The available data (i.e., X-ray tomography of the cores, Gamma Rays, neutron, nuclear magnetic resonance, acoustic and resistivity logging data) were examined carefully to define homogeneous representative samples, to focus the study on intervals of interest, avoiding unusually large grains, inclusions, cracks, carbonate "macro-beef" veins and nodules. Selected samples showed minimum heterogeneity in the X-ray linear attenuation coefficient (*LAC*) at the spatial resolution of the X-ray scanner (~1 mm), except sedimentary laminae. Petrophysical logs (including modeled mineral composition; calibrated *MULTIMIN* ©) and *LAC* were used to avoid wide mineralogical variation in the depth intervals immediately above and below the samples for further upscaling by comparison with logging tool results. The samples were chosen with similar expected mineral compositions but contrasted wave velocities, resistivities and porosities (Table 13). Moreover, all the selected samples were part of the same macro-lithofacies and, for the samples from oil and dry gas zones, the selected samples were also located in the same stratigraphic sequence. The aim of this sample selection was to study the effect

of burial and OM maturity without being impacted by variations in mineralogy and deposit processes. Cores packed into hermetically sealed plastic bags on the rig site were used for this study in order to limit water desaturation, but the packaging of full size samples from the oil zone was unfortunately damaged.

Laboratory X-ray µtomography and 3D localized sub-sampling

The seven core samples were scanned by X-ray µtomography using an EasyTom XL duo system (RX Solutions) with Hamamatsu reflection 150 kV microfocus X-ray tube, coupled to a Varian Paxscan 2520DX flat panel detector with a 1920x1536 pixel matrix. The entire cores were scanned in continuous helicoidal mode, by recording 1700 projections with a spot size of 60 µm, a target power of 39 W and an accelerating voltage of 140 kV. For each sample, a virtual 3D LAC volume with a voxel size of 78.8 µm was obtained through the use of a back-projection algorithm coupled with a beam drift and hardening correction (Figure 82.a).

Avizo® software was used to accurately localize the cutting planes and the sub-samples for the various subsequent laboratory measurements. From the 3D views, sub-regions of interest with horizontal layers presenting similar non-clay grain amounts, *LAC*, and no macro heterogeneities, were selected (blue selection, Figure 82). First avoiding large heterogeneities and perturbed zones, a 1.5-centimeter-thick block (with the full length of the core) was localized from the center of the core for resin impregnation and a subsequent use for autoradiography porosity mapping (Figure 82.a, IS block). Just in front of the IS block, a twin one (Figure 82.a, BS-block) was selected, from which the different sub-samples dedicated to the bulk measurements were localized (i.e., gas adsorption and MIP; Figure 82.c). Maximum and minimum 2D z-projection maps (i.e., detecting the maximum or minimum *LAC* through the thickness) were also calculated for the BS block in order to avoid sub-blocks with large "heavy" grains (carbonates and pyrite) and cracks/large voids, respectively (Figure 82.b). An exploded view of the sub sampling, performed on the BS block, is presented in Figure 82.c to illustrate the localization of each analyzed sub-sample. The NMR1, NMR2 and PS1, PS2 core chips were sub-sampled for nuclear magnetic resonance measurements and analyses on powder (quantitative mineralogy, thermal analysis and grain density measurements) respectively (Figure 82.a). Careful subsampling of the core, according to virtual cuts, allowed the proper spatial inter-comparison of various bulk methods with imaging techniques - i.e. the exact positions of sub-blocks for gas adsorption and MIP can be projected on the surface studied by imaging techniques (Figure 82.e). The virtual slices corresponding to the plane analyzed by autoradiography and vertical profile of LAC were estimated for further analyzing spatial heterogeneities (Figure 82.b).

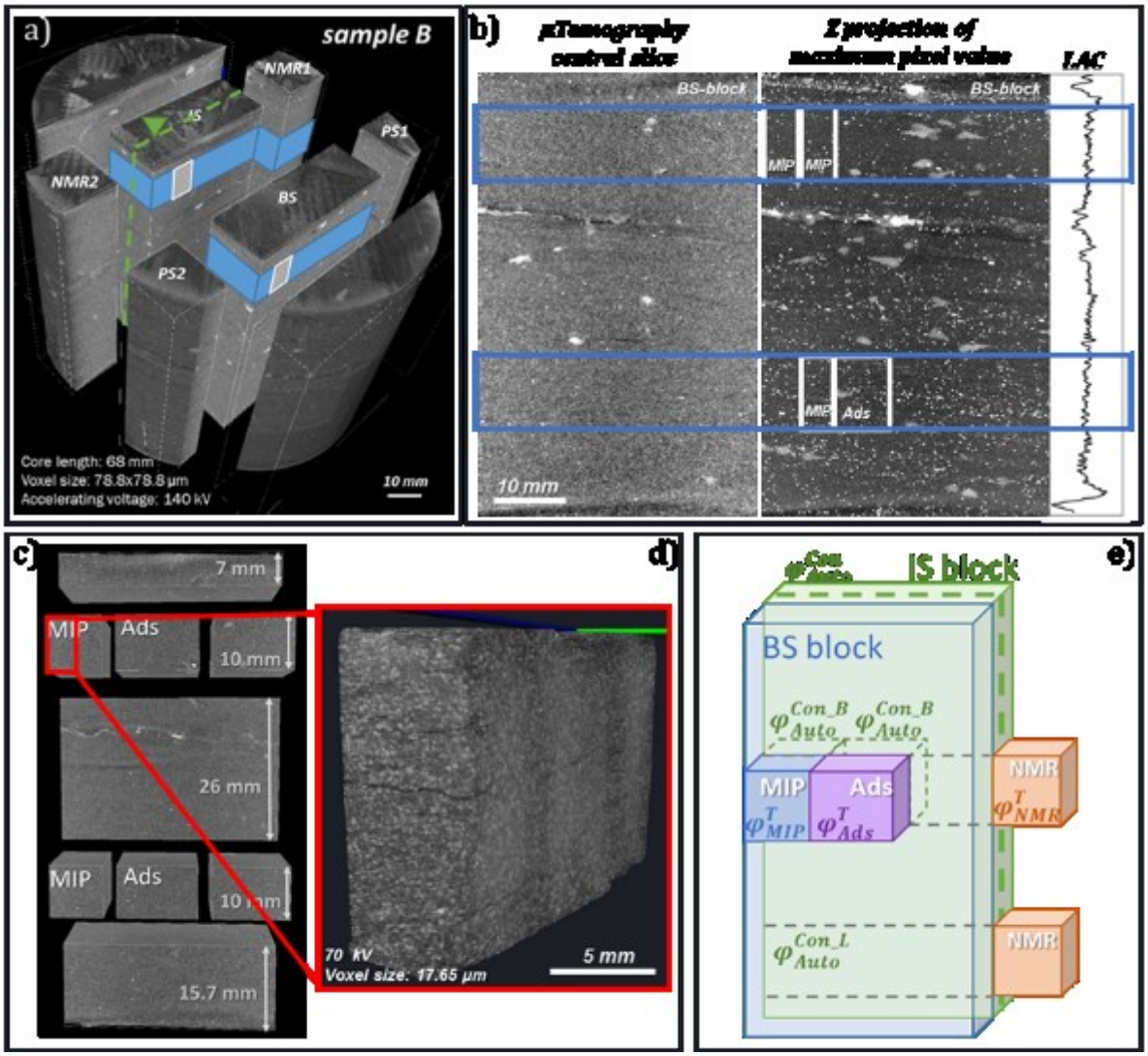

Figure 82. a) 3D µtomography exploded view of sample B (condensate zone) showing the localization of the different sub-samples within the full core: IS – block for impregnation and imaging techniques; BS – block for bulk porosity measurements; PS1&PS2 – blocks for powder analyses (quantitative mineralogy, He-pycnometry, TGA-MS); NMR1&NMR2 – blocks for nuclear magnetic resonance spectroscopy; b) 2D slice from 3D volume and Z projection of maximum pixel values displaying the distribution of the heavy grains (MIP – blocks for mercury intrusion porisimetry, Ads – blocks for gas adsorption); c) 3D view of the BS block showing the virtual cut of the sub-samples used for bulk porosity measurements; d) 3D view of one of the sub-sampled blocks with improved resolution; e) a scheme for the correlation of autoradiography porosity maps with other techniques: layers of interest and projections of blocks where bulk measurements were performed can be found on the autoradiography surface to extract the connected porosity value of corresponding areas ($\varphi_{Auto}^{Con\_L}$, $\varphi_{Auto}^{Con\_B}$, respectively).

Some of the small sub-samples prepared for MIP measurements were also scanned by µtomography at lower voltage (70 kV) to improve the resolution (voxel size: 17.65 µm) and measure the apparent volume and dry bulk density $\rho_{\mu Tomo}^{bulk}$ (Figure 82.d). Preliminary drying at 150°C under vacuum was performed, and images were acquired in a dry atmosphere.

Bulk quantitative mineralogy

The quantitative mineralogical composition of the selected samples was measured on crushed PS1/PS2 core chips with the in-house analytical method of Total, called *MinEval*. *MinEval* allows quantifying the mineralogical composition of rock samples through the integration of results from various measurements (i.e., X-ray diffraction pattern modelling, X-ray fluorescence and He-pycnometry techniques, among others) on crushed powders, after removal of soluble organics by chloroform using a Soxhlet.

Thermal analysis

To define an efficient drying temperature to be used for the different porosity characterization methods, thermal gravimetric analysis (TGA) coupled with mass spectroscopy (MS) was applied on powder from the localized sub-samples (PS, Figure 82.a). The experiments were performed on an SDT Q600 device (*TA Instruments*) in argon atmosphere (with gas flow 50 mL/min), coupled by a heated capillary column with a QGA Mass spectrometer from *Hiden Analytical*. The analysis was done on ~30-50 mg of powder sample by heating up to 800°C with a heating rate of 5°C/min. The products of thermal decomposition were investigated by mass spectroscopy.

Autoradiography quantitative porosity mapping

Autoradiography has been adapted for a long time on sedimentary clay rocks (Hellmuth et al., 1993; Sammartino et al., 2002; Prêt et al., 2004; Prêt et al., 2010a; 2010b; Gaboreau et al., 2016). This technique affords the possibility of mapping the connected porosity in a hydrated-like state on decimeter surface area with a micrometer pixel size. The entire autoradiography method including sample preparation, impregnation, polymerization and porosity mapping acquisition was performed according to the method developed by Prêt (2003). Before impregnation, all the samples were heated under vacuum at 150°C for at least 36 hours and cooled under vacuum. Before polymerization, the samples were impregnated with ^{14}C-methylmethacrylate (MMA) by molecular diffusion for several months. The properties of the monomer allow the sample to be completely impregnated, even within the micropores and the interlayer of swelling clay minerals (Prêt, 2003). Once impregnated, the large IS blocks were sawn perpendicular to the bedding plane (green dotted line, Figure 82.a). The polished surfaces (~25 cm^2) were then exposed in a dark room simultaneously with standards of known activity on the film (Kodak BioMax), which captured beta particles emission (contrasting the areas with varying amount of resin, i.e. porosity). The depth of this emission below the exposed surface was ~120 µm. After digitization of the autoradiographic film, pixel size is almost 10.5 µm. Data were treated using the *AUTORADIO* software (Prêt, 2003). For each sample, a quantitative porosity map was obtained, on a surface area of 6 x 4 cm (height and width respectively), where each pixel (10.5 µm) is associated to a local

connected porosity value including clay interlayer spaces, micropores, mesopores and macropores considering the IUPAC classification (Thommes et al., 2015).

NMR measurements

Localized NMR plugs (10 mm x 16 mm) were taken on both sides of the IS blocks corresponding to the layers of interest (Figure 82.a). After a Soxhlet extraction of liquid hydrocarbons by chloroform then isopropanol, followed by drying at 60°C for 3 days, they were analyzed by NMR. The full NMR protocol includes the estimation of total plug volume (V_t, [m^3]) and corresponding dry bulk density (ρ_{NMR}^{bulk} [kg/m^3]), measured by slide gauge and laser. The plugs were then saturated with a synthetic 70 g/L NaCl brine at the pressure of 200 bars for 2 days. NMR acquisitions were performed at 23 MHz, allowing determination of the total volume of brine (V_{NMR}, [m^3]). After NMR acquisition, the plugs were washed with isopropanol and dried at 150°C for 3 days to measure the solid volume (V_s, [m^3]) and associated grain density (ρ^{grain}, [kg/m^3]) by He-pycnometry.

From the ρ_{NMR}^{bulk} and the ρ^{grain}, the total porosity was calculated according to Equation 38, where φ_{NMR}^{T} is the total porosity measured on NMR blocks.

Equation 38.

$$\varphi_{NMR}^{T} = \frac{V_t - V_s}{V_t} = 1 - \frac{\rho_{NMR}^{bulk}}{\rho^{grain}}.$$

Additionally, µtomography-based volume estimation and MIP were used to obtain the dry bulk density ($\rho_{\mu Tomo}^{bulk}$, ρ_{MIP}^{bulk}, respectively) and total porosities. Besides the total porosity (φ_{NMR}^{T}), the connected NMR porosity (φ_{NMR}^{Con}) can be calculated using Equation 39, where m_{sat} – mass of the saturated sample [kg] and ρ^{brine} – density of the brine solution [kg/m^3].

Equation 39.

$$\varphi_{NMR}^{Con} = \frac{V_{NMR}}{V_{NMR} + \frac{m_{sat} - V_{NMR} \times \rho^{brine}}{\rho^{grain}}}.$$

NMR is considered to be the most representative way to obtain both connected and total porosity on the same sample considering that water fulfilling the pores is used as the probe.

Mercury intrusion porosimetry

Intrusion and extrusion curves were obtained using Micromeritics Autopore IV 9500 volumetric set up on localized sub-blocks (Figure 82.c, ~5 x 10 x 15 mm) from atmospheric pressure up to $200 \cdot 10^6$ Pa. All the samples were heated under vacuum at 150°C for at least 36 hours and cooled under vacuum. Cumulative pore throat size distribution, up to the critical pore diameter, is calculated from the intrusion curve based on Washburn's law and a contact angle of 141.3° (Washburn, 1921), assuming a

cylindrical pore shape. The bulk density (ρ_{MIP}^{bulk}) of each sample was also obtained before the first pressure step ($3{\cdot}10^3$ Pa) to calculate the total MIP porosity φ_{MIP}^{T}.with equation 1 and ρ^{grain}. The total intrusion porosity φ_{MIP} is also estimated from the maximum intruded specific volume of mercury ($V_{intr.max}$) [m^3/kg] and ρ_{MIP}^{bulk}, [kg/m^3] using Equation 40.

Equation 40.

$$\varphi_{MIP} = V_{intr.max} \times \rho_{MIP}^{bulk}.$$

All the curves were blank corrected (Sigal, 2009), by removing the impact of mercury compressibility under the high pressure applied.

Nitrogen adsorption

Nitrogen adsorption is a classical method widely used for shale sample characterization, but only applied on crushed powder in the available literature. Adsorption/desorption isotherms were therefore acquired on both crushed powders and non-crushed blocks, for the localized sub-samples of the BS block (Figure 82.c), with a BelSorpMax volumeter device. For these measurements, the samples were dried at 150°C under secondary vacuum. Drying efficiency was evaluated by monitoring the pressure decrease, which took up to 5 days for blocks (~5 x 10 x 15 mm) for reaching an equilibrium. The isotherms were acquired at 77 K with continuous nitrogen Dewar refilling and dead volume correction. The equilibrium kinetics for each relative pressure point were checked by recording the pressure variation in the sample cell versus time to stabilization, with the aim of finding the true equilibration point. Equilibration time per point of up to 1 day at low partial pressures and a total acquisition time of isotherms raising up to 20 days were observed for blocks. Adsorption porosity (φ_{Ads}) was calculated from the maximum adsorbed specific volumes of nitrogen in a liquid state (V_a, [m^3/kg]) at the maximum relative pressure (P/P_0) and ρ_{NMR}^{bulk}, [kg/m^3] (Equation 40).The t-plot approach (Harkins and Jura, 1944) was used to determine the specific volumes of micropores and the associated microporosity using Equation 40 (φ_{Ads}^{μ}). The PSD for mesopores and macropores up to 640 nm (for P/P0 = 0.997) was also achieved by applying the Barrett-Joyner-Halenda (BJH) treatment which implicates the Kelvin equation (Barrett et al., 1951), assuming cylindrical pores. The pore body and pore throat diameter distributions were calculated on adsorption curves (form factor of meniscus of 1), and desorption curves (form factor of meniscus of 2), respectively.

RESULTS

Thermal analysis and bulk mineralogy

Quantitative mineralogy results demonstrate low variation in the bulk mineral composition within the selected cores (Table 14). According to the classification of

Gamero-Diaz et al. (2012), the samples from oil and gas zones are classified as mixed mudstones while samples from the condensate zone exhibit larger variation in mineral composition and can be attributed to mixed carbonates (cores B and C) or carbonate/siliceous mudstones (core D). The clay fraction is similar for all the samples with illite and illite/smectite R3 mixed layer clay minerals and just minor traces of kaolinite for the shale gas samples (data are not shown).

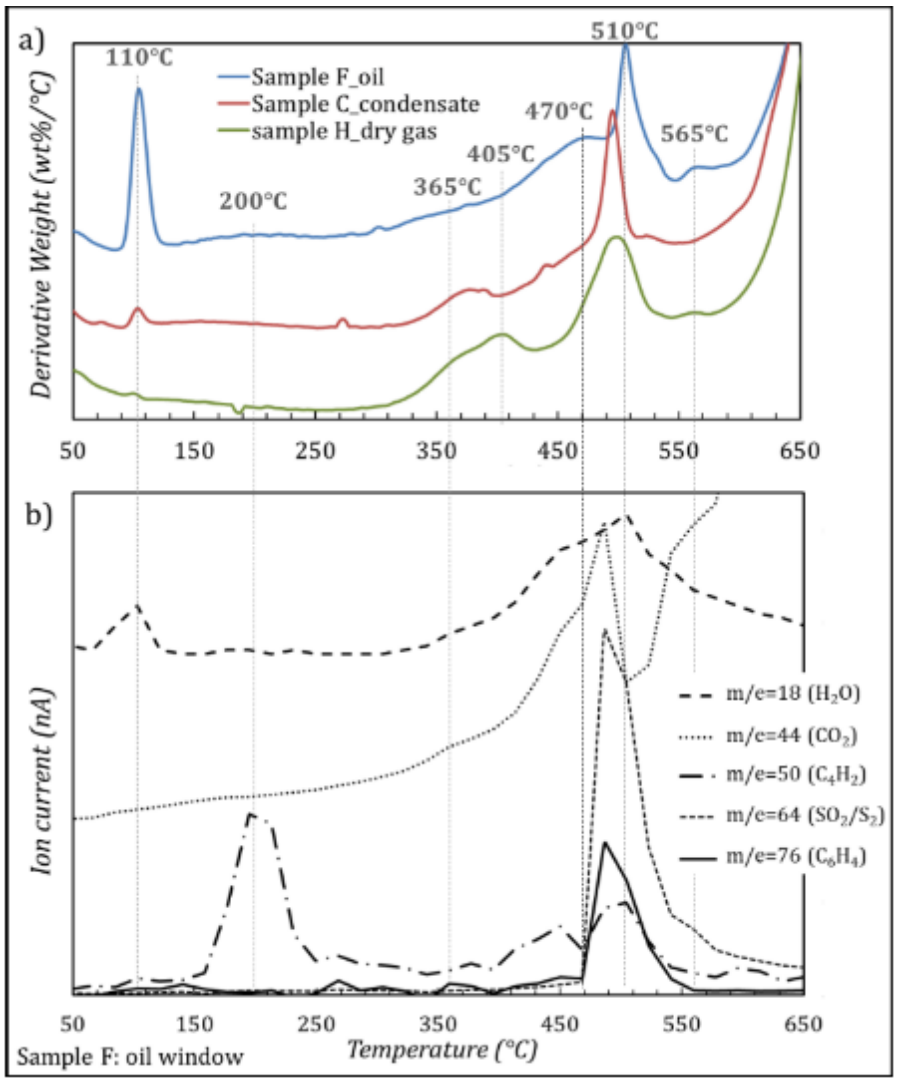

Figure 83. Results of the thermal analysis: a) first derivative of the mass loss for samples from different hydrocarbon production zones; b) mass spectra of some compounds detected under thermal stress for sample F.

Most porosimetry methods require complete removal of residual hydrocarbons and water before measurement to ensure the total access to the pore space. Combining the TGA with mass spectroscopy (MS) analysis, it is possible to evaluate the efficient drying temperature for the samples, at which all the fluids will be removed even from the narrow pores but without damaging the OM. Derivative thermogravimetric (dTG) curves are displayed for one sample from each of the three different hydrocarbon production zones (Figure 83.a). The mass spectra are also given, for the oil zone sample (Figure 83.b), to

illustrate the release of some compounds upon thermal decomposition. Different weight loss steps can be identified from the dTG curves (Figure 83). The first strong weight loss, centered on 100-110°C, is attributed to the outgassing of the free water in the pore space, which spreads up to 250°C with very low associated weight loss (Figure 83.a). The highest weight loss here is attributed to the sample from oil zone. The water release from the sample can be tracked by masses of 18 and 17 (H_2O and OH^- respectively). Another type of fluid release expected under thermal stress is hydrocarbons. While natural dry gas is highly volatile (not expected to be detected), the emission of oil compounds is detected at a temperature centered on 200°C (and up to 250°C) with the general formula C_xH_y on the mass spectra. The onset of the solid OM decomposition was identified in the range of 280-300°C. The second strong mass loss at the 350-550°C range is associated with solid OM (with emission of CO_2 and some C_xH_y/C_xH_yOH compounds) and pyrite (with sulfur compounds emitted) decomposition (Figure 83.b). Over these different weight losses and our previous experience, the temperature chosen for the sample outgassing to ensure the removal of free liquids can be reduced under vacuum down to 150°C without affecting the solid OM.

Autoradiography porosity mapping

Autoradiography porosity maps are displayed in Figure 84, with one map per production zone, revealing the connected porosity distribution over the full height (~6 cm) of the studied cores. The chosen color scale for encoding the porosity maps is 0-40%, on the basis of the spread of values detected on porosity frequency histograms (Figure 85). The overall map color evolves from red down to blue through white following the ranking oil, condensate to dry gas zone, revealing a decrease of porosity with OM maturity. For the oil zone samples, dense crack network is also well expressed parallel to the bedding of the sample, due to a drying artefact induced by poor core preservation. The local porosity measured for one pixel (10.5 by 10.5 µm) at the location of cracks is a function of their aperture. The thinner the fissure, the lower the pixel porosity (i.e., closer to the porosity of the surrounding matrix). According to the chosen color encoding of sample porosity between 0 and 40%, most of the fissures appear in red (porosity larger than 40%) or in white (porosity around 35-40%). For the condensate zone, sample D displays a "salt and pepper" texture with the presence of non-porous small grains (in dark blue). More heterogeneous samples are also observed, as for the gas zone sample I with the presence of large non-porous calcite "beef" in dark blue (at the mid height of core I) and laminae of various mineral composition and porosity, especially just above the "beef". Sample F (oil window) also exhibits laminae of varying porosity (i.e., alternation of white and dark blue in between the red cracks).

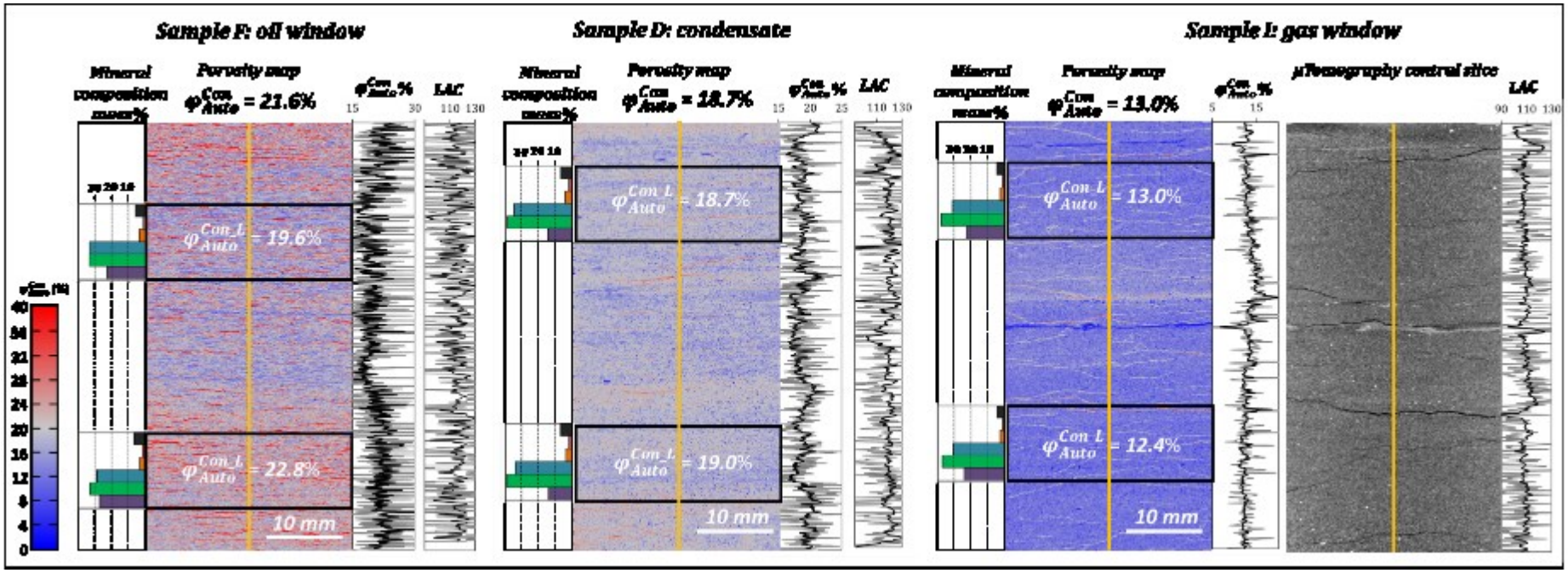

Figure 84. Porosity maps obtained by autoradiography for three core samples with, on their right, a vertical porosity profile through the center of the image (yellow line) obtained by autoradiography (in light gray, profile with 1-pixel width and in black – profile with 500-pixel width) and a LAC vertical profile through the center of the corresponding slice (yellow line) from µtomography 3D volume (in gray – with 1-pixel width and in black – profile with 300-pixel width); Quantitative mineralogical compositions are indicated for the layers of interest (purple – clay minerals, green – tectosilicates; blue – carbonates, orange – pyrite, red – accessory minerals, black – IOM).

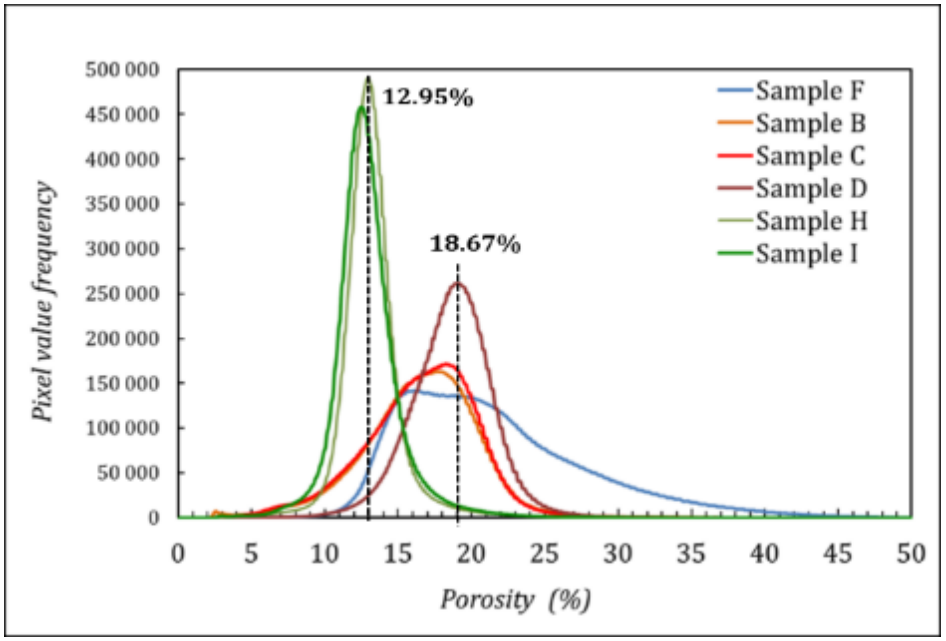

Figure 85. Pixel frequency histograms over the full autoradiography porosity maps.

From the autoradiography porosity maps (Figure 84), several quantitative types of information can be extracted, such as the total connected porosity of the entire core (i.e. over whole surface area, φ_{Auto}^{Con}), localized porosity of the layers of interest ($\varphi_{Auto}^{Con\_L}$), identified as black rectangles on the porosity maps, for which all other bulk techniques were applied on the localized sub-block (BS block, Figure 82.c). The total connected porosity values (φ_{Auto}^{Con}) measured from the whole surface areas (~ 25 cm^2) are 21.6, 18.7 and 13% for the oil, condensate and gas samples, respectively (Figure 84). Porosity values for the other samples from the condensate zone are lower than that of sample D (Table 15). Moreover, from the previous observations of color variations over the height of the samples, total connected porosities were measured for layers of interest. For samples D and I, the porosity values determined on both layers of interest are very similar (18.7-19% and 13.0-12.4% from top-to-bottom layers, respectively), representing the averaged porosity of the entire autoradiography surface (φ_{Auto}^{Con}= 18.7% and 13.0%, respectively). The mineral compositions measured for top and bottom layers of interest are also very similar for both samples. On the contrary, sample F (oil zone) exhibits a top layer of interest with a porosity at 19.6% while the bottom layer displays a higher porosity, at 22.8 mass%. The measured clay content of the bottom layer is 27 mass% compared to 23 mass% for the top layer, suggesting that there is a correlation between total porosity and clay content. Vertical profiles along the core axis (yellow line, Figure 84) and frequency histograms of porosity (whole surface, Figure 85) were also computed to highlight spatial heterogeneities. The quantitative vertical porosity profile, plotted from the autoradiography porosity map, reveals laminae and layers with contrasted porosity values, demonstrating the porosity evolution over the height of the sample. Thick laminae

are detected for sample F (oil zone) on the porosity profile and the part of the sample with the largest porosity is associated with the highest crack density. Indeed, these cracks correspond to high porosity peaks on the thin profile (light grey) regardless to the averaged profile (black) that reflect the matrix porosity. Although the top and bottom layers of interest of the samples D and I have similar porosity and mineral contents, samples D and I present laminae with high and low spatial frequency, respectively. Varying the vertical position over just a few millimeters on sample D implies a large porosity change whereas a smooth increase in porosity is evidenced at the middle of sample I, just above the "beef". Such a vertical porosity evolution is not detected by µtomography at the core scale as the contrast is weaker. Indeed, none of the vertical *LAC* profile (calculated on the virtual slice corresponding to the autoradiograph surface) reveals these porosity changes (Figure 84). Only poor detection of the widest crack observed on the autoradiograph of sample I was possible, but no lamination was observed. A slight *LAC* increase was detected at one third of the height of the core I, but not correlated to a porosity decrease on the autoradiograph (i.e. probably associated with increased carbonate content). The non-porous carbonate "beef" at the mid height of sample I was however well detected by µtomography.

Such porosity evolution is also evinced by the frequency histogram of porosity measured over the whole surfaces. Some samples display a unimodal Gaussian-shaped histogram, while others have asymmetric distribution (Figure 85), such as for samples from condensate zone (cores B and C), with porosity ranging from 15 to 19%. The porosity distribution (Figure 85) for samples from dry gas zone (cores I and H) is unimodal with a narrow peak at around 12.5-13% porosity, demonstrating a larger homogeneity within the sample when excluding local variation associated with large cracks or thick carbonate layers. For the sample from the oil zone (sample E was not analyzed), the porosity has a clear bimodal frequency histogram associated with two types of laminae (Sample F in Figure 85) with an additional large porosity trend corresponding to cracks with varying apertures.

The autoradiography 2D porosity maps, from which the spatial distribution of the porosity over the core length (~6 cm) was evaluated, demonstrate that porosity may vary strongly even over millimeter scale without lamination. Figure 86 illustrates the example of sample B (condensate zone), where the porosity measured from the overall surface (φ_{Auto}^{Con}) is 16.5%. The quantitative vertical porosity profile does not reveal the presence of laminae with strongly contrasted porosities but only slight variations from top to bottom, i.e., 17.1 to 15.96% in the layers of interest (Table 15). However, a sub-area containing large non-porous grains displays a lower porosity value (13.4%) compared to that of a relatively homogeneous area (17.3%). The difference of measured porosity on sub-areas with sizes corresponding to the cross section of blocks analyzed by the different

bulk methods (red rectangle: 5 x 5 mm and blue rectangle: 10 x 10 mm in Figure 86), can reach 4 to 5% within the same homogeneous core. In sample B, the porosity is decreasing down to 12.6% for a 5 x 5 mm area including a non-porous grain (Figure 86).

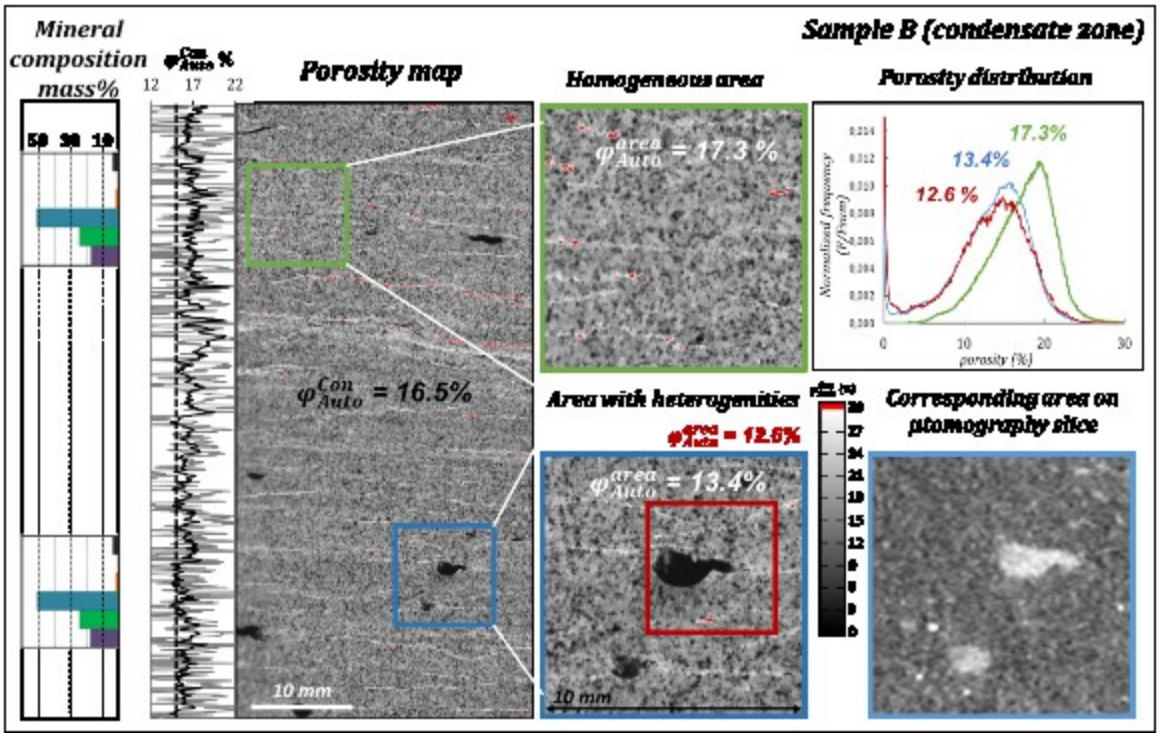

Figure 86. Autoradiography porosity map and frequency histograms of the IS block of sample B (condensate zone) and localized sub areas. Porosity profiles obtained through the center of the autoradiography image are plotted on the left (in light gray - profile with 1-pixel width and in black – profile with 500-pixel width); quantitative mineralogical compositions are indicated for the layers of interest (purple – clay minerals, green – tectosilicates; blue – carbonates, orange – pyrite, red – accessory minerals, black – IOM); the corresponding area of the blue rectangle, extracted from the µtomography slice, is shown on the bottom right corner.

The porosity frequency histograms of these sub areas exhibit slight shifts of the main mode which represents the local mean porosity of the matrix, explaining the asymmetric frequency histogram of the total surface area of the core (Figure 85). However, the large changes of mean porosity among these different sub-areas are mainly due to the relative intensity of the mode centered on a porosity of 0% which is associated with these non-porous millimetric non-clay grains. These grains are also visible on the corresponding slice of the µtomography volume with worse spatial resolution and contrast (Figure 86). As *LAC* values observed by µtomography are similar for tectosilicates and clay matrix but drastically larger for carbonates, such big non-clay grains greatly impacting the porosity estimations.

Bulk porosity and PSD measurements on localized blocks

Figure 87.a displays the connected porosity values measured by NMR versus the total porosity values estimated by laser on the same localized sub-samples (Figure 82.a).

A perfect positive correlation for the connected porosity measured by NMR with the total porosity was detected, indicating that all the pores probed by these techniques are interconnected. Considering the saturation process, the high penetration ability of the NaCl solution under high pressure, and the fact that the water in the pore space is used as the probe, NMR measurements are expected to provide an analysis of the full pore volume. The total porosity values decrease from 20-23% for the oil zone samples down to 11-12% for gas zone samples, through 15-19% for the condensate zone.

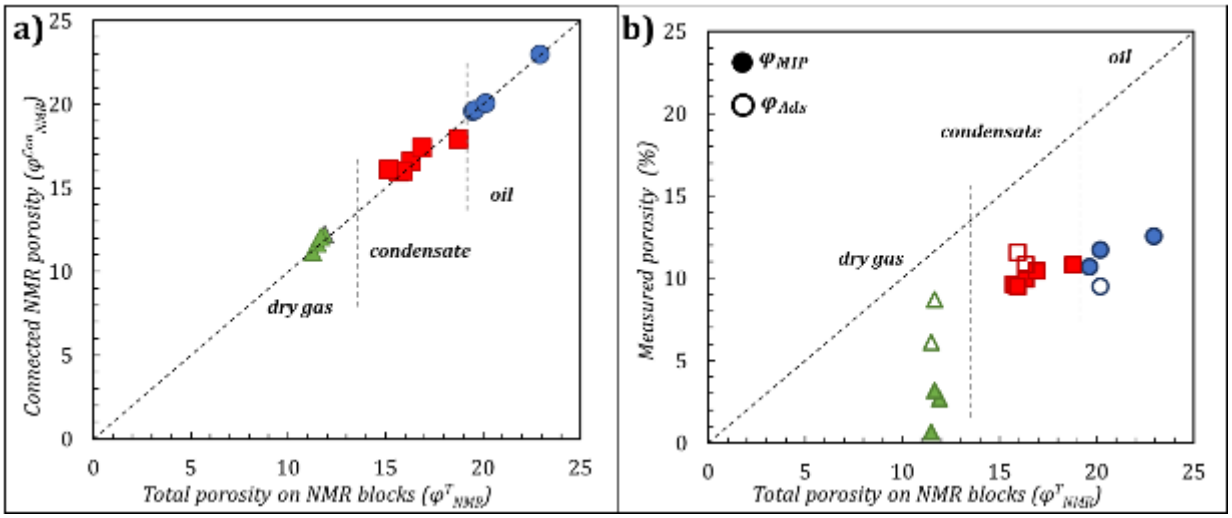

Figure 87. a) Connected porosity values measured by NMR using Equation 30 versus the total porosity, according to the Equation 38, estimated on the same blocks; b) porosity values obtained by MIP (closed symbols, φ_{MIP}) and gas adsorption (open symbols, φ_{Ads}), measured on the localized sub-blocks; triangles are for gas zone samples, squares - for condensate zone, circles - for oil zone.

Characteristic MIP intrusion/extrusion curves are presented in Figure 88.a for samples from each hydrocarbon maturity zone (oil, condensate, dry gas). The cumulative intrusion curves are similar for samples from the same zone (data not shown) and only absolute values of total intrusion volumes and associated φ_{MIP} are slightly different (Table 15 and Figure 88). Samples from condensate and dry gas zones present similar curves, with significantly lower amounts of intruded mercury for dry gas samples (Figure 88.a). Different curves are obtained for the oil zone samples, for which additional large pore throats, between 1 and 100 µm, were detected. This range of pore throats (1-100 µm) corresponds to cracks as detected by 3D X-ray µtomography (data not shown) and the autoradiography porosity maps (Figure 84). The difference is highlighted on the incremental curves (Figure 88.b), with a unimodal distribution of pores throats with mode around 7 and 15 nm for samples from dry gas and condensate zones, respectively, but with a bi-modal distribution with modes around 20 and 30,000 nm for the oil zone. For all the samples, most of the detected pore throats (without considering the cracks of the oil zone samples), were less than 30 nm in diameter and the mode around 7-20 nm was truncated on the left side of the distribution. This indicates the occurrence of throats

smaller than 7 nm. MIP intrusion curves show how throat size changes according to burial depth/OM maturation and can be ranked with decreasing size from oil to gas zones. The large amount of trapped mercury upon extrusion revealed by the mismatch of extrusion and intrusion curves points out that pore bodies are drastically larger than the measured pore throats (Figure 88.a). The MIP intrusion porosities (φ_{MIP}), calculated with the MIP bulk density (ρ_{MIP}^{bulk}) and the maximum intruded mercury volume, are also systematically lower than the porosity values obtained by NMR (Figure 87.b and Figure 88.a). The normalized pore throat size distribution (dividing the intruded porosity at each pressure by total NMR porosity; φ_{NMR}^{T}, Figure 88.b) shows that MIP probes only a small part of the pore volume. These discrepancies are related to the fact that mercury does not invade all the pores in shales, underestimating the total pore volume. Much of the pore throats are smaller in diameter than the percolation threshold (7 nm in this study) and not accounted for in the distribution. In Figure 88.b, the y-axis corresponds to the proportion of the pore space which is invaded. At the maximum pressure associated with the smallest throats invaded by mercury, only 20% of the pore space for dry gas zone samples and 60% for oil/condensate zone samples is probed. The volume of pores not probed by MIP (80%) is particularly high for the dry gas samples with the smallest throat size distribution detected, indicating that 80% of the pore space is connected by throats smaller than 7 nm. MIP probing such a low portion of the pore space for the gas zone is in line with the drastic underestimation of φ_{MIP} with respect to φ_{NMR}^{T} (Figure 87.b; Figure 88.a).

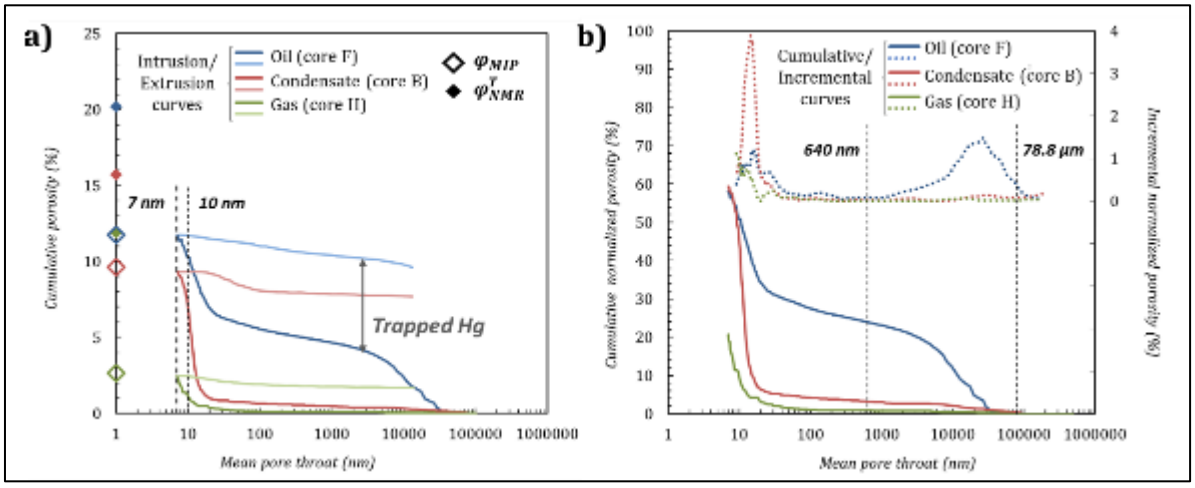

Figure 88. a) Cumulative intrusion and extrusion curves from different hydrocarbon maturity zones and porosity values measured by MIP (open symbols) and total porosity measured on NMR blocks (closed symbols), given for the samples from the same layers of interest; b) Normalized MIP cumulative intrusion curves (normalized according to the total porosity on NMR blocks) and incremental throat size distributions. Black dotted lines are for the different techniques' resolutions; blue lines and symbols are for the oil zone sample; red lines and symbols are for the condensate zone sample; and green lines and symbols are for the gas zone sample.

Nitrogen gas adsorption was performed to characterize the micropore (not accessible by MIP), mesopore and macropore size distribution up to 640 nm in diameter. Adsorption/desorption isotherms were acquired on powder and blocks for homogeneous sub-samples from the condensate zone (sample C) located in the same layer of interest (Figure 89.a). Type IV isotherms were obtained with a type H3 hysteresis loop for powders corresponding to complex slit or wedge shaped pores but with a type H2 hysteresis for blocks (Sing, 1998; Thommes et al., 2015). Such a hysteresis loop for the undamaged blocks indicates that pore's clogging and cavitation phenomena occur at P/P_0 of 0.42 upon desorption because of the occurrence of throats connecting the pore network with sizes drastically smaller than the pore bodies (smaller than 5 nm when cavitation occurs). Nitrogen adsorption curves also show an overestimation of specific gas volume adsorbed (V_a) on the powder sample at high relative pressure close to P/P_0=1, indicating the presence of larger amounts of macropores, created when crushing the sample (Figure 89.a). The cumulative PSD, obtained by the BJH treatment on the adsorption branch, confirmed that a significant additional amount of macropores larger than 100 nm were created in the powder but with cumulative PSD similar to the blocks values (i.e. parallel) for the smaller pores (Figure 89.b). The BJH method applied on the desorption curves to provide throat size distribution displays even larger differences between powder and block acquisitions. For block samples, the BJH distribution curves present different PSD between adsorption and desorption, while for powders the PSD of both adsorption and desorption are similar and well in line with an unrealistic wedge-shaped pore geometry. Pore throats are therefore drastically impacted by crushing and the true throat size distribution obtained on blocks is drastically narrower, indicating that most of the throat sizes are below 10 nm. The throat size distribution obtained on blocks is also in better agreement with MIP values (Figure 88.a). For sample C, the porosity of the powder calculated with the maximum adsorbed volume (φ_{Ads}; Equation 40) is significantly higher (13.6%) than the block value (11.6%), both being lower than the total porosity measured by NMR for the same layer of interest on blocks (φ_{NMR}^{T}=15.9%; Table 15). Some other nitrogen adsorption isotherm tests realized on powders gave completely unrealistic φ_{Ads} values, larger than φ_{NMR}^{T}, indicating that varying large amounts of macropores were created upon crushing (data not shown).

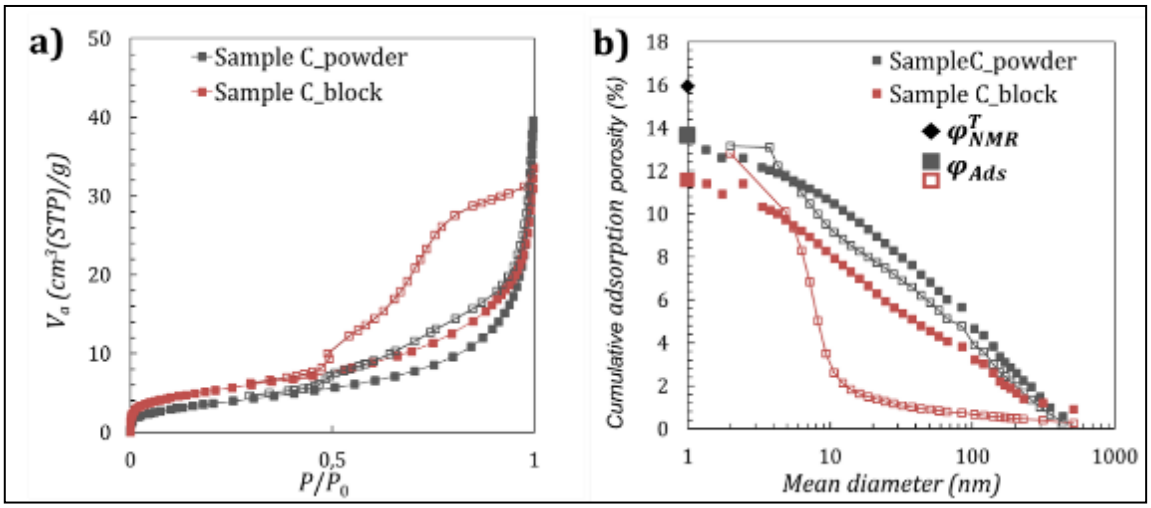

Figure 89. a) Nitrogen gas adsorption/desorption curves, obtained for the block (red symbols) and powder (gray symbols) from the core sample C (condensate zone); b) BJH cumulative distributions calculated for the block and powder (open symbols are for the pore throat sizes distribution, closed symbols – for the pore body sizes distribution). The reference total porosity value, obtained on NMR blocks for the corresponding layer, is marked with a diamond symbol.

In the present study, nitrogen adsorption isotherms were successfully acquired only on a set of five undamaged blocks as acquisition is really time consuming (Table 15). Isotherms obtained on samples from the different hydrocarbon maturity zones are presented on Figure 90. All of them can be described by type IV with a type H2 hysteresis loop (Sing, 1998), indicating the occurrence of mesopores, even for the gas zone sample (sample I). H2b hysteresis (Sing, 1998; Thommes et al., 2015) is associated with the occurrence of pore-blocking phenomena associated with throats smaller than pore bodies. The intense bump around P/P_0 of 0.42 on desorption branches reflects classical cavitation phenomena for pore throats smaller than 5 nm according to the Kelvin law. For these smallest throats, no size estimation is further possible, but the intensity of the bump is proportional to their content. The large increase of the adsorbed volume at the maximum relative pressure without any plateau indicates that additional and really large macropores are not accounted for by this technique. The isotherms acquired on different blocks from the condensate zone (sample B) and dry gas zone (sample H) were very similar to those presented in Figure 90 for samples from the same zones, with only slight variation in the total amounts of adsorbed gas (φ_{Ads}; Table 15).

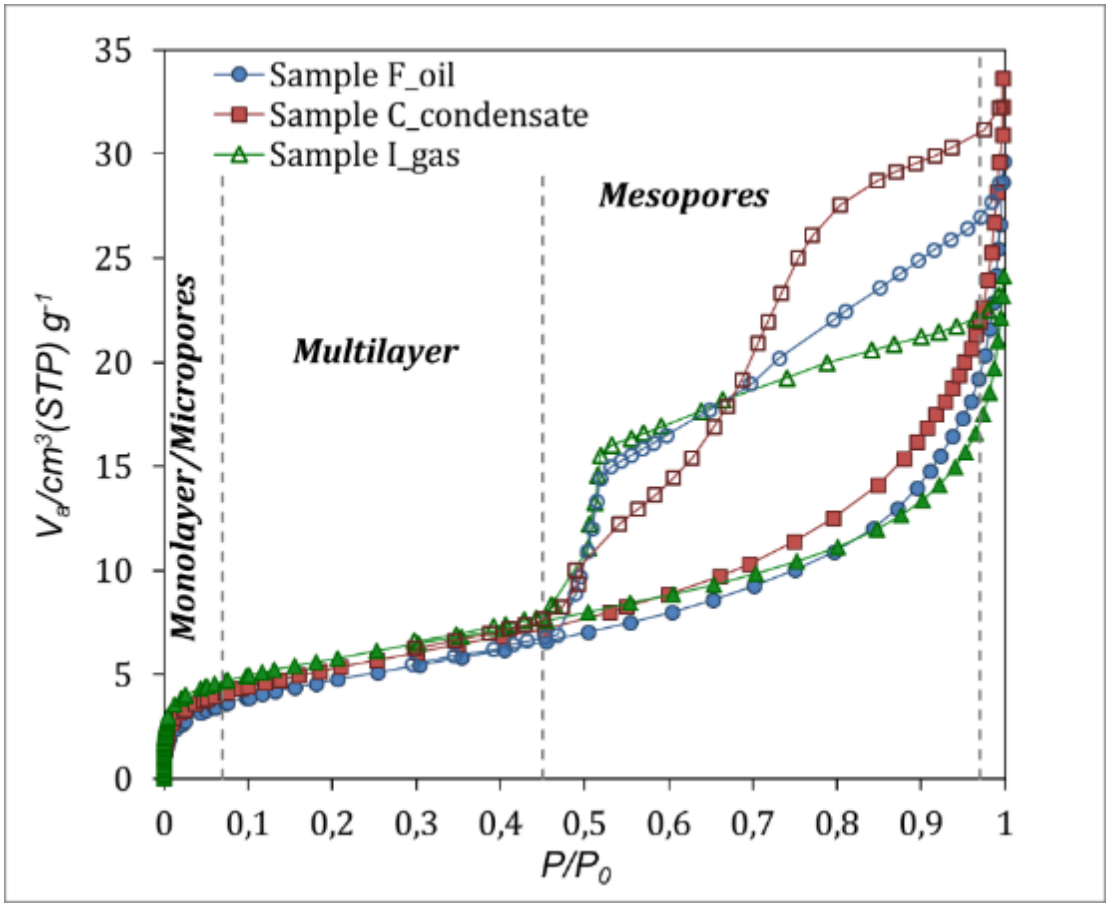

Figure 90. Nitrogen adsorption/desorption isotherms obtained on the different localized sub-samples: for oil (circles), condensate (squares) and dry gas (triangles) zones.

The porosity values measured from nitrogen adsorption (φ_{Ads}) range from 6.1-8.7% to 9.5% for gas to oil zone samples, through 10.8-11.6% for condensate zone (Table 15). These values are underestimated in comparison to total porosity measured by NMR on blocks (φ^{T}_{NMR}, Figure 87.b), as the pore size range probed includes the micropores but does not account for the largest pores (>640 nm) according to the Kelvin radius associated with the maximum P/P_0. This is especially the case for sample F from the oil zone, within which large cracks with aperture centered on 80 µm were detected by MIP, autoradiography and µtomography (Figure 84; Figure 88). The application of t-plot method also revealed a small amount of micropores but only for samples from the dry gas zone, where the microporosity (φ^{μ}_{Ads}) was measured in the 0.3-0.6% range. Volumes of the micropores represent 5.6 and 2.7% of the total probed volume of pores for cores H and I, respectively. The cumulative PSD obtained by the BJH treatment on adsorption branch shows that pore sizes are always broadly spread, with a log distribution through the mesopore and macropore range (Figure 91.a). The porosity values reached on the cumulative PSD, according the OM maturity, are significantly lower than the φ^{T}_{NMR} values. The very small contribution of the additional microporosity for the dry gas zone does not explain such a large mismatch. Only unprobed macropores larger than 640 nm (larger for

samples from the oil zone with large cracks) may be responsible for such large discrepancies. No clear evolution of PSD regardless of OM maturity or burial depth is observed. This is probably due to the varying contribution of the unprobed pores >640nm, which amount is the largest for the damaged oil window sample. The throat size distributions obtained by the BJH treatment of block desorption isotherms do not reflect a clear evolution with OM maturity either (not shown). Adding to these cumulative curves the throat size distribution obtained by MIP for the throats larger than 640 nm shows a clear shift in throat sizes towards lower values with burial (Figure 91.b).

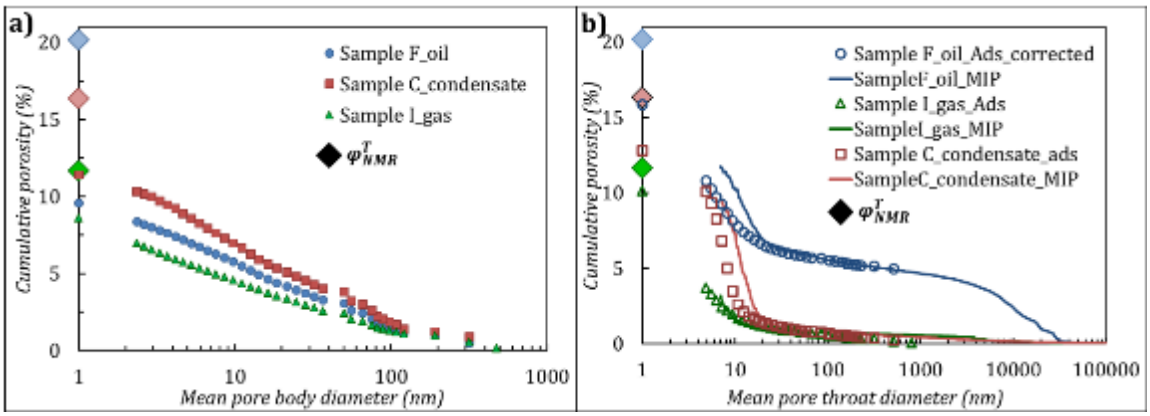

Figure 91. Cumulative pore size distribution with indication of total porosity measured by laser on NMR blocks (diamond symbol) for the corresponding layer of interest: a) pore body diameter distribution, calculated from the nitrogen adsorption curves (triangles are for gas zone samples, squares for condensate zone, circles for oil zone); b) pore throat diameter distribution calculated from the nitrogen desorption curves (open symbols; data for sample F are corrected by combination with results of MIP porosity >640 nm) and from MIP intrusion curves (lines).

DISCUSSION

Optimization of experimental parameters for bulk method coupling

Many experimental parameters in the acquisition pathway could induce bias in the characterization of the pore network in organic-rich shales. TGA (Figure 83) results have shown the temperature range to consider for ensuring total removal of water and oil without affecting the solid OM. A temperature up to 250°C (or 150°C under vacuum) is necessary to outgas the water and the residual oil from Vaca Muerta samples. This temperature allows complete removal of the physisorbed and capillary-bound liquid without applying any chemical treatment to extract liquid hydrocarbons. In the literature, depending on the field of expertise of the laboratory, authors use either low temperatures in 60-110°C range (Janssen et al., 2011; Chalmers et al., 2012b; Clarkson et al., 2012 ; Houben et al., 2016a; among many others) or higher up to 200°C (Kuila et al., 2014; Topór et al., 2016) for drying the sample before application of bulk techniques. When coupling different bulk methods on the basis of standard protocols, the drying conditions could also vary among the different techniques applied in a single study. Varying drying conditions impact the results, especially for the measurement of densities (bulk and

grain) and the gas adsorption isotherms. Here, applying a drying at 150°C under vacuum and removing the liquid hydrocarbons by solvent cleaning provides similar grain densities by He-pycnometry whereas classical drying at 105°C induces biased values (not shown). While free liquids can be easily removed from the pore space at low temperature, the presence of narrow throats, described for shale samples (see reviews of Nelson, 2009 or Loucks et al., 2012), induces a large amount of capillary-bound liquids (both hydrocarbons and water), which are released at higher temperature than free liquids (Lewis et al., 2013). A bias in the pore volume that remains accessible upon gas adsorption or mercury intrusion is induced.

According to the available information, all the data of gas adsorption on shale samples available in the literature were obtained by short isotherm recording (never longer than 50 hours) on powders. In the present study, measurements done on carefully localized sub-samples within the homogeneous core of sample C (Figure 89) for undamaged block and crushed powder differ significantly. The H2 hysteresis loop observed for blocks of Vaca Muerta samples demonstrates that the pore network is composed of pores with body sizes drastically larger than the throat sizes. This is highlighted by the pore and throat size distributions obtained (Figure 91) and is in agreement with the large amount of mercury trapped upon extrusion for MIP experiments (Figure 88.a). A satisfying matching of the MIP and adsorption throat size distributions was obtained when both measurements were made on blocks (Figure 91.b). On the contrary, powder isotherms exhibit H3 hysteresis associated with wedge-shaped pores with resulting similar size distributions for throats and pore bodies, which are unrealistic. This is in agreement with literature data for gas adsorption on shales. For example, when both adsorption and desorption curves were provided (Tian et al., 2013; Kuila et al., 2014) very weak hysteresis loops (type H3) were also observed on powder isotherms. Crushing damages rock organization, by modifying the particle contacts controlling the throat size distribution, and additional large macropores are induced. Such a modification of the PSD detected for powder explains the overestimation of total porosity measured by gas adsorption (φ_{Ads}) that could be linked to the overestimated values in the literature (Figure 81). Literature φ_{Ads} values obtained by nitrogen adsorption/desorption isotherms on crushed samples are therefore not reliable and should be discarded. For relevant measurements, nitrogen adsorption/desorption isotherms have to be acquired on undamaged rock samples.

Nevertheless, in the present study, a slight shift is observed in between the throat size distribution obtained by MIP and nitrogen adsorption (Figure 91.b). Adjusting the contact angle used in the Washburn law for MIP does not successfully reduce the mismatch between the two distributions. One may argue that the high pressure used during mercury injection could damage the organization but BJH method is known to

significantly underestimate the pore diameters because it does not account for the local structure and the modified thermodynamics of fluids confined in narrow mesopores (Ravikovitch and Neimark, 2001).

Representativity of the samples analyzed regardless of spatial heterogeneities

The multi-technique approach applied in this study, where imaging techniques (µtomography and autoradiography) are coupled with classical bulk measurements, was proposed to tackle problems of spatial heterogeneity and representativeness in order to provide quantitative pore balances and PSD.

In the literature, the representativeness of shale samples probed for porosity analysis is only discussed in the context of imaging techniques by estimating representative elementary surfaces or volumes. The field of view never exceeds the mm-µm scale, while the larger sample size for bulk techniques (mm-cm scale) is generally assumed to be representative and results of bulk methods are often used in addition to imaging techniques to validate the measurements (Chalmers et al., 2012a, Houben et al., 2016a, etc.).

In the present study, the 2D autoradiograph porosity maps and the 3D *LAC* imaging by µtomography allowed to highlight in pluri-centimetric areas and volumes (i.e. at the core scale), spatial heterogeneities occurring at the µm scale. The coupling of µtomography with autoradiography is thus a powerful tool (i) to visualize the full core, (ii) to discard the heterogeneities impacting porosity analysis (i.e. "beef", carbonate nodules and laminae), (iii) to localize regions of interest for bulk measurement previous to sub-samplings and (iv) to provide a quantitative spatial distribution of total porosity. Autoradiography provides maps of the connected porosity variations depending on the spatial distribution of porous and non-porous material with no direct information about mineral composition/distribution. On the other hand, *LAC*, mapped by X-ray µtomography, reflects variations in both porosity and mineral phases. Some highly absorbing minerals, such as carbonates and pyrite, are resolved but tectosilicates are not detected. This property helps distinguish low porosity non-clay grains in 3D but with worse contrast and resolution than with 2D autoradiographs. For sample I, the minimum porosity values ($\sim 0 - 5\%$) are for example obtained in the layer associated with non-porous calcite veins ("beef"), where the increase of linear attenuation coefficient is measured. Very local carbonate nodules are also well detected for sample B whereas autoradiographs demonstrate that they are non-porous and deeply impact porosity measurements on small blocks. The use of the nondestructive 3D imaging by µtomography is thus recommended to discard such objects from sub-samples analyzed later by bulk methods. 2D autoradiography provides better laminae contrast with various porosities than 3D µtomography but is also more sensitive for detecting the crack network. Also, the sub-blocks, investigated by bulk measurements, can be projected on

the autoradiography surface, with the aim of evaluating their porosity ($\varphi_{Auto}^{Con\_B}$), such a spatial comparison is possible due to lateral homogeneity of the layers of interest over the core.

The absolute values of total porosity obtained by different techniques are comparable, indicating the robustness of each method when efficient drying conditions are applied. Autoradiography, which was applied for the first time on organic-rich shale, gives accurate values in agreement with the other techniques. The total porosity measured on NMR blocks for the selected layers of interest (Table 15), where both connected porosity, grain and bulk densities were obtained on the same blocks, is considered as the reference value.

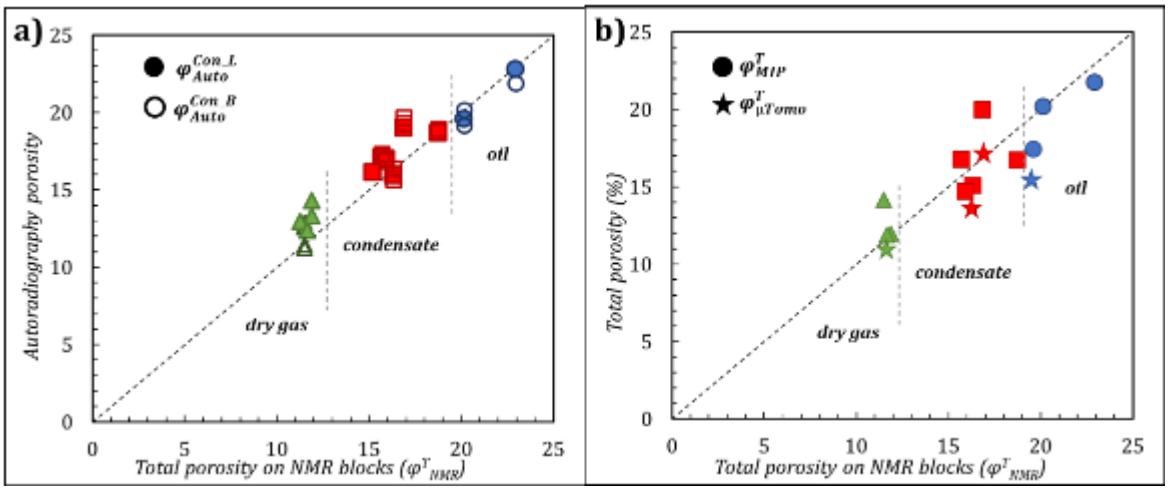

Figure 92. a) Quantitative porosity measurements from the autoradiography surface on the localized layers of interest (closed symbols) and on projections of blocks on the autoradiography surface (open symbols), where other bulk techniques were applied: triangles are for gas zone samples, squares - for condensate zone, circles - for oil zone; b) total porosity on MIP blocks and total µtomography porosity on the same blocks, calculated from the measured dry bulk densities and the grain density measured on NMR blocks: stars.

The total NMR porosities were compared to the total porosity values obtained by autoradiography for the layers of interest on a surface area corresponding to the same thickness, but with the width of the full core ($\varphi_{Auto}^{Con\_L}$, Table 15). The porosities obtained from the autoradiography porosity maps are equivalent to the total porosity obtained on NMR blocks (Figure 92.a; Figure 93). The correlation of the porosity values extracted from the projections of the small blocks of bulk measurements on the autoradiography surface (Figure 82.e) also demonstrates good agreement with total NMR porosity for the same layers of interest (Figure 92.a). Note that the scattering of the points around the linear trend is similar for the projected 5 mm wide blocks and the full layer. The measurement of porosity on 5 mm wide areas or blocks is thus representative for laminae that are homogeneous laterally along the sedimentary plane and when excluding areas with large non-porous carbonate nodules.

As previously described, the bulk volume of the sample, required to calculate the total porosity (Equation 38), can be measured by various techniques. The measurements performed either by laser on the NMR blocks or on MIP blocks by immersion in mercury, into homogeneous layers of interest, gave consistent values of bulk density and associated total porosity (Figure 92.b). The statistical error of bulk density values below ± 0.05 g/cm^3 induces variation in total porosity up to 3%, which is revealed by larger scattering of values around the mean trend in comparison to previous NMR and autoradiograph correlations (Table 15; Figure 92). Some blocks were scanned with µtomography before the MIP measurements, with the aim of defining the bulk volumes of the dry samples. The total porosity values calculated with bulk densities, obtained by these two different methods, demonstrate nearly perfect superimposition and no reduced statistical error by the imaging approach (Figure 92.b). Both values are impacted by the grain density measured on NMR blocks several centimeters away in the same laminae (Figure 82.e), indicating that slight lateral variations of mineral composition and OM content exist within a layer and impact the grain and bulk densities as well as the calculated porosity. When a bulk density value measured a few centimeters away is used for converting adsorbed or intruded volumes of liquid into porosity values (as done for gas adsorption), similar slight errors are expected. Thus, the size of all the blocks analyzed are large enough to be representative and to be compared, when selected in homogeneous laminae discarding big carbonates nodules and grains by imaging techniques.

Quantitative pore balance and PSD

The main objective of the present study was to achieve a quantitative pore balance of the studied Vaca Muerta shale samples using an integrated methodology from the 3D localization of the sampling to the imaging of the spatial distribution of total porosity, through the acquisition and inter-comparison of different bulk measurements realized in localized homogeneous areas of interest. Localizing similar sub-samples on homogeneous areas and jeopardizing "beefs" or carbonate nodules was crucial for the quantitative coupling of bulk techniques. The use of appropriate drying conditions and measurements done on well-preserved blocks, including for gas adsorption isotherms, are also essential to reach accurate pore balances. Nevertheless, the reliability of the measured PSD is a function of the detection limits of the methods used, which are controlled by the physical properties of the fluid involved, not only the molecule size of the probing fluid.

Mercury intrusion curves provide information only about the pore throat distribution in the ~0.007 – 100 µm range, while gas adsorption can distinguish both pore body and pore throat distributions but covering pore sizes from micropores up to macropores with a 0.64 µm diameter. As a result, measurements done by MIP and nitrogen adsorption both underestimate the total porosity. For mercury intrusion, the strongest underestimation is for samples from the dry gas zone (only 20% of total

porosity was probed for samples H and I), indicating that pore throat size distribution is dominated by throats lower than 7 nm in diameter. For nitrogen adsorption, the strongest underestimation was for samples from the oil zone (only 47% of total porosity probed for samples E and F), due to the largest number of thick cracks. Isotherm shapes at large partial pressure moreover indicate that unprobed macropores larger than 640 nm always occurred and were missing on the provided PSD. As a result, the total porosity measured by gas adsorption was always lower than the total ones measured by NMR (Figure 87.b). Moreover, from the cavitation phenomenon observed on the desorption isotherms throat size distribution cannot be estimated for sizes lower than 5 nm, whereas pore sizes including micropores are analyzed on adsorption branches. Nevertheless, the combination of the throat size distributions provided by MIP and gas adsorption is successfully proven (Figure 91.b).

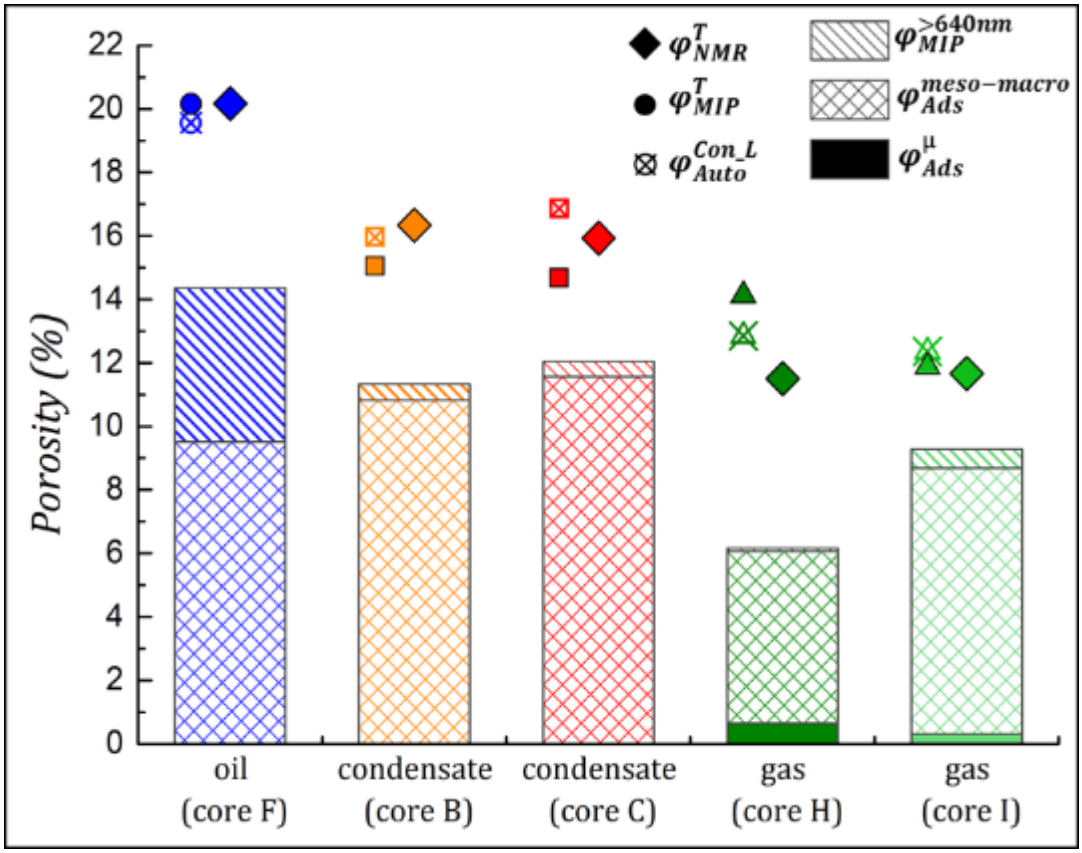

Figure 93. Porosity balances based on the combination of bulk measurements: φ^{T}_{NMR}– total porosity on NMR blocks, φ^{T}_{MIP}–total porosity on MIP blocks, φ^{Con}_{Auto}– autoradiography connected porosity for localized layers, $\varphi^{>640nm}_{MIP}$– results of the porosity, corresponding to the MIP volumes intruded into the pores with pore throat >640 nm, $\varphi^{meso-macro}_{Ads}$ – measured adsorption porosity > 2 µm, φ^{μ}_{Ads}- microporosity < 2 µm, revealed by gas adsorption.

A first attempt to combine the different porosity measurement results was made to achieve quantitative porosity balances (Figure 93). This pore balance demonstrates that the methodology proposed in this study can achieve comparable total porosity values

provided by autoradiograph, NMR and MIP (by using the bulk density). Some of the keys to achieving pore balance are sample selection, visualization of the region of interest, sample preparation, and accurate measurement on well preserved samples. The cumulative volume contents of micropores and mesopores plus macropores (< 640 nm) provided by gas adsorption on blocks do not match the total porosity for the entire sample. Microporosity represents a minor part of the network when they are detected for the samples from the gas zone. As large cracks are detected by MIP and assuming that throats are similar to body sizes for cracks and slit shaped pores, the porosity corresponding to the intruded volume of mercury for throats larger than 640 nm was added to the previous contributions. This additional porosity value may account for the crack porosity unanalyzed by gas adsorption. The crack porosity is negligible except for samples from the oil zone. The unprobed amount of large macropores >640 nm corresponding to the remaining gap to reach the total porosity values is then almost constant for all the samples. This result advocates for a low shrinkage of the oil sample core upon desaturation (i.e. the total porosity remains true) and a redistribution of the porosity among the cracks and the matrix in between, which is bearing the mesopores and macropores. Dynamic monitoring of the deformation at different scales and the crack opening upon desaturation of a shale core pointed out similar behavior in a quantitative way (Fauchille et al., 2016). Some large cracks may not be interconnected to the rest of the crack network and are probably missing from the amount estimated by MIP. However, regardless of the linear cumulative PSD observed on semi-log plots, it is highly probable that large pores different than cracks account for the missing porosity in the pore balances. Additional imaging methods should be further applied to confirm their content and estimate their associated PSD.

Connectivity of the pore network

One of the pivotal parameters for understanding and modelling oil/gas permeability in organic matter-rich shale is the connectivity of the pore network. Based on the observations published on various shales, both inorganic and organic phases host a pore network with narrow pore throats. Nevertheless, little data are available on the connectivity of each phase and their inter-connectivity. Some authors have shown 3D FIB/SEM images of partially connected porosity inside kerogen at the mesoscale (Curtis et al., 2012a), while others have attempted to discuss the connectivity between organic and inorganic interfaces according to the gas storage capacity of the pore volume hosted by each component (i.e. Rexer et al., 2014). Beyond this data, which are mostly at the micro or meso scale, there is no consensus explaining the role of organic and inorganic hosted pore volume in the storage of resources and how they are interconnected.

NMR measurements, considering the T_2 relaxation time of solute, are an accurate petrophysical measurement to quantify the pore volume. This method detects hydrogen

nuclei, which is usually associated with water molecules in the pore space or in a clay mineral interlayer (Coates et al., 1999). In the present study, NMR data obtained for core plugs taken in homogeneous areas of interest show that the total porosity is fully accessible by brine water when using high injection pressure, suggesting complete connectivity of the pore network (Figure 87.a). Complete connectivity is also supported by the excellent agreement between total connected porosity values obtained on the autoradiography porosity maps with total porosity values measured by NMR, including for samples from the dry gas zone that are exhibiting some micropores (Figure 92.a). For samples from the dry gas zone, for which the autoradiography porosity map (Figure 84) revealed the presence of low porous "micro-beef" phases at the core scale (Lejay et al., 2017), the pore network within the homogeneous layers of interest is connected without any distinction between OM and mineral rich areas. The incomplete connectivity of pore network detected by 3D FIB/SEM imaging within various shale samples by some authors (e. g. Curtis et al., 2012a) should be considered with regard to the spatial resolution of the method and the throat size distribution of the samples. Optimization of FIB/SEM data by energy filtering of the back-scattered electrons imaged and image restoration provides 3D images of clay materials with a resolution of 5 nm and good pore network connectivity (Gaboreau et al., 2016). Without energy filtering of the collected electron and image restoration (Curtis et al., 2012a), the true spatial resolution is limited at 10 nm. On the basis of the throat size distributions measured for the seven Vaca Muerta shale samples (Figure 88.a), none of the pore throats for the samples from the dry gas zone and only half of them for the condensate/oil zone would be detected by FIB/SEM with a resolution of 10 nm. This would by itself explain the low connectivity observed by FIB/SEM.

Evolution of pore network with OM maturity and burial

The measured total porosity values clearly decrease with the increase in OM maturity and burial depth. Even if the sample set is limited, observing this evolution is facilitated by the choice of samples from the same stratigraphic sequence and with negligible variations in mineral composition. This result however differs from the one proposed by (Han et al., 2017), showing increased porosity with increasing maturity, related to the generation of secondary organic porosity when the thermal maturation of OM occurs (Jarvie et al., 2007; Loucks et al., 2009; Curtis et al., 2012a; 2014; Bernard et al., 2012a; 2012b; Pommer and Milliken, 2015). The evolution displayed by the samples from the Vaca Muerta formation is more in agreement with a classical porosity-depth relationship (Sclater and Christie, 1980; Tissot and Welte, 1984), but the absolute values measured for samples from the oil zone could be slightly biased by the presence of significant amounts of cracks due to poor sample preservation, even if a limited core shrinkage is expected (Fauchille et al., 2016).

The link between pore space evolution and OM maturation is the question of great interest for many researchers and has controversial results. For example, Mastalerz et al. (2013), demonstrated that maximum CO_2 adsorption mainly in micropores was noted for immature samples and at the same time for the post mature ones. The same non-linear evolution of porosity with maturity was observed by Han et al. (2017), and by Pommer and Milliken (2015). This shows that the evolution of the pore network in shale samples cannot be correlated only with compaction and that its development is much more complex. These authors observed the creation of secondary pores (or increased sizes up to the microscope resolution) in OM with increased burial depth associated with the cracking of kerogen for mature samples. The powder N_2 adsorption results published by Ojha et al. (2017) demonstrated an increase of pore network complexity with OM maturation. Meanwhile, other studies based on the comparison of CO_2 and N_2 powder adsorption results (Ross and Marc Bustin, 2009; Rexer et al., 2014, Ko et al., 2017) have stated increased micropore volume. In the present study of Vaca Muerta core samples, micropores were only detected for samples from the dry gas zone. Throat sizes in the mesopore range decreased with OM maturity and burial depth according to the measurements done by MIP and for the first time by nitrogen desorption isotherms on blocks. Pore body sizes in the mesopore/macropore range measured from unbiased adsorption isotherms on blocks also decreased from condensate to gas zone. However, the dehydration of the samples from the oil zone due to poor preservation generated a lot of cracks and shrinkage in the porous matrix in between the cracks. The associated decrease in the volume of mesopores and macropores detected by gas adsorption is revealed on the pore balance. This implies a partial contraction of the pores as huge capillary pressures are involved upon water evaporation and an underestimation of pore size on the measured PSD, so no clear evolution can be detected for the full set of samples.

CONCLUSIONS

An integrated downscaling approach for analyzing unconventional shale gas/oil samples with spatially heterogeneous and multiscale pore networks was successfully applied in this work on core samples from the Vaca Muerta formation, collected on three wells within different hydrocarbon maturity areas in the Neuquén Basin, in Argentina. Well log data down to laboratory sub-samples measurements, involving 3D µtomography acquisitions, were used to localize and spatialize well-defined areas of interest within full-size cores for representative laboratory measurements. From this localized sub-sampling, based on 3D views, a multiscale correlated approach was applied, using autoradiography porosity maps and classic bulk techniques to characterize the pore network (pore volume and PSD). Autoradiography was applied for the first time on organic-rich shale. This method has provided the possibility of mapping in 2D the spatial distribution of the total

connected porosity with micrometric pixel size and over pluri-centimetric field of view reaching the core scale. On the other hand, autoradiography probes the full range of the connected pores whatever their size is. As demonstrated in this study, local calcite veins ("beef") and carbonate nodules are non-porous and should be absolutely avoided in sub-samples used for bulk methods as they drastically impact the representativeness of measured porosity values. Fortunately, 3D µtomography and 2D autoradiography are reliable methods to successfully resolve the detection of these local heterogeneities even though the resolution and contrast of µtomography are not optimal. Nevertheless, additional vertical porosity evolution associated with different laminae with varying spatial frequency among the samples was detected by autoradiography but not by µtomography. Results have also shown that the porosity values measured on areas corresponding to the size of sub-blocks used for bulk measurements are representative of the laterally homogeneous laminae detected on autoradiography porosity mapping.

Autoradiography and NMR data presented in this study clearly indicate that the total pore space is fully connected from micro to macropores in the samples of the Vaca Muerta formation regardless of the hydrocarbon maturity ranging between 1.1 and 1.6% VReq (oil to dry gas). Moreover, it was shown that by carefully selecting the sub-sampling, a coherent set of porosity data could be produced. All the methods, both imaging and bulk techniques, provide similar total porosity values (except the values obtained by using directly intruded/adsorbed volumes of fluids) when applied to comparable homogeneous and well preserved sub-samples (i.e., without crushing). Indeed, it was proven that nitrogen adsorption data of shale are deeply biased when applied on powder. Quantitative balances of porosity and pore/throat size distributions were reached revealing lower porosities and throat/pore size as burial/hydrocarbon maturity increases, even if microporosity appears for samples from the dry gas zone. But the balances confirm that not all the pores can be probed by a unique bulk method and the non-negligible pores larger than 640 nm are not analyzed in the provided PSD. Their content is only estimated by difference with the total porosity.

Although the multiscale/multitool approach used in the present study has allowed reaching a quantitative spatial distribution of porosity for seven full size core samples from macrometer to nanometer scale, and the inter-correlation with petrophysical measurement data acquired on representative sub-samples, the use of SEM imaging is now needed to validate the amount of the largest unprobed pores and to estimate their PSD. In addition, the superimposition of autoradiograph porosity maps with SEM mineral and porosity mapping (Prêt et al., 2010a; 2010b; Robinet et al., 2012; Fauchille et al., 2016) would be interesting for identifying (i) the relationship between the varying mineral compositions and the contrasted porosities through the different laminae, and (ii) measuring the specific porosity associated with clay and OM.

Table 13. Mineral compositions and physical parameters estimated from log data by a calibrated *MULTIMIN* © approach for the selected samples from three different exploration wells in zones of various hydrocarbon maturities (*Vreq* - maximum thermal maturity measured on bitumen, *LAC* – linear attenuation coefficient, *DTSM* – shear slowness, *DTCO* – compressional slowness, *PhiT* – total porosity, *PhiE* – effective porosity).

		Estimated MULTIMIN composition, mass%								**Estimated petrophysical parameters**						
Zone	**Core sample**	**Wet clay**	**Quartz**	**Pyrite**	**Calcite**	**Accessory minerals**	**Hydro-carbons**	**Water**	**Vreq, %**	**Standard Gamma Ray, API**	**Bulk density (RHOB), g/cm³**	**Average LAC**	**Resistivity, Ω·m**	**Sonic (DTSM/ DTCO), µs/m**	**MULTI-MIN PhiT, %**	**MULTI-MIN PhiE, %**
Oil	Core E	19	25.5	2.5	33	9.5	9.5	1	1.1	37	2.35	50	20	518/331	14	10
	Core F	21.5	26.5	1.5	35	8.5	5	2		39	2.4	75	20	509/308	12.5	8
Condensate	Core B	18.5	18.5	3.5	38	7.5	9	5	1.3	38	2.3	85	4	558/338	17.5	15
	Core C	20	22.5	3	37.5	8	5	4		40	2.4	85	4	522/325	12.5	10
	Core D	20.5	21.5	2.5	37	4.5	11	3		40	2.35	50	10	535/328	16	13
Dry gas	Core H	22	31	1	33	8	5	0	1.6	38	2.4	75	20	476/289	9	5
	Core I	24	32	0.5	32	5.5	6	0		42	2.4	75	20	492/302	10	6

Table 14. Quantitative mineraligal compositions obtained using the *MinEval* method of Total on the localized layers of interest within the selected cores (*sum of barite, anatase and apatite). Errors are in the order of +/- $X^{0.35}$ mass% at 95% confidence (for example 30.0 +/- 3.3 mass%).

Zone	Core sample	Layer of interest	Interval from the top of oriented core, mm	Mineral composition, mass%						
				Clay minerals	Quartz	Albite	Carbonates	Pyrite	Accessory minerals *	Insoluble organic matter
Oil	Core E	E_layer2	10 - 20	22.1	26.3	11.9	29.9	2.4	1.4	6.1
		E_layer4	51 - 61	20.4	26.8	10.3	32.2	2.3	1.4	6.7
	Core F	F_layer2	27- 37	22.8	23.9	10.2	33.3	3. 7	1.1	5.8
		F_layer4	59 - 69	27.3	20.8	12.0	28.9	3.1	1.4	6.5
Condensate	Core B	B_layer2	6 - 16	17.4	18.3	6.3	50.9	2.2	1.1	3.9
		B_layer4	42 - 52	17.6	18.2	6.3	50.7	2.3	1.1	3.9
	Core C	C_layer2	6 - 16	17.8	16.6	7.8	50.0	2.7	1.2	3.9
		C_layer4	50 - 60	17.8	16.8	7.6	50.1	2.7	1.1	3.9
	Core D	D_layer2	14 - 24	14.4	30.9	7.7	34.4	4.1	1.9	6.8
		D_layer4	50 - 60	14.2	31.9	7.3	34.0	3.7	1.9	7.0
Dry gas	Core H	H_layer2	10 - 20	25.7	19.1	13.3	32.4	3.7	0.9	5.0
		H_layer3	21 - 31							
		H_layer4	31 - 41	26.9	20.3	13.7	29.7	3.5	1.0	4.9
		H_layer5	48 - 58							
	Core I	I_layer2	7 - 17	22.7	24.0	13.9	31.2	2.6	1.2	4. 6
		I_layer4	40 - 50	24.1	23.5	13.7	30.5	2.6	1.2	4.4

Table 15. Total porosity values calculated or measured on comparable blocks by different techniques (*for total porosity values the method for bulk volume measurement is indicated; grain density was obtained by He-pycnometry on plugs; NMR – nuclear magnetic resonance spectroscopy; MIP – mercury intrusion porosimetry).

Zone	Core sample	Layer of interest	Interval from the top of oriented core, mm	Grain density, g/cm^3	Total calculated porosity*, %			Measured porosity, %			Autoradiography	
					Laser	Immersion in mercury	µTomography	NMR	MIP	N_2 adsorption		
					φ^{T}_{NMR}	φ^{T}_{MIP}	$\varphi^{T}_{\mu Tomo}$	φ^{Con}_{NMR}	φ_{MIP}	φ_{Ads}	$\varphi^{Con\_L}_{Auto}$	φ^{Con}_{Auto}
Oil	Core E	E_layer2	10 - 20	2.588	19.5			19.6				
		E_layer4	51 - 61	2.570	19.6	17.4		19.6	10.7			
	Core F	F_layer2	27- 37	2.600	20.2	20.2		20.0	11.7	9.5	19.6	21.6
		F_layer4	59 - 69	2.639	23.0	21.7		23.0	12.5		22.8	
Condensate	Core B	B_layer2	6 - 16	2.625	15.7	16.7	13.6	15.9	9.6		17.1	16.5
		B_layer4	42 - 52	2.628	16.3	15.0		16.5	10.0	10.8	16.0	
	Core C	C_layer2	6 - 16	2.646	15.9	14.7		16.0	9.5	11.6	16.9	16.6
		C_layer4	50 - 60	2.637	15.2			16.0			16.1	
	Core D	D_layer2	14 - 24	2.578	18.8	16.7	17.2	17.9	10.8		18.7	18.7
		D_layer4	50 - 60	2.578	17.0	19.9	15.4	17.4	10.4		19.0	
Dry gas	Core H	H_layer2	10 - 20	2.637	11.5			11.7			12.6	13.4
		H_layer3	21 - 31			14.1			0.6	6.1	12.9	
		H_layer4	31 - 41	2.632	11.9			12.2			13.3	
		H_layer5	48 - 58			12.0	10.9		2.7		14.3	
	Core I	I_layer2	7 - 17	2.622	11.3			11.2			13.0	13.0
		I_layer4	40 - 50	2.633	11.7	11.9		12.1	3.2	8.7	12.4	

SYMBOLS

DTCO - compressional slowness.
DTSM - shear slowness.
LAC - linear attenuation coefficient.
PhiT - total porosity, defined by *MULTIMIN* © approach of well log data treatment.
PhiE - effective porosity, defined by *MULTIMIN* © approach of well log data treatment.
m_{sat} - mass of sample saturated with brine solution.
Vreq - maximum thermal maturity measured on bitumen.
V_a - volume of adsorbed nitrogen in liquid state.
$V_{intr.max}$ - maximum volume of intruded mercury.
V_{NMR} - volume detected by NMR technique.
V_s - volume of solid parts.
V_t - total volume of the sample, measured by laser.
ρ^{brine} - density of brine solution.
ρ_{MIP}^{bulk} - bulk density, defined by immersion in mercury of the MIP blocks (~750 mm^3).
ρ_{NMR}^{bulk} - bulk density of the block, through the laser volume.
$\rho_{\mu Tomo}^{bulk}$ - bulk density, defined with µtomography of MIP blocks.
ρ^{grain} - grain density of the sample.
φ_{Auto}^{Con} - connected porosity of the whole autoradiography surface (~2100 mm^2).
$\varphi_{Auto}^{Con\_B}$ - porosity of the bulk block projection on the autoradiography surface (~50-100 mm^2).
$\varphi_{Auto}^{Con\_L}$ - porosity of the layer of the interest on the autoradiography surface (~300 mm^2).
φ_{NMR}^{Con} - connected porosity of the block (~2250 mm^3), through NaCl saturated volume and grain density measurements.
φ_{Ads} - total adsorption porosity of the block (~750mm^3), recalculated from adsorbed volumes.
φ_{Ads}^{μ} - adsorption microporosity of the block (~750mm^3), by t-plot technique.
φ_{MIP} - total intrusion porosity of the block (~750mm^3), recalculated from mercury intruded volumes.
$\varphi_{MIP}^{>640nm}$ - intrusion porosity of the block (~750mm^3), on the >640 nm range of pores throats diameter, recalculated from mercury intruded volumes.
φ_{MIP}^{T} - total porosity of the MIP block (~750mm^3), recalculated with bulk density ρ_{MIP}^{bulk}.
φ_{NMR}^{T} - total porosity of the block (~2250 mm^3), through laser volume and grain density.
$\varphi_{\mu Tomo}^{T}$ - total porosity of the block (~750mm^3), recalculated with bulk density $\rho_{\mu Tomo}^{bulk}$.

ABBREVIATIONS

BJH - Barrett-Joyner-Halenda method.
dTG - derivative thermogrametric curve.
LUT - Look up tables.
MIP - Mercury intrusion porosimetry.
MS - Mass spectroscopy.
NMR - Nuclear magnetic resonance spectroscopy.
OM - Organic matter.
PSD - Pore size distribution.
SANS - Small angle neutron scattering.
SEM - Scanning electron microscopy.
TGA - Thermogravimetric analysis.
XRD - X-Ray diffraction analysis.
XRF - X-Ray fluorescence spectroscopy.

REFERENCES

Anovitz, L. M., and D. R. Cole, 2015, Characterization and analysis of porosity and pore structures: Reviews in Mineralogy and Geochemistry, v. 80, p. 61-164, doi: 10.2138/rmg.2015.80.04.

Badessich, M. F., D. E. Hryb, M. Suarez, L. Mosse, N. Palermo, S. Pichon, and L. Reynolds, 2016, Vaca Muerta shale - taming a giant: Oildfield Review, v. 28, p. 26-39.

Barrett, E. P., L. G. Joyner, and P. P. Halenda, 1951, The determination of pore volume and area distribution in porous substance. I. Computations from nitrogen isotherms: The Volume and Area Distributions in Porous Substance, v. 73, p. 373-380, doi: 10.1021/ja01145a126.

Bernard, S., B. Horsfield, H.-M. Schulz, A. Schreiber, R. Wirth, T. T. Anh Vu, F. Perssen, S. Könitzer, H. Volk, N. Sherwood, and D. Fuentes, 2010, Multi-scale detection of organic and inorganic signatures provides insights into gas shale properties and evolution: Chemie der Erde - Geochemistry, v. 70, p. 119-133, doi: 10.1016/j.chemer.2010.05.005.

Bernard, S., B. Horsfield, H.-M. Schulz, R. Wirth, A. Schreiber, and N. Sherwood, 2012a, Geochemical evolution of organic-rich shales with increasing maturity: a STXM and TEM study of the Posidonia Shale (Lower Toarcian, Northern Germany): Marine and Petroleum Geology, v. 31, p. 70-89, doi: 10.1016/j.marpetgeo.2011.05.010.

Bernard, S., R. Wirth, A. Schreiber, H.-M. Schulz, and B. Horsfield, 2012b, Formation of nanoporous pyrobitumen residues during maturation of the Barnett Shale (Fort Worth Basin): International Journal of Coal Geology, v. 103, p. 3-11, doi: 10.1016/j.coal.2012.04.010.

Bryndzia, L. T., and N. R. Braunsdorf, 2014, From source rock to reservoir: the evolution of self-sourced unconventional resource plays: Elements, v. 10, p. 271-276, doi: 10.2113/gselements.10.4.271.

Chalmers, G. R., R. M. Bustin, and I. M. Power, 2012a, Characterization of gas shale pore systems by porosimetry, pycnometry, surface area, and field emission scanning electron microscopy/transmission electron microscopy image analyses: examples from the Barnett, Woodford, Haynesville, Marcellus, and Doig units: AAPG Bulletin, v. 96, p. 1099-1119, doi: 10.1306/10171111052.

Chalmers, G. R. L., D. J. K. Ross, and R. M. Bustin, 2012b, Geological controls on matrix permeability of Devonian gas shales in the Horn River and Liard Basins, northeastern British Columbia, Canada: International Journal of Coal Geology, v. 103, p. 120-131, doi: 10.1016/j.coal.2012.05.006.

Clarkson, C. R., and R. M. Bustin, 1996, Variation in micropore capacity and size distribution with composition in bituminous coal of the Western Canadian sedimentary basin: Fuel, v. 75, p. 1483-1498, doi: 10.1016/0016-2361(96)00142-1.

Clarkson, C. R., and R. M. Bustin, 1999, The effect of pore structure and gas pressure upon the transport properties of coal: a laboratory and modeling study. 1. Isotherms and pore volume distributions: Fuel, v. 78, p. 1333-1344, doi: 10.1016/S0016-2361(99)00055-1.

Clarkson, C. R., M. Freeman, L. He, M. Agamalian, Y. B. Melnichenko, M. Mastalerz, R. M. Bustin, A. P. Radliński, and T. P. Blach, 2012, Characterization of tight gas reservoir pore structure using USANS/SANS and gas adsorption analysis: Fuel, v. 95, p. 371-385, doi: 10.1016/j.fuel.2011.12.010.

Clarkson, C. R., N. Solano, R. M. Bustin, A. M. M. Bustin, G. R. L. Chalmers, L. He, Y. B. Melnichenko, A. P. Radliński, and T. P. Blach, 2013, Pore structure characterization of North American shale gas reservoirs using USANS/SANS, gas adsorption, and mercury intrusion: Fuel, v. 103, p. 606-616, doi: 10.1016/j.fuel.2012.06.119.

Coates, G., L. Xiao, and G. Prammer, 1999, NMR logging. Principles and applications, Halliburton Energy Services, 234 p.

Curtis, M. E., B. J. Cardott, C. H. Sondergeld, and C. S. Rai, 2012a, Development of organic porosity in the Woodford Shale with increasing thermal maturity: International Journal of Coal Geology, v. 103, p. 26-31, doi: 10.1016/j.coal.2012.08.004.

Curtis, M. E., E. T. Goergen, J. D. Jernigen, C. H. Sondergeld, and C. S. Rai, 2014, Mapping of organic matter distribution on the centimeter scale with nanometer resolution: Unconventional Resources Technology Conference, Denver, Colorado, USA, August 25-27, URTeC 1922757, 7 p, doi: 10.15530/urtec-2014-1922757.

Curtis, M. E., C. H. Sondergeld, R. J. Ambrose, and C. S. Rai, 2012b, Microstructural investigation of gas shales in two and three dimensions using nanometer-scale resolution imaging: AAPG Bulletin, v. 96, p. 665-677, doi: 10.1306/08151110188.

Fauchille, A.-L., S. Hedan, V. Valle, D. Pret, J. Cabrera, and P. Cosenza, 2016, Multi-scale study on the deformation and fracture evolution of clay rock sample subjected to desiccation: Applied Clay Science, v. 132-133, p. 251-260, doi: 10.1016/j.clay.2016.01.054.

Fleury, M., 2014, Characterization of shales with low field NMR: International Symposium of core analysis, Avignon, France, September 8-11 SCA2014-014, 12 p.

Fleury, M., and M. Romero-Sarmiento, 2016, Characterization of shales using T1–T2 NMR maps: Journal of Petroleum Science and Engineering, v. 137, p. 55-62, doi: 10.1016/j.petrol.2015.11.006.

Gaboreau, S., J. C. Robinet, and D. Prêt, 2016, Optimization of pore-network characterization of a compacted clay material by TEM and FIB/SEM imaging: Microporous and Mesoporous Materials, v. 224, p. 116-128, doi: 10.1016/j.micromeso.2015.11.035.

Gamero-Diaz, H., C. Miller, and R. Lewis, 2012, sCore: a classification scheme for organic mudstones based on bulk mineralogy: Search and Discovery Articles, #40951.

Gu, X., D. F. R. Mildner, D. R. Cole, G. Rother, R. Slingerland, and S. L. Brantley, 2016, Quantification of organic porosity and water accessibility in Marcellus Shale using neutron scattering: Energy & Fuels, v. 30, p. 4438-4449, doi: 10.1021/acs.energyfuels.5b02878.

Han, Y., B. Horsfield, R. Wirth, N. Mahlstedt, and S. Bernard, 2017, Oil retention and porosity evolution in organic-rich shales: AAPG Bulletin, v. 101, p. 807-827, doi: 10.1306/09221616069.

Harkins, W. D., and G. Jura, 1944, Surfaces of solids. XIII. A vapor adsorption method for the determination of the area of a solid without the assumption of a molecular area, and the areas occupied by nitrogen and other molecules on the surface of a solid.: Journal of American Chemical society, v. 66, p. 1366-1373, doi: 10.1021/ja01236a048.

Hellmuth, K. H., M. Siitari-Kauppi, and A. Lindberg, 1993, Study of porosity and migration pathways in crystalline rock by impregnation with 14C-polymethylmethacrylate: Journal of Contaminant Hydrology, v. 13, p. 403-418, doi: 10.1016/0169-7722(93)90073-2.

Houben, M. E., A. Barnhoorn, J. Lie-A-Fat, T. Ravestein, C. J. Peach, and M. R. Drury, 2016a, Microstructural characteristics of the Whitby Mudstone Formation (UK): Marine and Petroleum Geology, v. 70, p. 185-200, doi: 10.1016/j.marpetgeo.2015.11.011.

Houben, M. E., A. Barnhoorn, L. Wasch, J. Trabucho-Alexandre, C. J. Peach, and M. R. Drury, 2016b, Microstructures of Early Jurassic (Toarcian) shales of Northern Europe: International Journal of Coal Geology, v. 165, p. 76-89, doi: 10.1016/j.coal.2016.08.003.

Janssen, C., R. Wirth, A. Reinicke, E. Rybacki, R. Naumann, H.-R. Wenk, and G. Dresen, 2011, Nanoscale porosity in SAFOD core samples (San Andreas Fault): Earth and Planetary Science Letters, v. 301, p. 179-189, doi: 10.1016/j.epsl.2010.10.040.

Jarvie, D. M., R. J. Hill, T. E. Ruble, and R. M. Pollastro, 2007, Unconventional shale-gas systems: the Mississippian Barnett Shale of North-central Texas as one model for thermogenic shale-gas assessment: AAPG Bulletin, v. 91, p. 475-499, doi: 10.1306/12190606068.

Kaufhold, S., G. Grathoff, M. Halisch, M. Plotze, J. Kus, K. Ufer, R. Dohrmann, S. Ladage, and C. Ostertag-Henning, 2016, Comparison of methods for the determination of the pore system of a potential German gas shale: The Clay Minerals Society Workshop Lectures Series, v. 21, p. 163-190, doi: 10.1346/cms-wls-21.13.

Kelly, S., H. El-Sobky, C. Torres-Verdín, and M. T. Balhoff, 2015, Assessing the utility of FIB-SEM images for shale digital rock physics: Advances in Water Resources, v. 95, p. 302-316, doi: 10.1016/j.advwatres.2015.06.010.

Klaver, J., G. Desbois, R. Littke, and J. L. Urai, 2015, BIB-SEM characterization of pore space morphology and distribution in postmature to overmature samples from the Haynesville and Bossier shales: Marine and Petroleum Geology, v. 59, p. 451-466, doi: 10.1016/j.marpetgeo.2014.09.020.

Ko, L. T., R. G. Loucks, S. C. Ruppel, T. Zhang, and S. Peng, 2017, Origin and characterization of Eagle Ford pore networks in the South Texas Upper Cretaceous shelf: AAPG Bulletin, v. 101, p. 387-418, doi: 10.1306/08051616035.

Kuila, U., D. K. McCarty, A. Derkowski, T. B. Fischer, T. Topór, and M. Prasad, 2014, Nano-scale texture and porosity of organic matter and clay minerals in organic-rich mudrocks: Fuel, v. 135, p. 359-373, doi: 10.1016/j.fuel.2014.06.036.

Kuila, U., and M. Prasad, 2013, Understanding pore-structure and permeability in shales: SPE Annual Technical Conference and Exhibition, Denver, Colorado, USA, 30 October-2 November, SPE-146869-MS, 13 p, doi: 10.2118/146869-ms.

Lejay, A., S. Larmier, F. Gelin, and A. Zanella, 2017, The role of porosity in the development of parallel bedded calcite filled fractures (or beef) in the Vaca Muerta: an integrated analysis from high resolution core data.: Unconventional Resources and Technology Conference, Austin, USA, July 24-27, URTeC 2668071, doi: 10.15530/urtec-2017-2668071.

Lewis, R., P. Singer, T. Jiang, E. Rylander, S. Sinclair, and R. H. McLin, 2013, NMR T2 distributions in the Eagle Ford shale: reflections on pore size: SPE Unconventional Resources Conference, The Woodlands, Texas, USA, April 10-12, SPE-164554-MS, doi: 10.2118/164554-ms.

Loucks, R. G., R. M. Reed, S. C. Ruppel, and U. Hammes, 2012, Spectrum of pore types and networks in mudrocks and a descriptive classification for matrix-related mudrock pores: AAPG Bulletin, v. 96, p. 1071-1098, doi: 10.1306/08171111061.

Loucks, R. G., R. M. Reed, S. C. Ruppel, and D. M. Jarvie, 2009, Morphology, genesis, and distribution of nanometer-scale pores in siliceous mudstones of the Mississippian Barnett Shale: Journal of Sedimentary Research, v. 79, p. 848-861, doi: 10.2110/jsr.2009.092.

Ma, Y., N. Zhong, D. Li, Z. Pan, L. Cheng, and K. Liu, 2015, Organic matter/clay mineral intergranular pores in the Lower Cambrian Lujiaping Shale in the north-eastern part of the upper Yangtze area, China: a possible microscopic mechanism for gas preservation: International Journal of Coal Geology, v. 137, p. 38-54, doi: 10.1016/j.coal.2014.11.001.

Magoon, L. B., and W. G. Dow, eds., 1994, The petroleum system-from source to trap: AAPG Memoir, v. 60, 639 p, doi: 10.1306/M60585C1.

Mastalerz, M., A. Schimmelmann, A. Drobniak, and Y. Chen, 2013, Porosity of Devonian and Mississippian New Albany Shale across a maturation gradient: insights from organic petrology, gas adsorption, and mercury intrusion: AAPG Bulletin, v. 97, p. 1621-1643, doi: 10.1306/04011312194.

Milliken, K. L., L. T. Ko, M. Pommer, and K. M. Marsaglia, 2014, SEM petrography of Eastern Mediterranean sapropels: analogue data for assessing organic matter in oil and gas shales: Journal of Sedimentary Research, v. 84, p. 961-974, doi: 10.2110/jsr.2014.75.

Milliken, K. L., M. Rudnicki, D. N. Awwiller, and T. Zhang, 2013, Organic matter-hosted pore system, Marcellus Formation (Devonian), Pennsylvania: AAPG Bulletin, v. 97, p. 177-200, doi: 10.1306/07231212048.

Nelson, P. H., 2009, Pore-throat sizes in sandstones, tight sandstones, and shales: AAPG Bulletin, v. 93, p. 329-340, doi: 10.1306/10240808059.

Noiriel, C., 2015, Resolving time-dependent evolution of pore-scale structure, permeability and reactivity using X-ray microtomography: Reviews in Mineralogy and Geochemistry, v. 80, p. 247-285, doi: 10.2138/rmg.2015.80.08.

Ojha, S. P., S. Misra, A. Sinha, Dang, C. Sondergeld, and C. Rai, 2017, Estimation of pore network characteristics and saturation-dependent relative permeability in organic-rich shale samples obtained from Bakken, Wolfcamp and woodford shale formations SPWLA 58th Annual Logging Symposium, Society of Petrophysicists and Well-Log Analysts, June 17-21.

Passey, Q. R., K. M. Bohacs, W. L. Esch, R. Klimentidis, and S. Sinha, 2010, From oil-prone source rock to gas producing shale reservoir—Geologic and petrophysical characterization of unconventional shale-gas reservoirs: Society of Petroleum Engineers International Oil and Gas, Conference and Exhibition in China, Beijing, June 8-10, SPE-131350, 29 p, doi: 10.2118/131350-MS.

Pommer, M., and K. Milliken, 2015, Pore types and pore-size distributions across thermal maturity, Eagle Ford Formation, Southern Texas: AAPG Bulletin, v. 99, p. 1713-1744, doi: 10.1306/03051514151.

Prêt, D., 2003, Nouvelles méthodes quantitatives de cartographie de la minéralogie et de la porosité dans les matériaux argileux: application aux bentonites compactées des barrières ouvragées, University of Poitiers, 281 p.

Prêt, D., S. Sammartino, D. Beaufort, M. Fialin, P. Sardini, P. Cosenza, and A. Meunier, 2010a, A new method for quantitative petrography based on image processing of chemical element maps: Part II. Semi-quantitative porosity maps superimposed on mineral maps: American Mineralogist, v. 95, p. 1389-1398, doi: 10.2138/am.2010.3433.

Prêt, D., S. Sammartino, D. Beaufort, A. Meunier, M. Fialin, and L. J. Michot, 2010b, A new method for quantitative petrography based on image processing of chemical element maps: Part I. Mineral mapping applied to compacted bentonites: American Mineralogist, v. 95, p. 1379-1388, doi: 10.2138/am.2010.3431.

Prêt, D., P. Sardini, D. Beaufort, R. Zellagui, and S. Sammartino, 2004, Porosity distribution in a clay gouge by image processing of 14C-Polymethylmethacrylate (14C-PMMA) autoradiographs: Applied Clay Science, v. 27, p. 107-118, doi: 10.1016/j.clay.2004.03.005.

Ravikovitch, P. I., and A. V. Neimark, 2001, Characterization of nanoporous materials from adsorption and desorption isotherms: Colloids and surfaces, v. 187-188, p. 11-21, doi: 10.1016/S0927-7757(01)00614-8.

Rexer, T. F., E. J. Mathia, A. C. Aplin, and K. M. Thomas, 2014, High-pressure methane adsorption and characterization of pores in Posidonia shales and isolated kerogens: Energy & Fuels, v. 28, p. 2886-2901, doi: 10.1021/ef402466m.

Robinet, J.-C., P. Sardini, D. Coelho, J.-C. Parneix, D. Prêt, S. Sammartino, E. Boller, and S. Altmann, 2012, Effects of mineral distribution at mesoscopic scale on solute diffusion in a clay-rich rock: Example of the Callovo-Oxfordian mudstone (Bure, France): Water Resources Research, v. 48, p. n/a-n/a, doi: 10.1029/2011wr011352.

Ross, D. J. K., and R. Marc Bustin, 2009, The importance of shale composition and pore structure upon gas storage potential of shale gas reservoirs: Marine and Petroleum Geology, v. 26, p. 916-927, doi: 10.1016/j.marpetgeo.2008.06.004.

Rouquerol, J., D. Avnir, C. W. Fairbridge, D. H. Everett, J. H. Haynes, N. Pernicone, J. D. F. Ramsay, K. S. W. Sing, and K. K. Unger, 1994, Recommendations for the characterization of porous solids: Pure and Applied Chemistry, v. 66, p. 1739-1758, doi: 10.1351/pac199466081739.

Sammartino, S., M. Siitari-Kauppi, A. Meunier, P. Sardini, A. Bouchet, and E. Tevissen, 2002, An imaging method for the porosity of sedimentary rocks: adjustment of the PMMA method - example of the characterization of calcareous shale: Journal of Sedimentary Research, v. 72, p. 937-943, doi: 10.1306/053002720937.

Sclater, J. G., and P. A. F. Christie, 1980, Continental stretching: an explanation of the Post-Mid-Cretaceous subsidence of the central North Sea Basin: Journal of Geophysical Research: Solid Earth, v. 85, p. 3711-3739, doi: 10.1029/JB085iB07p03711.

Sigal, R. F., 2009, A methodology for blank and conformance corrections for high pressure mercury porosimetry: Measurement Science and Technology, v. 20, p. 12, doi: 10.1088/0957-0233/20/4/045108.

Sigal, R. F., 2013, Mercury capillary pressure measurements on Barnett core: SPE Reservoir Evaluation & Engineering, v. Spe -167607-PA, p. 432-442.

Sing, K. S. W., 1998, Adsorption methods for the characterization of porous materials: Advances in Colloid and Interface Science, v. 76-77, p. 3-11, doi: 10.1016/S0001-8686(98)00038-4.

Sørland, G. H., K. Djurhuus, H. C. Widerøe, J. R. Lien, and A. Skauge, 2007, Absolute pore size distributions from NMR: Diffusion Fundamentals, v. 5, p. 4.1-4.15.

Tian, H., L. Pan, X. Xiao, R. W. T. Wilkins, Z. Meng, and B. Huang, 2013, A preliminary study on the pore characterization of Lower Silurian black shales in the Chuandong Thrust Fold Belt, southwestern China using low pressure N2 adsorption and FE-SEM methods: Marine and Petroleum Geology, v. 48, p. 8-19, doi: 10.1016/j.marpetgeo.2013.07.008.

Tissot, B. P., and D. H. Welte, 1984, Petroleum formation and occurrence, Springer and Verlag, 699 p, doi: 10.1007/978-3-642-87813-8.

Topór, T., A. Derkowski, U. Kuila, T. B. Fischer, and D. K. McCarty, 2016, Dual liquid porosimetry: A porosity measurement technique for oil- and gas-bearing shales: Fuel, v. 183, p. 537-549, doi: 10.1016/j.fuel.2016.06.102.

Washburn, E. W., 1921, Note on a method of determining the distribution of pore sizes in a porous material: Proceedings of the National Academy of Sciences of the USA, v. 7, p. 115-116, doi: 10.1073/pnas.7.4.115.

3.2. Additional measurements on VM samples

3.2.1. Mineral composition

The quantitative mineralogical composition of the localized layers of interest (crushed PS1/PS2 core blocks) was achieved using the reference quantitative mineralogy method of *Total*, called *MinEval QM* from the combination of XRD and XRF techniques (Table 16). The results confirm the similarity of mineral composition between the cores selected from the well log data (Figure 58, Table 9). The main mineral phases, detected within these organic-rich shale samples are clay minerals, carbonates and quartz; other significant, but in minor quantities, phases include pyrite, albite and IOM.

The two cores from oil window present similar petrophysical properties, based on well log data (Table 9), at the scale of tenth centimeters, while some discrepancies in mineral composition were obtained by XRD-XRF analysis, reflecting the heterogeneities at the mm scale. The clay mineral mass fraction increases from 22.8 up to 27.3 mass%, from top to the bottom, respectively, within core F, while core E exhibits a slight decrease of clay minerals contents from top to the bottom (from 22.1 to 20.4 mass%). The invers trend can be noticed for carbonates as well: for core F, the carbonates content decreases from 33.3 down to 28.9 mass%, while for core E it increases from 29.9 up to 32.2 mass%, from the top to bottom. Quartz content ranges from 20.8 to 26.8 mass% (higher for core E), pyrite is in the 2.3 – 3.7 mass% (higher for core F) and the content of IOM varies from 5.8 to 6.7 mass% range for the both cores.

Samples from condensate zone demonstrate lower contents in clay minerals and higher (for the cores B and C) or similar (core D) carbonates contents, compared with the samples from oil window. The two cores B and C, from the condensate zone, have nearly the same mineral composition with 17.4-17.8 mass% of clay minerals, 24.4-24.6 mass% of the sum of quartz and albite, 50.1-50.9 mass% of carbonates, 2.2-2.7 mass% of pyrite and 3.9 mass% of the IOM (Table 16). Both cores demonstrate homogeneous vertical distribution of minerals (compaire layers 2 and 4). Meanwhile, the third sample from the same zone, core D, exhibits a mineral composition different from the cores B and C, with lower clay minerals (14.4 to 14.2 mass% from top to the bottom respectevely) and carbonates (34.4 to 34.0 mass%) contents, and higher ammounts of quartz (up to 31.9 mass%), pyrite (up to 4.1 mass%) and IOM (up to 7 mass%). Core D demonstrates higher vertical variation of the mineral phases, than cores B and C (compaire layers 2 and 4, Table 16).

The selected samples from gas window are characterized by higher clay contents, in comparison with less mature samples from condensate and oil zones: 25.7 – 26.9 mass% for core H and 22.7 – 24.1 mass% for core I, from top to the bottom, respectively (Table

16). Core I exhibits higher quartz content, than core H (23.5-24.0 mass% versus 19.1-20.3 mass%). In addition, core H demonstrates slightly higher content of pyrite (up to 3.7 mass%) and IOM (up to 5.0 mass%), than core I (pyrite: 2.6 mass%; IOM: 4.4 - 4.6 mass%).

Table 16. Quantitative mineralogic compositions obtained with the *MinEval* method of Total on the localized layers of interest within the selected cores (*sum of barite, anatase and apatite). Errors are in the order of $\pm X^{0.35}$ mass% at 95% confidence (for example, 30.0 ± 3.3 mass%).

Zone	Core	Layer of interest	Interval from the top of oriented core, mm	Mineral composition, mass%						
				Clay minerals	Quartz	Albite	Carbonates	Pyrite	Accessory minerals *	IOM
Oil	Core E	E_layer2	10 - 20	22.1	26.3	11.9	29.9	2.4	1.4	6.1
		E_layer4	51 - 61	20.4	26.8	10.3	32.2	2.3	1.4	6.7
	Core F	F_layer2	27- 37	22.8	23.9	10.2	33.3	3.7	1.1	5.8
		F_layer4	59 - 69	27.3	20.8	12.0	28.9	3.1	1.4	6.5
Condensate	Core B	B_layer2	6 - 16	17.4	18.3	6.3	50.9	2.2	1.1	3.9
		B_layer4	42 - 52	17.6	18.2	6.3	50.7	2.3	1.1	3.9
	Core C	C_layer2	6 - 16	17.8	16.6	7.8	50.0	2.7	1.2	3.9
		C_layer4	50 - 60	17.8	16.8	7.6	50.1	2.7	1.1	3.9
	Core D	D_layer2	14 - 24	14.4	30.9	7.7	34.4	4.1	1.9	6.8
		D_layer4	50 - 60	14.2	31.9	7.3	34.0	3.7	1.9	7.0
Dry gas	Core H	H_layer2	10 - 20	25.7	19.1	13.3	32.4	3.7	0.9	5.0
		H_layer3	21 - 31							
		H_layer4	31 - 41	26.9	20.3	13.7	29.7	3.5	1.0	4.9
		H_layer5	48 - 58							
	Core I	I_layer2	7 - 17	22.7	24.0	13.9	31.2	2.6	1.2	4. 6
		I_layer4	40 - 50	24.1	23.5	13.7	30.5	2.6	1.2	4.4

The fraction < 5 μm contains clay minerals and has similar composition (Table 17) r for all the samples with illite and illite/smectite mixed layer clay minerals (R3 ordered; Figure 94.A) detected as the major clay fraction, and with just minor traces of kaolinite for the samples B, H and I. The interstratified layers of illite and smectite may be identified as R3-ordered (Figure 94.B), that means a four layer structure ordered with non-nearest-neighbor layer dependence, with up to 80 mass% of illite layers (Figure 94.B, Brigatti et al., 2013). CEC measurements do not reveal high reactive capacity for the samples, confirming the mineral composition measurements. Indeed, the higher CEC would have

been expected in the presence of pure smectite minerals, which were not detected. Based on measured CEC and assuming a theoretical CEC value of pure illite of 25 meq/100g and CEC of pure montmorillonite of 80 meq/100g (Meunier, 2005), the mass fraction of smectite layers in I/S (illite/smectite) mixed layer was roughly estimated (Table 17), which does not exceed the 10 – 20 mass% range.

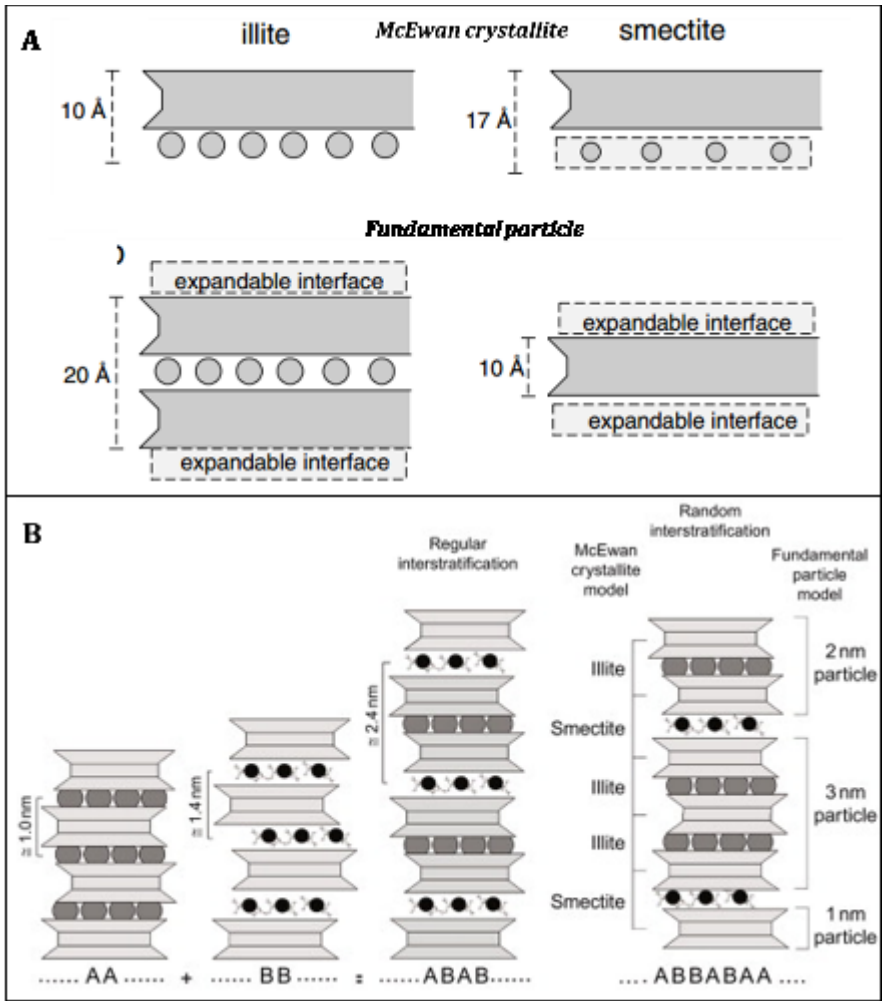

Figure 94. A) The two concepts of crystal structure of mixed-layer minerals: McEwan crystallite (top) and fundamental particle (bottom) (Meunier, 2005). B) Organisation of the mixed-layered minerals structure with the illite (A) and smectite (B) layers (Brigatti et al., 2013).

Table 17. CEC measurements and XRD mineral composition results of the fraction <5µm, on the localized layers of interest within the selected cores (PT – possible trace; *calculations done assuming theoretical CEC of pure illite of 25 meq/100g and CEC of pure montmorillonite of 80 meq/100g, Meunier, 2005).

Zone	Core sample	Layer of interest	Interval from the top of oriented core, mm	CEC, meq/100g		Mineral composition of fraction <5µm, mass%					Estimated fraction of smectite layers in I/S*, mass%
				Calcu-lated	ISS/Lab measured on powder at 150°C	Smectite	Illite and/or Illite/smectite Ordered R3	Micas	Kaolinite	Chlorite	
Oil	Core E	E_layer2	10 - 20	5.128	4.98	0	100	0	0	0	14.5
		E_layer4	51 - 61	4.692	4.84	0	100	0	0	0	15.3
	Core F	F_layer2	27- 37	5.149	4.94	0	100	0	0	0	14.0
		F_layer4	59 - 69	6.231	5.41	0	100	0	0	0	12.8
Condensate	Core B	B_layer2	6 - 16	4.138	4.98	0	100	0	PT	0	18.5
		B_layer4	42 - 52	4.413	5.27	0	100	0	0	0	19.3
	Core C	C_layer2	6 - 16	4.464	4.80	0	100	0	0	0	17.4
		C_layer4	50 - 60	4.455	4.58	0	100	0	0	0	16.6
	Core D	D_layer2	14 - 24	3.593	2.96	0	100	0	0	0	13.3
		D_layer4	50 - 60	3.545	3.20	0	100	0	0	0	14.6
Dry gas	Core H	H_layer2	10 - 20	6.592	7.04	0	>95	0	<5	PT	17.7
		H_layer3	21 - 31								
		H_layer4	31 - 41	6.868	6.10	0	>95	0	<5	PT	14.7
		H_layer5	48 - 58								
	Core I	I_layer2	7 - 17	5.759	6.04	0	>95	0	<5	PT	17.2
		I_layer4	40 - 50	6.135	5.67	0	>95	0	<5	PT	15.2

The mineral compositions of the VM samples plotted on a simple ternary plot classification (Figure 95), demonstrate that the accurate choice of the samples allowing to define a similar class group of samples with minimum variations in mineral composition. According to the classification of Gamero-Diaz et al. (2012), the samples from oil and gas zones may be classified as mixed mudstones (Figure 95.B), while samples from the condensate zone exhibit larger variation in mineral composition and can be identified as mixed carbonates (cores B and C) or carbonate/siliceous mudstones (core D). It can be noted that the highest differences between *MULTIMIN*© and XRD-XRF results for the mineral composition appears for the sample from the condensate zone (Figure 95.B), with higher clay content at the log scale, than at the centimetric.

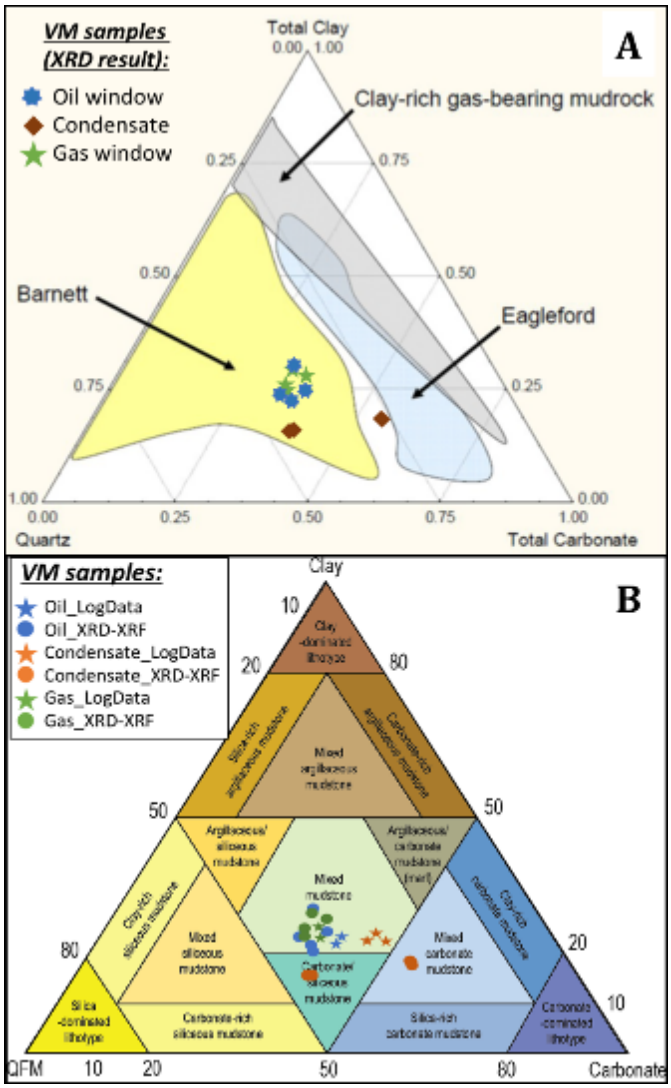

Figure 95 Position of the VM samples on the shales samples ternary plot classification: A) proposed by Passey et al. (2010); B) proposed by Gamero-Diaz et al. (2012).

3.2.2. Thermal analysis

The main objectives of the thermal analysis carried out in the presented research were: (i) to evaluate the efficient drying temperature (i.e., the temperature, at which all the liquids would be removed from the pore space, including water and liquid hydrocarbons); and (ii) to characterize the main solid components of the samples (both, inorganic and solid organic compounds) and their behavior over the temperature range from 50 up to 900 °C.

Thermogravimetric analysis (TGA) have been done in two different environments (argon and air) to test the impact of the gas atmosphere on the thermal decomposition of the compounds. Powder (PS block, Figure 61.A) from sample H (dry gas window) were heated under both atmospheres. The two derivatives of TGA curves (dTG) show two large endothermic peaks at ~450°C and at ~650°C (Figure 96).

The main difference between these results appears in the range 250-530°C (Figure 96), displaying a shift and different mass loss during the thermal decomposition. This change indicates the presence of combustible components in the sample due to organic matter decomposing effects. Meanwhile, the intensity and the position of the event, with the onset at 530°C, remains the same at different atmospheres, suggesting an inorganic nature of the decomposed matter (Warne, 1991). The intensity at ~440°C decreases in the presence of inert gas argon, indicating the removal of misleading reactions of the sample decomposition products - air here. From this observation all the following TGA curves were acquired in argon atmosphere, to evaluate the OM pure thermal decomposition reactions.

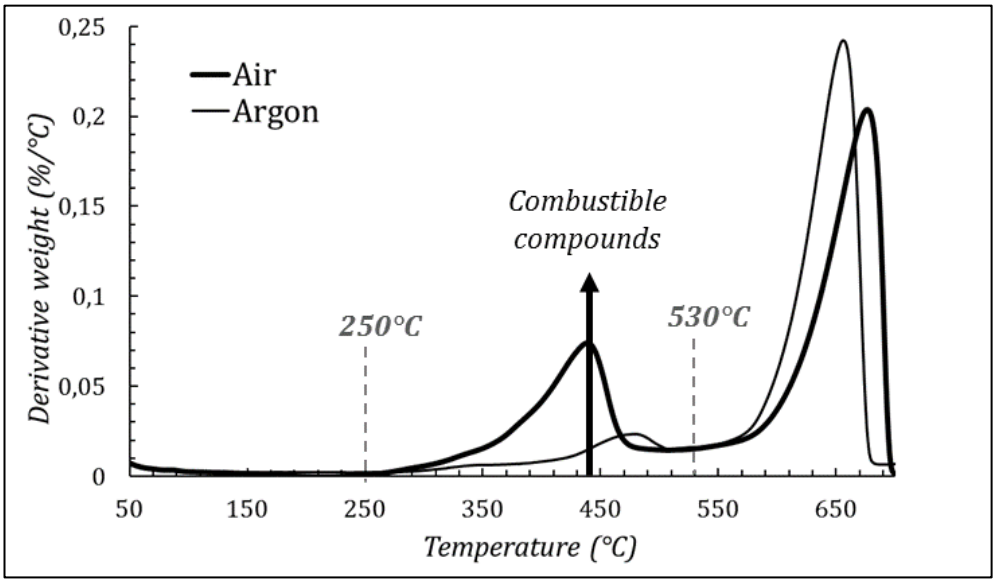

Figure 96. dTG curves, recorded for dry gas sample (powder from the core H) in argon (thin line) and air (thick line) atmospheres with a 1°C/min heating ramp.

TGA curves were, thus, acquired for one sample from each production zone (samples F, C and H were selected), expecting that the samples from the same zone would provide similar result due to close mineral and organic compounds composition. The derivative of TGA curves for the three samples (Figure 97) were sub-divided considering three main temperature ranges: 50 – 250°C; 250 – 550°C and > 550°C.

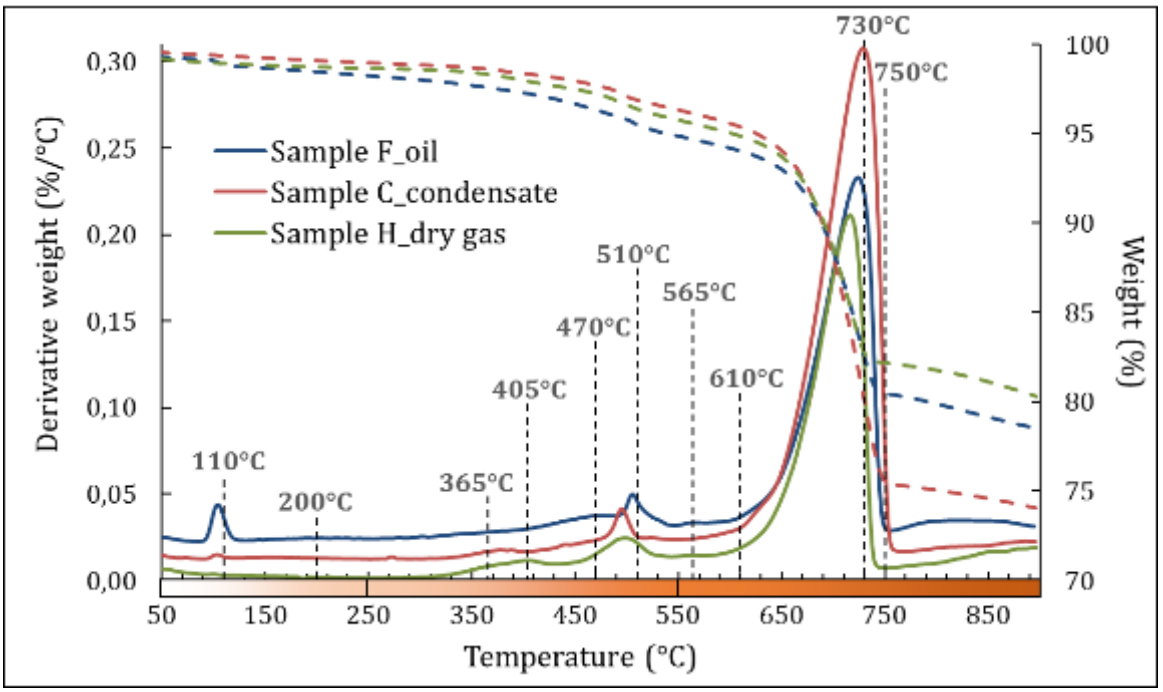

Figure 97. Weight loss (doted lines) and dTG (solid lines) curves recorded for samples from zones with various hydrocarbons types (blue lines are for oil window, sample F; red – for condensate zone, sample C; green – for gas window, sample H); with a heating ramp of 5 °C/min in an argon atmosphere.

50 – 250°C temperature range

In the 50 – 250°C temperature range, difference of mass loss can be found in-between the samples. A peak centered at around ~110°C is well expressed for the oil window sample (F) and smoothly disappears for the condensate to gas window samples (C and H, respectively). The increase in mass loss at 110°C corresponds to the outgassing of H_2O molecules regarding to the mass spectrometry analysis (Figure 97.B) and reflecting the amount of water adsorbed in the pore space (Figure 97). The water weight loss, corresponding to the sample dehydration, is noted at 100-110°C, but the process is spreading up to 220°C.

The coupling of TGA with mass spectroscopy results, allows to associate the events on the thermal curve with the composition of the environment in the sample chamber,

which consists only of inert argon and products of the sample decomposition under the thermal stress.

Following this approach, the spectra of the compounds with masses 18 and 17 (H_2O and OH^- respectively) and the TGA curves allow to evaluate the amount of emitted water (H_2O and OH^-, respectively; Figure 98.B, only spectra for H_2O, mass 18, are shown, spectra for OH^-, mass 17, demonstrated the same evolution with significantly lower intensities). The water loss at 105°C is clearly confirmed for sample F (oil window) by mass spectra of 18 and 17 while for samples H and C no peak with a clear position on the spectra is identified, but the emission is detected (Figure 98.B).

At a temperature higher than 105°C, an event up to 220°C can be observed with the emission maximum at around 200 °C. It is mainly pronounced for the oil and gas samples (F and H, respectively), while almost negligible increase can be found for the condensate zone sample (C), making it complicated to clearly distinguish the completion point of sample dehydration. Other fluids, which may be extracted under thermal stress from the pore space, based on the composition of the samples (Table 9), are liquid organic compounds (or hydrocarbons, gas and oil). While gas is highly volatile (not expected to be found in crushed sample from the dry gas window), the products of oil decomposition or/and emission may be detected. This event can be correlated, for example, with CO_2 emission on the spectra in the 50-250°C range (Figure 98.C), which is smeared on the broad range of temperature. Additional peaks of compound's emission with mass 41 (C_3H_5, Figure 99.B) can be observed at 105°C (as well as low intensity for masses 42 i.e., C_2H_2O/C_3H_6, and 43 i.e., CH_3CO/C_3H_7; data are not shown), and assumed to appear due to outgassing of volatile liquid organic compounds as no thermal transformation of solid organic matter is expected at this temperature (Smykatz-Kloss et al., 1991). An event at ~200°C on the mass spectra of 50 (C_4H_2) can be evidenced only for the sample from oil window, (Figure 98.C), this event is well correlated with the observed mass loss in this region. At approximately 110°C, a broad emission of compound with mass 55 (C_4H_9, data not shown) was detected only for sample H(dry gas window), and another for mass 57 (C_4H_9) has been found for both, oil and dry gas samples, but not for the sample from the condensate zone (Figure 99.C). These masses are mainly attributed to CxHy compounds, corresponding to the liquid hydrocarbons release from the sample, simultaneously with water emission, inducing the change in sample weight at large range of temperatures.

250 – 550°C temperature range

The largest differences in between the samples with various maturity of organic matter are observed in the temperature range of 250-550°C (Figure 97, Figure 98.A). This range is attributed to the transformations of combustible compounds (Figure 96, Warne, 1991).

The onset of the solid organic matter decomposition process for samples from zones with different organic matter maturity has been identified in the range of 280 – 300°C (with the shift for the higher temperature for the sample from condensate zone; Figure 97). However, the interpretations are not straightforward, and difficulties arise because of the overlap of thermal decompositions of various compounds in this range.

Among others, compounds with masses 64 (SO_2/S_2) and 48 (SO, data not shown) were detected (Figure 98.D) in between 490°C and 510°C. Their intensity increases from dry gas to oil samples. Release of sulfur groups can be expected, due to the thermal decomposition of pyrite (Fe_2O_3, SO_2 and SO_3 compounds are expected to be released in this range of temperatures, Concer et al., 2017). Meanwhile, some sulfur may be present in the organic matter as well and its emission would occur at the same temperature range (Durand, 1980), explaining the higher emission for oil sample, since the amount of pyrite is similar for sample H (gas) and sample F (oil) (Table 16).

The main indicator of thermal transformation of organic matter is the emission of CO_2 (mass 44, Figure 99.C). Several thermal events can be detected in the 250 – 550°C range on the spectra of mass 44 for the three samples. The first event associated with the CO_2 release is at 350°C and remains the same for all the samples, with a different intensity between the samples. The position, intensity and shape of the most intense peak at ~490 – 500°C evolve between the samples, smoothing the emission and losing the intensity from the oil to the dry gas window sample.

In literature, numerous measurements on the extracted organic matter can be found and illustrate the complexity of this issue (e.g., kerogen can be extracted from different physical-chemical techniques, which can strongly modify its chemical composition; Torrente and Galán, 2011). They also show the difficulty in identifying the solid organic matter decomposition products by mass spectroscopy.

In general two steps of organic matter thermal decomposition are expected (Durand, 1980). The first stage is attributed to easily removable compounds, such as water, CO_2, eventually SO_2 and H_2S in smaller quantities. In the end of this step some release of heteroatoms, can occur (S_2, O_2, N_2). If a strong weight loss is detected at this first step, then the organic matter may be assumed to be rich in oxygenated products. The second stage of organic matter thermal degradation includes the emission H_2O and CO_2 as well but in smaller quantities, and the release of hydrocarbons provoking larger weight loss, with general formula C_xH_y, also H_2S, SO_2, S_2.

With regards to the present result, some of the compounds, which were detected at the lower temperature range, can be correlated with the solid organic matter decomposition in the 250 – 550°C range as well. Compounds with masses 41 (C_3H_5), 42 (C_2H_2O/C_3H_6), 43 (CH_3CO/C_3H_7) repeat the shape of the spectra CO_2 with the positions of the peaks and the evolution between the samples: the peaks intensities decrease in

intensity and shifts to lower temperature (Figure 99.B only data for the compound with mass 41 are shown, Figure 98.C). The same correlation with CO_2 can be observed for the compound with mass 50 (C_4H_2), detected only for samples H and F (Figure 98.C). Some compounds are also detected on the mass spectra with peak position at around ~460 – 500°C. For sample F, compounds with masses 45 (CH_2OCH_3/ CH_3CHOH/ OCH_2CH_3), 46 (NO_2), 60 ($CH_2C(OH)OH$); 66 (C_5H_6/H_2S_2); 76 (C_6H_4) can be detected at 490-500°C (Figure 99.D). All the listed compounds exhibit the same evolution with various intensities (except the spectrum for mass 76, which shows the lowest signal to noise ratio).

Compared to samples C and H, sample F from oil window exhibits a larger variability of the detected compounds resulting from the solid organic matter decomposition. Emission of compounds with the masses 53 (at 460°C - C_4H_5); 54 (at 440°C - C_4H_6); 57 (at 450°C - C_4H_9); 67 (at 457°C - C_5H_7); 68 (at 445°C - C_5H_8); 70 (at 440°C - C_5H_{10}); 71 (at 440°C - C_5H_{11}/C_3H_7CO) were detected (all the spectra of the listed masses show the same evolution, only the data for mass 57 is displayed, Figure 99.C). Among these compounds, and considering the sample H from dry gas window, only compounds with masses 55 (data not shown) and 57 were detected with a very low intensity of emission (Figure 99.C).

In conclusion, most of the detected compounds, released at this range of temperatures, correspond to the C_xH_y general formula of hydrocarbons. This statement allows to conclude that the solid organic matter present in the samples can be assumed as rich in hydrocarbons, according to Durand (1980). However, a clear evolution of organic matter composition with maturity cannot be identified, due to the low emission intensity of most of the detected compounds and the overlap of thermal events in raw multicomponent sample.

550-900°C temperature range

Classically it is easy to identify most of carbonates (i.e. dolomite, calcite and siderite): their thermal decomposition induces different exothermic processes at temperature higher than 600°C (with the exception for more soluble types, such as siderite, which has a much lower decomposition temperature at around 500°C; Pallasser et al., 2013). The fraction of carbonates present in the samples is expected to provide a high weight loss during the thermal decomposition. Other mineral phases, which are expected to show a thermal reaction at the same range of 500 – 700°C, are clay minerals (Grim and Bradley, 1948). Here the lattice dehydroxylation may occur, inducing an additional exothermic reaction (Table 5). However, a very high total content of carbonates within the samples induces a very intense peak at this range of temperatures, making impossible to distinguish these two events (i.e., decomposition of carbonates or dehydroxylation of clay minerals).

With regard to present results, the change of this peak intensity between the samples agrees with carbonates content variation (Table 16), for which the maximum intensity can be observed for sample C (Figure 97). Mass spectroscopy only revels a very intense emission of CO_2 (m/e=44, data not shown for this temperature range), which may correspond to the product of carbonates decomposition. Indeed, for pure synthetic calcite the theoretical mass loss sis equivalent to 44% of carbonates initial mass fraction (Frost et al., 2008). This theoretical mass loss correlates well with the main mass losses observed at 650 – 700°C (Figure 97).

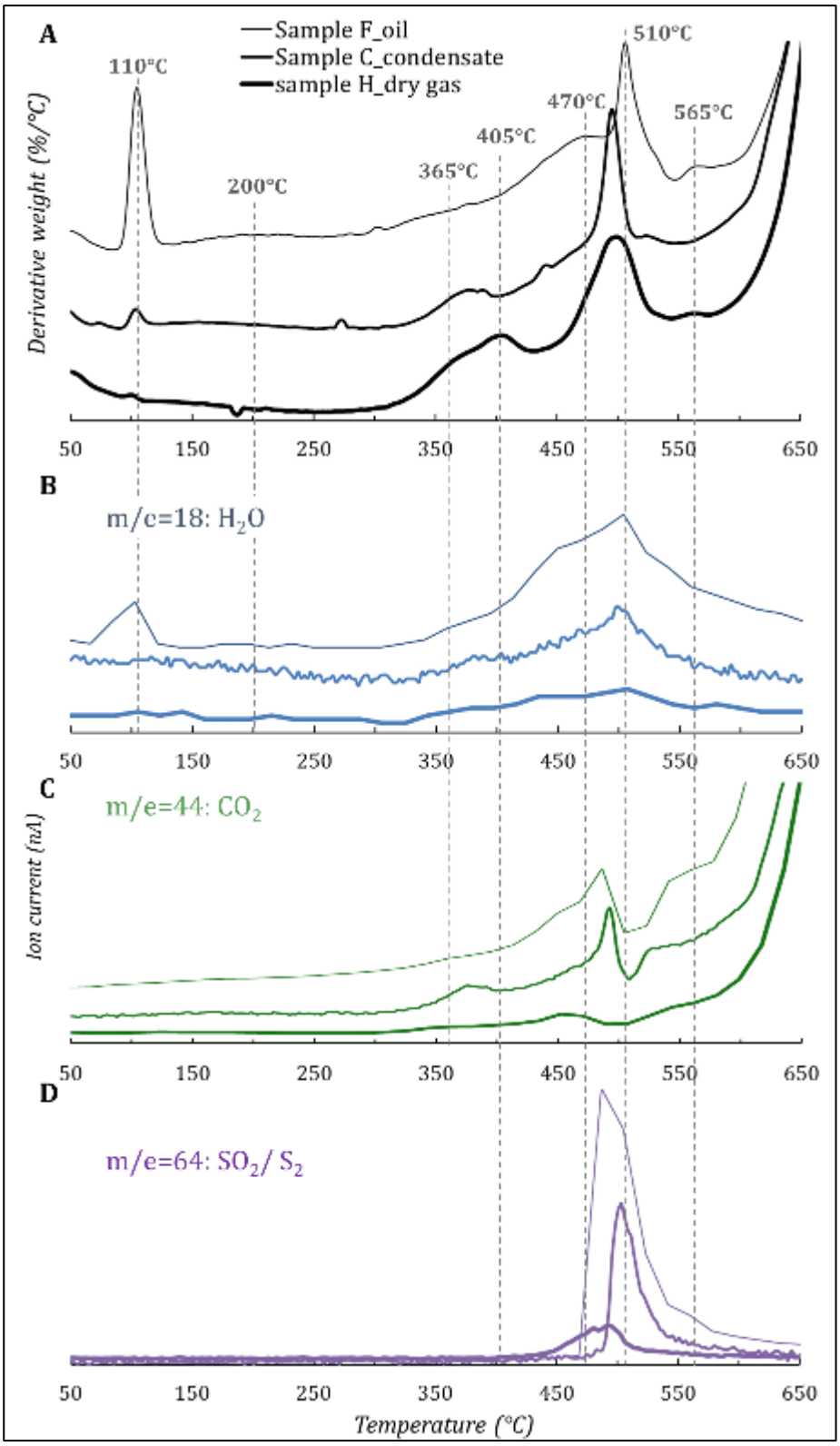

Figure 98. Results of TGA-MS analysis for samples from zones with various hydrocarbons types (5°C/min, argon atmosphere): A) derivative weight loss curves; B) spectra of mass 18 (H_2O); C) spectra of mass 44 (CO_2); D) spectra of mass 64 (SO_2/S_2).

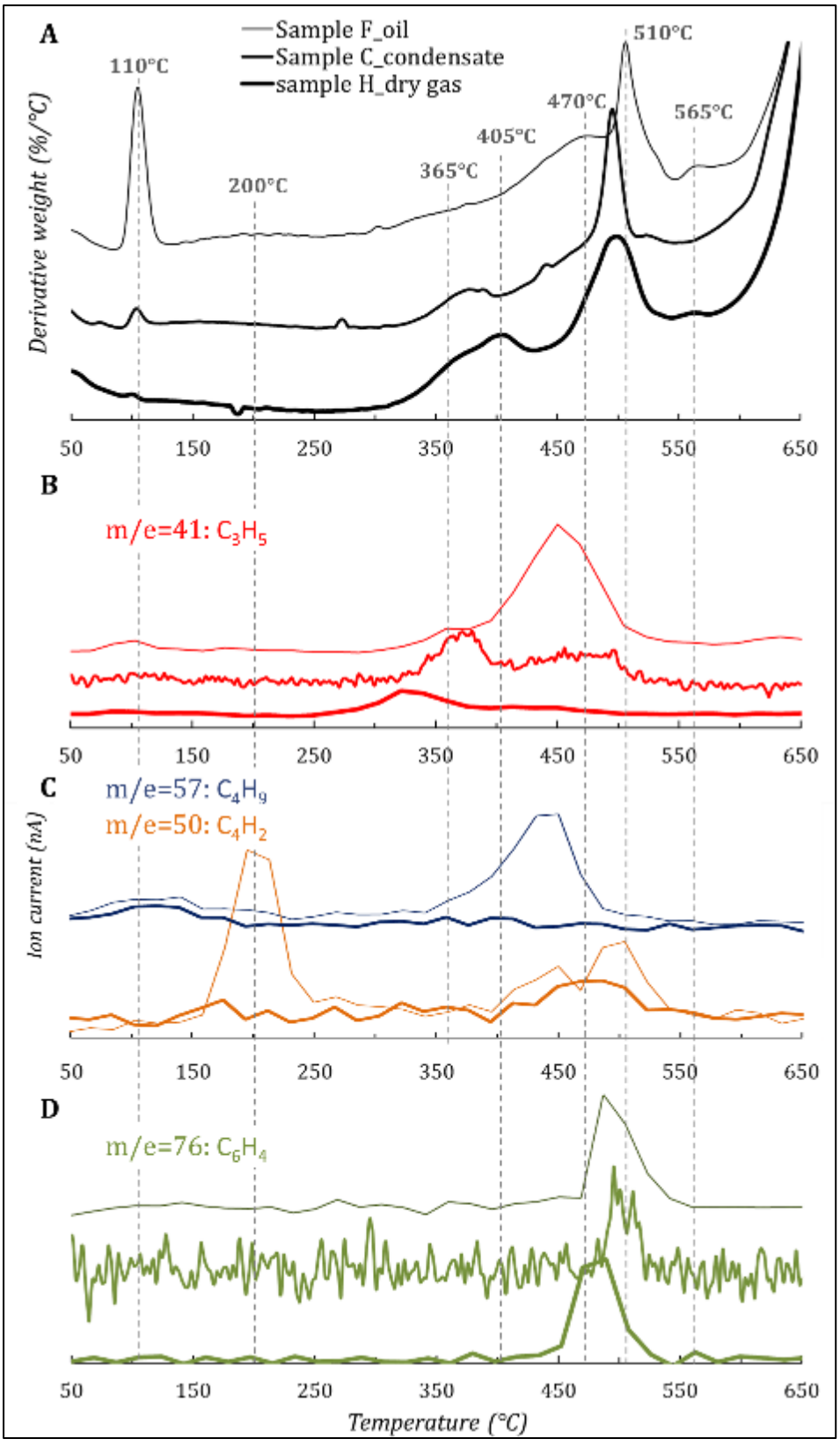

Figure 99. Result of TGA-MS analysis for samples from zones with various hydrocarbons types (5°C/min, argon atmosphere): A) derivative weight loss curves; B) spectra of mass 41 (C_3H_5); C) spectra of masses 50 (C_4H_2) and 57 (C_4H_9); these compounds have been detected only for samples F and H (no data for sample C is present); D) spectra of mass 76 (C_6H_4).

3.2.3. Total porosity estimation

The total porosity calculation requires both, grain and bulk, densities (see section 2.2.4). The grain densities have been measured by He-pycnometry analysis on localized samples, prepared in separate ways (Figure 63). The values of ρ_{aver}^{grain} were obtained on raw sample (Soxhlet method was not applied here) and on sample only dried at 110°C. While for the other samples, Soxhlet method was applied and samples were dried at temperature up to 150°C under vacuum. While ρ_{aver}^{grain} and ρ_{PS}^{grain} correspond to the measurements on powder, ρ_{NMR}^{grain} has been obtained on the preserved cylindrical block.

The results of these measurements significantly vary (Table 18). It can be noticed that ρ_{aver}^{grain} is significantly lower for samples from oil and condensate samples than other results, obtained on localized sub-samples (ρ_{PS}^{grain}, measured on powder from PS blocks, and ρ_{NMR}^{grain}, measured on NMR blocks). Meanwhile, no large discrepancy for sub-samples from gas window has been detected. The difference in grain densities is up to 0.09 g/cm^3, leading to discrepancies in calculated total porosity values of up to ± 3%. The presence of liquid hydrocarbons is expected only in powder samples from oil and condensate zone (gas is highly volatile and is not expected to be found in the crushed samples), agreeing with the obtained result for grain density. Indeed, the liquid hydrocarbons, left in the pore space before He-pycnometry measurements would lead to the underestimation of the grain density. While liquid hydrocarbons removal is crucial for grain density measurements, the temperature of the sample preparation affected less significantly the measured values. Here the ρ_{PS}^{grain} was measured on the samples from PS blocks dried at 110°C and ρ_{NMR}^{grain} – on the samples from NMR blocks dried at 150°C (Table 18). It can be noticed that ρ_{PS}^{grain} is equal to ρ_{NMR}^{grain}, or slightly lower, indicating that not all the samples were fully dried at 110°C and residual liquid hydrocarbons and water (see section 3.2.2) may have been present in the PS samples, leading to slightly lower solid densities. The maximum difference has been noted for sample F, where the maximum water release has been detected by TGA-MS (Figure 97) under thermal stress.

Bulk density has been measured by different methods on localized sub-blocks (Table 18). All the samples have been prepared with the same procedure by outgassing at 150°C during at least 36 hours. The discrepancies detected for bulk densities measured on MIP and NMR sub-blocks (ρ_{MIP}^{bulk} and ρ_{NMR}^{bulk}, respectively), could be explained by the error of the measurements with MIP technique. As density estimation here is based on the masses measurements (Equation 20), a large error may be expected. Some sub-blocks prepared for MIP tests were additionally scanned with µtomography. No large discrepancy between values obtained from bulk density, measured by MIP and by µtomography on the same sub-block, has been found (Table 18), confirming the reliability of MIP measurements.

Table 18. Results of grain and bulk densities measurements by various techniques.

Zone	Core	Layer of interest	Interval from the top of oriented core, mm	Measured grain density, g/cm³			Measured bulk density, g/cm³		
				Averaged probe,	PS blocks	NMR blocks	Mercury immersion	Laser	μTomo-graphy
				ρ_{aver}^{grain}	ρ_{PS}^{grain}	ρ_{NMR}^{grain}	ρ_{MIP}^{bulk}	ρ_{NMR}^{bulk}	$\rho_{\mu Tomo}^{bulk}$
Oil	Core E	E_layer2	10 - 20	2.50	2.57	2.59		2.08	
		E_layer4	51 - 61		2.56	2.57	2.12	2.07	
	Core F	F_layer2	27- 37	2.54	2.60	2.60	2.08	2.08	
		F_layer4	59 - 69		2.57	2.64	2.07	2.03	
Condensate	Core B	B_layer2	6 - 16	2.59	2.62	2.63	2.26	2.21	2.27
		B_layer4	42 - 52		2.62	2.63	2.23	2.20	
	Core C	C_layer2	6 - 16	2.56	2.63	2.65	2.26	2.22	
		C_layer4	50 - 60		2.63	2.64		2.24	
	Core D	D_layer2	14 - 24	2.51	2.57	2.58	2.15	2.09	2.14
		D_layer4	50 - 60		2.58	2.57	2.06	2.14	2.18
Dry gas	Core H	H_layer2	10 - 20	2.60	2.62	2.64		2.33	
		H_layer3	21 - 31				2.26		
		H_layer4	31 - 41		2.63	2.63		2.32	
		H_layer5	48 - 58				2.32		2.35
	Core I	I_layer2	7 - 17	2.61	2.61	2.62		2.33	
		I_layer4	40 - 50		2.62	2.63	2.32	2.33	

3.2.4. Nuclear magnetic resonance spectroscopy

NMR measurements allow to estimate the connected porosity (see section 2.2.10). Figure 100 displays the connected porosity values measured by NMR technique versus the total porosity values estimated on the same localized sub-samples (see section 2.2.4). The plot demonstrates perfect superimposition of the NMR porosities calculated with Equation 30 and Equation 31, confirming the high reliability of the NMR measurements. That is why only one value has been selected to be presented in the article (Table 15; $\varphi_{NMR}^{Con}=\varphi_{NMR}^{Con\_Vs}$; Equation 30). A perfect positive correlation for both, the connected porosity and the total porosity, indicates that all the pores probed by these techniques are interconnected. The total porosity (φ_{NMR}^{T}) values decrease from 20-23% for the oil zone samples down to 11-12% for gas zone samples, through 15-19% for the condensate zone samples.

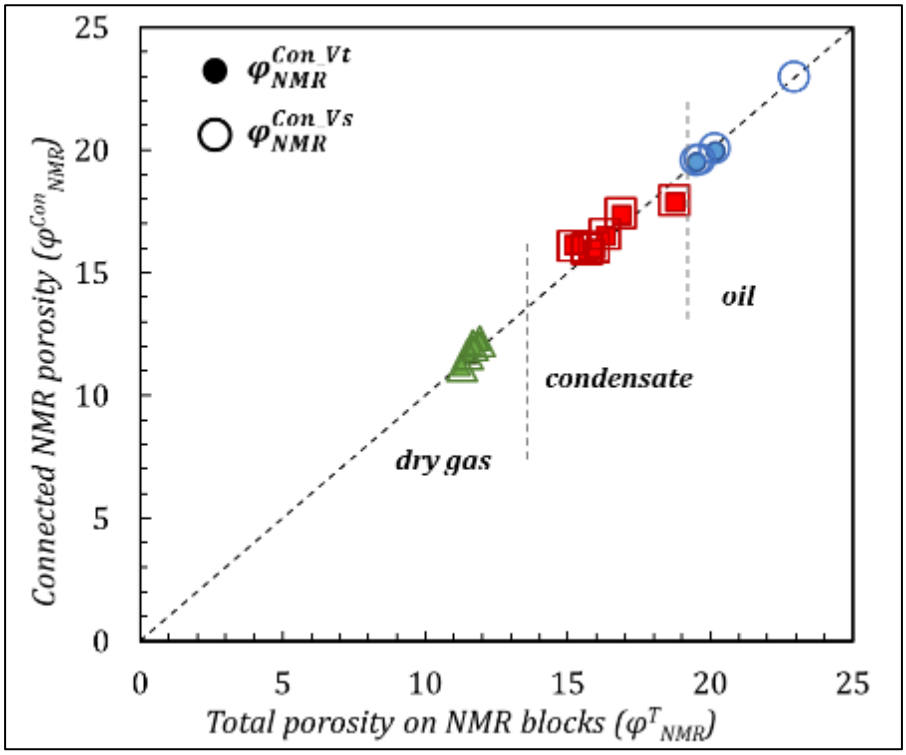

Figure 100. Connected porosity values, measured by NMR using Equation 30 and Equation 31, versus the total porosity, measured on the same blocks (triangles are for gas zone samples, squares – for condensate zone, and circles – for oil zone).

3.2.5. Mercury intrusion porosimetry

MIP intrusion/extrusion curves are presented in the article for the samples taken from each hydrocarbon maturity zone (oil, condensate, dry gas, Figure 88.a). All the intrusion/extrusion curves (converted to absolute porosity values), obtained for the samples from each zone, are given in Figure 101. It can be noted that for each zone the cumulative intrusion curves display the same shape (Figure 101) and only absolute values of total intrusion volumes and associated φ_{MIP} are different between the samples. Samples from condensate and dry gas zones present similar shaped curves, with significantly lower amounts of intruded mercury for dry gas samples (Figure 101.C). Different curves have been obtained for the oil zone samples, for which additional large pore throats, between 1 and 100 µm, were detected. This range of pore throats (1-100 µm) corresponds to cracks detected by 3D X-ray µtomography and the autoradiography porosity maps (Figure 106 and Figure 107). For all the samples, the main mode of detected pore throats (without considering the cracks of the oil zone samples), were less than 20 nm in diameter and the mode around 7-15 nm was truncated on the left side of the distribution (Figure 101). This indicates the occurrence of throats smaller than 7 nm. MIP intrusion curves show how throat size changes according to burial depth/OM maturation and can be ranked with decreasing size from oil to gas zones (from 15 to 7 nm, for oil and gas samples respectively, Figure 88.a).

Since all the pore volume has not been invaded by mercury, volume stabilization at the maximum intrusion pressure has not been reached. Consequently, the values of grain density, obtained at the maximum applied pressure are significantly lower than those measured by He-pycnometry.

The large amount of trapped mercury upon extrusion is almost similar for the samples from different zones and in the range 70-85% of the total intruded mercury volume. The normalized pore throat size distribution (dividing the intruded porosity at each pressure by total NMR porosity; φ_{NMR}^{T},) shows that MIP probes only a small part of the pore volume (Figure 101). For oil and condensate samples only ~55% of the total pore volume is probed, and for dry gas – only 25%, compared with φ_{NMR}^{T}. These discrepancies are related to the fact that mercury does not invade all the pores in shales, underestimating the total pore volume. Much of the pore throats are smaller in diameter than the percolation threshold (7 nm in this study) and are not accounted in the distribution, obtained by this technique.

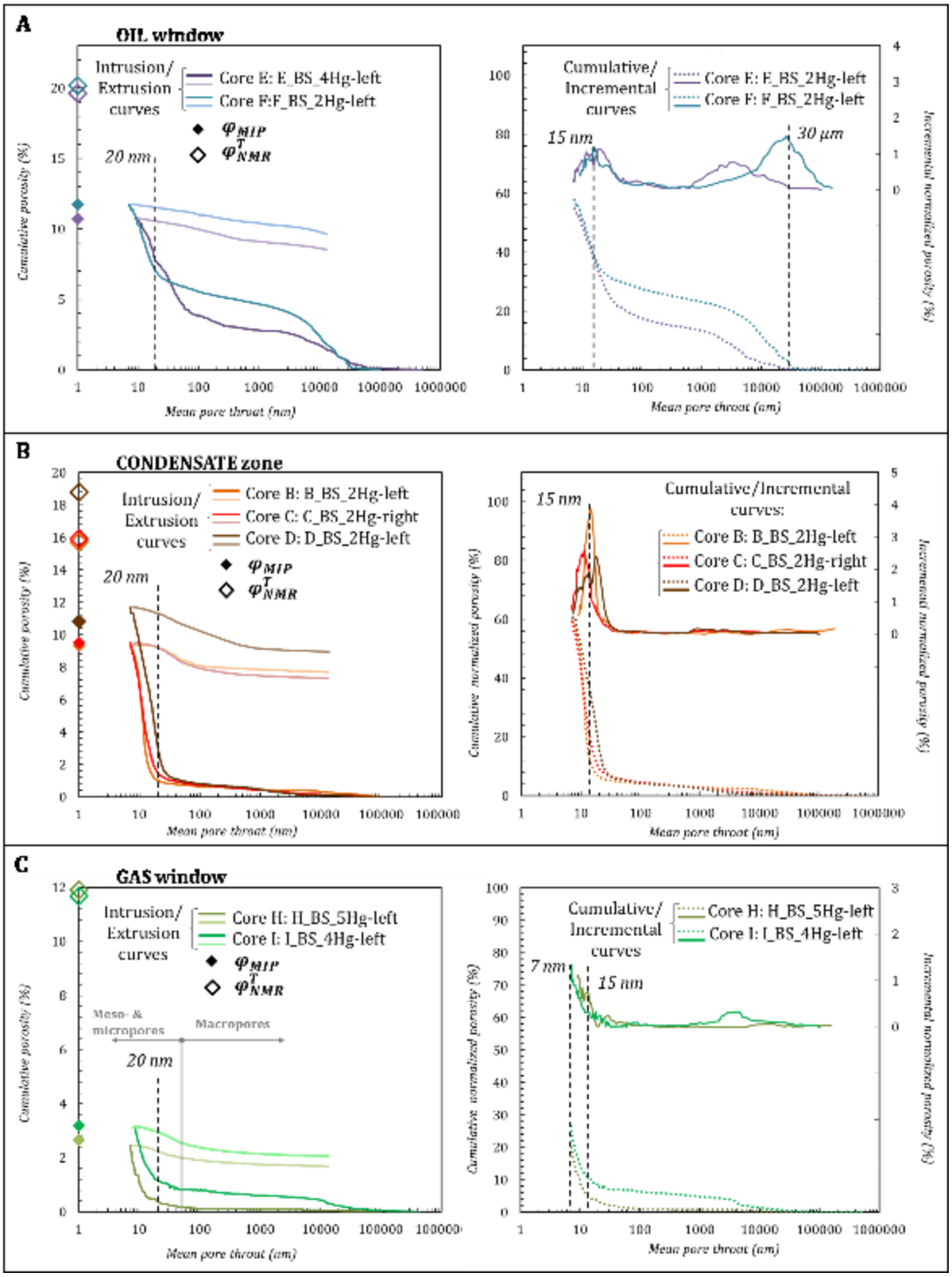

Figure 101. Mercury intrusion porosimetry results for zones of various hydrocarbons production; on the right: non-normalized cumulative intrusion and extrusion curves and porosity values measured by MIP (closed symbols, φ_{MIP}) and total porosity measured on NMR blocks (open symbols, φ^{T}_{NMR}), given for the samples from the same layers of interest; on the left: normalized MIP cumulative intrusion curves (normalized according to the total porosity measured on NMR blocks) and incremental throat size distributions: A) for oil window; B) for condensate zone; C) for dry gas window.

3.2.6. Nitrogen adsorption

Nitrogen gas adsorption was performed to characterize the micropores (not accessible by MIP), mesopores and macropores size distribution up to 640 nm in diameter (Equation 4; Barrett et al., 1951). In the present study nitrogen adsorption isotherms were successfully acquired on five undamaged blocks (Figure 102.A). The isotherms obtained on samples from the different hydrocarbon maturity zones can be described by type IV with a type H2 hysteresis loop (Sing, 1998), indicating the presence of mesopores, even for the gas zone sample (samples H and I). H2 hysteresis (Sing, 1998) is associated with the occurrence of pore-blocking phenomena associated with throats smaller than pore bodies. The intense bump around P/P_0 of 0.42 on desorption branches reflects classical cavitation phenomena for pore throats smaller than 5 nm according to the Kelvin law (Equation 4). For these smallest throats, no size estimation is further possible, but the intensity of the bump is proportional to their content. The large rise of the adsorbed volume at the maximum relative pressure without any plateau indicates that additional large macropores (> 640 nm), which are not accounted for by this technique, leading to the underestimation of the total porosity, (only 40-70% of the total porosity probed by this technique). This is especially the case for sample F from the oil zone (only 47% the total pore volume is probed), within which large cracks with aperture centered on 80 µm were detected by MIP, autoradiography and µtomography (Figure 107). The application of t-plot method (Equation 6; Harkins and Jura, 1944) also reveals a small amount of micropores but only for samples from the dry gas zone, where the microporosity (φ_{Ads}^{μ}) was measured in the 0.3-0.6% range (absolute value). Volumes of the micropores represent 5.6 and 2.7% of the total probed volume of pores for cores H and I, respectively. The cumulative PSD obtained by the BJH treatment (Barrett et al., 1951), applied on adsorption branch, shows that pore sizes are always broadly spread over the mesopores and macropores range (Figure 102.D). The porosity values reached on the cumulative PSD, according the OM maturity, are significantly lower than the φ_{NMR}^{T} values. The cumulative PSD obtained by the BJH, applied on desorption branch, shows that most of the pores throats are less than 10 nm in diameter (Figure 102.C), in agreement with the MIP results.

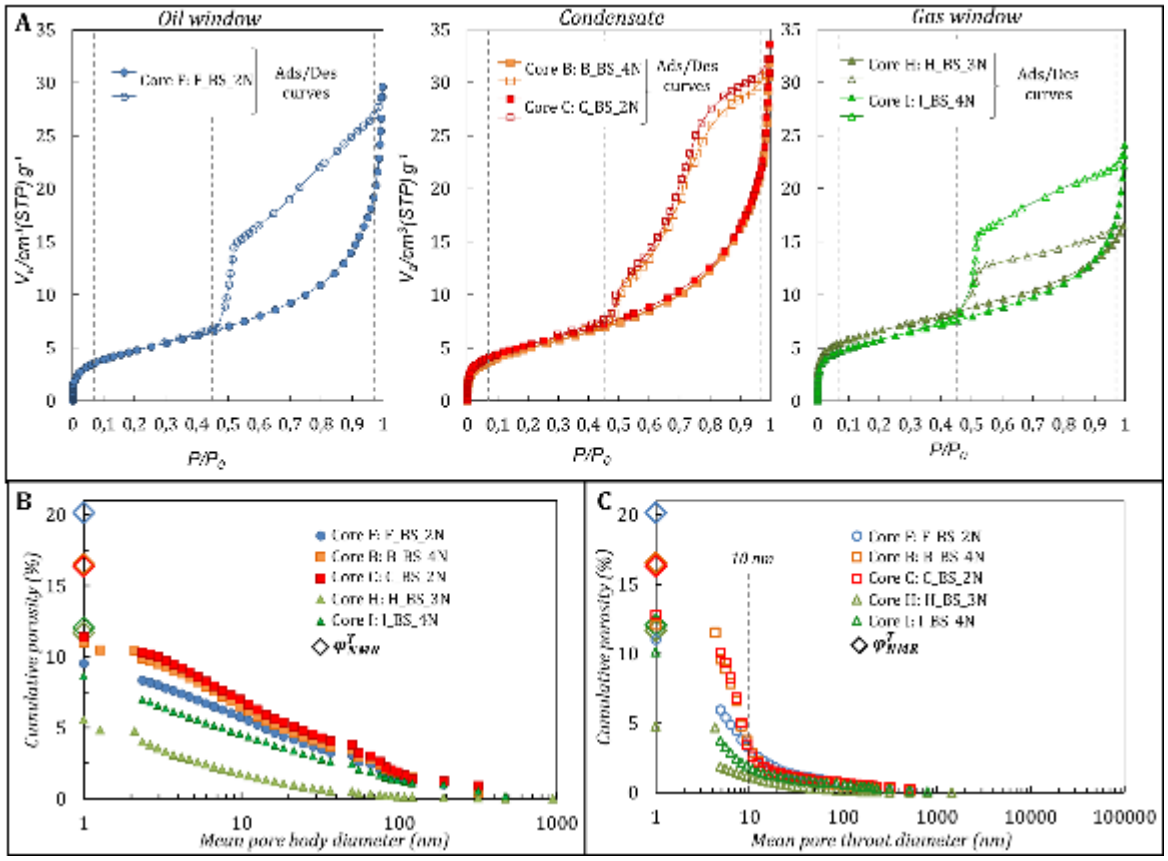

Figure 102. Gas adsorption on blocks of the different localized sub-samples: for oil (circles), condensate (squares) and dry gas (triangles) zones: A) nitrogen adsorption/desorption isotherms; B) cumulative pore body diameter distributions, calculated from the adsorption curves; C) cumulative pore throat diameter distribution calculated from the desorption curves; with indication of total porosity measured by laser on NMR blocks (diamond symbol) for the corresponding layer of interest.

3.2.7. Autoradiography porosity maps

Autoradiography provided (i) measurements of the connected porosity (as NMR technique) and (ii) maps of connected porosity values distribution over the full surfaces (~6 cm height and ~3.5 cm width) of the studied cores. Autoradiography porosity maps for all the polished samples of this study are displayed in Figure 104. The quantitative vertical porosity profiles, extracted from these maps, reveal laminae and layers with contrasted porosity values, illustrating the porosity evolutions over the height of the samples (Figure 104).

For the oil zone sample (core F), a dense crack network is well expressed: it is parallel to the bedding of the sample, likely due to an artifact, induced by the poor core preservation. The local porosity measured for one pixel (10.5 by 10.5 µm) at the location of cracks is a function of their aperture. The thinner the fissure, the lower the pixel

porosity (i.e., closer to the porosity of the surrounding matrix). The change in the cracks density within core F explains the change in local porosity value (19.6% for the top and 22.8% for the bottom) and leads to the bimodal distribution on the pixel value frequency histogram, given in Figure 104. The mode centered at 15% represents the area in between the cracks and the one with higher porosity, centered at 20%, accounts for the distribution of areas associated with cracks. The laminae of varying porosity for this samples are expressed in alternation of red and light blue (porosity of the entire surface is 21.6%).

The samples from the condensate zone (Figure 104) display a "salt and pepper" texture with the presence of non-porous grains (in dark blue). Porosity values calculated for the entire surfaces for the cores B and C are close (16.5 – 16.6%). Sample C exhibits a homogeneous porosity distribution with low local fluctuations on the vertical profile (16.9% to 16.1%, from top to the bottom respectively), while sample B shows higher local fluctuations due to presence of large non-porous grain of few mm (porosity decreases from top to the bottom: 17.1 to 16.0%). Sample D differs significantly from other cores from the condensate zone, exhibiting higher porosity over the full surface (18.7%) with laminae of various porosity, displayed on the vertical profile. Although the selected layers of interest have close porosity values (18.7 and 19.0% for the top and the bottom layers respectively).

Gas window samples can be characterized by lower porosity values (13.4% for the core H and 12.95% for the core I). Sample H shows a relatively homogeneous porosity distribution (here the layers with the highest porosity values are associated with cracks, in red), while core I exhibits a decrease in porosity from top to bottom (13.0% to 12.4%), with the presence of large non-porous calcite "beef" (non-porous dark blue layer at the mid height of core I).

The values of porosity obtained from the autoradiographs represent the connected porosity, reflecting the resin intrusion into the interconnected pore space. The good agreement between the autoradiography porosities ($\varphi_{Auto}^{Con\_L}$), the connected NMR porosities (both, $\varphi_{NMR}^{Con\_Vs}$ and $\varphi_{NMR}^{Con\_Vt}$) and the total porosity values, measured on the same layer of interest by laser on NMR blocks (φ_{NMR}^{T}), confirm the connectivity of the pore space for the studied samples within the selected homogeneous layers of interest (Figure 103).

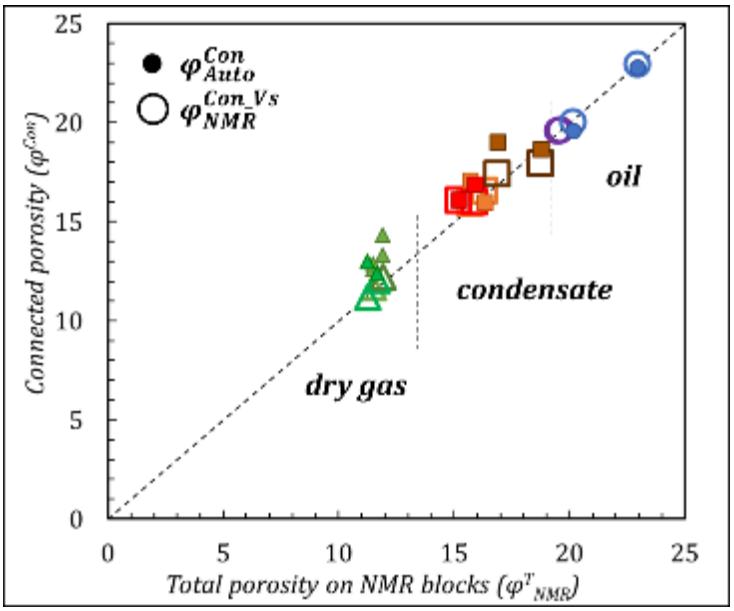

Figure 103. Correlation of the connected porosity (measured by NMR and autoradiography) with total porosity (measured by laser): triangles are for gas zone samples, squares for condensate zone, and circles for oil zone.

It must be noted, that all the layers of interest, selected for these measurements, are highly homogeneous, but not fully representative of the entire core. For instance, the carbonate "beef", located in the middle right of sample I (gas window), shows a porosity value lower than 5 % (Figure 112.D). Consequently, the extrapolation of the conclusion about sample connectivity to the entire core of 7 cm length is questionable for such a heterogenous sample. Meanwhile, some cores (like sample C, Figure 109, condensate zone) exhibit homogeneous microstructure at the scale of autoradiography porosity map and µtomography images, that allows to expect the same connectivity for the entire core as for the measured layers of interest.

In conclusion, the autoradiography porosity maps have provided porosity values, which agree with (i) those obtained from NMR and with (ii) the total porosity values inferred from bulk techniques. Consequently, it can be concluded that all the pore space is interconnected in such organic-rich shales samples. This conclusion is valid as far as porosity has been measured on homogeneous layers, avoiding non-porous carbonates large grains and nodules (Figure 86). Moreover, in this study, while bulk techniques can obtain mean total values for local probes, autoradiography allows to map the spatial fluctuations of total porosity and to visualize heterogeneities at the sample scale for cm fields of view.

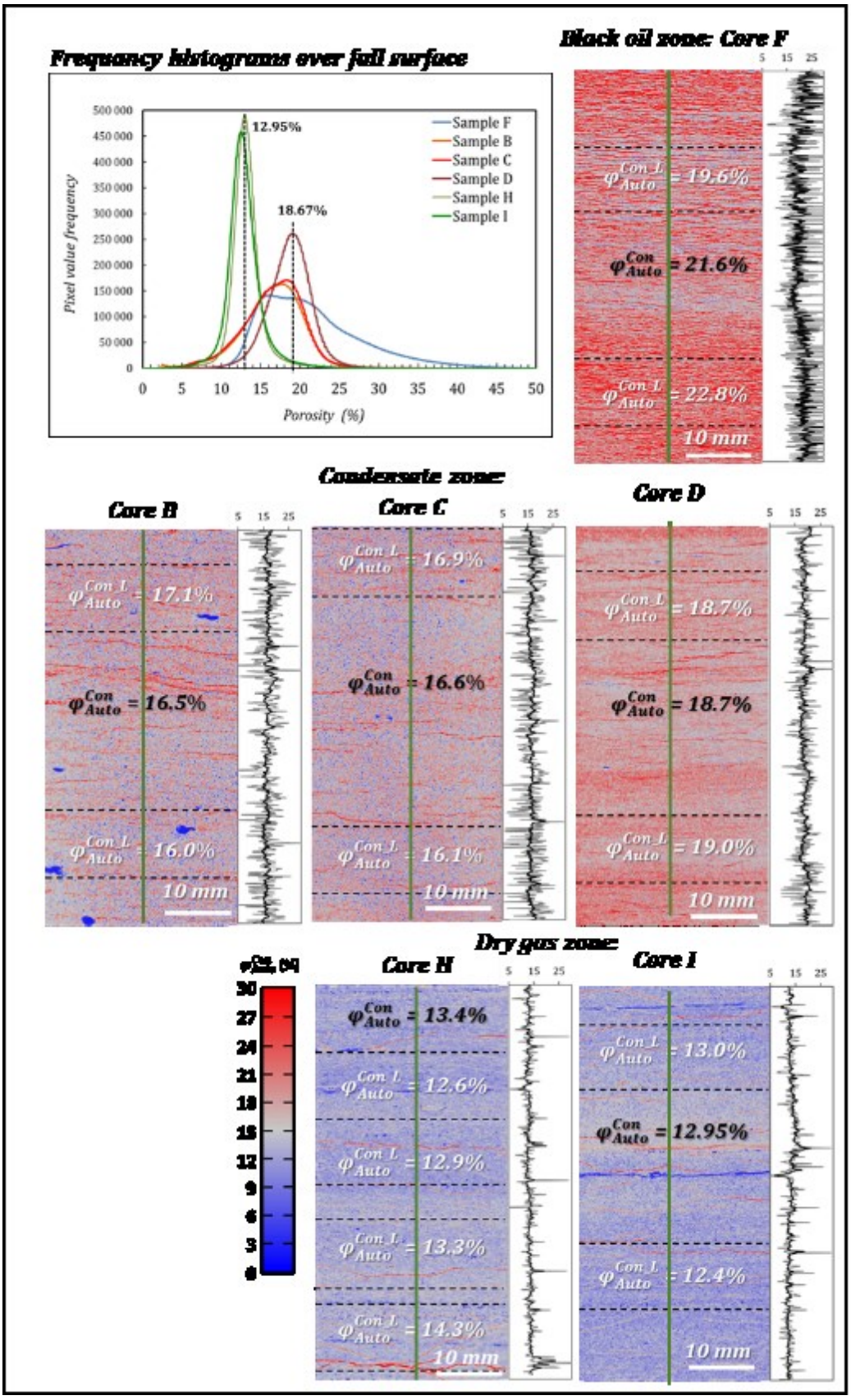

Figure 104. Pixel value frequency histograms over the full surfaces and porosity maps obtained, by autoradiography for core samples with, on their right, a vertical porosity profile through the center of the image (green line; in light gray – profile with 1-pixel width, and in black – profile with 500-pixel width); maps are ranged in 0-30% porosity values; *LUT = Phase*.

3.3. Correlation of autoradiography result with bulk measurements

A multiscale approach has been applied to characterize the porosity and the microstructure of seven samples from VM formation. According to a procedure of 3D µtomography localization, two layers of interest were selected within each core, where bulk measurements have been performed on sub-blocks (Figure 61). Figures 105 to 111 show for each core:

- the localization of the sub-blocks over the µtomography central slice of BS block, correlated with the autoradiography porosity map;
- the pore throat distribution obtained by MIP (intrusion and extrusion curves) and nitrogen desorption curves;
- the pore body size distribution from N_2 adsorption curves;
- the mineral composition of layers of interest.

Figure 106 displays the result of pore network characterization obtained for sample E (oil window), which is one of the two oil samples, not well-preserved after its extraction (the damage is characterized by a network of cracks parallel to the bedding). *LAC* vertical profile through the central slice of the BS block (Figure 106.C) shows a low variability from top to bottom. This variability is expressed by local fluctuations due to the high density of cracks. The total porosity, measured on the NMR blocks, revealed similar porosity values for the layer of interest (19.5% and 19.6% for the top and bottom respectively). Only one measurement of MIP was performed on this core, showing a bimodal pore throats distribution (Figure 106.A) with modes at around 15 nm and 3 µm. The mode at 3µm is consistent with cracks aperture (Figure 106.B). The mercury intrusion porosity is 10.7% and corresponds to 55% of the total porosity (compared with φ_{NMR}^{T}). No nitrogen adsorption measurements are available for this core, neither autoradiography porosity map.

As sample E, sample F (oil window, Figure 107) shows a similar network of cracks parallel to the bedding. It is also due to the poor preservation of the sample. The cracks network is well-illustrated by autoradiography porosity map (Figure 107.D), where porosity vertical profile exhibits high local variations of the porosity. The increase of the clay minerals and decrease of carbonates contents from top to the bottom is consistent with the porosity ($\varphi_{Auto}^{Con\_L}$) increase (from 19.6 to 22.8%). This trend is in the agreement with total porosity, measured on NMR blocks (φ_{NMR}^{T} is 20.17 and 22.95%, for the top and bottom respectively). The increase in porosity values is also well correlated with the change in the cracks intensity, highlighted by autoradiography porosity map. The MIP intrusion curves (Figure 107.A) for the two layers of interest, show similar shapes, but

different absolute values of the maximum intruded volumes, which agree with other measurements (intrusion porosity values (φ_{MIP}) are 11.7 and 12.5%, for the top and bottom respectively). However, these MIP curves underestimate the total porosity (only 58 and 55% of the total porosity probed, compared with φ^{T}_{NMR}). The nitrogen adsorption measurement was performed only on the block from the top layer and provided pore bodies distribution (Figure 107.B), with adsorption porosity (φ_{Ads}= 9.5%) much lower than total one (φ^{T}_{MIP}= 20.2%) for the neighboring block. The combination of the pore throat distribution obtained by MIP and by nitrogen desorption may be nearly matched, when the values about the porosity >640 nm are added to the BJH treated desorption curve. However, the complete pores balances are not obtained (Figure 105.A). The segmentation of cracks from µtomography volume could reveal the missing pores volumes (Figure 105.C). The volume of cracks measured for the same sub-block (virtually cut from the 3D visualized core) is 6.96% ($\varphi^{>100\mu m}_{\mu Tomo}$) for the sub-block used for MIP measurements. But the reliability of this approach is mostly limited by the low contrast between the crack borders and the porous clay matrix (indeed, in practice, it is difficult to rigorously discriminate the cracks borders and porous clay matrix, due to close densities of these phases).

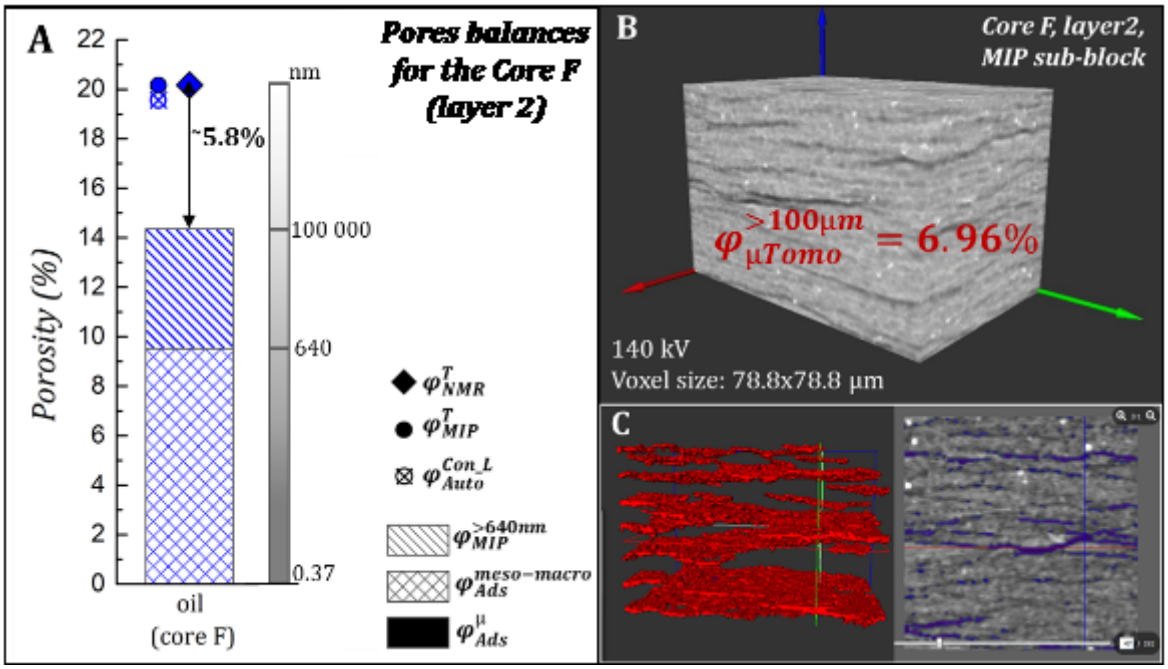

Figure 105. A) Pore balances obtained by combination of various techniques, applied on the sub-block from layer 2, core F (oil window); B) the 3D view of virtual cut of sub-block for MIP measurements; C) segmented cracks within the sub-block for MIP measurements.

Figure 108 displays the results obtained on the sample B (condensate zone). The characterization of this sample, based on *LAC* vertical variation over the core length,

highlights inclusions of the large "heavy" grains (pyrite and carbonates), in agreement with mineral composition, and displays a homogeneous vertical distribution of phases (Figure 108. C). Several MIP measurements were performed on the core B for both layers of interest on the edging homogeneous sub-blocks (Figure 108.A). These MIP measurements provided almost equivalent results of the intrusion porosity (φ_{MIP} = 9.3 – 9.9%), which are consequently lower, than the total porosity values (note, that only 61% of the pores are probed, in comparison with φ^{T}_{NMR}). All the intrusion curves show the same shape. The total porosity calculated from the bulk density, measured by MIP (φ^{T}_{MIP}) and by µtomography ($\varphi^{T}_{\mu Tomo}$) on the same block, provided close results. Nonetheless the total porosity values (φ^{T}_{MIP}) calculated for the two sub-blocks are different with one at 16.7% and the second one at 13.6%. Meanwhile, the highest values are consistent with autoradiography porosity values of the layers. The pore throats distributions obtained by MIP and nitrogen desorption nearly matches, except for the throats smaller than 10 nm in diameter, for which a small discrepancy can be observed. Pore body distribution (Figure 108.B), calculated from the adsorption isotherm, shows that the cumulative porosity continuously decreases when pore diameter increases. The adsorption porosity (φ_{Ads}) is 10.8%, probing only 66% of the total pores volume (compared with φ^{T}_{NMR}). The autoradiography porosity map reveals the slight decrease of the porosity from top to the bottom of the core ($\varphi^{Con\_L}_{Auto}$ is decreasing from 17.1 to 16.0% respectively), with the lamination highlighted.

Sample C (condensate zone, Figure 109) is the most homogeneous core. This homogeneity is especially demonstrated by the low local fluctuations of *LAC* (Figure 109.C). The mineral composition does not exhibit discrepancies in phases distribution from top to the bottom. The MIP and nitrogen adsorption measurements were performed only on the neighboring blocks located at the top layer. Mercury intrusion (φ_{MIP}) and N_2 adsorption (φ_{Ads}) porosities (9.5 and 11.6% respectively), both underestimate the total porosity, measured on NMR block (φ^{T}_{NMR} =15.9%). Nonetheless the total porosity calculated with bulk density obtained by MIP (φ^{T}_{MIP}) is consistent with the autoradiography porosity ($\varphi^{Con\_L}_{Auto}$) value (14.7% and 16.9% respectively) for the same layer of interest. Pore throats distributions measured by MIP and nitrogen desorption matches for the pore throats >20 nm (Figure 109.A). As for sample B, pore body distribution (Figure 109.B) shows, that the porosity continuously decreases when pore diameter increases. The autoradiography porosity map confirmed the homogeneity of the core, here the porosity ($\varphi^{Con\_L}_{Auto}$) slightly decreases from 16.9 to 16.1% (calculated for the top and bottom layers respectively).

Sample D (condensate zone, Figure 110) exhibits a homogeneous *LAC* profile with local fluctuations at the "heavy" grains (carbonates and pyrite), which are homogeneously distributed over the core length (Figure 110.C). Mineralogical analysis does not reveal

high variation in composition from top to the bottom. Several MIP measurements were carried out on the core D at both layers of interest on the neighboring homogeneous blocks (Figure 110.C), providing comparable results of mercury intrusion porosity (φ_{MIP}= 10.0 – 11.2%). These porosity values are consequently lower than total porosity values (only 58-61% of the pore volume is probed, in comparison with φ^{T}_{NMR}). All the intrusion curves show the same shape (Figure 110.A). The pore throats distribution (Figure 110.B) is monomodal with a mode around 15 nm for all measured blocks. No nitrogen adsorption measurements are available for this core. The total porosities calculated based on bulk density, measured by MIP (φ^{T}_{MIP}) and by µtomography ($\varphi^{T}_{\mu Tomo}$) on the same block, provide a close result (φ^{T}_{MIP}=16.7% and $\varphi^{T}_{\mu Tomo}$=17.2 for the layer 2; φ^{T}_{MIP}= 16.4% and $\varphi^{T}_{\mu Tomo}$= 15.4% for the layer 4). The MIP measurements indicate comparable results for the both layers of interest (φ_{MIP}= 10.8% for the layer 2, and φ_{MIP}=10.4% for the layer 4). These porosity values are significantly lower than autoradiography porosity values, which demonstrate a higher variation ($\varphi^{Con\_L}_{Auto}$ is 18.65% and 19.0% for the top and bottom respectively) (Figure 110.D). However, the autoradiography map reveals some laminations within the sample with layers with higher and lower porosity (white and blue laminations). And as for the sample B total porosity values (φ^{T}_{MIP}) vary from block to block in the same layer (from 16.4 to 19.7% for two neighboring blocks in the layer 4), demonstrating the lateral variability and the representativity of data.

Samples H and I (gas window, Figure 111 and Figure 112 respectively), both exhibit the lowest porosity values within the set of samples. In sample H (Figure 111), *LAC* values display a significant variability along the vertical profile associated with local presences of "heavy" grains and cracks (Figure 111.C). The MIP intrusion curves on the neighboring blocks (Figure 111.A) from the bottom layer of interest (the measurement for the top layer has been failed, orange block, Figure 111.C) have the same shape with variations of the intrusion porosity (φ_{MIP}), and in agreement with the presence of cracks, which can be observed on the µtomography 2D view (Figure 111.C). The intrusion porosity (φ_{MIP}), strongly underestimates the total one (only 5 to 20% of the total pore volume is probed), indicating that most of the pores throats are less than 7 nm in diameter and not accessible by MIP. The pore throat size distribution estimated by MIP and nitrogen desorption cannot be compared directly, since they have been obtained for different layers of interest (they only match for throats >40 nm in diameter). Pore body distribution (Figure 111.B) demonstrates that porosity continuously increases when pore dimeter decreases. Adsorption porosity (φ_{Ads}) is 6.1%, probing 43% of the total pore volume (compared with φ^{T}_{NMR}). Micropores have been detected with an absolute value of the micropores volume (φ^{μ}_{Ads}) of 0.65%. The total porosity calculated with bulk density, measured by mercury (φ^{T}_{MIP}) and by µtomography ($\varphi^{T}_{\mu Tomo}$) on the same block, provided a close result (12.0%

and 10.9% respectively). These results agree with autoradiography porosity ($\varphi_{Auto}^{Con\_L}$) and are well-correlated with other measurements (Figure 111.D). The total porosity obtained on the full surface is 13.4%, some variations from layer to layer are measured with the following values 12.6%, 12.9%, 13.3% and 14.3%, from top to the bottom respectively. This variation may be linked with the distribution of cracks over the layers.

Sample I (Figure 112), is expected to be homogeneous on the basis of *LAC* distribution over the core length, which is agreement with the quantitative mineralogy measurements (Figure 112.C). The MIP intrusion curve (Figure 112.A) was obtained only for the bottom layer and does not match very well the pore throat distribution obtained by nitrogen desorption. The mercury intrusion porosity (φ_{MIP} = 3.2%) and nitrogen adsorption porosity (φ_{Ads} = 8.7%), both strongly underestimate the total one (φ_{NMR}^{T}= 11.7%, measured on NMR block). Pore body distribution (Figure 112.B) shows a continuous evolution, like the other cores. Low micropores volumes detected (micropores volume in absolute values, φ_{Ads}^{μ}, is 0.32%,). Considering the profile, plotted on the autoradiography surface (Figure 112.D, green line) the local increase of porosity is well correlated with the presence of cracks, which can be distinguished on both, µtomography slices and autoradiography porosity maps. The minimum porosity values here are associated with the presence of carbonate “beef” layers, which appear in dark blue on the porosity map with porosity < 5 % on the profile.

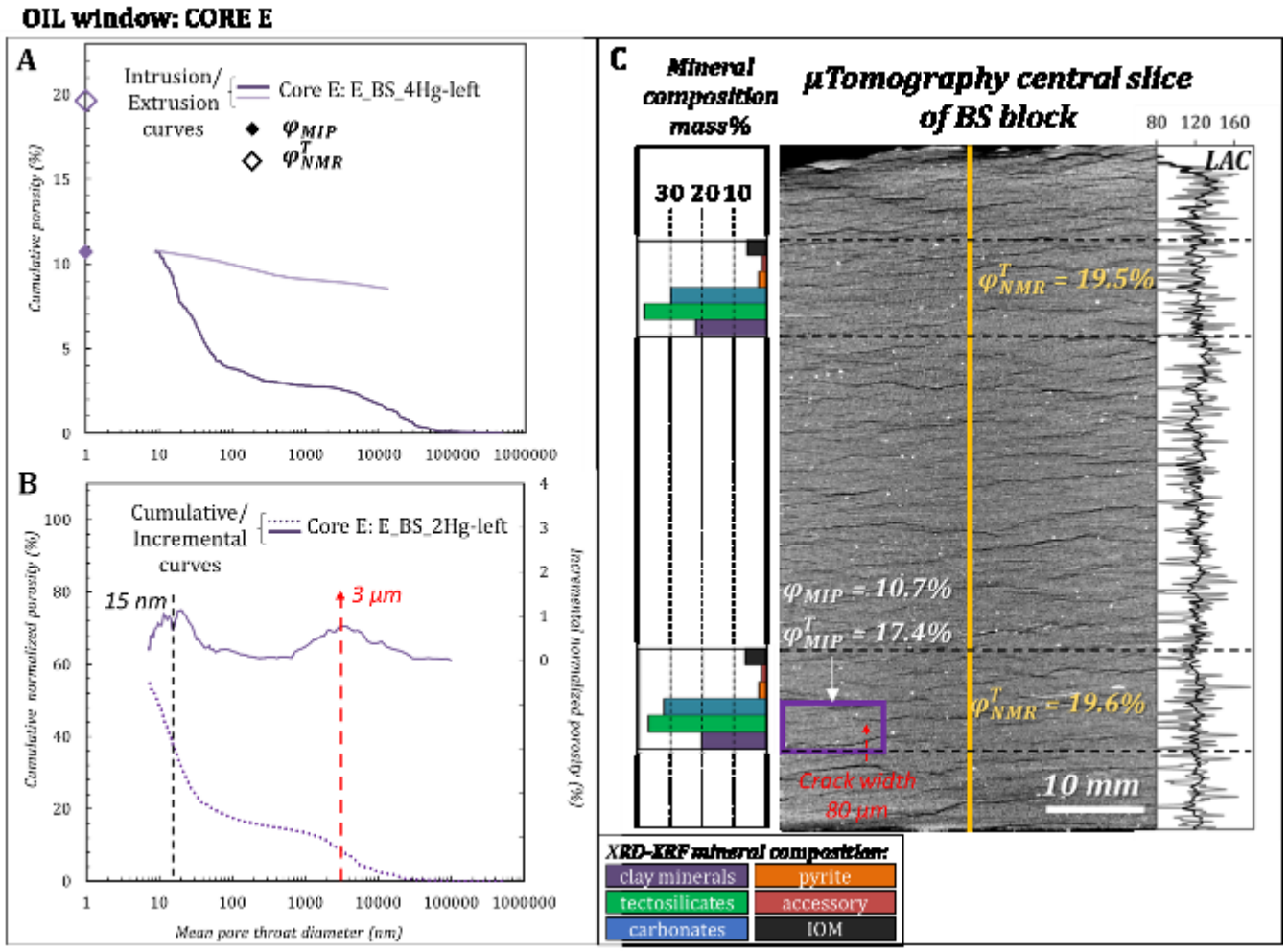

Figure 106. Core sample E (oil window): A) MIP intrusion and extrusion curves; open diamond symbol is for the MIP intrusion porosity (φ_{MIP}), close diamond – for total porosity on NMR blocks (φ^{T}_{NMR}); B) normalized MIP cumulative intrusion curve and incremental throat size distribution; C) μtomography central slice of BS block with the localization of sub-blocks positions and obtained porosity values; mineral composition is indicated for the layers of interest; on the right: *LAC* profile plotted through the center of the core (yellow line).

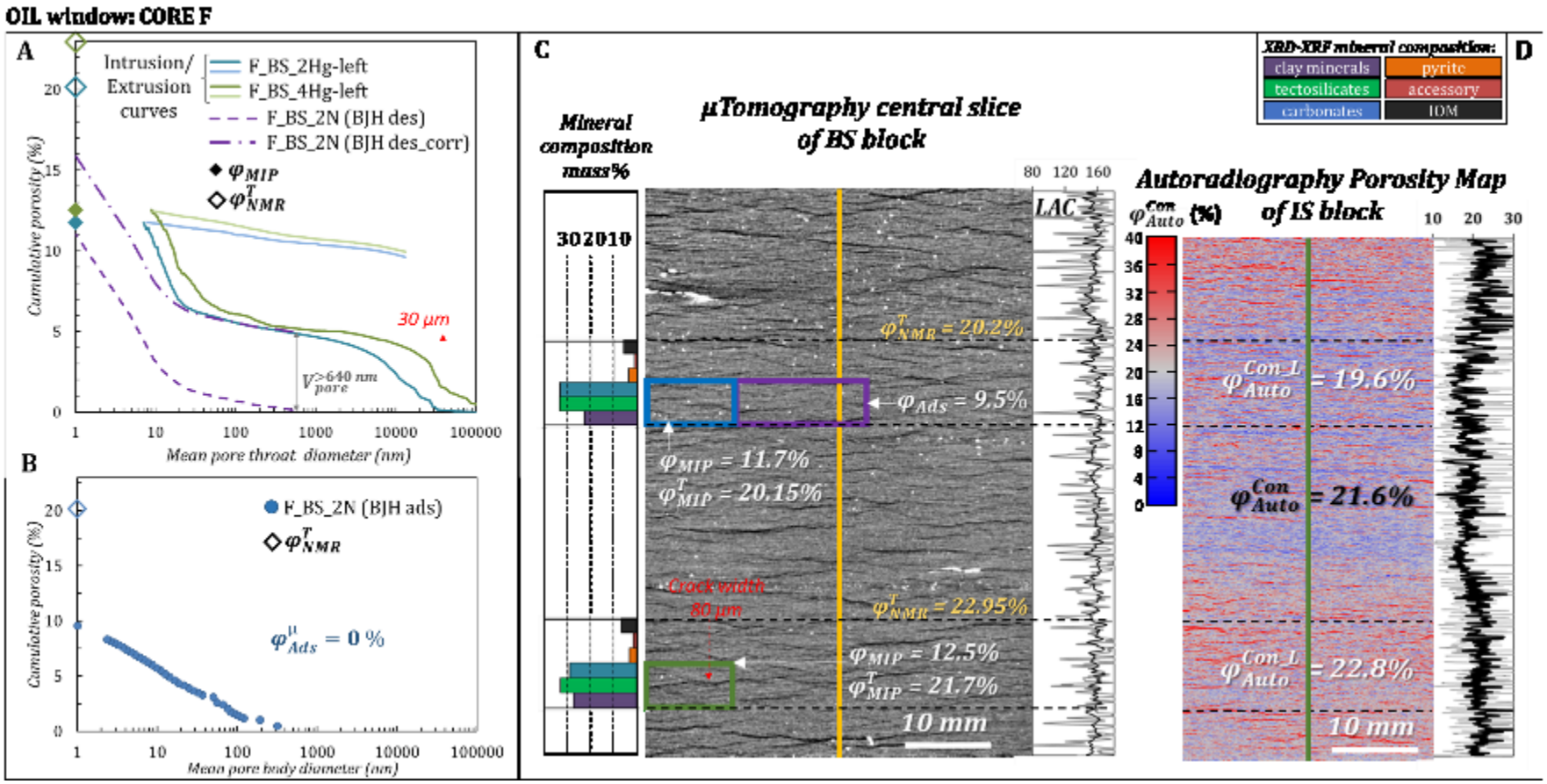

Figure 107. Core sample F (oil window): A) MIP intrusion and extrusion curves; BJH pore throat distribution from N_2 desorption curve; open diamond symbol is for the MIP intrusion porosity (φ_{MIP}), close diamond – for total porosity on NMR blocks (φ^{T}_{NMR}); B) BJH pore body size distribution from N_2 adsorption curve; C) μtomography central slice of BS block with the localization of the sub-blocks positions (colors are corresponding to the color of the curve from the PSD) and obtained porosity values; mineral composition is indicated for the layers of interest; on the right: *LAC* profile plotted through the center of the core (yellow line); D) porosity map obtained by autoradiography with a vertical porosity profile through the center of the image (green line).

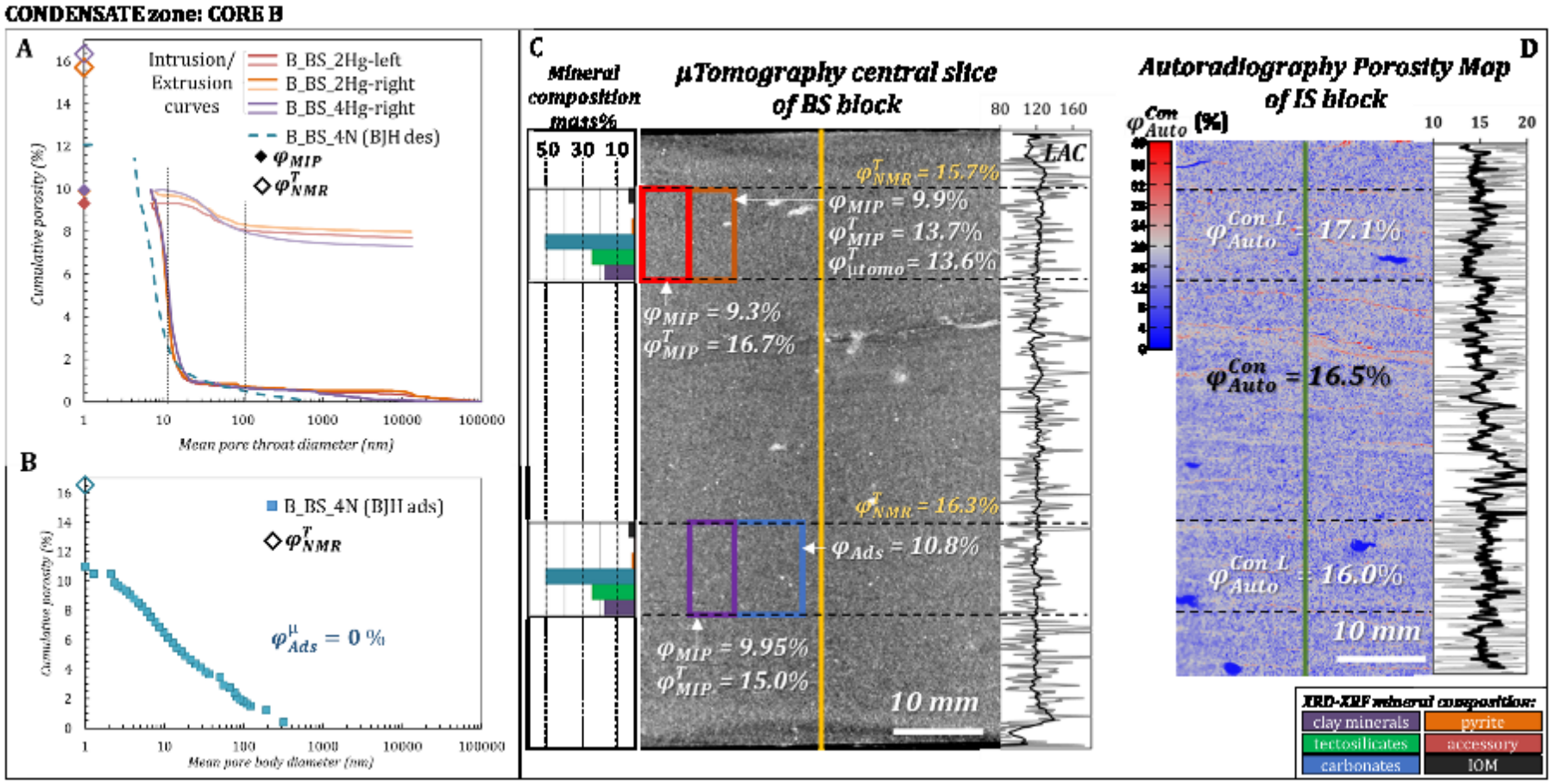

Figure 108. Core sample B (condensate zone): A) MIP intrusion and extrusion curves; BJH pore throat distribution from N_2 desorption curve; open diamond symbol is for the MIP intrusion porosity (φ_{MIP}), close diamond – for total porosity on NMR blocks (φ^{T}_{NMR}); B) BJH pore body size distribution from N_2 adsorption curve; C) µtomography central slice of BS block with the localization of the sub-blocks positions (colors are corresponding to the color of the curve from the PSD) and obtained porosity values; mineral composition is indicated for the layers of interest; on the right: *LAC* profile plotted through the center of the core (yellow line); D) porosity map obtained by autoradiography with a vertical porosity profile through the center of the image (green line).

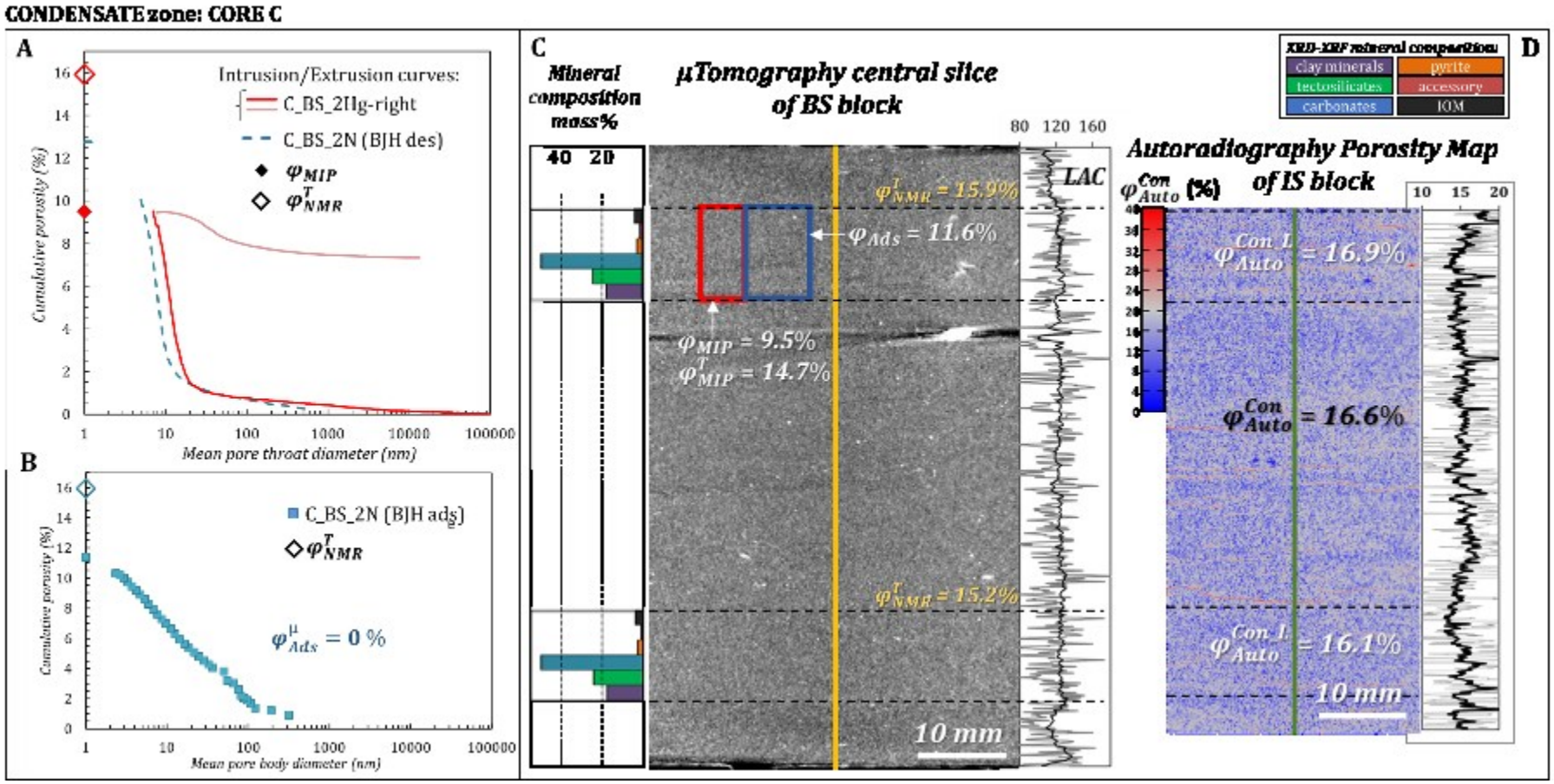

Figure 109. Core sample C (condensate zone): A) MIP intrusion and extrusion curves; BJH pore throat distribution from N_2 desorption curve; open diamond symbol is for the MIP intrusion porosity (φ_{MIP}), close diamond – for total porosity on NMR blocks (φ^{T}_{NMR}); B) BJH pore body size distribution from N_2 adsorption curve; C) µtomography central slice of BS block with the localization of the sub-blocks positions (colors are corresponding to the color of the curve from the PSD) and obtained porosity values; mineral composition is indicated for the layers of interest; on the right: *LAC* profile plotted through the center of the core (yellow line); D) porosity map obtained by autoradiography with a vertical porosity profile through the center of the image (green line).

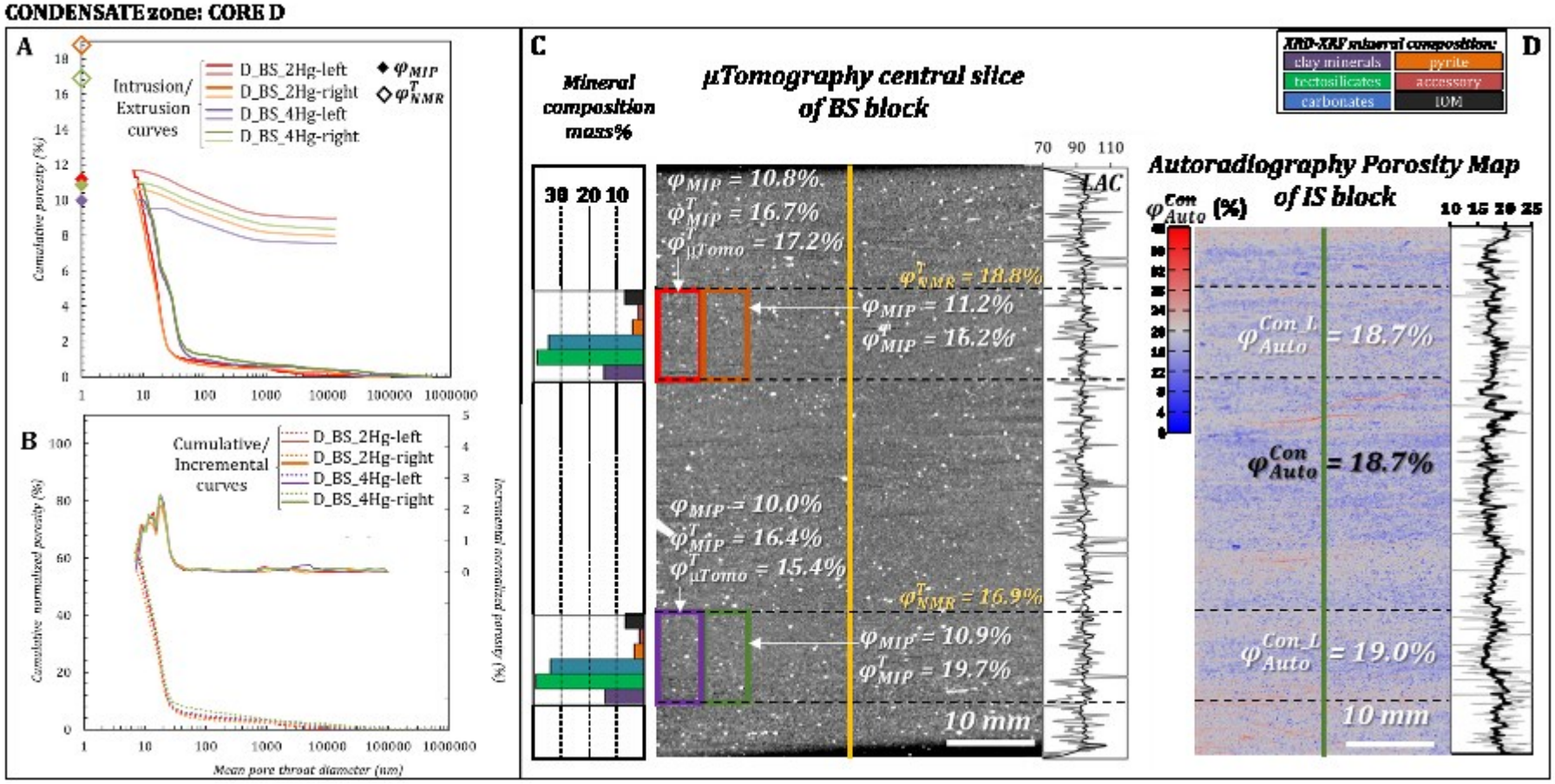

Figure 110. Core sample D (condensate zone): A) MIP intrusion and extrusion curves; open diamond symbol is for the MIP intrusion porosity (φ_{MIP}), close diamond – for total porosity on NMR blocks (φ^{T}_{NMR}); B) normalized MIP cumulative intrusion curve and incremental throat size distribution; C) μtomography central slice of BS block with the localization of the sub-blocks positions (colors are corresponding to the color of the curve from the PSD) and obtained porosity values; mineral composition is indicated for the layers of interest; on the right: *LAC* profile plotted through the center of the core (yellow line); D) porosity map obtained by autoradiography with a vertical porosity profile through the center of the image (green line).

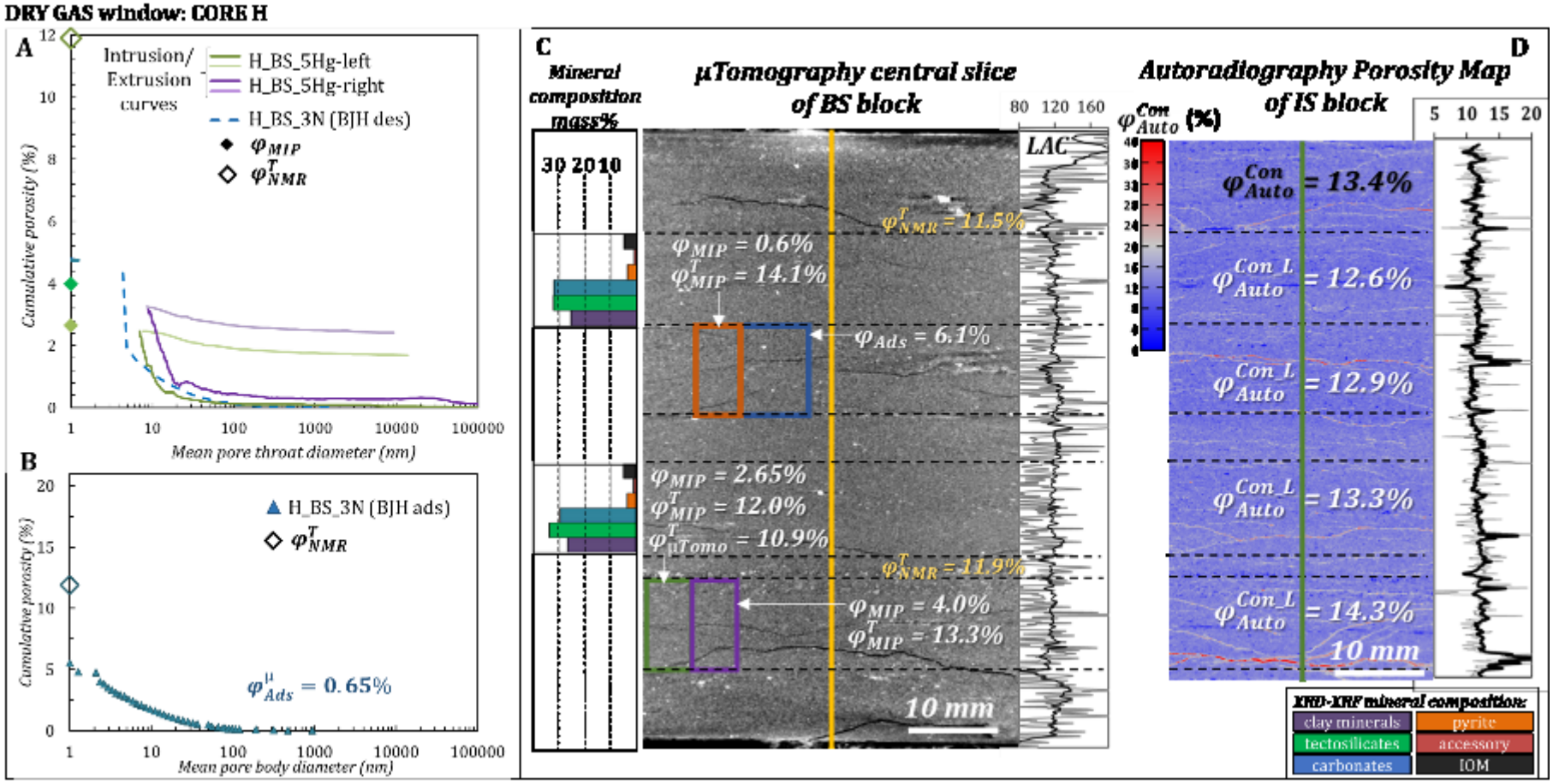

Figure 111. Core sample H (gas window): A) MIP intrusion and extrusion curves; BJH pore throat distribution from N_2 desorption curve; open diamond symbol is for the MIP intrusion porosity (φ_{MIP}), close diamond – for total porosity on NMR blocks (φ^{T}_{NMR}); B) BJH pore body size distribution from N_2 adsorption curve; C) µtomography central slice of BS block with the localization of the sub-blocks positions (colors are corresponding to the color of the curve from the PSD, test on orange block was failed) and obtained porosity values; mineral composition is indicated for the layers of interest; on the right: *LAC* profile plotted through the center of the core (yellow line); D) porosity map obtained by autoradiography with a vertical porosity profile through the center of the image (green line).

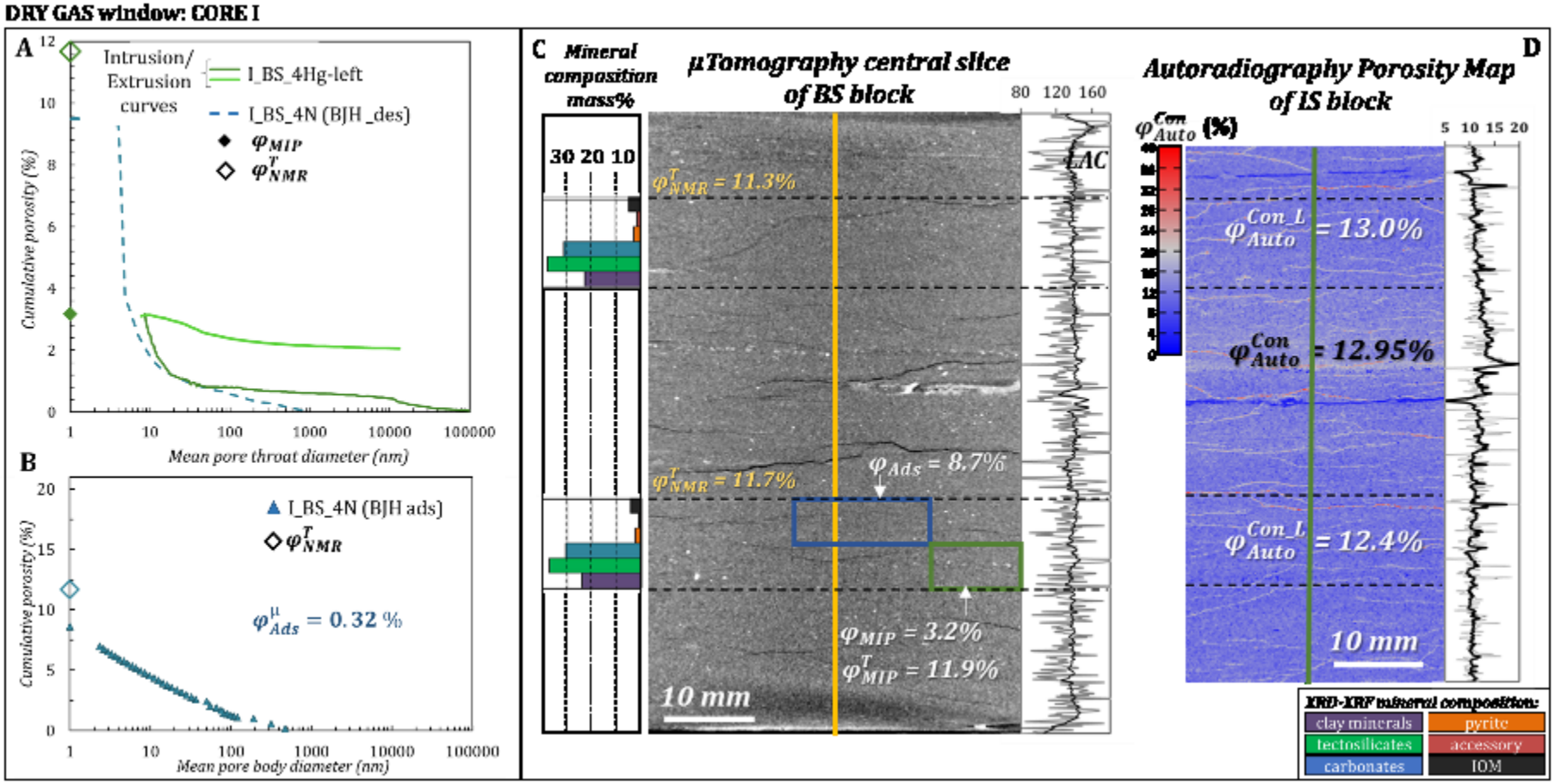

Figure 112. Core sample I (gas window): A) MIP intrusion and extrusion curves; open diamond symbol is for the MIP intrusion porosity (φ_{MIP}), close diamond – for total porosity on NMR blocks (φ^{T}_{NMR}); B) normalized MIP cumulative intrusion curve and incremental throat size distribution; C) µtomography central slice of BS block with the localization of the sub-blocks positions (colors are corresponding to the color of the curve from the PSD) and obtained porosity values; mineral composition is indicated for the layers of interest; on the right: *LAC* profile plotted through the center of the core (yellow line); D) porosity map obtained by autoradiography with a vertical porosity profile through the center of the image (green line).

Conclusions

An integrated downscaling approach for analyzing the pore volume of unconventional gas/oil samples with heterogeneous and multiscale pore networks was successfully applied in this work on seven core samples from the Vaca Muerta formation. The application of bulk methods on localized comparable sub-samples allowed to achieve the complete quantitative pore balances and pore size distributions. These bulk measurements were combined with quantitative autoradiography porosity maps, that have allowed to confirm the reliability of the bulk result and to obtain the porosity distribution over large fields of view at the core scale. Moreover, the accurate localization of the analyzed samples has allowed to show that even with the choice of comparable sub-blocks some discrepancies could exist between neighboring sub-blocks. These differences of porosity reveal the scale of variability, in both vertical and lateral dimensions, and thus allows to conclude, that the size and the localization of subsampling is crucial for any measurements on shale samples.

Autoradiography and NMR also clearly indicate that the total pore volume is fully interconnected from micro- to macropores in the samples of the Vaca Muerta formation whatever their hydrocarbon maturity. The multitool & multiscale approach can quantitatively describe the pore balances of such organic rich shale samples. Moreover, for the pore network being fully connected, autoradiography affords the possibility to map the total porosity over the size of a core (25 cm^2) with a micrometric resolution, when areas with large non-porous grains and carbonates nodules are avoided. The distribution of the total porosity is thus accessible, allowing to visualize the different heterogeneities. At this step, the intercomparison of porosity map with mineralogical map could improve the description of the microstructure by correlating pore volumes and organic/inorganic phases. This intercomparison could allow to access the missing porosity range, obtained on the balances. Such a way will be done by the acquisition of 2D phases distribution through SEM mosaics images. The correlation between the porosity and mineralogical maps at sub-micrometer scale is present in chapter 4. The intercomparison of autoradiography and SEM mosaics may reveal the spatial relationships between the measured porosity values and phases distribution (both organic and mineral) within the samples. These spatial relationships could allow to extrapolate the bulk measurements, obtained for the selected layers of interest to the entire core length, upscaling the information from the laboratory sample to the core. These relationships could also contribute to a better characterization and understanding of the evolution of the pore network with organic matter maturation. To be able to fully characterize the pore network, and to identify the factors controlling the spatial

fluctuations of porosity at the mm-μm scale, the SEM mosaics are acquired for large representative areas.

Chapter 4 Multiscale correlation of minerals and porosity distribution

Introduction

The characterization of pore volume of such a heterogeneous shale requires a multitool approach to access it at a multiscale. While the bulk methods provide various information about total porosity and pore size distribution on large representative samples, each method by itself is covering only specified range of pores. To obtain a multiscale description of pore network and complete pore balances, several methods must be combined. Meanwhile, bulk measurements provide the information about the porosity and pore size distributions, but do not reveal the association of the pores distribution with the solid phases, detected by XRD-XRF method (see section 2.2.2), and no information about the spatial distribution of the microstructural heterogeneities is accessible.

In this chapter, the correlative approach developed for coupling bulk results about mineralogy and porosity will be used, and extended to imaging technics, in order to identify the relationships between solid and pore distribution at different scales. The imaging techniques are the only suitable tool for providing the spatial information about the pore volume. Autoradiography supplies the porosity maps, which demonstrate the connected porosity distribution over the core scale. To achieve the local information, SEM images have been acquired on the same mechanically polished surface, where the autoradiography expositions have been done. The performance of both, SEM and autoradiography, on the same surface, allows the direct intercomparison of the mineral phases and porosity spatial distribution at the grain scale. In addition, the analysis of the largest pores range (>640 nm) is expected.

4.1. Integrated multiscale approach

The selected core samples, based on well log data, are approximately 7 cm in length. Meanwhile, the information, obtained by logging tools (Table 9; Chapter 2, section 2.1.2), about the porosity and mineral composition of these cores, has the maximum resolution at ~0.1 m (~1 m – for the neutron log, and ~0.1 m – for the density log, Schlumberger, 1991b). Such a resolution allows a potential spatial correlation at the sedimentary basin scale (Robinet et al., 2015).

For the possible intercorrelation of the data at the core scale, each sub-sample was carefully selected, using µtomography (see section 2.2.1). As it was described, for each

core, investigated in the present study, two homogeneous layers of interest were identified, where all the bulk measurements were done.

Several methods were combined to obtain the information about quantitative porosity and mineralogy at a multiscale (Table 19). Samples used for bulk methods proved to be representative of each homogeneous sedimentary layer for heterogeneous cores. This correlative approach allows a potential spatial correlation at the core/large sedimentary lamina scales.

Table 19. Penetration methods limitations and assumptions used in literature for shale samples characterization.

Method	**Penetrating fluid**	**Volume of the probe**	**Pores probed, nm**	**Modell applied**	**Information**	**Assumptions applied**
Pycnometry	He	mm-cm	10^7-0.256		Grain density	
MIP	Hg	mm-cm	10^5 – 3	Washburn's equation d=f(Pi) Bunch of cylinders	- Pore throat distribution, - Pore-to-body ratio - Bulk density	- no Hg/sample interactions
Gas adsorption	N_2	mm-cm	200-0.37	Kelvin's equation BJH	Pore body distribution Pore throats distribution Microporosity Mesoporosity PSD	- Cylinders - Perfect wetting - Liquid state at the pores
NMR	NaCl solution	mm-cm	10^7-0.265		Connected accessible porosity	
Autoradio-graphy	^{14}C-MMA	mm-cm	10^7 – 0.343	non	Connected porosity value	-Uniform grain density - Uniform density of resin

Autoradiography is an imaging technique, where each pixel provides the information about the local connected porosity at the core scale, and which includes all the pores, even interlayer and micropores. Meanwhile, the pore size, probed by autoradiography, is limited by the molecular size of the resin, used for the impregnation (see section 1.3.3). However, the spatial resolution of the obtained porosity map is limited by the lateral range of beta particles emitted by ^{14}C (around 120µm in solid phases), which induce a blurring of the images (Table 20).

Table 20. Imaging techniques and achieved resolutions.

Method	**Field of view, cm²**	**Pixel/ voxel size, µm**	**Information**
Autoradiography	~25	10.65	Connected porosity
µTomography	~49	78.8	LAC
	~1.5	17.65	
CFM	0.0018	0.13	Z topography (resolution 2 nm)
SEM mosaics	0.6-1.9	0.16	BSE coefficient

To obtain the information about the porosity associated with various solid phases at the grain (µm) and at the sedimentary lamina (mm-cm) scales, large field BSE-SEM mosaics were acquired to produce minerals and pores maps to be compared with the autoradiography porosity maps (Figure 113). The BSE-SEM mosaic and autoradiography porosity maps, both are perfectly localized within the surface of impregnated IS blocks. This superimposition allows to locally correlate the mineral composition, obtained on sub-areas (i.e. a window), with the local connected porosity value measured by autoradiography. This mineral/porosity correlation is done through sliding window method, which discretizes the whole surface according to a definite square sliding window. By displacing such a sliding window simultaneously over both surfaces, the local correlation of the porosity and phase contents variations can be analyzed.

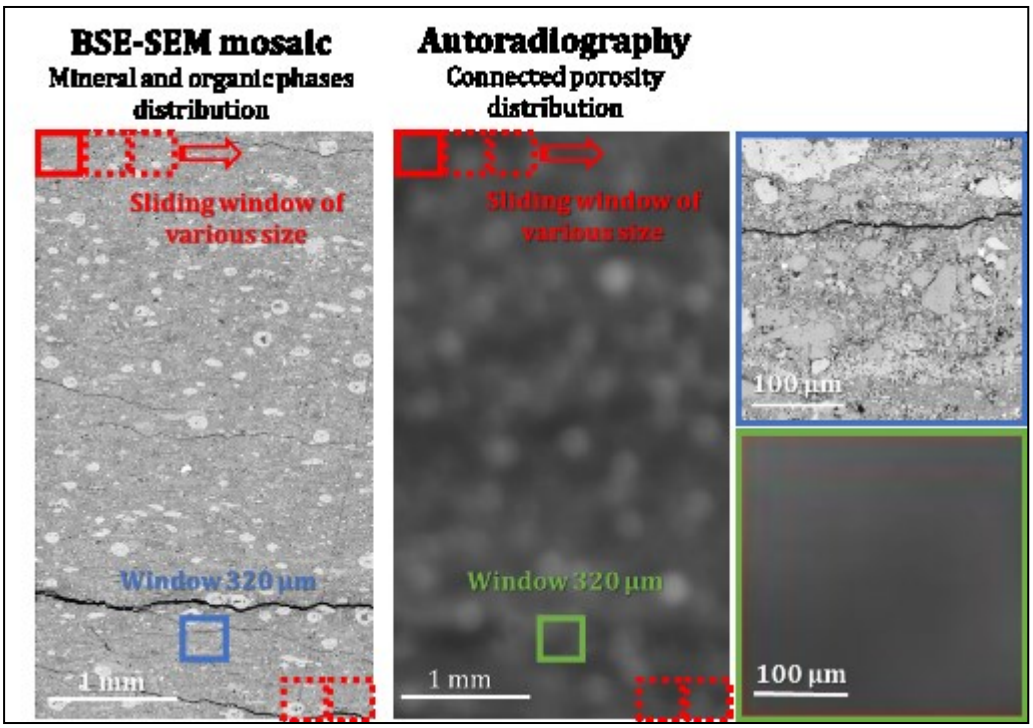

Figure 113. A scheme of correlative mineralogical and porosity quantification throught the comparison of autoradiography and SEM mosaic results.

4.2. Correlation of porosity and mineralogy at the core scale (cm-dm)

Measurements of the porosity by bulk methods provide the punctual information (i.e. homogenized mean value) about the porosity for the centimetric layers of interest, allowing the evaluation of the porosity at the core large lamina scales. Quantitative bulk mineralogy obtained by XRD-XRF on powder localized samples (PS block, Figure 61.A) revealed mineral composition (i.e. homogenized mean value) with quartz, albite, carbonates, pyrite, clay and accessory minerals, as mineral phases. Over this mineral composition, while clay matrix and solid organic phases are expected to be highly porous, other minerals are generally non-porous or contain negligible volume of pores (Prêt et al., 2010a; Prêt et al., 2010b; Robinet et al., 2012; Loucks et al., 2012; Pommer and Milliken, 2015). According to the correlative coupling in 3D of this full set of bulk results (see section 2.2.1), the volumetric contents of both, porous and non-porous (or nearly non-porous), phases were directly compared with total porosity (Figure 114), calculated for NMR blocks (see section 2.2.10).

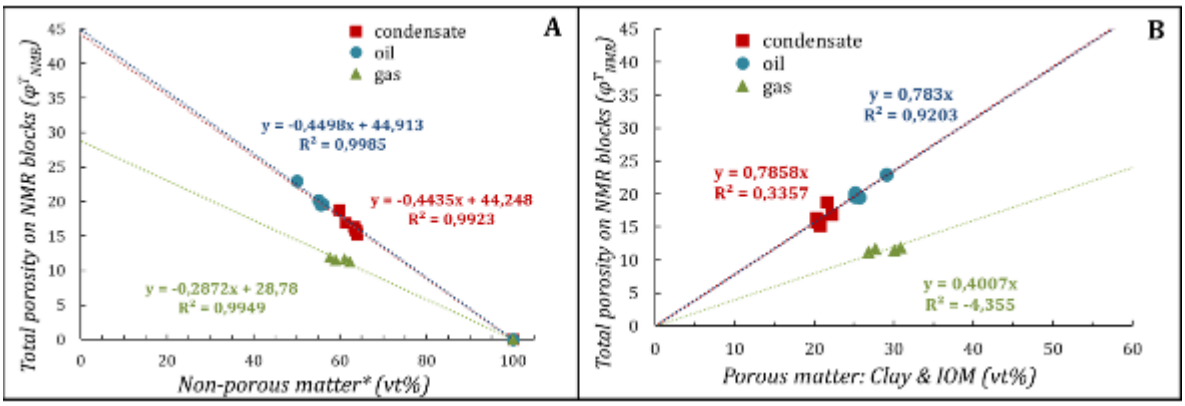

Figure 114. Correlation of total porosity measured on NMR blocks with mineral composition for the same layers of interes, measured by XRD-XRF method: A) non-porous matter volumetric contents (*sum of quartz, albite, carbonates, pyrite and accessory minerals); B) porous matter (clay minerals and IOM) volumetric contents. Circles are for samples from oil window; squares – for condensate zone; and triangles – for the dry gas window.

A positive correlation was obtained between total porosity and volume content of porous phases (clay and OM), when considering the sum of both (Figure 114.A), for all the samples Such an observation confirms that the pore network is mainly hosted within these phases. The volume contents (vt%) correspond to the volume of the solids without accounting the pores. The XRD measurements, expressed in mass%, are basically converted by using theoretical grain density for each component. The evaluation of the specific porosity of this porous matter is, thus, not straightforward. When plotting the total porosity as a function of the volume content of the sum of the other phases, which are assumed as non-porous, a perfect negative correlation is observed. Assuming only porous matter (clay and OM) in composition of the samples (volume of non-porous phase is 0%), the specific porosity of matrix can be estimated by the intercept of the linear trend with the vertical plot axis (Figure 114.B). Samples from oil and condensate zones demonstrate nearly the same trend, indicating the porosity of clay and OM matrix at 44% and 45% for samples from condensate zone and oil window, respectively. Significantly lower specific porosity of the matrix was found for the samples from dry gas window (around 29%). Such a low matrix porosity for the dry gas window could be due to (i) an easier compaction when organic liquids are released upon dry gas generation; or (ii) similar type of sedimentary deposition processes for the oil and condensate samples studied, which contrast with the dry gas samples ones.

4.3. Large field mineral mapping from SEM-BSE mosaics

The acquisition of the large field FEG-SEM mosaics on the surfaces, from which autoradiography images were acquired, has been described in the section 2.2.11. The choice of the mapped areas for one sample per hydrocarbon production zone was done to cover large variations of porosity detected on the autoradiograph profiles and to overlap the previously analyzed layers where bulk porosity measurements have been applied (Figure 115).

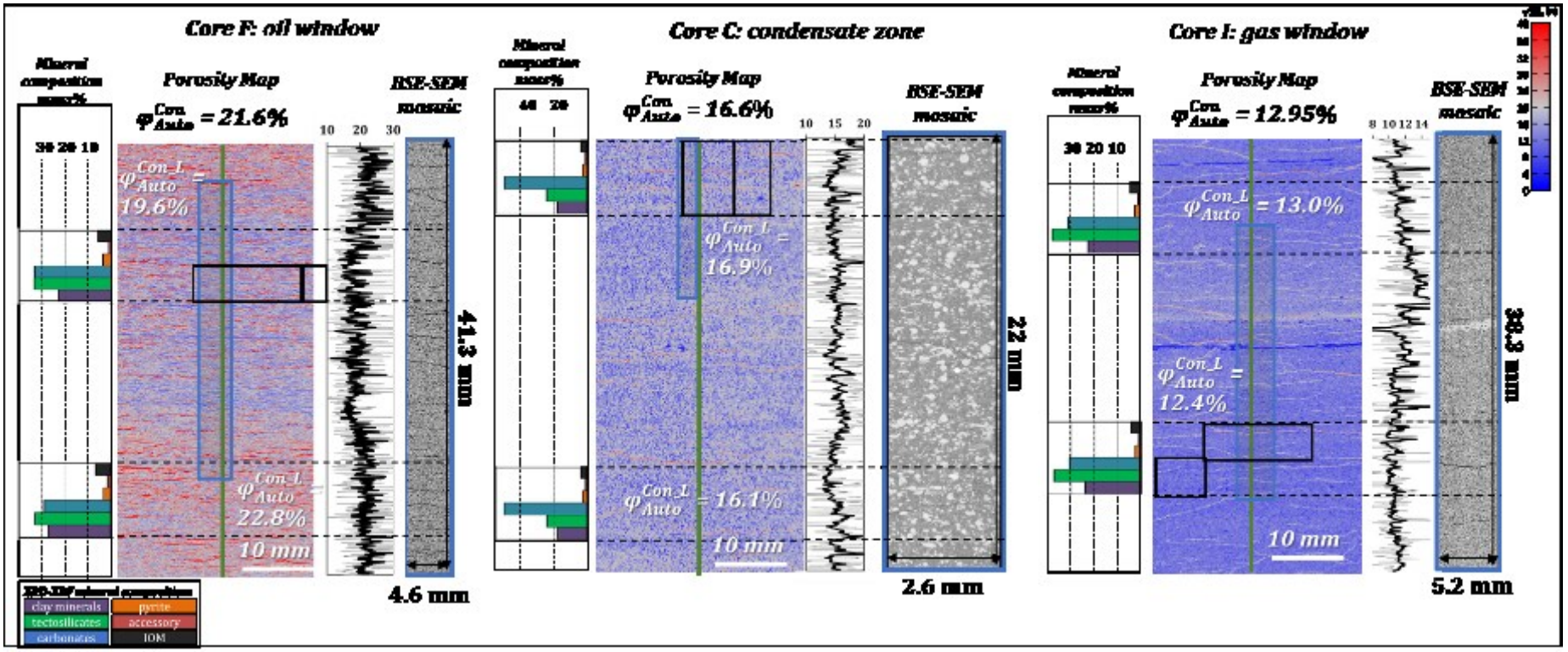

Figure 115. Porosity map obtained by autoradiography with positions of the BSE-SEM mosaic (blue rectangles); on the right, a vertical porosity profile through the center of the image (green line) and the corresponding BSE-SEM mosaic overview; mineral composition is indicated for the layers of interest, on the left and black rectangles correspond to the projection of blocks used for bulk porosity measurements.

4.3.1. Mosaic reconstruction from individual tiles

Based on the set of tiles (i.e. individual images) acquired for each mosaic, the ATLAS© software was used to merge the tiles with each other to build up the final mosaic image. This step implies a correlation process on the similar areas between neighboring images as an overlap of 6% of the tiles size was applied upon the acquisition. Such a correlation permits to find the exact position of each tile, because error of stage motion and electron beam drift always occurs. However, this treatment, when applied with the ATLAS© software, is not efficient enough to reach an accuracy of positioning at the level of a few pixels and a time consuming manual refinement is needed (up to one day of treatment). In addition, even if the merged mosaics seem satisfying at first sight, the detailed comparison of similar areas between initial tiles and the final mosaic shows some random set of pixels blurred upon the merging (i.e. not always at the position of the overlap between two neighboring tiles) and some footprints of objects slightly mixed with the true image. This non-robust mosaic recalculation does not permit an accurate recognition of phases by image analysis for complex materials like shales (e.g., light green patches and lines on Figure 116)

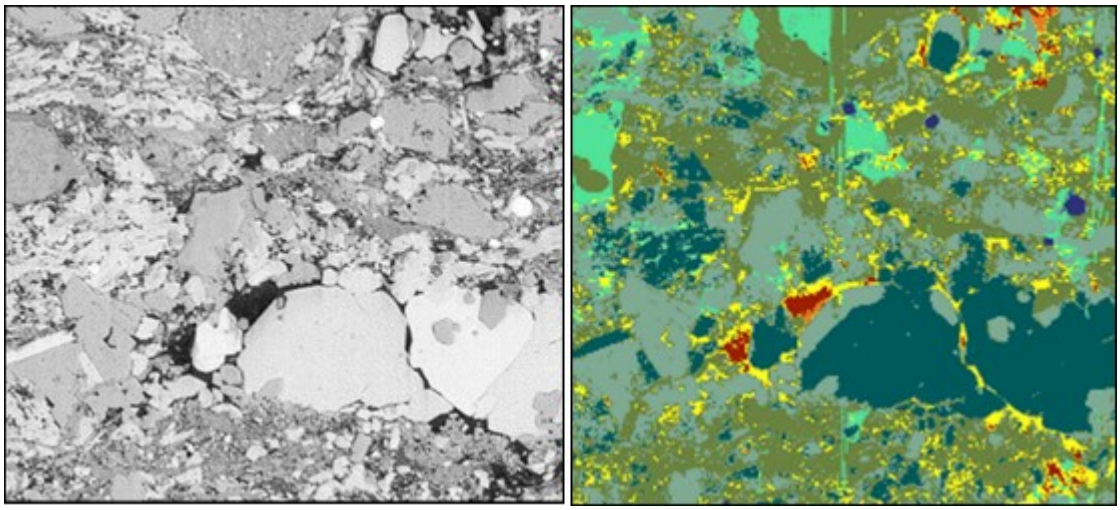

Figure 116. One individual initial tile acquired from a full mosaic (left) and the mineral map segmented from the same area of the recalculated full mosaic (right).

The analysis at the large scale of the merged mosaics with the ATLAS© software also reveals a progressive and not always linear shift of the mean grey level in various directions across the mosaics. For example, for sample C (condensate zone), a linear evolution along the mosaic length is observed whereas no probe current drift was measured (Figure 117.B). This grey level corresponds to a lateral shift of the grey level histograms (Figure 117.E) correlated with a blurring of images (Figure 117.D). Such a

phenomenon appears due to a varying distance of the sample surface from the objective lens (Fauchille et al., in preparation), which can be associated to a surface tilt or a faceting upon polishing. Indeed, even if a specific sample holder was developed to minimize such an artefact, polishing a surface at the core scale with a flatness at the micron scale remains challenging.

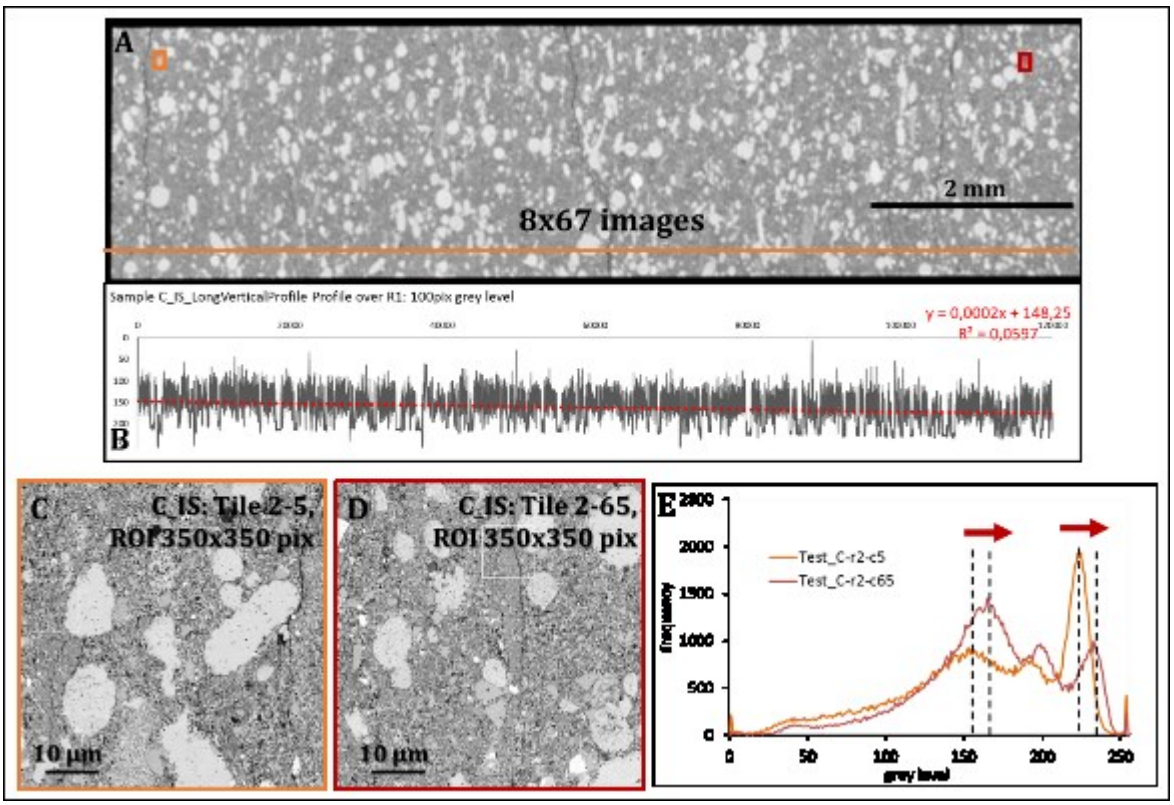

Figure 117. A) The overview of the acquired mosaic (C_IS, core C, condensate) with the location of ROI (orange and red squares) observed at full magnification (C and D); B) horizontal profile at mid height of the mosaic (orange line, 100 pixels width); D) grey level frequency histograms of orange and red ROI.

The simultaneous evolution of blurring and grey level of images is illustrated by the Figure 118. When the sample surface shifts down along the z axis of the microscope due to a tilted sample, the crossover of the electron beam at the working distance is no more corresponding to the sample surface z position. The beam is, thus, defocused at this point and the probe diameter increases with an associated blurring. In addition, the distance to the detector increases, reducing the solid angle of detection of BSE and the amount of BSE collected (i.e. the grey level) in a proportional way (Goldstein et al., 2003). A post-acquisition correction of the contrast of the image (by multiplying the grey level with a constant value) is, thus, needed to restore the image histogram and to recover the true position of each mode (Fauchille et al., in preparation). For complex and weakly contrasted shale samples, this correction is pivotal for the further application of image

analysis algorithms to identify the different phases on the BSE mosaic regardless to their grey level.

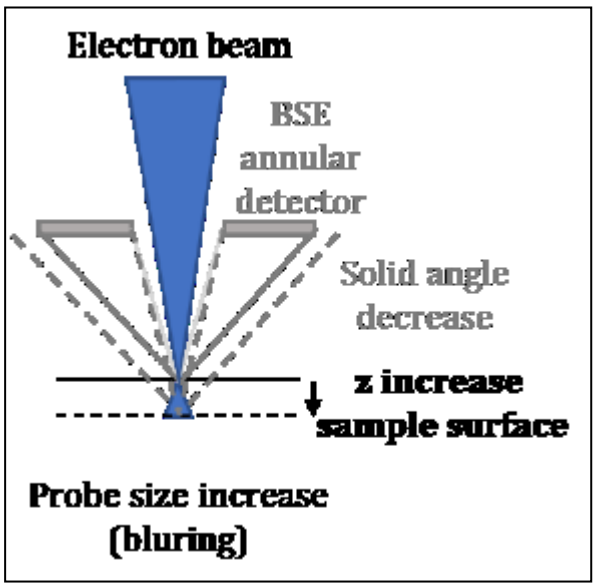

Figure 118. Effect of varying the z position of the sample surface on solid angle of detection of BSE and simultaneous defocusing.

According to the limitations and artefacts observed with the ATLAS© software, a set of in house Image J macros and plugins (Prêt, personal communication) was used to (i) normalize the histograms of each tile, (ii) recover the accurate position of the tiles by a fast Fourier correlation algorithm GPU parallelized (calculation time of only a few minutes without manual refinement needed) and (iii) building the final mosaic image.

The Figure 119 illustrates the normalization procedure of the grey level for each tile of the mosaic for the sample F from the oil production window. The position of the mode corresponding to the mean grey level of tectosilicate (around 180) is evolving at the beginning of each row of the mosaic for the initial tiles (yellow line on the scatterplot). After detecting its position and normalizing the histograms by an automatic contrast algorithm, the mode of tectosilicates (maximum intensity variation along green vertical trend on the center scatterplot) no more varies in term of grey level position. This is well illustrated by comparing the initial and normalized histograms of the tiles of columns 6 and 30 of the second row of the mosaic.

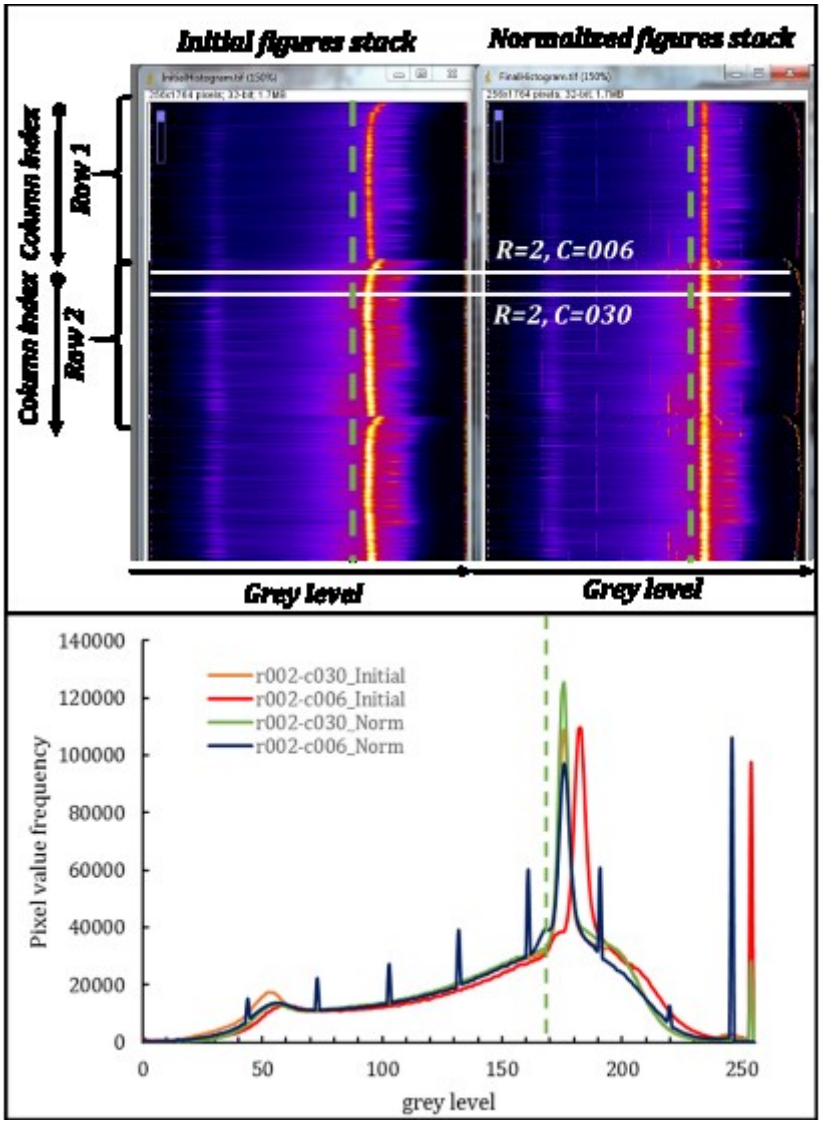

Figure 119. Illustration of the treatment done to normalize the histograms of the set of tiles of the mosaic of sample F. Left: Scatterplot of the set of initial grey level histogram, one line corresponds to one histogram viewed from the top and with a color encoding of the pixel frequency. Centre : Scatterplot of the normalized histograms. Right: Initial and normalized histograms of the tiles of columns 6 and 30 of the second row of the mosaic.

After normalization and accurate positioning of individual tiles, the full image of the mosaic of sample F was build up to reach a final image of almost 275000 pixels in length (4.4 cm) with a pixel size of 160nm (Figure 113). Only the sample F mosaic was firstly treated in order to evaluate the full procedure.

4.3.2. Mineral mapping

According to the data size of the final mosaic, corresponding to more than 6 Gbytes (Table 11 in section 2.2.11), no usual software, to our knowledge, were able to open and treat such an 8-bit image, whatever the memory available on the computer is used. Indeed, *ImageJ* and *Avizo*© are limited to individual images with maximum size of 2

GBytes and 4 GBytes (with an automatic recalling to a 32-bit image), respectively. In addition, simple thresholding procedures are not efficient enough for recognition of tectosilicates on BSE images for example (Robinet et al., 2012). The thresholding of the different phases observed on BSE was done through an in house bivariate algorithm corresponding to an improved and mixed approach of the procedure of (Prêt et al., 2010a; Robinet et al., 2012). The C++ algorithm was implemented in the *µPhaseMap* software (Prêt, 2003; Prêt et al., 2010a; Prêt et al., 2010b) without any limitation of image size (Prêt, personal communication). However, the full treatment implies a calculation time over one month without parallelizing the code for such a big data. CPU parallelization would poorly reduce calculation time, forbidding successive refinements of the thresholding parameters to obtain accurate results. An optimized version of the massively GPU parallelized algorithm (Prêt, personal communication) was used to decrease the computation time down to 32 minutes for calculating the mineral map of the full mosaic on a NVDIA Quadro K2000M graphic card (Figure 120).

The large field mineral map obtained cover a length of 4.4cm with a pixel size of 160 nm. The quantitative observation of the shale organization is thus now possible continuously over 6 decades of scale. For example, the blue ROI with a field of view of 120 µm in the middle of (Figure 120) is not visible on the full printed mineral map as such a small area represents a negligible size. Only the yellow ROI 4 times wider is observed at this scale of observation. No deep petrographic analyses has been applied yet but a clear orientation of the carbonate and tectosilicates biggest grains is observed. Patches with a thickness of 20-100µm and elongated along the sedimentary plane are also detected and correspond to an aggregation of small micritic calcite grains (i.e. on the different ROI highlighted on Figure 120).

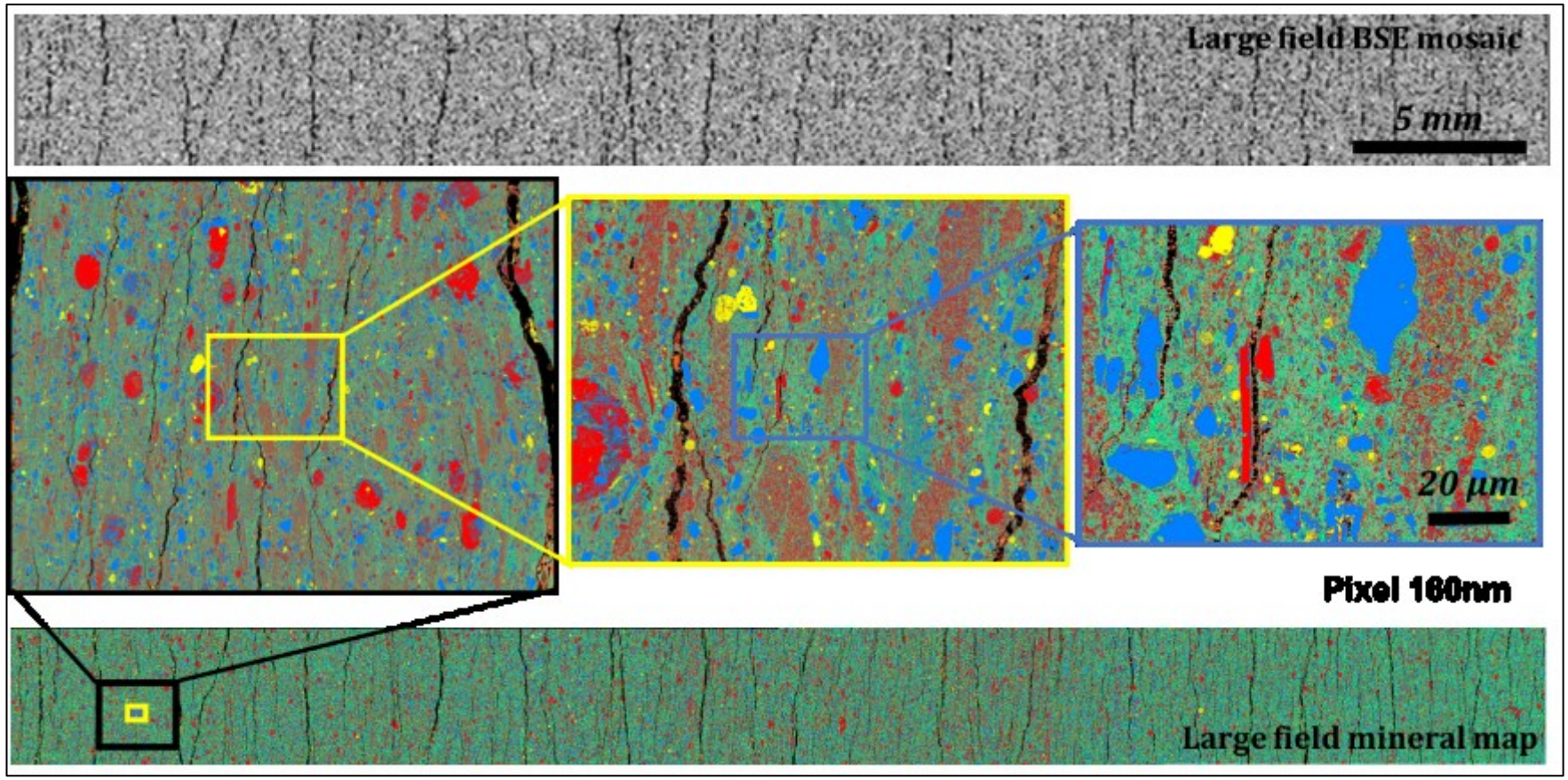

Figure 120. Large BSE mosaic of sample F (top) and the resulting mineral map (bottom). The ROI black, yellow and blue (centre) correspond to a contineous zooming at one location of the map. Carbonates in red , tectosilicates in blue and purple, solid organic matter in orange tones , resin in black, heavy minerals in yellow and clay matrix in green.

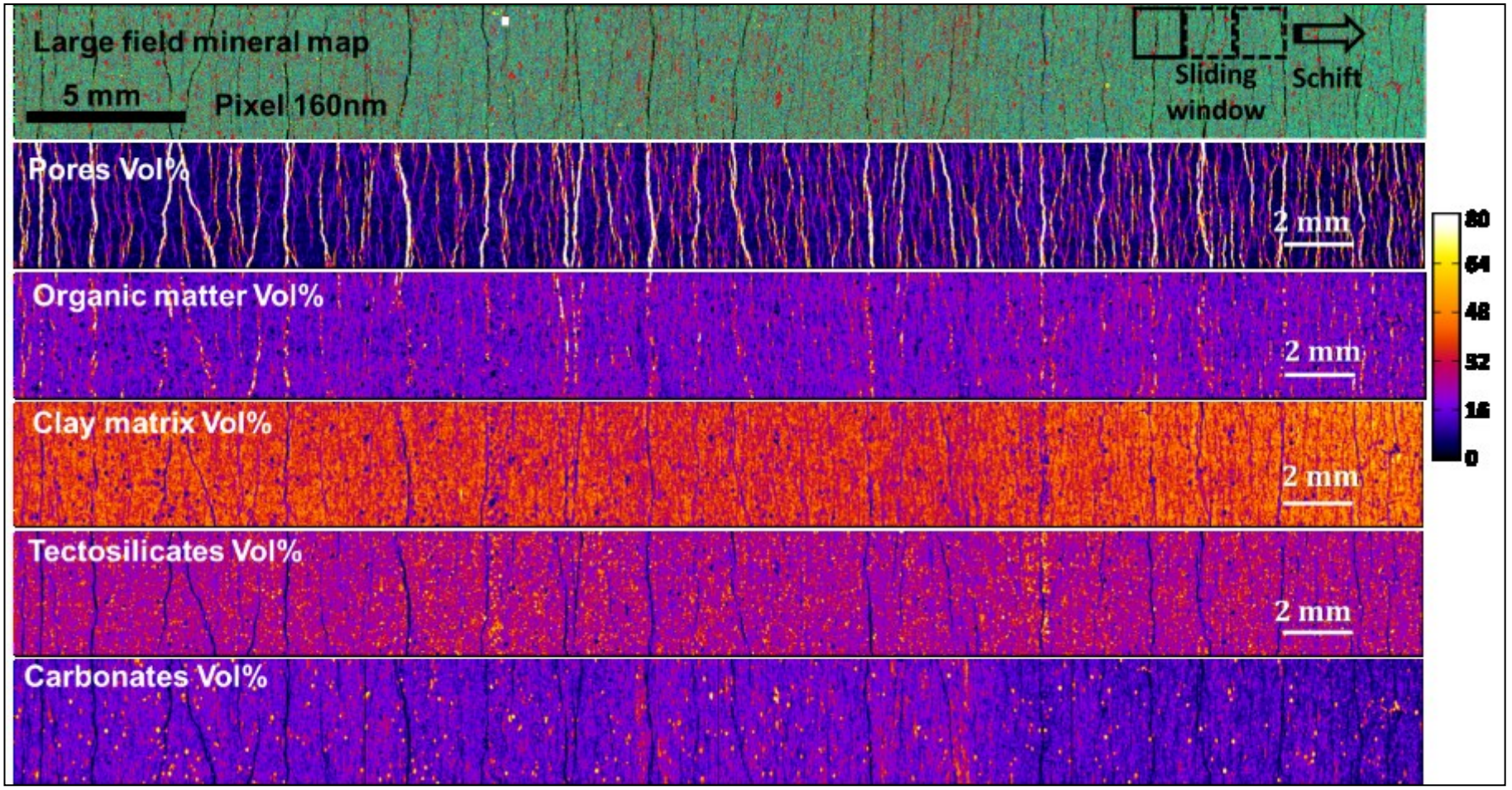

Figure 121. Mineral map (top) and the associated mapping of the volumetric contents of the main phases by a sliding windows approach.

The sliding window approach was applied to calculate local contents of each phase with a window size of 50µm shifted successively of 25µm each in both, vertical and horizontal, directions. The obtained maps display the spatial variations of volume contents and, among them, low and large scale (on the right side) laminae with varying amounts of tectosilicates, carbonates and clay (Figure 121). To better reveal such features, horizontal profiles of volume contents were computed by averaging the values along each column (Figure 122). Mainly, at a distance of 2.8 cm from the top of the mosaic, a lamina with progressive increase of the contents of clay and of the first type tectosilicate is detected. This behavior is negatively correlated with the contents of carbonates and heavy minerals (e.g. pyrite). Such an increase of the clay content on a large lamina is correlated to the increase of the total porosity detected by autoradiograph profile, further confirming that the pore network is mainly associated to this phase. At the opposite, no evolution of the OM and of the largest pores segmented (constant mean porosity of 7.2% including a lot of cracks) is detected.

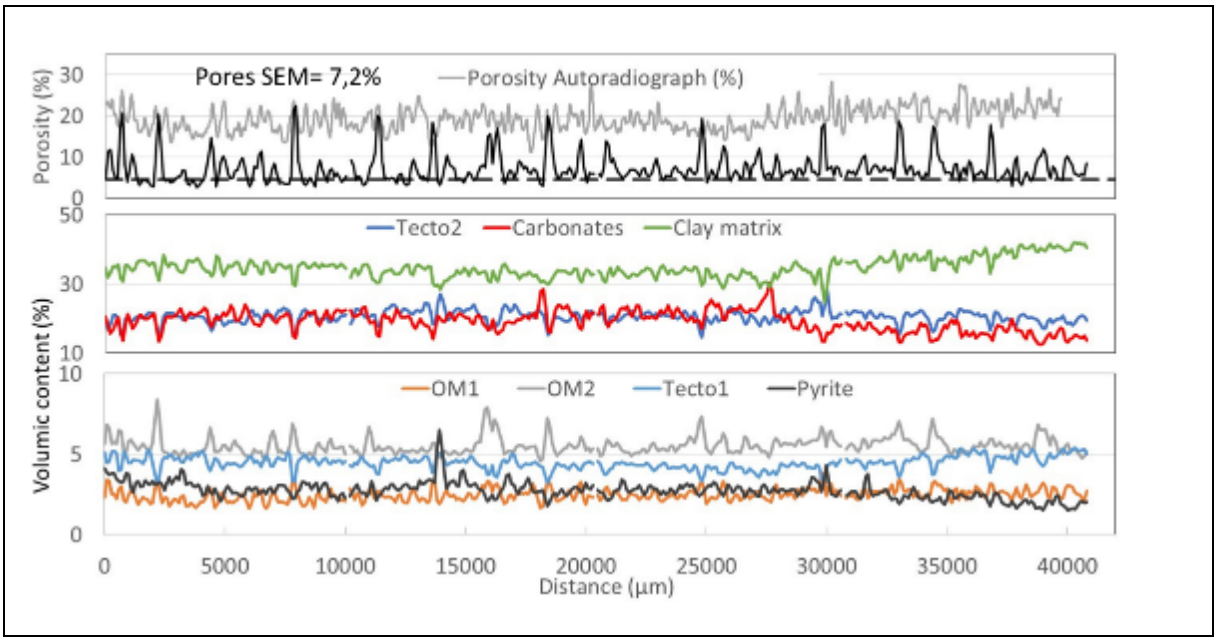

Figure 122. Horizontal profiles of volumic phase contents along the large field mineral map. On top, porosity evolution according to the SEM mosaic segmentation (macropore evolution in black) and by autoradiography (macropore, mesopore and micropore) and the two others graphs represent the evolution of the segmented phases obtained from the SEM mosaic mineralogical map.

According to the grain density, ρ_i^{grain} [kg/m^3], of each phase i and their specific porosity, φ_i^{spec} , the Equation 41 permits to calculate the mass concentrations (wt%) for the further comparison of the results with bulk mineralogy measurements for bulk density, ρ^{bulk} [kg/m^3].

Equation 41.

$$\text{wt\%} = \frac{\rho_i^{grain} \cdot vol\% \cdot (1-\varphi_i^{spec})}{\rho^{bulk}},$$

where *vol%* is the volume fraction of the phase *i*.

To adjust the total porosity profile by autoradiograph with the calculated one by SEM when averaging the porosity ϕ^I of each phase by their volume content, all the phases has been considered as non-porous except the clay matrix with a specific porosity of 42%. This is agreement with the value extrapolated at core scale when plotting the total NMR porosity as a function of non-porous grain contents (Figure 123). For such a correlation, clay and organic were considered as porous matrices to reach a better correlation mainly for gas windows samples. These profiles of weight concentrations still reveal the large-scale lamination detected at 2.8cm but small-scale ones are also observed with some peaks with negatively correlated contents of carbonates and tectosilicates.

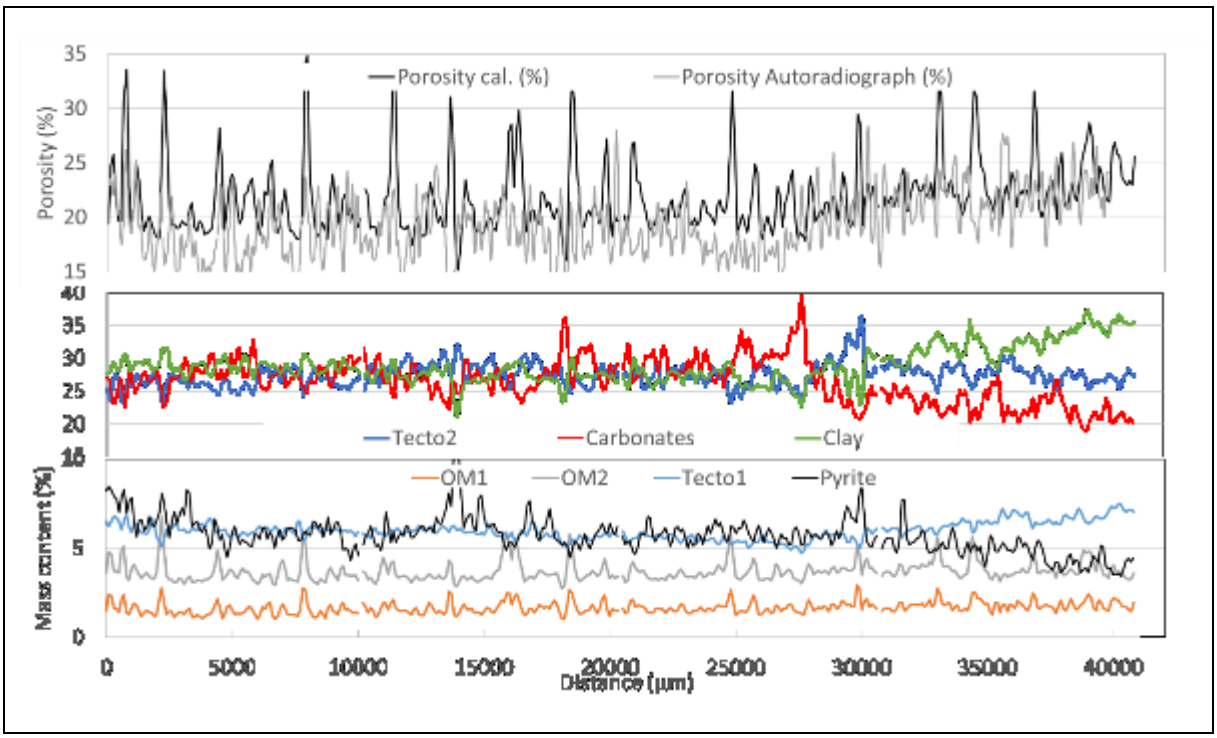

Figure 123. Horizontal profiles of weight phase concentrations and SEM/autoradiograph porosities along the large field mineral map.

Adding the constant macropores volume of 7.2% obtained from SEM mosaic for the sample F to the porosity probed by gas adsorption fairly improve the previously calculated balances of porosity obtained by bulk measurements. But still the cumulative value do not reach the total porosity as the set of parameters used for thresholding the SEM mosaics needs to be refined. (Figure 124)

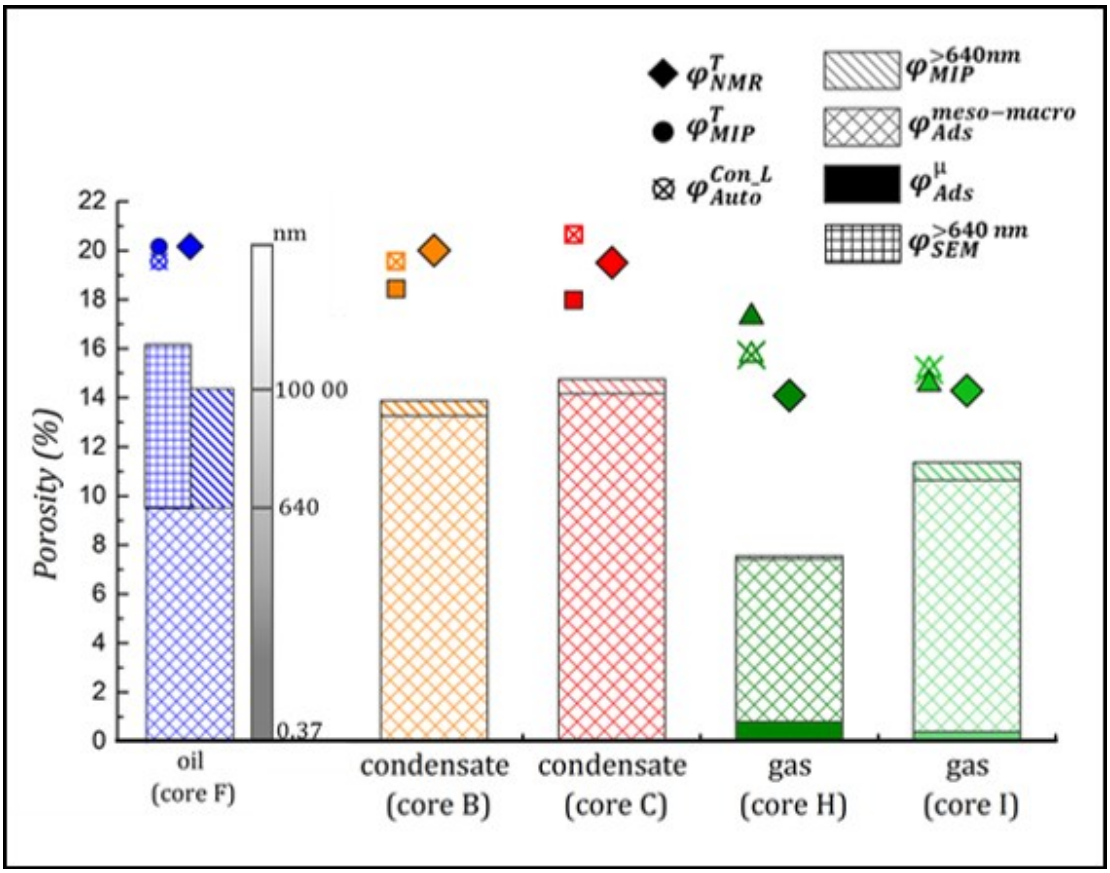

Figure 124. Porosity balances based on the combination of bulk measurements and imaging techniques: φ^{T}_{NMR}– total porosity on NMR blocks, φ^{T}_{MIP}–total porosity on MIP blocks, φ^{Con}_{Auto}– autoradiography connected porosity for localized layers, $\varphi^{>640nm}_{MIP}$– results of the porosity, corresponding to the MIP volumes intruded into the pores with pore throat >640 nm, $\varphi^{meso-macro}_{Ads}$ – measured adsorption porosity > 2 µm, φ^{μ}_{Ads}- microporosity < 2 µm, revealed by gas adsorption, $\varphi^{>640nm}_{SEM}$ – porosity obtained from the segmented SEM mosaics.

4.4. 2D correlation of porosity and mineralogy at the grain/small lamina scales (cm-nm)

To access the correlation of the porosity maps with mineral and organic phases distribution at the gain scale, the large SEM mosaics were acquired on the same surfaces, exposed with autoradiography (IS blocks, Figure 61; chapter 2, section 2.2.1). In comparison to the autoradiograph porosity map provided in the chapter 3, an additional polishing of the sample surface was done to efficiently refine the sample surface quality for SEM analysis. The slightly different sample surfaces have been further exposed for a new autoradiograph porosity mapping and by using a larger exposure time (295h instead of 149h) for improving the contrast for most of the samples. However, at the opposite, the sample F which is the most porous is slightly over exposed regardless the others. A resulting loss of porosity contrast is observed on the porosity histogram achieved with a

symmetric and narrow distribution no more refection the true distribution reached for the shorter time (Figure 125)

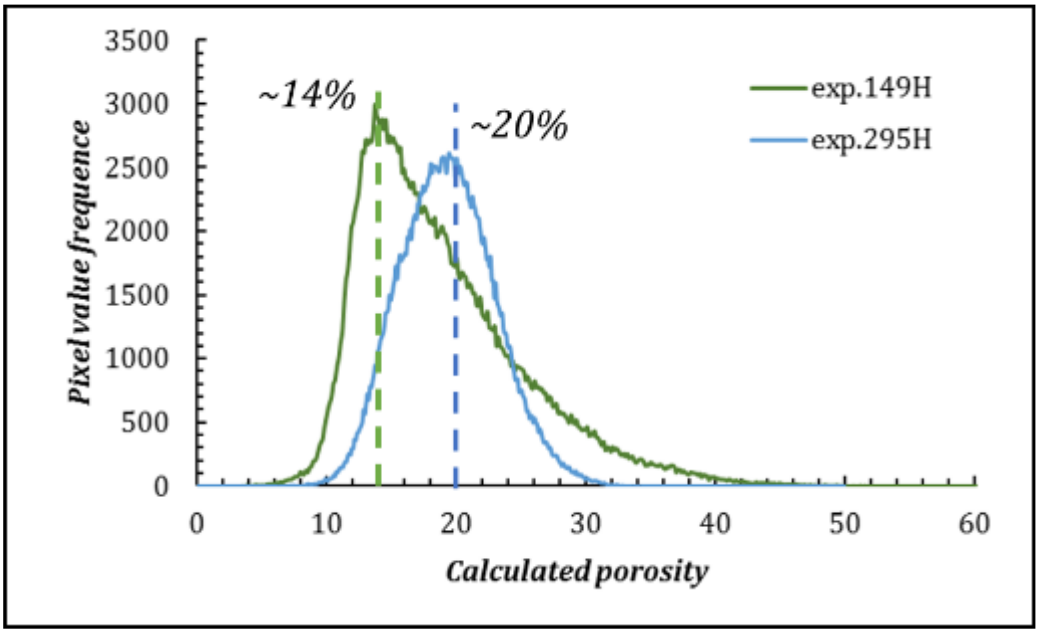

Figure 125. Autoradiograph porosity frequency histo grams of F-IS sub-sample surface initially obtained for an exposure time of 149h and latter for 295h, after repolishing for SEM imaging techniques application.

A shorter exposure time will be needed to recover a contrast good enough for the final spatial coupling with mineralogy. Here, a first raw attempt was done by a sliding window approach (window width of 200µm) to estimate local mean porosities on autoradiograph and associated mineral contents (Figure 126). Such a window on the mineral map is fairly representative of the grain organization as the biggest features remains smaller. Even if this window size is quite large regarldess to classical SEM observations, this ROI represent an extremely small part of the full mosaic (indicated as a white square on the mineral map). At the opposite, this window is associated to a blurred porosity map by autoradiograph. This feature is due to the range of ^{14}C beta particles (120 µm) defining the radius and the depth of the volume averaged at each point. Previous use of ^{3}H MMA for autoradiograph porosity mapping of bentonite and shales demonstrate a large improve of the spatial resolution at grain scale (Prêt, 2003; Robinet et al., 2012).

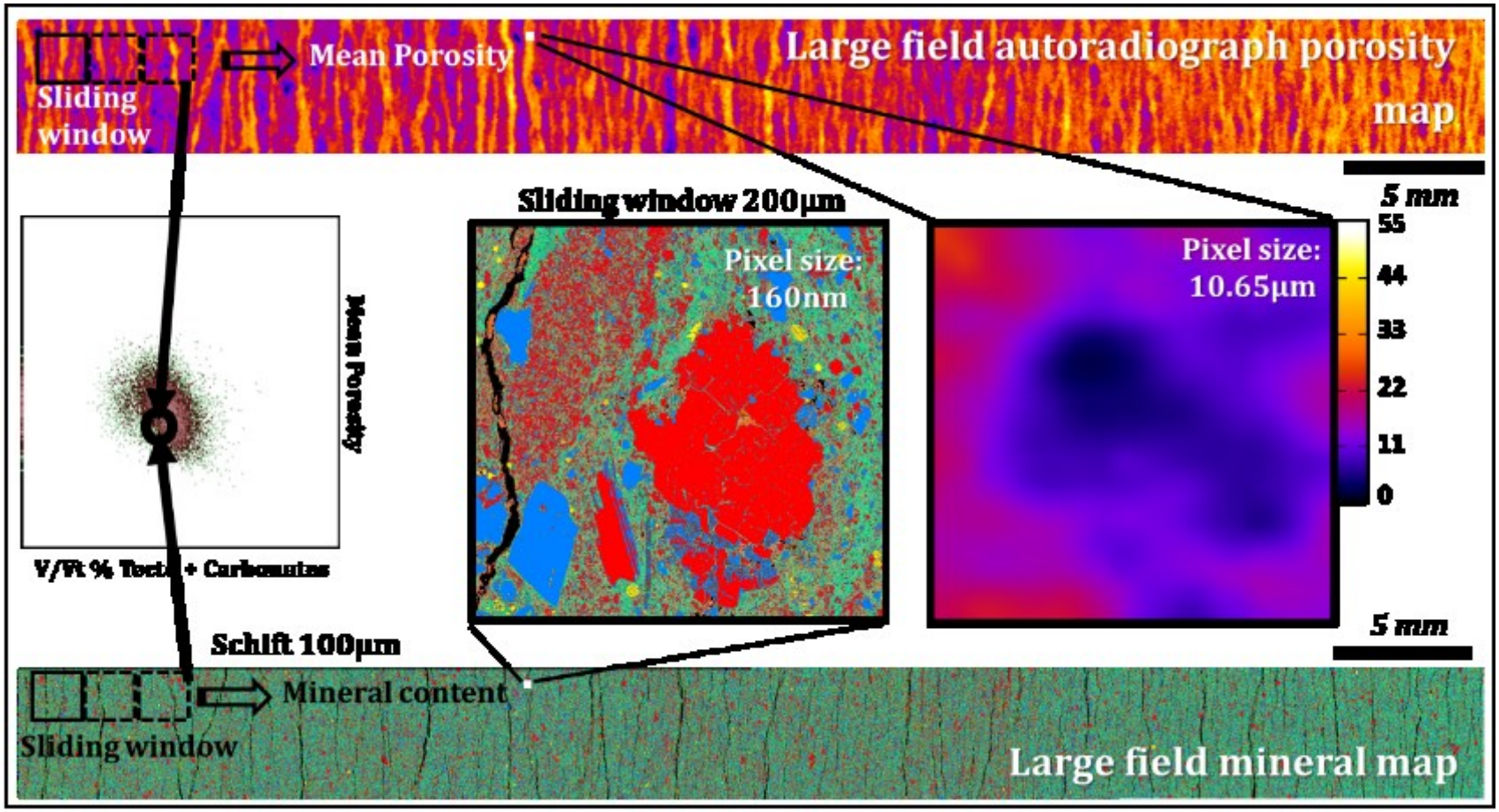

Figure 126. The correlation of large field autoradiography porosity map with the mineral map, calculated from BSE-SEM mosaic. Top: porosity map; center: correlative plot of mean porosity vs the sum of tectosilicates and carbonates (vol%), sliding windows of 200 µm size; bottom: BSE-SEM mineral map

.

The preliminary results of the spatial comparison of porosity and mineral contents was done using the *µPhaseMap* software for creating 2D scatterplots of the amount of pixels with a given couple of porosity and mineral contents values (Prêt, 2003; Prêt et al., 2010a; Prêt et al., 2010b). Slightly asymmetric clusters are reached with positions close to those of bulk measurements. However, the poor actual porosity contrast limits the detection of different well-defined clusters of points corresponding to local areas with varying porosity/mineralogy relationships. After refining the exposure time, a back projection of these different clusters on a map is expected to spatialize them (Figure 127).

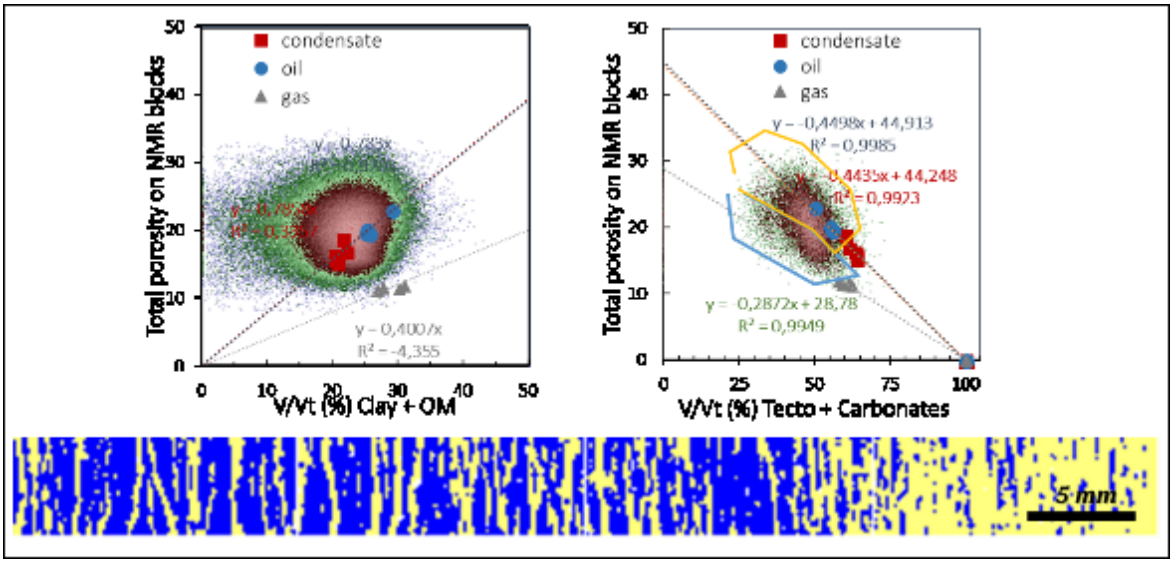

Figure 127. Correlation of connected porosity obtained from autoradiography with mineral phases distribution, obtained from BSE-SEM mosaics. Left: porous matter (clay minerals and IOM) volumetric contents; right: non-porous matter (tectosilicates and carbonates) volumetric contents. Circles are for samples from oil window; squares – for condensate zone; and triangles – for the dry gas window.

Conclusions

A new correlative approach was applied by coupling autoradiography porosity and mineralogical maps obtained on the same surface area to identify the spatial relationships between solid and pore distribution at different scales. Regard to the algorithm development done to achieve such a result, the data treatment was performed for only one sample (sample F, oil window). The quantitative correlation between mineralogy and porosity reveals that the clay content is positively associated with the porosity, confirming that the pore network is mainly created with the clay matrix.

This recent development, even if only preliminary results are shown, allows to illustrate the potential of such a correlative method to display the quantitative spatial distribution of solids and OM volumes and the intrinsic porosity of each phase at the grain scale.

To finalize this study, the full set of mosaic data acquired on samples from each hydrocarbon production zone should be treated in a near future to inter-compare with the bulk data obtained on the localized layers of interest. Some improvements on the segmentation procedure (e.g., refinement of thresholding parameters) have to be done (i) to reach comparative data to bulk mineralogy for layers of interest and (ii) to well dissociate the fractions of solid OM and resin, which overlap the same range of grey level. The information obtained in this way would allow to refine pore balances and extract 2D PSD to complete bulk multiscale PSD.

General conclusions and perspectives

Due to the increasing scarcity of conventional oil reserves, unconventional shale reservoirs are playing an increasing role in oil and gas production. However, the strong heterogeneity at different space scales of shales makes macroscopic and microscopic characterization highly challenging.

Since the 80's, all the studies, which are dedicated to the characterization of shales, have improved the description of the microstructure of these organic rich formations. The published activities mainly described the pore morphology, volume and geometry using various petrophysical techniques to cover the multiscale pore network of such heterogeneous organic rich sedimentary formations. However, these experimental investigations have shown that quantitative pore balance is still complicated to achieve, when the data sets are intercompared, due to the high heterogeneity of the systems of interest and the lack of spatialization and localization of the probed sub-samples. More recently, with the evolution of imaging techniques, a more complete description of the pore space has been proposed in connection with pore hosted phases. But, the achievement of quantitative spatial distribution of the pore network, using imaging techniques, is challenging, because it requires the coupling of large probed areas (several mm) with high-resolution images.

In summary, all the available literature shows that an integrated multi-techniques approach, applied on carefully localized core/sub-samples, prior to the different analysis, is required to fully characterize the multiscale pore network of shale reservoirs. With regard to this requirement, the twofold objective of this study was to develop a new approach:

(i) To accurately characterize the pore network of shale at a multiscale range in connection with the varying microstructure at the core and at the formation scales. A combination of bulk methods (gas adsorption, NMR, He-pycnometry, MIP, etc.) was applied on a full cores set from zones with various hydrocarbons production, imaged by 3D µtomography and autoradiography to localize homogeneous and inter-comparable sub-samples.

(ii) To achieve images of an analyzed representative area with a resolution giving access to most of the microstructure details. The imaging technique developed in this study was based on recent works on correlative imaging methods offering the possibility to map large fields of view with nanometric pixel size. The acquisition and the treatment of large field SEM image mosaics to calculate mineralogical map has been performed to correlate mineralogy and porosity map with a resolution of hundred nanometers within a multi-centimeter field of view.

Such an innovative approach has been applied on 7 cores collected from three wells within different hydrocarbon maturity areas from the Vaca Muerta formation in the Neuquén Basin, Argentina. The main results that have been obtained are summarized below.

First, it was demonstrated that proposed multiscale/multitool approach can be successfully applied on the core samples from the Vaca Muerta formation. Well log data down to laboratory sub-samples measurements, involving 3D µtomography acquisitions, were used to localize and spatialize well-defined areas of interest within full-size cores for representative laboratory measurements. From this localized sub-sampling, based on 3D views, a multiscale correlated approach was applied, using autoradiography porosity maps and classic bulk techniques to characterize the pore volumes (porosity and PSD). It should be noted that autoradiography was applied for the first time on organic-rich shale. This method has provided the possibility of mapping in 2D the spatial distribution of the connected porosity with micrometric pixel size and over multi-centimeter field of view reaching the core scale. Moreover, autoradiography probes the full range of the connected pores whatever their size is. As shown in this study, local calcite veins ("beef") and carbonate nodules are non-porous. They should be absolutely avoided in sub-samples used for bulk methods as they drastically impact the representativeness of measured porosity values. 3D µtomography and 2D autoradiography are reliable methods to resolve the detection of these local heterogeneities even though the resolution and contrast of µtomography are not optimal. However, additional vertical porosity evolution associated with different laminae with varying spatial frequency among the samples was evidenced by autoradiography but not by µtomography. Results have also shown that the porosity values measured on areas corresponding to the size of sub-blocks used for bulk measurements are representative of the laterally homogeneous laminae detected on autoradiography porosity mapping.

In addition, autoradiography and NMR data acquired in this work clearly show that the total pore space is fully connected from micro to macropores in the samples of the Vaca Muerta formation regarding the hydrocarbon maturity ranging between 1.1 and 1.6% VReq (oil to dry gas). Moreover, it was demonstrated that by carefully selecting the sub-sampling, a consistent set of quantitative porosity data could be produced. All the methods, imaging and bulk techniques, provide similar total porosity values (except the values obtained through directly intruded/adsorbed volumes of fluids), when applied on comparable homogeneous and well preserved sub-samples (i.e., without crushing). Indeed, it was proved that nitrogen adsorption data for shales are deeply biased, when applied on powder. Quantitative balances of porosity and pore/throat size distributions were reached showing lower porosities and pore/throat size as burial/hydrocarbon maturity increases, even if microporosity appears for the samples from dry gas zone. But the balances confirm that not all the pores can be probed by a unique bulk

method and the non-negligible pores larger than 640 nm are not analyzed in the provided PSD. Their content is estimated by difference with the total porosity and/or with the MIP data.

Moreover, bulk measurements only give punctual values (homogenized mean value), for which no spatial information is available since shales are heterogeneous materials. The use of imaging techniques is a way to overcome the problem of spatialization and representativity, but these methods are limited in the achieved field of view. Recent development in correlative imaging software allows acquiring accurate and large mosaics. Such mosaics give the possibility to map large field of view (cm^2) at the core scale with nanometric pixel size covering 6 decades of scale. Beyond the problem of big data treatment, considering the size of the mosaic images, this method of correlative images was applied through the selected core samples to quantify the mineralogy and couple the results with the autoradiography porosity maps.

This new correlative approach was thus applied by coupling autoradiography porosity and mineralogical maps obtained on the same surface area in order to identify the relationships between solid and pore distribution at different scales. Regard to the algorithm development done to achieve such a result, the data treatment was done for only one sample (sample F, oil window). The quantitative correlation between mineralogy and porosity reveals that the clay content is positively associated with the porosity, confirming that the pore network is mainly associated with the clay.

This recent development, even if only preliminary results were provided, allows to illustrate the potential of such a correlative method to display the quantitative spatial distribution of solid and OM volumes and the intrinsic porosity of each phase at the grain scale.

To finalize this study, the full set of mosaic data acquired on each hydrocarbon production zone should be treat in a near future to inter-compare with the bulk data for all the production zones. Some improvements on the segmentation procedure have to be done to well dissociate the fraction of OM and resin, which overlap at the same range of grey level. The last step and perspective of this work will be to extract the pore size distribution at the grain scale and to perform a deeper downscaling approach by the acquisition of 3D FIB-SEM volume to access the pore size distribution regard to the production zone (oil window vs. gas window).

These results allow to propose some potential developments and perspectives following two directions: (i) towards the upscaling up to geological formation; and (ii) towards the further downscaling to archive the complete information about the nano-structure.

Following the first direction, the upscaling could concern two aspects. The first objective would be to apply the developed methodology to other samples taken from different wells of the same formation to establish spatial correlations at the basin scale. These correlations involving connected porosity and maturity inferred from different wells could provide some insights to the reservoir modeling of the Vaca Muerta formation. The second objective would be to apply on the large mosaics, numerical upscaling techniques (or homogenization schemes)

to quantify macroscopic petrophysical properties (permeability, transport and geomechanical properties) which are difficult to obtain at the basin scale.

Following the second direction, downscaled investigations could be realized through the application of the imaging techniques with smaller pixel sizes. First of all, the same surfaces of the studied samples can be used for the application of other 2D techniques, like SEM with smaller FOV (smaller pixel size), as well the development of 3D FIB-SEM, which allows to achieve the information about the pore space with few nm pixel size. The information about the structure organization at a nano-scale would help to understand the processes of liquid hydrocarbons generation and storage within the smallest pores and to evaluate the transformations of solid OM and its porosity with the maturation.

Symbols & Abbreviations

Table 21. Symbols used in the manuscript.

A	- atomic weight.
A_o	- activity.
C	- energy constant for BET transformations.
D	- optical density.
D_{BSE}	- diameter of the emission volume of backscattered electrons.
D_{H2O}	- self-diffusion coefficient of water.
d_p	- pore diameter.
$DPHI$	- density porosity of the formation.
$DTCO$	- compressional slowness of the formation.
$DTSM$	- shear slowness of the formation.
E	- energy.
f	- form factor defining the geometry of pore.
$HCGR$	- corrected gamma ray index.
HI	- hydrogen index.
I	- X-rays intensity.
G_a	- volumetric fraction of hydrocarbons stored as gas adsorbed on the pores' walls.
G_d	- volumetric fraction of hydrocarbons stored as dissolved gas.
G_f	- volumetric fraction of hydrocarbons stored as free gas.
G_{st}	- total gas in-place volume.
K^{DR}	- DR equation constant.
k_{NMR}	- diffusion regime parameter.
LAC	- linear attenuation coefficient.
l_p	- pore length.
M	- median value for the set of pixels.
m_s	- mass of solids.
m_{sat}	- mass of sample saturated with brine solution.
N_g	- mean grey level.
N_{g0}	- background grey level.
$NPHI$	- neutron porosity of the formation.
P	- pressure.
P_{BSE}	- depth of the emission volume of backscattered electrons.
$PhiE$	- effective porosity defined by MULTIMIN approach of well log data treatment.

$PhiT$ - total porosity defined by MULTIMIN approach of well log data treatment.

$RHOB$ - bulk density measured directly from the neutron log tool.

R - Kernel radius.

R_{gas} - gas constant.

r_k - Kelvin radius.

R_{KO} - electron range calculated with Karaya-Okayama equation.

r_p - pore radius.

SLD - scattering length density.

S_A - surface roughness.

S_p - pore 2D surface.

S_t - total 2D surface of the sample.

t - monolayer of adsorbed nitrogen thickness.

T - temperature.

T_1 - longitudinal relaxation time.

T_2 - bulk fluid relaxation time.

T_{2B} - transvers bulk fluid relaxation time.

T_{2S} - transvers surface relaxation time.

V_μ - volume of micropores.

υ - pixel value from the digital image.

V_a - volume of adsorbed nitrogen in liquid state.

Var - variance.

$V_{intr.max}$ - maximum volume of intruded mercury.

V_N - molar volume of adsorbed nitrogen.

V_{NMR} - volume detected by NMR technique.

$vol\%$ - volumetric fraction of the phase.

$VReq$ - maximum thermal maturity measured on bitumen.

V_p - volume of pores.

V_s - volume of solid parts.

V_t - total volume of the sample.

W_a - weight of liquid adsorbed.

$wt\%$ - weight fraction of the phase.

α_d - average distance of a proton travel before encountering a paramagnetic site.

β - correction factor of the radiation absorption by sample.

γ - liquid surface tension.

θ - liquid/solid contact angle.

$\boldsymbol{\lambda}$ - wave length.

$\boldsymbol{\rho_a}$ - density of adsorbed liquid.

$\boldsymbol{\rho_b}$ - bulk density of the formation.

$\boldsymbol{\rho_{ma}}$ - density of the formation matrix.

$\boldsymbol{\rho_f}$ - density of the formation fluids.

$\boldsymbol{\rho^{brine}}$ - density of brine solution.

$\boldsymbol{\rho^{bulk}}$ - bulk density of the sample.

$\boldsymbol{\rho^{bulk}_{\mu Tomo}}$ - bulk density defined with µtomography of MIP blocks.

$\boldsymbol{\rho^{bulk}_{MIP}}$ - bulk density defined by immersion in mercury before the first pressure step.

$\boldsymbol{\rho^{bulk}_{NMR}}$ - bulk density of the block through the laser volume.

$\boldsymbol{\rho^{grain}}$ - grain density of the sample.

$\boldsymbol{\rho^{grain}_{aver}}$ - grain density measured on the averaged probe.

$\boldsymbol{\rho^{grain}_{NMR}}$ - grain density of the sample measured on localized NMR blocks.

$\boldsymbol{\rho^{grain}_{MIP}}$ - grain density defined by mercury intrusion at the last pressure step.

$\boldsymbol{\rho^{grain}_{PS}}$ - grain density measured on the localized PS blocks.

$\boldsymbol{\rho^{OM}}$ - density of organic matter.

$\boldsymbol{\rho_r}$ - surface relaxivity.

$\boldsymbol{\varphi_{Ads}}$ - total adsorption porosity of the sample recalculated from adsorbed volumes.

$\boldsymbol{\varphi^{\mu}_{Ads}}$ - adsorption microporosity of the sample by t-plot technique.

$\boldsymbol{\varphi^{Con}_{Auto}}$ - connected porosity of the whole autoradiography surface.

$\boldsymbol{\varphi^{Con\_B}_{Auto}}$ - porosity of the bulk block projection on the autoradiography surface.

$\boldsymbol{\varphi^{Con\_L}_{Auto}}$ - porosity of the layer of the interest on the autoradiography surface.

$\boldsymbol{\varphi_{MIP}}$ - total intrusion porosity of the sample recalculated from mercury intruded volumes.

$\boldsymbol{\varphi^{>640nm}_{MIP}}$ - intrusion porosity of the sample at the >640 nm range of pores throats diameter recalculated from mercury intruded volumes.

$\boldsymbol{\varphi^{T}_{MIP}}$ - total porosity measured by MIP.

$\boldsymbol{\varphi^{Con\_Vs}_{NMR}}$ - connected porosity of the sample through NaCl saturated volume and grain density measurements.

$\boldsymbol{\varphi^{Con\_Vt}_{NMR}}$ - connected porosity of the sample through NaCl saturated volume and bulk density measurements.

$\boldsymbol{\varphi^{>640\ nm}_{SEM}}$ - porosity of the sample obtained from BSE-SEM mosaics.

$\boldsymbol{\varphi^{Spec}}$ - specific porosity of the phase.

$\boldsymbol{\varphi^{T}_{NMR}}$ - total porosity of the sample through laser volume and grain density.

$\boldsymbol{\varphi^{T}}$ - total porosity.

$\boldsymbol{\varphi^{T}_{2D}}$ - total porosity of the 2D surface.

$\boldsymbol{\varphi^{T}_{\mu Tomo}}$ - total porosity of the sample defined with µtomography technique.

$\boldsymbol{x}$ - sample thickness.

Z - atomic number.

z_i - absolute value of the surface topography measurement.

$z_{ar.mean}$ - arithmetic mean of the topography measurements over the surface.

Table 22. Abbreviations used in the manuscript.

ADF	- Annular dark-field detector.
AE	- Adsorbed electrons.
AEM	- Analytical electron microscopy.
BET	- Brunauer, Emmet and Teller method.
BIB	- Broad ion beam milling.
BJH	- Barrett-Joyner-Halenda method.
BSE	- Back scattered electrons.
CBS	- Circular back scattered detector.
CEC	- Cation exchange capacity.
CFM	- Confocal microscopy.
CT	- Computer tomography.
DR	- Dubinin and Radushkevich equation.
dTG	- Derivative thermogrametric curve.
ECS	- Elementary capture spectroscopy.
EDS	- Energy dispersive detector.
EDX (EDAX)	- Energy dispersive x-ray analysis.
EsB	- Energy selective backscattered electrons detector.
ETD	- Everhart-Thornley detector.
F	- cathodoluminescence.
FE	- Field emission.
FEG	- Field emission gun.
FIB	- Focus ion beam milling.
FOV	- Field of view.
HAADF	- High angle annular dark-field detector.
HJ	- Harkins and Jura equation.
IOC	- Insoluble organic carbon.
IOM	- Insoluble organic matter.
IR	- Insoluble residue.
LOI	- Lost on ignition.
LUT	- Look up tables.
MIP	- Mercury intrusion porosimetry.
MMA	- Methylmethacrylate.
MS	- Mass spectroscopy.

NLM - Non-local mean denoising.

NMR - Nuclear magnetic resonance spectroscopy.

OM - Organic matter.

PSD - Pore size distribution.

REA - Representative elementary area.

REV - Representative elementary volume.

ROI - Region of interest.

SDD - Silicon drift detector.

SANS - Small angle neutron scattering.

SE - Secondary electrons.

SEM - Scanning electron microscopy.

STEM - Scanning transmission electron microscopy.

STP - Standard temperature and pressure conditions.

STXM - Scanning transmission x-ray microscopy.

TA - Thermal analysis.

TEM - Transmission electron microscopy.

TGA - Thermogravimetric analysis.

TLD - Through-lens detector.

TOC - Total organic carbon.

USANS - Ultra-small angle neutron scattering.

VM - Vaca Muerta.

WD - Working distance.

XRD - X-Ray diffraction analysis.

XRF - X-Ray fluorescence spectroscopy.

Appendix. Parameters conversion

Table 23. Conversion of parameters used in the literature and in the manuscript to the SI units (Taylor and Thompson, 2008).

Parameter	Unit from the literature	SI-unit	Conversion
Activity	μCi/ml	Bq/m^3	1 μCi/ml = $3.7 \cdot 10^9$ Bq/m^3
Permeability	1 Darcy	m^2	1D = $9.869233e^{-13}$ m^2
	1 μDarcy		1μD = $9.869233e^{-19}$ m^2
	1 nDarcy		1nD = $9.869233e^{-22}$ m^2
	1 pDarcy		1pD = $9.869233e^{-25}$ m^2
Scattering intensity	cm^{-1}	m^{-1}	1 cm^{-1} = 10^2 m^{-1}
Scattering length density	cm^{-2}	m^{-2}	1 cm^{-2} = 10^4 m^{-1}
Specific volume	scf/ton	m^3/kg	1 scf/ton = 28.3168466 m^3/kg
	cm^3/g		1 cm^3/g (cc/g) = 10^{-3} m^3/kg
	mL/g		1 mL/g = 10^{-3} m^3/kg

References

Ambrose, R. J., 2011, Microstructure of gas shales and its effects on gas storage and production performance, PhD thesis, University of Oklahoma, Graduate colledge, p. 160.

Ambrose, R. J., R. C. Hartman, M. Diaz-Campos, I. Y. Akkultu, and C. Sondergeld, 2010, New Pore-scale Considerations for Shale Gas in Place Calculations: SPE North American unconventional Gas Conference and Exhibition, Pitsburg, USA, v. SPE 131772, p. 17.

Anovitz, L. M., and D. R. Cole, 2015, Characterization and analysis of porosity and pore structures: Reviews in Mineralogy and Geochemistry, v. 80, p. 61-164, doi: 10.2138/rmg.2015.80.04.

Arthur, M. A., and D. R. Cole, 2014, Unconventional Hydrocarbon Resources: Prospects and Problems: Elements, v. 10, p. 257-264, doi: 10.2113/gselements.10.4.257.

Badessich, M. F., D. E. Hryb, M. Suarez, L. Mosse, N. Palermo, S. Pichon, and L. Reynolds, 2016, Vaca Muerta shale - taming a giant: Oildfield Review, v. 28, p. 26-39.

Bagdigian, R. M., and A. S. Myersont, 1986, The adsorption of Thiobacillus ferrooxidans: Biotechnology and Bioengineering, v. 28, p. 467-479.

Barrett, E. P., L. G. Joyner, and P. P. Halenda, 1951, The determination of pore volume and area distribution in porous substance. I. Computations from nitrogen isotherms: The Volume and Area Distributions in Porous Substance, v. 73, p. 373-380, doi: 10.1021/ja01145a126.

Behroozmand, A. A., K. Keating, and E. Auken, 2014, A Review of the Principles and Applications of the NMR Technique for Near-Surface Characterization: Surveys in Geophysics, v. 36, p. 27-85, doi: 10.1007/s10712-014-9304-0.

Bernard, S., and B. Horsfield, 2014, Reply to comment on “Formation of nanoporous pyrobitumen residues during maturation of the Barnett Shale (Fort Worth Basin)”: International Journal of Coal Geology, v. 127, p. 114-115, doi: 10.1016/j.coal.2014.01.005.

Bernard, S., B. Horsfield, H.-M. Schulz, A. Schreiber, R. Wirth, T. T. Anh Vu, F. Perssen, S. Könitzer, H. Volk, N. Sherwood, and D. Fuentes, 2010, Multi-scale detection of organic and inorganic signatures provides insights into gas shale properties and evolution: Chemie der Erde - Geochemistry, v. 70, p. 119-133, doi: 10.1016/j.chemer.2010.05.005.

Bernard, S., B. Horsfield, H.-M. Schulz, R. Wirth, A. Schreiber, and N. Sherwood, 2012a, Geochemical evolution of organic-rich shales with increasing maturity: a STXM and TEM study of the Posidonia Shale (Lower Toarcian, Northern Germany): Marine and Petroleum Geology, v. 31, p. 70-89, doi: 10.1016/j.marpetgeo.2011.05.010.

Bernard, S., R. Wirth, A. Schreiber, H.-M. Schulz, and B. Horsfield, 2012b, Formation of nanoporous pyrobitumen residues during maturation of the Barnett Shale (Fort Worth Basin): International Journal of Coal Geology, v. 103, p. 3-11, doi: 10.1016/j.coal.2012.04.010.

Berthonneau, J., O. Grauby, M. Abuhaikal, R. J. M. Pellenq, F. J. Ulm, and H. Van Damme, 2016, Evolution of organo-clay composites with respect to thermal maturity in type II organic-rich source rocks: Geochimica et Cosmochimica Acta, v. 195, p. 68-83, doi: 10.1016/j.gca.2016.09.008.

Blunt, M. J., B. Bijeljic, H. Dong, O. Gharbi, S. Iglauer, P. Mostaghimi, A. Paluszny, and C. Pentland, 2013, Pore-scale imaging and modelling: Advances in Water Resources, v. 51, p. 197-216, doi: 10.1016/j.advwatres.2012.03.003.

Borysenko, A., B. Clennell, I. Burgar, D. Dewhurst, R. Sedev, and J. Raltson, 2009, Application of low field and solid-state NMR spectroscopy to study the liquid/liquid interface in porous spae of clay minerals and shales: Diffusion Fundamentals, v. 10, p. 2.1-2.4.

Borysenko, A., B. Clennell, R. Sedev, J. Raltson, M. Raven, and D. Dewhurst, 2006, Wettability measurments in model and reservoir shale system: International Symposium of the Society of Core Analyses, Trondheim, Norway, SCA2006-03.

Bousige, C., C. M. Ghimbeu, C. Vix-Guterl, A. E. Pomerantz, A. Suleimenova, G. Vaughan, G. Garbarino, M. Feygenson, C. Wildgruber, F. J. Ulm, R. J. Pellenq, and B. Coasne, 2016, Realistic molecular model of kerogen's nanostructure: Nat Mater, v. 15, p. 576-82, doi: 10.1038/nmat4541.

Brigatti, M. F., E. Galán, and B. K. G. Theng, 2013, Chapter 2 - Structure and Mineralogy of Clay Minerals, *in* F. Bergaya, and G. Lagaly, eds., Developments in Clay Science, v. 5, Elsevier, p. 21-81, doi: doi.org/10.1016/B978-0-08-098258-8.00002-X.

Brownstein, K. R., and C. E. Tarr, 1979, Importance of classical diffusion in NMR studies of water in biological cells: Physical Review A, v. 19, p. 2446-2453.

Brunke, O., K. Brockdorf, S. Drews, B. Müller, T. Donath, J. Herzen, and F. Beckmann, 2014, Comparison between X-ray tube based and synchrotron radiation based µCT: SPIE Developments in X-Ray Tomography VI, v. 7078, doi: 10.1117/12.794789.

Brydson, R., A. Brown, L. G. Benning, and K. Livi, 2014, Analytical transmission electron microscopy: Reviews in Mineralogy and Geochemistry, v. 78, p. 219-269, doi: 10.2138/rmg.2014.78.6.

Bryndzia, L. T., and N. R. Braunsdorf, 2014, From source rock to reservoir: the evolution of self-sourced unconventional resource plays: Elements, v. 10, p. 271-276, doi: 10.2113/gselements.10.4.271.

Buades, A., B. Coll, and J.-M. Morel, 2011, Non-Local Means Denoising: Image Processing On Line, v. 1, doi: 10.5201/ipol.2011.bcm_nlm.

Carpentier, G., 2004, FFTRemoveStreaks macro for removing interference streaks from confocal images: ImageJ News, v. 1.33o.

Chalmers, G. R., R. M. Bustin, and I. M. Power, 2012a, Characterization of gas shale pore systems by porosimetry, pycnometry, surface area, and field emission scanning electron microscopy/transmission electron microscopy image analyses: examples from the Barnett, Woodford, Haynesville, Marcellus, and Doig units: AAPG Bulletin, v. 96, p. 1099-1119, doi: 10.1306/10171111052.

Chalmers, G. R. L., and R. M. Bustin, 2007, The organic matter distribution and methane capacity of the Lower Cretaceous strata of Northeastern British Columbia, Canada: International Journal of Coal Geology, v. 70, p. 223-239, doi: 10.1016/j.coal.2006.05.001.

Chalmers, G. R. L., D. J. K. Ross, and R. M. Bustin, 2012b, Geological controls on matrix permeability of Devonian gas shales in the Horn River and Liard Basins, northeastern British Columbia, Canada: International Journal of Coal Geology, v. 103, p. 120-131, doi: 10.1016/j.coal.2012.05.006.

Cheng, A.-L., and W.-L. Huang, 2004, Selective adsorption of hydrocarbon gases on clays and organic matter: Organic Geochemistry, v. 35, p. 413-423, doi: 10.1016/j.orggeochem.2004.01.007.

Clarkson, C. R., and R. M. Bustin, 1996, Variation in micropore capacity and size distribution with composition in bituminous coal of the Western Canadian sedimentary basin: Fuel, v. 75, p. 1483-1498, doi: 10.1016/0016-2361(96)00142-1.

Clarkson, C. R., and R. M. Bustin, 1999a, Binary gas adsorptionrdesorption isotherms: effect of moisture and coal composition upon carbon dioxide selectivity over methane: Fuel, v. 78, p. 1345-1362.

Clarkson, C. R., and R. M. Bustin, 1999b, The effect of pore structure and gas pressure upon the transport properties of coal: a laboratory and modeling study. 1. Isotherms and pore volume distributions: Fuel, v. 78, p. 1333-1344, doi: 10.1016/S0016-2361(99)00055-1.

Clarkson, C. R., M. Freeman, L. He, M. Agamalian, Y. B. Melnichenko, M. Mastalerz, R. M. Bustin, A. P. Radliński, and T. P. Blach, 2012, Characterization of tight gas reservoir pore structure using USANS/SANS and gas adsorption analysis: Fuel, v. 95, p. 371-385, doi: 10.1016/j.fuel.2011.12.010.

Clarkson, C. R., N. Solano, R. M. Bustin, A. M. M. Bustin, G. R. L. Chalmers, L. He, Y. B. Melnichenko, A. P. Radliński, and T. P. Blach, 2013, Pore structure characterization of North American shale gas reservoirs using USANS/SANS, gas adsorption, and mercury intrusion: Fuel, v. 103, p. 606-616, doi: 10.1016/j.fuel.2012.06.119.

Close, D., S. Stirling, D. Cho, and F. Horn, 2010, Tight gas geophysics: AVO inversion for reservoir characterization: CSEG Recorder, v. 35, p. 28-35.

Coates, G., L. Xiao, and G. Prammer, 1999, NMR logging. Principles and applications, Halliburton Energy Services, 234 p.

Concer, P. H., C. M. d. Oliveira, O. R. K. Montedo, E. Angioletto, M. Peterson, M. A. Fiori, and R. d. F. P. M. Moreira, 2017, Kinetics of the oxidation reactions and decomposition of pyrite: Cerâmica, v. 63, p. 39-43.

Cronin, M. B., 2014, Core-scale heterogeneity and dual-permeability pore structure in the Barnett shale, University of Texas and Austin.

Cui, X., A. M. M. Bustin, and R. M. Bustin, 2009, Measurements of gas permeability and diffusivity of tight reservoir rocks: different approaches and their applications: Geofluids, v. 9, p. 208-223, doi: 10.1111/j.1468-8123.2009.00244.x.

Curtis, M. E., and R. J. Ambrose, 2010, Investigating the Microstructure of Gas shales by FIB/SEM Tomography and STEM Imaging: SPE, SPE 137693.

Curtis, M. E., B. J. Cardott, C. H. Sondergeld, and C. S. Rai, 2012a, Development of organic porosity in the Woodford Shale with increasing thermal maturity: International Journal of Coal Geology, v. 103, p. 26-31, doi: 10.1016/j.coal.2012.08.004.

Curtis, M. E., E. T. Goergen, J. D. Jernigen, C. H. Sondergeld, and C. S. Rai, 2014, Mapping of organic matter distribution on the centimeter scale with nanometer resolution: Unconventional Resources Technology Conference, Denver, Colorado, USA, August 25-27, URTeC 1922757, 7 p, doi: 10.15530/urtec-2014-1922757.

Curtis, M. E., C. H. Sondergeld, R. J. Ambrose, and C. S. Rai, 2012b, Microstructural investigation of gas shales in two and three dimensions using nanometer-scale resolution imaging: AAPG Bulletin, v. 96, p. 665-677, doi: 10.1306/08151110188.

D'Alessandro, D. M., B. Smit, and J. R. Long, 2010, Carbon dioxide capture: prospects for new materials: Angew Chem Int Ed Engl, v. 49, p. 6058-6082, doi: 10.1002/anie.201000431.

Dewers, T. A., J. Heath, R. Ewy, and L. Duranti, 2012, Three-dimensional pore networks and transport properties of a shale gas formation determined from focused ion beam serial imaging: Gas and Coal Technology, v. 5, p. 229-248.

Durand, B., 1980, Kerogen: Insoluble Organic Matter from Sedimentary Rocks, Editions technip.

Earnest, C. M., 1991, Thermal analysis of selected illite and smectite clay minerals. Part I. Illite clay specimens: Thermal Analysis in the Geosciences, Berlin, Heidelberg, 270-286 p.

EIA, 2013, The Annual Energy Outlook 2013: U.S. Energy Information Administration.

Erdman, N., and N. Drenzek, 2013, Integrated preparation and imaging techniques for the microstructural and geochemical characterization of shale by scanning electron microscopy, *in* W. Camp, E. Diaz, and B. Wawak, eds., Electron Microscopy of Shale Hydrocarbon Reservoirs: AAPG Memoir, v. 102, p. 7-14, doi: 10.1306/13391700m1023581.

Ethington, E. F., 1990, Interfacial contact angle measurements of water, mercury, and 20 organic liquids on quartz, calcite, biotite, and Ca-montmorillonite substrates, p. 18.

Fauchille, A.-L., 2015, Déterminismes microstructuraux et minérologoques de la fissuration hydrique dans les argilites de Tournemire: apports couplés de la pétrographie quantitative et de la corrélation d'images numériques, University of Poitiers, France, 275 p.

Fauchille, A.-L., S. Hedan, V. Valle, D. Pret, J. Cabrera, and P. Cosenza, 2016, Multi-scale study on the deformation and fracture evolution of clay rock sample subjected to desiccation: Applied Clay Science, v. 132-133, p. 251-260, doi: 10.1016/j.clay.2016.01.054.

Fauchille, A.-L., D. Prêt, S. Hédan, V. Valle, J. Cabrera, and P. Cosenza, in preparation, Large field and beam drift corrected mosaic of BSE images for mineral mapping of shales: applications for quantitative petrography and experimental mechanics: Applied Clay Science.

Fialips, C. I., B. Labeyrie, V. Burg, V. Mazière, Y. Munerel, H. Haurie, I. Jolivet, R. Lasnel, J.-P. Laurent, L. Lambert, and L. Jacquelin-Vallée, 2018, Quantitative mineralogy of Vaca Muerta and Alum shales fromcCore chips and drill cuttings by calibrated SEM-EDS mineralogical mapping: URTeC 2018, v. 2902304, doi: 10.15530/urtec-2018-2902304.

Fishman, N. S., P. C. Hackley, H. A. Lowers, R. J. Hill, S. O. Egenhoff, D. D. Eberl, and A. E. Blum, 2012, The nature of porosity in organic-rich mudstones of the Upper Jurassic Kimmeridge clay Formation, North Sea, offshore United Kingdom: International Journal of Coal Geology, v. 103, p. 32-50, doi: 10.1016/j.coal.2012.07.012.

Fleury, M., 2014, Characterization of shales with low field NMR: International Symposium of core analysis, Avignon, France, September 8-11 SCA2014-014, 12 p.

Fleury, M., E. Kohler, F. Norrant, S. Gautier, J. M'Hamdi, and L. Barré, 2013, Characterization and quantification of water in smectites with low-feld NMR: The Journal of Physical Chemistry C, v. 117, p. 4551-4560, doi: 10.1021/jp311006q.

Fleury, M., and M. Romero-Sarmiento, 2016, Characterization of shales using T1–T2 NMR maps: Journal of Petroleum Science and Engineering, v. 137, p. 55-62, doi: 10.1016/j.petrol.2015.11.006.

Frost, R. L., M. C. Hales, and W. N. Martens, 2008, Thermogravimetric analysis of selected group (II) carbonateminerals — Implication for the geosequestration of greenhouse gases: Journal of Thermal Analysis and Calorimetry, v. 95, p. 999, doi: 10.1007/s10973-008-9196-7.

Gaboreau, S., D. Prêt, E. Tinseau, F. Claret, D. Pellegrini, and D. Stammose, 2011, 15 years of in situ cement–argillite interaction from Tournemire URL: Characterisation of the multi-scale spatial heterogeneities of pore space evolution: Applied Geochemistry, v. 26, p. 2159-2171, doi: 10.1016/j.apgeochem.2011.07.013.

Gaboreau, S., J. C. Robinet, and D. Prêt, 2016, Optimization of pore-network characterization of a compacted clay material by TEM and FIB/SEM imaging: Microporous and Mesoporous Materials, v. 224, p. 116-128, doi: 10.1016/j.micromeso.2015.11.035.

Gamero-Diaz, H., C. Miller, and R. Lewis, 2012, sCore: a classification scheme for organic mudstones based on bulk mineralogy: Search and Discovery Articles, #40951.

Gan, H., S. P. Nandi, and P. L. Walker, 1972, Nature of porosity in american coals: Fuel, v. 51, p. 272-277.

Gasparik, M., T. F. T. Rexer, A. C. Aplin, P. Billemont, G. De Weireld, Y. Gensterblum, M. Henry, B. M. Krooss, S. Liu, X. Ma, R. Sakurovs, Z. Song, G. Staib, K. M. Thomas, S. Wang, and T. Zhang, 2014, First international inter-laboratory comparison of high-pressure CH4, CO2 and C2H6 sorption isotherms on carbonaceous shales: International Journal of Coal Geology, v. 132, p. 131-146, doi: 10.1016/j.coal.2014.07.010.

Giffin, S., R. Littke, J. Klaver, and J. L. Urai, 2013, Application of BIB–SEM technology to characterize macropore morphology in coal: International Journal of Coal Geology, v. 114, p. 85-95, doi: 10.1016/j.coal.2013.02.009.

Gitman, I. M., M. B. Gitman, and H. Askes, 2005, Quantification of stochastically stable representative volumes for random heterogeneous materials: Archive of Applied Mechanics, v. 75, p. 79-92, doi: 10.1007/s00419-005-0411-8.

Goldstein, J. I., C. E. Lyman, D. E. Newbury, E. Lifshin, P. Echlin, L. Sawyer, D. C. Joy, and J. R. Michael, 2003, Scanning electron microscopy and X-ray microanalysis: New York, Kluwer Academic/Plenum Publishers, 689 p.

Gregg, S. J., and K. S. W. Sing, 1982, Adsorption, surface area and porosity, Academic Press.

Grim, R. E., and W. F. Bradley, 1948, Rehydration and dehydration of the clay minerals: American Mineralogist, v. 33, p. 50-59.

Gu, X., D. R. Cole, G. Rother, D. F. R. Mildner, and S. L. Brantley, 2015, Pores in Marcellus Shale: A Neutron Scattering and FIB-SEM Study: Energy & Fuels, v. 29, p. 1295-1308, doi: 10.1021/acs.energyfuels.5b00033.

Gu, X., D. F. R. Mildner, D. R. Cole, G. Rother, R. Slingerland, and S. L. Brantley, 2016, Quantification of organic porosity and water accessibility in Marcellus Shale using neutron scattering: Energy & Fuels, v. 30, p. 4438-4449, doi: 10.1021/acs.energyfuels.5b02878.

Han, Y., B. Horsfield, R. Wirth, N. Mahlstedt, and S. Bernard, 2017, Oil retention and porosity evolution in organic-rich shales: AAPG Bulletin, v. 101, p. 807-827, doi: 10.1306/09221616069.

Harkins, W. D., and G. Jura, 1944, Surfaces of solids. XIII. A vapor adsorption method for the determination of the area of a solid without the assumption of a molecular area, and the areas occupied by nitrogen and other molecules on the surface of a solid.: Journal of American Chemical society, v. 66, p. 1366-1373, doi: 10.1021/ja01236a048.

Hartman, R. C., P. Lasswell, and N. Bhatta, 2008, Recent advances in the analytical methods used for shale gas reservoir gas-in-place assessment, v. #40317, p. 32.

Heath, J. E., T. A. Dewers, B. J. O. L. McPherson, R. Petrusak, T. C. Chidsey, A. J. Rinehart, and P. S. Mozley, 2011, Pore networks in continental and marine mudstones: Characteristics and controls on sealing behavior: Geosphere, v. 7, p. 429-454, doi: 10.1130/ges00619.1.

Hellmuth, K. H., M. Shtari-Kauppi, and A. Lindberg, 1991, Applications of the Carbon-14-Polymethylmethacrylate (PMMA) Impregnation Method in Studies on Porosity and Matrix Diffusion: MRS Proceedings, v. 257, p. 649, doi: 10.1557/PROC-257-649.

Hellmuth, K. H., and M. Siitari-Kauppi, 1990, Investigation of the porosity of rocks. Impregnation with 14C-polymethylmethacrylate (PMMA) ,a new technique STUK-B-VALO 63, p. 67.

Hellmuth, K. H., M. Siitari-Kauppi, and A. Lindberg, 1993, Study of porosity and migration pathways in crystalline rock by impregnation with 14C-polymethylmethacrylate: Journal of Contaminant Hydrology, v. 13, p. 403-418, doi: 10.1016/0169-7722(93)90073-2.

Hemes, S., G. Desbois, J. L. Urai, M. De Craen, and M. Honty, 2014, Variations in the morphology of porosity in the Boom Clay Formation: insights from 2D high resolution BIB-SEM imaging and Mercury injection Porosimetry: Netherlands Journal of Geosciences, v. 92, p. 275-300, doi: 10.1017/s0016774600000214.

Holmes, M., A. Holmes, and D. Holmes, 2012, A petrophysical model for shale reservoirs to distinguish macro porosity, free shale porosity and TOC, AAPG ACE, California, USA.

Houben, M. E., A. Barnhoorn, J. Lie-A-Fat, T. Ravestein, C. J. Peach, and M. R. Drury, 2016a, Microstructural characteristics of the Whitby Mudstone Formation (UK): Marine and Petroleum Geology, v. 70, p. 185-200, doi: 10.1016/j.marpetgeo.2015.11.011.

Houben, M. E., A. Barnhoorn, L. Wasch, J. Trabucho-Alexandre, C. J. Peach, and M. R. Drury, 2016b, Microstructures of Early Jurassic (Toarcian) shales of Northern Europe: International Journal of Coal Geology, v. 165, p. 76-89, doi: 10.1016/j.coal.2016.08.003.

Houben, M. E., G. Desbois, and J. L. Urai, 2013, Pore morphology and distribution in the Shaly facies of Opalinus Clay (Mont Terri, Switzerland): Insights from representative 2D BIB–SEM investigations on mm to nm scale: Applied Clay Science, v. 71, p. 82-97, doi: 10.1016/j.clay.2012.11.006.

Houben, M. E., G. Desbois, and J. L. Urai, 2014, A comparative study of representative 2D microstructures in Shaly and Sandy facies of Opalinus Clay (Mont Terri, Switzerland) inferred

form BIB-SEM and MIP methods: Marine and Petroleum Geology, v. 49, p. 143-161, doi: 10.1016/j.marpetgeo.2013.10.009.

Howell, J. A., E. S. Schwarz, L. A. Spalletti, and G. D. Veiga, 2005, The Neuquén Basin: an overview: Geological Society London Special Publications, v. 252, p. 1-14.

ISO 25178-2, A., 2012, Geometrical product specifications (GPS). Surface texture: Areal. Part 2: Terms, definitions and surface texture parameters, v. NF EN ISO 25178-2, p. 58.

Janssen, C., R. Wirth, A. Reinicke, E. Rybacki, R. Naumann, H.-R. Wenk, and G. Dresen, 2011, Nanoscale porosity in SAFOD core samples (San Andreas Fault): Earth and Planetary Science Letters, v. 301, p. 179-189, doi: 10.1016/j.epsl.2010.10.040.

Jarvie, D. M., R. J. Hill, T. E. Ruble, and R. M. Pollastro, 2007, Unconventional shale-gas systems: the Mississippian Barnett Shale of North-central Texas as one model for thermogenic shale-gas assessment: AAPG Bulletin, v. 91, p. 475-499, doi: 10.1306/12190606068.

Jiao, K., S. Yao, C. Liu, Y. Gao, H. Wu, M. Li, and Z. Tang, 2014, The characterization and quantitative analysis of nanopores in unconventional gas reservoirs utilizing FESEM–FIB and image processing: An example from the lower Silurian Longmaxi Shale, upper Yangtze region, China: International Journal of Coal Geology, v. 128-129, p. 1-11, doi: 10.1016/j.coal.2014.03.004.

Jin, L., G. Rother, D. R. Cole, D. F. R. Mildner, C. J. Duffy, and S. L. Brantley, 2011, Characterization of deep weathering and nanoporosity development in shale-a neutron study: American Mineralogist, v. 96, p. 498-512, doi: 10.2138/am.2011.3598.

Kanaya, K., and S. Okayama, 1972, Penetration and energy-loss theory of electrons in solid targets: Journal of Physics D: Applied Physics, v. 5, p. 43.

Kaufhold, S., G. Grathoff, M. Halisch, M. Plotze, J. Kus, K. Ufer, R. Dohrmann, S. Ladage, and C. Ostertag-Henning, 2016, Comparison of methods for the determination of the pore system of a potential German gas shale: The Clay Minerals Society Workshop Lectures Series, v. 21, p. 163-190, doi: 10.1346/cms-wls-21.13.

Kelly, S., H. El-Sobky, C. Torres-Verdín, and M. T. Balhoff, 2015, Assessing the utility of FIB-SEM images for shale digital rock physics: Advances in Water Resources, v. 95, p. 302-316, doi: 10.1016/j.advwatres.2015.06.010.

Kietzmann, D. A., A. L. Ambrosio, J. Suriano, M. S. Alonso, F. G. Tomassini, G. Depine, and D. Repol, 2016, The Vaca Muerta–Quintuco system (Tithonian–Valanginian) in the Neuquén Basin, Argentina: a view from the outcrops in the Chos Malal fold and thrust belt: AAPG Bulletin, v. 100, p. 743-771, doi: 10.1306/02101615121.

Kietzmann, D. A., R. M. Palma, and G. S. Bressan, 2008, Facies y microfacies de la rampa tithoniana–berriasiana de la Cuenca Neuquina (Formación Vaca Muerta) en la sección del Arroyo Loncoche – Malargüe, provincia de Mendoza.: Revista de la Asociación Geológica Argentina, v. 63, p. 696–713.

Kietzmann, D. A., and V. V. Vennari, 2013, Sedimentology and stratigraphy of the Vaca Muerta Formation in the Cerro Domuyo area, Northern Neuquén, Argentina: Andean Geology, v. 40, doi: 10.5027/andgeoV40n1-a02.

Kim, J. W., D. R. Peacor, D. Tessier, and F. Elsass, 1995, A technique for maintaining texture and permanent expansion of smectite interlayers for TEM observations.: Clays and Clay Minerals, v. 43, p. 51-57.

Klaver, J., G. Desbois, R. Littke, and J. L. Urai, 2015, BIB-SEM characterization of pore space morphology and distribution in postmature to overmature samples from the Haynesville and Bossier shales: Marine and Petroleum Geology, v. 59, p. 451-466, doi: 10.1016/j.marpetgeo.2014.09.020.

Klaver, J., G. Desbois, J. L. Urai, and R. Littke, 2012, BIB-SEM study of the pore space morphology in early mature Posidonia Shale from the Hils area, Germany: International Journal of Coal Geology, v. 103, p. 12-25, doi: 10.1016/j.coal.2012.06.012.

Ko, L. T., R. G. Loucks, S. C. Ruppel, T. Zhang, and S. Peng, 2017, Origin and characterization of Eagle Ford pore networks in the South Texas Upper Cretaceous shelf: AAPG Bulletin, v. 101, p. 387-418, doi: 10.1306/08051616035.

Krinsley, D. H., K. Pye, S. J. Boggs, and N. K. Tovey, 2005, Backscattered Scanning Electron Microscopy and Image Analysis of Sediments and Sedimentary Rocks, Cambridge University Press.

Kuila, U., D. K. McCarty, A. Derkowski, T. B. Fischer, T. Topór, and M. Prasad, 2014, Nano-scale texture and porosity of organic matter and clay minerals in organic-rich mudrocks: Fuel, v. 135, p. 359-373, doi: 10.1016/j.fuel.2014.06.036.

Kuila, U., and M. Prasad, 2013, Understanding pore-structure and permeability in shales: SPE Annual Technical Conference and Exhibition, Denver, Colorado, USA, 30 October-2 November, SPE-146869-MS, 13 p, doi: 10.2118/146869-ms.

Lazar, O. R., K. M. Bohacs, J. H. S. Macquaker, J. Schieber, and T. M. Demko, 2015, Capturing Key Attributes of Fine-Grained Sedimentary Rocks In Outcrops, Cores, and Thin Sections: Nomenclature and Description Guidelines: Journal of Sedimentary Research, v. 85, p. 230-246, doi: 10.2110/jsr.2015.11.

Lee, S., 1991, Oil Shale Technology.

Lejay, A., S. Larmier, F. Gelin, and A. Zanella, 2017, The role of porosity in the development of parallel bedded calcite filled fractures (or beef) in the Vaca Muerta: an integrated analysis from high resolution core data.: Unconventional Resources and Technology Conference, Austin, USA, July 24-27, URTeC 2668071, doi: 10.15530/urtec-2017-2668071.

Leon y Leon, C. A., 1998, New perspectives in mercury porosimetry: Advances in Colloid Interface Science, v. 76-77, p. 341-372.

Lewis, R., P. Singer, T. Jiang, E. Rylander, S. Sinclair, and R. H. McLin, 2013, NMR T2 distributions in the Eagle Ford shale: reflections on pore size: SPE Unconventional Resources Conference, The Woodlands, Texas, USA, April 10-12, SPE-164554-MS, doi: 10.2118/164554-ms.

Löhr, S. C., E. T. Baruch, P. A. Hall, and M. J. Kennedy, 2015, Is organic pore development in gas shales influenced by the primary porosity and structure of thermally immature organic matter?: Organic Geochemistry, v. 87, p. 119-132, doi: 10.1016/j.orggeochem.2015.07.010.

Loucks, R. G., R. M. Reed, S. C. Ruppel, and U. Hammes, 2012, Spectrum of pore types and networks in mudrocks and a descriptive classification for matrix-related mudrock pores: AAPG Bulletin, v. 96, p. 1071-1098, doi: 10.1306/08171111061.

Loucks, R. G., R. M. Reed, S. C. Ruppel, and D. M. Jarvie, 2009, Morphology, genesis, and distribution of nanometer-scale pores in siliceous mudstones of the Mississippian Barnett Shale: Journal of Sedimentary Research, v. 79, p. 848-861, doi: 10.2110/jsr.2009.092.

Lowell, S., J. E. Shields, M. A. Thomas, and M. Thommes, 2004, Characterization of porouse solids and powders: surface area, pore size and density, *in* B. Scarlett, ed., New York, Springer Science.

Ma, L., A.-L. Fauchille, P. J. Dowey, F. Figueroa Pilz, L. Courtois, K. G. Taylor, and P. D. Lee, 2017a, Correlative multi-scale imaging of shales: a review and future perspectives: Geological Society, London, Special Publications, v. 454, p. 175-199, doi: 10.1144/sp454.11.

Ma, L., K. G. Taylor, P. J. Dowey, L. Coutois, A. Gholinia, and P. D. Lee, 2017b, Multi-scale 3D characterisation of porosity and organic matter in shales with variable TOC content and thermal maturity: Examples from the Lublin and Baltic Basins, Poland and Lithuania: International Journal of Coal Geology, v. 180, p. 100-112, doi: 10.1016/j.coal.2017.08.002.

Ma, L., K. G. Taylor, P. D. Lee, K. J. Dobson, P. J. Dowey, and L. Coutois, 2016, Novel 3D centimetre-to nano-scale quantification of an organic-rich mudstone: The Carboniferous Bowland Shale, Northern England: Marine and Petroleum Geology, v. 72, p. 193-205, doi: 10.1016/j.marpetgeo.2016.02.008.

Ma, Y., N. Zhong, D. Li, Z. Pan, L. Cheng, and K. Liu, 2015, Organic matter/clay mineral intergranular pores in the Lower Cambrian Lujiaping Shale in the north-eastern part of the upper Yangtze area, China: a possible microscopic mechanism for gas preservation: International Journal of Coal Geology, v. 137, p. 38-54, doi: 10.1016/j.coal.2014.11.001.

Magoon, L. B., and W. G. Dow, eds., 1994, The petroleum system-from source to trap: AAPG Memoir, v. 60, 639 p, doi: 10.1306/M60585C1.

Marsh, H., 1987, Adsorption methods to study microporosity in coals and carbons - a critique: Carbon, v. 25, p. 49-58.

Mastalerz, M., A. Schimmelmann, A. Drobniak, and Y. Chen, 2013, Porosity of Devonian and Mississippian New Albany Shale across a maturation gradient: insights from organic petrology, gas adsorption, and mercury intrusion: AAPG Bulletin, v. 97, p. 1621-1643, doi: 10.1306/04011312194.

McCain, W. D., 1990, The properties of petroleum fluids, PennWell Books.

McCarthy, K., K. Rojas, M. Niemann, D. Palmowski, K. Peters, and A. Stankiewicz, 2011, Basic petroleum geochemistry for source rock evaluation: Oilfield review, v. summer 2011.

Melnichenko, Y. B., L. He, R. Sakurovs, A. L. Kholodenko, T. Blach, M. Mastalerz, A. P. Radliński, G. Cheng, and D. F. R. Mildner, 2012, Accessibility of pores in coal to methane and carbon dioxide: Fuel, v. 91, p. 200-208, doi: 10.1016/j.fuel.2011.06.026.

Meunier, A., 2005, Clays, Springer, 472 p.

Micromeritics, 2012, Manual book for AutoPore IV equipment. Application notes.

Milliken, K. L., L. T. Ko, M. Pommer, and K. M. Marsaglia, 2014, SEM petrography of Eastern Mediterranean sapropels: analogue data for assessing organic matter in oil and gas shales: Journal of Sedimentary Research, v. 84, p. 961-974, doi: 10.2110/jsr.2014.75.

Milliken, K. L., M. Rudnicki, D. N. Awwiller, and T. Zhang, 2013, Organic matter-hosted pore system, Marcellus Formation (Devonian), Pennsylvania: AAPG Bulletin, v. 97, p. 177-200, doi: 10.1306/07231212048.

Minsky, M., 1988, Memoir on inventing the confocal scanning microscope: Scanning, v. 10, p. 128-138.

Münch, B., and L. Holzer, 2008, Contradicting geometrical concepts in pore size analysis attained with electron microscopy and mercury intrusion: Journal of the American Ceramic Society, v. 91, p. 4059-4067, doi: 10.1111/j.1551-2916.2008.02736.x.

Nelson, P. H., 2009, Pore-throat sizes in sandstones, tight sandstones, and shales: AAPG Bulletin, v. 93, p. 329-340, doi: 10.1306/10240808059.

NIST, 2015, Scattering length density calculator: National Institute of Standards an Technology (NIST) Center for Neutron Research, Gainthersburg, MD.

Noiriel, C., 2015, Resolving time-dependent evolution of pore-scale structure, permeability and reactivity using X-ray microtomography: Reviews in Mineralogy and Geochemistry, v. 80, p. 247-285, doi: 10.2138/rmg.2015.80.08.

Odusina, E. O., C. H. Sondergeld, and C. S. Rai, 2011, NMR study of shale wettability: Canadian Unconventional Resources Conference, 15-17 November, Alberta, Canada, Alberta, Canada, November 15-17, SPE-147371-MS, doi: 10.2118/147371-ms.

Ojha, S. P., S. Misra, A. Sinha, Dang, C. Sondergeld, and C. Rai, 2017, Estimation of pore network characteristics and saturation-dependent relative permeability in organic-rich shale samples obtained from Bakken, Wolfcamp and woodford shale formations SPWLA 58th Annual Logging Symposium, Society of Petrophysicists and Well-Log Analysts, June 17-21.

Orsini, L., and J. C. Remy, 1976, Utilisation du chlorure de cobaltihexammine pour la détermination simultanée de la capacité d'échange et des bases échangeables des sols. : Bulletin de l'AFES, Science du Sol, v. 4, p. 269-275.

Otsu, N., 1979, Threshold Selection Method from Gray-Level Histograms.: IEEE, v. 9, p. 62-66.

Ougier-Simonin, A., F. Renard, C. Boehm, and S. Vidal-Gilbert, 2016, Microfracturing and microporosity in shales: Earth-Science Reviews, v. 162, p. 198-226, doi: 10.1016/j.earscirev.2016.09.006.

Pallasser, R., B. Minasny, and A. B. McBratney, 2013, Soil carbon determination by thermogravimetrics: PeerJ, v. 1, p. e6, doi: 10.7717/peerj.6.

Panahi, H., M. Kobchenko, F. Ranard, A. Mazzini, J. Scheibert, D. K. Dysthe, B. Jamtveit, A. Malthe-Sorenssen, and P. Meakin, 2017, A 4D synchrotron X-ray tomography study of the formation of hydrocarbon migration pathways in heated organic-rich shale.

Passey, Q. R., K. M. Bohacs, W. L. Esch, R. Klimentidis, and S. Sinha, 2010, From oil-prone source rock to gas producing shale reservoir—Geologic and petrophysical characterization of unconventional shale-gas reservoirs: Society of Petroleum Engineers International Oil and Gas,

Conference and Exhibition in China, Beijing, June 8-10, SPE-131350, 29 p, doi: 10.2118/131350-MS.

Peng, S., T. Zhang, R. G. Loucks, and J. Shultz, 2017, Application of mercury injection capillary pressure to mudrocks: Conformance and compression corrections: Marine and Petroleum Geology, v. 88, p. 30-40, doi: https://doi.org/10.1016/j.marpetgeo.2017.08.006.

Pommer, M., and K. Milliken, 2015, Pore types and pore-size distributions across thermal maturity, Eagle Ford Formation, Southern Texas: AAPG Bulletin, v. 99, p. 1713-1744, doi: 10.1306/03051514151.

PR40-1, A., 1998, Recommended practices for core analysis: American Petrolium Institute, v. API PR40-1, p. 236.

Prêt, D., 2003, Nouvelles méthodes quantitatives de cartographie de la minéralogie et de la porosité dans les matériaux argileux: application aux bentonites compactées des barrières ouvragées, University of Poitiers, 281 p.

Prêt, D., E. Ferrage, E. Tertre, M. Pelletier, J. C. Robinet, M. Faurel, I. Bihannic, and F. Huber, 2013, X-ray tomography and impregnation methods to analyze pore spacehetreogeneities at the hydrated state: NEA/RWM/CLAYCLUB(2013)1/REV.

Prêt, D., S. Sammartino, D. Beaufort, M. Fialin, P. Sardini, P. Cosenza, and A. Meunier, 2010a, A new method for quantitative petrography based on image processing of chemical element maps: Part II. Semi-quantitative porosity maps superimposed on mineral maps: American Mineralogist, v. 95, p. 1389-1398, doi: 10.2138/am.2010.3433.

Prêt, D., S. Sammartino, D. Beaufort, A. Meunier, M. Fialin, and L. J. Michot, 2010b, A new method for quantitative petrography based on image processing of chemical element maps: Part I. Mineral mapping applied to compacted bentonites: American Mineralogist, v. 95, p. 1379-1388, doi: 10.2138/am.2010.3431.

Prêt, D., P. Sardini, D. Beaufort, R. Zellagui, and S. Sammartino, 2004, Porosity distribution in a clay gouge by image processing of 14C-Polymethylmethacrylate (14C-PMMA) autoradiographs: Applied Clay Science, v. 27, p. 107-118, doi: 10.1016/j.clay.2004.03.005.

Radlinski, A. P., 2006, Small-Angle Neutron Scattering and the Microstructure of Rocks: Reviews in Mineralogy and Geochemistry, v. 63, p. 363-397, doi: 10.2138/rmg.2006.63.14.

Rajeshwar, K., 1981, The kinetics of the thermal decomposition of green river oil shale kerogen by non-Isothermal thermogravimetry, v. 45, 253-263 p, doi: 10.1016/0040-6031(81)85086-1.

Rasband, W. S., 2010, ImageJ, http://imagej.nih.gov/ij/, U.S. National Institutes of Health, Bethesda, Maryland.

Rasband, W. S., 2012, Gaussian Blur 3D plugin: https://imagej.nih.gov/ij/plugins/gaussian-blur-3d/index.html.

Ratner, M., and M. Tiemann, 2014, An overview of unconventional oil and natural gas: resources and federal actions, p. 30.

Ravikovitch, P. I., and A. V. Neimark, 2001, Characterization of nanoporous materials from adsorption and desorption isotherms: Colloids and surfaces, v. 187-188, p. 11-21, doi: 10.1016/S0927-7757(01)00614-8.

Reed, R. M., R. G. Loucks, and S. C. Ruppel, 2014, Comment on "Formation of nanoporous pyrobitumen residues during maturation of the Barnett Shale (Fort Worth Basin)" by Bernard et al. (2012): International Journal of Coal Geology, v. 127, p. 111-113, doi: 10.1016/j.coal.2013.11.012.

Reed, S. J. B., 1996, Electron microprobe analysis and scanning slectron microscopy in geology Cambridge University press, 238 p.

Renard, F., B. Cordonnier, M. Kobchenko, N. Kandula, J. Weiss, and W. Zhu, 2017, Microscale characterization of rupture nucleation unravels precursors to faulting in rocks, v. 476, 69-78 p, doi: 10.1016/j.epsl.2017.08.002.

Rexer, T. F., E. J. Mathia, A. C. Aplin, and K. M. Thomas, 2014, High-pressure methane adsorption and characterization of pores in Posidonia shales and isolated kerogens: Energy & Fuels, v. 28, p. 2886-2901, doi: 10.1021/ef402466m.

Rezaee, R., 2015, Fundamentals of gas shale reservoirs: Wiley, USA.

Robinet, J.-C., P. Sardini, D. Coelho, J.-C. Parneix, D. Prêt, S. Sammartino, E. Boller, and S. Altmann, 2012, Effects of mineral distribution at mesoscopic scale on solute diffusion in a clay-rich rock: Example of the Callovo-Oxfordian mudstone (Bure, France): Water Resources Research, v. 48, p. n/a-n/a, doi: 10.1029/2011wr011352.

Robinet, J. C., P. Sardini, M. Siitari-Kauppi, D. Prêt, and B. Yven, 2015, Upscaling the porosity of the Callovo-Oxfordian mudstone from the pore scale to the formation scale; insights from the 3H-PMMA autoradiography technique and SEM BSE imaging: Sedimentary Geology, v. 312, p. 1-10.

Ross, D. J. K., and R. Marc Bustin, 2009, The importance of shale composition and pore structure upon gas storage potential of shale gas reservoirs: Marine and Petroleum Geology, v. 26, p. 916-927, doi: 10.1016/j.marpetgeo.2008.06.004.

Rouquerol, J., D. Avnir, C. W. Fairbridge, D. H. Everett, J. H. Haynes, N. Pernicone, J. D. F. Ramsay, K. S. W. Sing, and K. K. Unger, 1994, Recommendations for the characterization of porous solids: Pure and Applied Chemistry, v. 66, p. 1739-1758, doi: 10.1351/pac199466081739.

Rozenbaum, O., and S. R. du Roscoat, 2014, Representative elementary volume assessment of three-dimensional x-ray microtomography images of heterogeneous materials: application to limestones: Physical Review E, v. 89, doi: 10.1103/PhysRevE.89.053304.

Sammartino, S., M. Siitari-Kauppi, A. Meunier, P. Sardini, A. Bouchet, and E. Tevissen, 2002, An imaging method for the porosity of sedimentary rocks: adjustment of the PMMA method - example of the characterization of calcareous shale: Journal of Sedimentary Research, v. 72, p. 937-943, doi: 10.1306/053002720937.

Sanchez del Rio, M., and R. J. Dejus, 2011, XOP v2.4: recent developments of the xray optics software toolkit Processing SPIE: 814115, v. 8141, doi: dx.doi.org/10.1117/12.893911.

Schieber, J., 2013, SEM observations on ion-milled samples of Devonian Black Shales from Indiana and New York: the petrographic context of multiple pore types, *in* W. Camp, E. Diaz, and B. Wawak,

eds., Electron Microscopy of Shale Hydrocarbon Reservoirs: AAPG Memoir v. 102, p. 153-171, doi: 10.1306/13391711m1023589.

Schlumberger, 1991a, Log interpretation principles/applications: Shlumberger Wireline and Testing.

Schlumberger, 1991b, Vertical resolution of well logs: recent developments: Oilfield review, v. 3, p. 24-28.

Schmidt, N. G., J. C. Alonso, A. Giusiano, C. Lauri, and T. Sales, 2014, El shale de la formacion Vaca Muerta: integracion de datos y estimacion de recursos de petroleo y gas asociado: IX Congreso de Ewploracion y Desarrollo de Hidrocaruros: Simposio de Recursos No convencionales.

Sclater, J. G., and P. A. F. Christie, 1980, Continental stretching: an explanation of the Post-Mid-Cretaceous subsidence of the central North Sea Basin: Journal of Geophysical Research: Solid Earth, v. 85, p. 3711-3739, doi: 10.1029/JB085iB07p03711.

Serra, O., 1984, Fundamentals of Well-log Interpretation: The acquisition of logging data, Elsevier.

Sigal, R. F., 2009, A methodology for blank and conformance corrections for high pressure mercury porosimetry: Measurement Science and Technology, v. 20, p. 12, doi: 10.1088/0957-0233/20/4/045108.

Sigal, R. F., 2013, Mercury capillary pressure measurements on Barnett core: SPE Reservoir Evaluation & Engineering, v. Spe -167607-PA, p. 432-442.

Sing, K. S. W., 1998, Adsorption methods for the characterization of porous materials: Advances in Colloid and Interface Science, v. 76-77, p. 3-11, doi: 10.1016/S0001-8686(98)00038-4.

Sing, K. S. W., 2001, The use of nitrogen adsorption for the characterisation of porous materials: Colloids and Surfaces, v. 187-188, p. 3-9.

Smith, A. J., P. R. Munroe, T. Tran, and M. S. Wainwright, 2001, FIB preparation of a sensitive porous catalyst for TEM elemental mapping at high magnifications: Journal of Material Science, v. 36, p. 3519-3524.

Smykatz-Kloss, W., A. Heil, L. Kaeding, and E. Roller, 1991, Thermal analysis in environmental studies: Thermal Analysis in the Geosciences, Berlin, Heidelberg, 352-367 p.

Smykatz-Kloss, W., and S. S. J. Warne, 1991, Thermal Analysis in the Geosciences doi: 10.1007/bfb0010257.

Sørland, G. H., K. Djurhuus, H. C. Widerøe, J. R. Lien, and A. Skauge, 2007, Absolute pore size distribution from NMR: Diffusion Fundamentals, v. 5, p. 4.1-4.15.

Taylor, B. N., and A. Thompson, 2008, The International System of Units (SI) (Special publication 330).

Tessier, D., 1984, Etude expérimentale de l'organisation des matériaux argileux. Hydratation, gonflement et structuration au cours de la dessiccation et de la ré-humectation. , *in* U. P. VII, ed., INRA Versailles Ed, p. 361.

Thommes, M., K. Kaneko, A. V. Neimark, J. P. Olivier, F. Rodriguez-Reinoso, J. Rouquerol, and K. S. W. Sing, 2015, Physisorption of gases, with special reference to the evaluation of surface area and

pore size distribution (IUPAC technical report): Pure and Applied Chemistry, v. 87, p. 1051–1069, doi: 10.1515/pac-2014-1117.

Tian, H., L. Pan, X. Xiao, R. W. T. Wilkins, Z. Meng, and B. Huang, 2013, A preliminary study on the pore characterization of Lower Silurian black shales in the Chuandong Thrust Fold Belt, southwestern China using low pressure N2 adsorption and FE-SEM methods: Marine and Petroleum Geology, v. 48, p. 8-19, doi: 10.1016/j.marpetgeo.2013.07.008.

Tissot, B. P., and D. H. Welte, 1984, Petroleum formation and occurrence, Springer and Verlag, 699 p, doi: 10.1007/978-3-642-87813-8.

Tiwari, P., 2012, Oil shale pyrolysis: Benchscale experimental studies and modeling, University of Utah, Departament of Chemical Engineering.

Topór, T., A. Derkowski, U. Kuila, T. B. Fischer, and D. K. McCarty, 2016, Dual liquid porosimetry: A porosity measurement technique for oil- and gas-bearing shales: Fuel, v. 183, p. 537-549, doi: 10.1016/j.fuel.2016.06.102.

Torrente, M. C., and M. A. Galán, 2011, Extraction of Kerogen from Oil Shale (Puertollano, Spain) with Supercritical Toluene and Methanol Mixtures: Industrial & Engineering Chemistry Research, v. 50, p. 1730-1738, doi: 10.1021/ie1004509.

Total.com, 2014, Atypical Reservoirs: Tight Gas, Shale Gas and Coalbed Methane, http://www.total.com/en/energies-expertise/oil-gas/exploration-production/strategic-sectors/unconventional-gas/presentation/three-main-sources-unconventional-gas.

Tovey, N. K., and M. W. Hounslow, 1995, Quantitative micro-porosity and orientation analysis in soils and sediments: Journal of Geological Society, v. 152, p. 119-129.

Vandenbroucke, M., and C. Largeau, 2007, Kerogen origin, evolution and structure: Organic Geochemistry, v. 38, p. 719-833, doi: 10.1016/j.orggeochem.2007.01.001.

Vermesse, J., D. Vidal, and P. Malbrunot, 1996, Gas adsorption on zeolites at high pressure: Langmuir, v. 12, p. 4190-4196.

Vidic, R. D., S. L. Brantley, J. M. Vandenbossche, D. Yoxtheimer, and J. D. Abad, 2013, Impact of shale gas development on regional water quality: Science, v. 340, p. 1235009, doi: 10.1126/science.1235009.

Warne, S. S. J., 1991, Variable atmosphere thermal analysis — methods, gas atmospheres and applications to geoscience materials: Thermal Analysis in the Geosciences, Berlin, Heidelberg, 61-83 p.

Washburn, E. W., 1921, Note on a method of determining the distribution of pore sizes in a porous material: Proceedings of the National Academy of Sciences of the USA, v. 7, p. 115-116, doi: 10.1073/pnas.7.4.115.

Washburn, K. E., and J. E. Birdwell, 2013, Updated methodology for nuclear magnetic resonance characterization of shales: J Magn Reson, v. 233, p. 17-28, doi: 10.1016/j.jmr.2013.04.014.

Wust, R. A. J., A. Cui, N. B.R., and R. M. Bustin, 2014, Rock characteristics of oil-, condensate- and dry gas-producing wells of the unconventional Devonian Duvernay Formation, Canada: International Petrolium Technology Conference, Kuala Lumpur, Malaysia.

Yang, R., S. He, Q. Hu, M. Sun, D. Hu, and J. Yi, 2017, Applying SANS technique to characterize nano-scale pore structure of Longmaxi shale, Sichuan Basin (China): Fuel, v. 197, p. 91-99, doi: 10.1016/j.fuel.2017.02.005.

Zeller, M., 2013, Facies, Geometries and Sequence Stratigraphy of the Mixed Carbonate - Siliciclastic Quintuco - Vaca Muerta System in the Neuquen Basin, Argentina: An Integrated Approach, *in* U. o. Miami, ed.

Zeller, M., K. Verwer, G. P. Eberli, J. L. Massaferro, E. Schwarz, and L. Spalletti, 2015, Depositional controls on mixed carbonate-siliciclastic cycles and sequences on gently inclined shelf: Sedimentology, v. 62, p. 2009-2037, doi: 10.1111/sed.12215.

Zhang, B., A. M. Gomaa, H. Sun, Q. Qu, and J.-H. Chen, 2014, A study of shale wettability using NMR measurements: International Symposium of the Society of Core Analysis, Avignon, France.

Zhang, D., R. Zhang, S. Chen, and W. E. Soll, 2000, Pore scale study of flow in porous media: Scale dependency, REV, and statistical REV: Geophysical Research Letters, v. 27, p. 1195-1198, doi: 10.1029/1999gl011101.

Zhang, S., R. E. Klimentidis, and P. Barthelemy, 2012, Micron to millimeter upscalling of shale rock properties based on 3D imaging and modelling, International Symposium of the Society of Core Analysis, Aberdeen, Scotland, UK.